KU LEUVEN

ARENBERG DOCTORAL SCHOOL
Faculty of Science

Probing the Semi-Magicity of ^{68}Ni via the ^{66}Ni(t,p)^{68}Ni Two-Neutron Transfer Reaction in Inverse Kinematics

Jytte Elseviers

Dissertation presented in partial fulfillment of the requirements for the degree of Doctor in Science

January 2014

Probing the Semi-Magicity of ^{68}Ni via the ^{66}Ni(t,p)^{68}Ni Two-Neutron Transfer Reaction in Inverse Kinematics

Jytte ELSEVIERS

Supervisory Committee:
Prof. dr. M. Huyse, chair
Prof. dr. R. Raabe, supervisor
Prof. dr. P. Van Duppen, co-supervisor
Prof. dr. G. Neyens
Prof. dr. N. Severijns
Prof. dr. A. Vantomme
Prof. dr. Y. Blumenfeld
(Université Paris-Sud)

Dissertation presented in partial fulfillment of the requirements for the degree of Doctor in Science

January 2014

D/2014/10.705/5
ISBN 978-90-8649-696-9

Dit werk kwam mede tot stand met steun van het

Fonds voor Wetenschappelijk Onderzoek (FWO) Vlaanderen

Dankwoord

Deze thesis zou niet tot stand zijn gekomen zonder de hulp van velen, daarom wil ik hen graag via deze weg bedanken.

In de eerste plaats zou ik graag mijn promotoren Mark, Piet en Riccardo willen bedanken die mij de kans hebben gegeven om een doctoraat te starten op het IKS. Ik apprecieer ten zeerste dat jullie deuren altijd open stonden voor discussies.

The members of the examination committee should not be forgotten; Gerda, Nathal, André and Prof. Dr. Yorick Blumenfeld. Thank you for the careful reading of my thesis and the fruitful discussion at my preliminary defense.

Many thanks go to the people that made the successful outcome of this experiment possible. Especially Dennis, Katharina, Steffie, Kathrin and Vinzenz should be thanked to make the setup phase of T-REX enjoyable. Also Didier and Frederik belong in this list, as they made a lot of efforts to deliver us a clean ^{66}Ni beam.

Concerning the analysis and interpretation of the results I would like to thank Freddy for the many discussions that helped to solve the encountered problems.

Er zijn een aantal collega's die een bijzonder bedankje moeten krijgen, namelijk Céline, Jan, Lars, Nele en Simon. Dank jullie voor de ontspannende momenten op het werk (en buiten het werk). Zeker de gezellige middagen sinds we onze kaartclub hebben opgericht mogen niet vergeten worden. Verder wil ook graag Annelore bedanken voor de vele babbels wanneer het nodig was. Ook de andere leden van het IKS mogen niet vergeten worden.

Het secretariaat, in het bijzonder, Isabelle, Sally, Martine, Fabienne en Dannielle, zou ik graag bedanken om mij te helpen bij alle administratieve rompslomp.

Natuurlijk zijn er ook mensen buiten het werk die bedankt moeten worden.

Hierbij denk ik eerst en vooral aan de LUAK, waarmee ik al vier jaar op rij een mooie vakantie in de bergen heb kunnen doorbrengen. In het bijzonder wil ik Elien en Sofie bedanken die de laatste jaren mijn vaste klimpartners zijn geworden. Dank jullie om van bijna elke dinsdag- en donderdagavond weer een leuke ontspannende klimavond te maken. Ook Marianne mag niet vergeten worden, waarmee ik mijn eerste klimstappen op echte rots heb gezet. Verder zijn er nog een hele hoop vrienden in Antwerpen en Leuven die ik niet mag vergeten te bedanken voor alle gezellige spelletjesavonden, vermoeiende mountainbiketochten, restaurant bezoekjes, 'tetter'-avonden enzovoort.

Graag wil ik ook nog een woord van dank richten aan moeke en vake voor mij de kans te geven om in Leuven te studeren en mij altijd te blijven steunen. Als laatste mag natuurlijk Koen ook niet vergeten worden, bedankt om het ondertussen al vier jaar met mij uit te houden. Dat er nog vele jaren mogen volgen.

Jytte

Preface

Two main subjects are presented in this PhD work; the β decay and β-delayed fission studies of ^{180}Tl and the two-neutron transfer reaction ^{66}Ni(t,p)^{68}Ni. The first part results from the analysis of an experiment performed at ISOLDE, CERN (Geneva, Switzerland) and resulted in two papers:

1. J. Elseviers, A. N. Andreyev, S. Antilac, A. Barzakh, N. Bree, T. E. Cocolios, V. F. Comas, J. Diriken, D. Fedorov, V. N. Fedosseyev, S. Franchoo, J. A. Heredia, M. Huyse, O. Ivanov,U. Köster, B. A. Marsh, R. D. Page, N. Patronis, M. Seliverstov, I. Tsekhanovich, P. Van den Bergh, J. Van De Walle, P. Van Duppen, M. Venhart, S. Vermote, M. Veselský and C. Wagemans
Shape coexistence in ^{180}Hg studied through the β decay of ^{180}Tl
Physical Review C **84**, 034307 (2011)

2. J. Elseviers, A. N. Andreyev, S. Antilac, A. Barzakh, N. Bree, T. E. Cocolios, V. F. Comas, J. Diriken, D. Fedorov, V. N. Fedosseyev, S. Franchoo, L. Ghys, J. A. Heredia, M. Huyse, O. Ivanov,U. Köster, B. A. Marsh, R. D. Page, N. Patronis, M. Seliverstov, I. Tsekhanovich, P. Van den Bergh, J. Van De Walle, P. Van Duppen, M. Venhart, S. Vermote, M. Veselský and C. Wagemans
β-Delayed Fission of ^{180}Tl
Physical Review C **88**, 044321 (2013)

The results from these analyzes will not be further discussed in this thesis work, however both papers are given in Appendix C.

The aim of the experiment studying the ^{66}Ni(t,p)^{68}Ni reaction was to characterize and disentangle the structure of the low-lying 0^+ and 2^+ states in ^{68}Ni. This experiment was also performed at ISOLDE and used the REX

post-accelerator. The resulting particles and γ rays were detected with the T-REX particle detection array and the Miniball cluster. A paper where the results of this analysis work will be presented is in preparation:

1. J. Elseviers, F. Flavigny, A. N. Andreyev, V. Bildstein, B. A. Brown, J. Diriken, V. N. Fedosseev, S. Franchoo, R. Gernhauser, M. Huyse, S. Ielva, S. Klupp, Th.Kr öll, R. Lutter, B. A. Marsh, D. Muecher, K. Nowak, J. Pakarinen, N. Patronis, R. Raabe, F. Recchia, T. Roger, S. Sambi, M. D. Seliverstov, P. Van Duppen, M. Von Schmid, D. Voulot, N. Warr, F. Wenander, and K. Wimmer
Probing the 0^+ States in ^{68}Ni via the Two-Neutron Transfer Reaction ^{66}Ni(t,p)
In preparation for publication

To introduce the research, the nuclear structure relevant to the region around the ^{68}Ni nucleus will be discussed in Chapter 1. In Chapter 2 the theory concerning transfer reactions will be briefly discussed, with the addition of some performed DWBA calculations for the two-neutron transfer reaction to ^{68}Ni. The experimental setup is outlined in Chapter 3. In Chapters 4 to 6 the analysis, results and discussion of the experimental campaign are presented. The thesis closes with a conclusion and outlook in Chapter 7.

Summary

The region around the nucleus ^{68}Ni, with a shell closure for its protons at Z = 28 and a harmonic oscillator shell gap for its neutrons at N = 40, has drawn considerable interest over the past decades. ^{68}Ni has properties that are typical for a doubly-magic nucleus, such as a high excitation energy and low B($E2{:}2^+ \rightarrow 0^+$) transition probability for the first excited 2^+ level and a 0^+ level as the first excited state. However, it has been suggested that the magic properties of ^{68}Ni arise due to the fact that the N = 40 separates the negative parity pf-shell from the positive parity $1g_{9/2}$ orbital, and indeed, recent mass measurements have not revealed a clear N = 40 energy gap. Despite all additional information that was acquired over the last decade the specific role of the N = 40 is not yet understood and a new experimental approach to study ^{68}Ni was proposed. Namely, a two-neutron transfer reaction on ^{66}Ni to characterize and disentangle the structure of the low-lying 0^+ and 2^+ states in ^{68}Ni.

The experiment was performed at the ISOLDE facility at CERN, Geneva, Switzerland. A radioactive ^{66}Ni beam was produced in several steps. It started with an impingement of high energetic protons on a thick uranium-carbide target, after which the desired isotopes were ionized and accelerated to 30 keV and finally, to eliminate contamination of the beam, the beam was passed through a mass separator. However, in order to perform transfer experiments a higher beam energy is required and thus the ^{66}Ni beam was post-accelerated to 2.6 MeV/u with the REX linear accelerator. The ^{66}Ni beam was then guided towards a radioactive tritium-loaded titanium foil, where the reaction took place. The reaction products were detected with T-REX and Miniball. T-REX is a position-sensitive particle detection array, consisting out of several silicon detectors, while Miniball is an array of position-sensitive γ ray detectors consisting of high-purity germanium detectors.

A first step in the analysis was the calibration of the data and performing

a particle identification. From proton-gamma and proton-gamma-gamma coincidences a level scheme of ^{68}Ni could be constructed. No new levels were identified in this research, however, the excitation energy of the level that is populated in ^{68}Ni can be deduced from the detected proton energy. Out of the probability of populating different states, structure information can be derived. By looking at the excitation energy spectra it was clear that most of the feeding in the two-neutron (t,p) transfer reaction to ^{68}Ni goes to highly excited levels between 5-9 MeV. Also, a strong feeding to the ground and a direct population of the first excited 0_2^+ at 1604 keV and 2_1^+ state at 2033 keV was observed, namely respectively 4.2(16) % and 29.3(29) % of the ground state feeding. Direct population of other known 0^+ and 2^+ states in ^{68}Ni was not detected, only upper limits could be determined.

In a second step of the analysis the angular distributions constructed for the ground state and first excited 0^+ and 2^+ state were compared with theoretical DWBA calculations performed with FRESCO, where input from the shell-model code NUSHELL was used. The predicted magnitude of the angular distributions for the ground and 0_2^+ state is in good agreement with the data, while that for the 2_1^+ state is an order of magnitude too small. This discrepancy is currently not understood. The agreement of the feeding of the 0^+ states with the calculations indicates that the structure of the 0_2^+ state consists dominantly of two neutrons in the $g_{9/2}$ orbital.

Further, the obtained results for ^{68}Ni were compared to the systematics of the (t,p) reactions on the lighter, stable nickel isotopes and to its valence counterpart ^{90}Zr, which has a shell closure for its neutrons at $N = 50$ and a harmonic oscillator shell closure for its protons at $Z = 40$. An outlook for new experiments to study ^{68}Ni closes the thesis. .

Nederlandse Samenvatting

De regio rond de kern ^{68}Ni, met een schilsluiting voor de protonen bij $Z = 28$ en een harmonische oscillator subschilsluiting bij $N = 40$, heeft de laatste decennia veel aandacht gekregen. ^{68}Ni heeft eigenschappen die typisch zijn voor een dubbel-magische kern, zoals een hoge excitatie-energie en een lage $B(E2{:}2^+ \rightarrow 0^+)$ overgangswaarschijnlijkheid voor de eerste geëxciteerde 2^+ toestand en een 0^+ toestand als eerste geëxciteerde toestand. Er wordt daarentegen gesuggereerd dat de magische eigenschappen van ^{68}Ni voortkomen uit het feit dat de harmonische subschilsluiting bij $N = 40$ de pf-schil met negatieve pariteit scheidt van het $1g_{9/2}$ orbitaal met positieve pariteit. En inderdaad, recente massametingen hebben geen duidelijke energie-kloof bij $N = 40$ blootgelegd. Ondanks alle aanvullende informatie die tijdens het laatste decennium verworven is, heerst er nog steeds onduidelijkheid over wat er bij $N = 40$ net gebeurt. Daarom werd een nieuwe experimentele benadering om ^{68}Ni te bestuderen voorgesteld, namelijk een twee-neutron transferreactie op ^{66}Ni om de laagliggende 0^+ en 2^+ toestanden in ^{68}Ni te karakteriseren en hun structuur te ontwarren.

Het experiment werd uitgevoerd aan de ISOLDE faciliteit in CERN, Genève, Zwitserland. Een radioactieve ^{66}Ni bundel werd in verschillende stappen geproduceerd. Eerst werden er hoogenergetische protonen op een dikke uranium-carbide trefschijf geschoten, waarna de gewenste isotopen geïoniseerd werden en versneld werden tot 30 keV. Uiteindelijk werd de bundel door een massaseparator gestuurd om eventuele contaminatie te verwijderen. Om een transferexperiment uit te voeren, is echter een hogere bundelenergie nodig. Daarom werd de ^{66}Ni bundel naversneld tot 2.6 MeV/u met de lineaire versneller REX. De ^{66}Ni bundel werd dan naar een titanium folie, die met radioactief tritium geladen werd, geleid, waar de reactie plaatsvond. De reactieproducten werden dan gedetecteerd met T-REX en Miniball. T-REX is een positiegevoelige deeltjesdetector, bestaande uit verschillende silicium detectoren, terwijl Miniball een positiegevoelige gammadetector is, bestaande

uit verschillende hoogzuivere germanium detectoren.

In een eerste stap in de analyse moest een calibratie van de data en een deeltjesidentificatie toegepast worden. Uit proton-gamma en proton-gamma-gamma coïncidenties kon het niveauschema van ^{68}Ni opgebouwd worden. Er werden geen nieuwe toestanden geïdentificeerd in dit onderzoek, echter, uit de gemeten protonenergie, kan de excitatie-energie van de bezette niveaus in ^{68}Ni bepaald worden. Uit de kans dat bepaalde toestanden gevoed worden, kan structuur informatie afgeleid worden. Door te kijken naar de excitatiespectra was het duidelijk dat de meeste voeding in de twee-neutron (t,p) transferreactie naar ^{68}Ni naar hoge excitatie-energieën tussen 5 en 9 MeV gaat. Verder werd er ook een sterke voeding van de grondtoestand en een directe populatie van de eerste geëxciteerde 0^+ op 1604 keV en 2^+ toestand op 2033 keV geobserveerd. Meerbepaald werd er een voeding van 4.2(16) % en 29.3(29) %, relatief ten opzichte van 100 % grondtoestandvoeding, naar respectievelijk de 0^+_2 en 2^+_1 toestand gemeten. Directe populatie van andere gekende 0^+ en 2^+ toestanden werd niet gedetecteerd, enkel bovenlimieten konden worden bepaald.

In een tweede stap van de analyse werden de hoekdistributies van de grondtoestand en eerste geëxciteerde 0^+ en 2^+ toestand in ^{68}Ni geconstrueerd en vergeleken met theoretische DWBA berekeningen die uitgevoerd werden met FRESCO, waarbij input van de schillenmodelcode NUSHELL gebruikt werd. De voorspelde grootte van de hoekdistributies voor de grondtoestand en 0^+_2 kwam goed overeen met de data, terwijl deze van de 2^+_1 toestand een grootteorde te klein was. Dit verschil is momenteel niet begrepen. De overeenkomst van de voeding van de 0^+ toestanden met de berekeningen geeft aan dat de structuur van de 0^+_2 toestand gedomineerd wordt door twee neutronen in het $g_{9/2}$ orbitaal.

Als laatste stap werden de resultaten van ^{68}Ni vergeleken met de systematiek van (t,p)-reacties op de lichtere, stabiele nikkel isotopen en met zijn valentie tegenhanger ^{90}Zr, welke een schilsluiting heeft voor de neutronen bij $N = 50$ en een harmonische oscillator subschilsluiting voor de protonen bij $Z = 40$. De thesis wordt afgesloten met een vooruitzicht voor nieuwe experimenten die zouden uitgevoerd kunnen worden om (de regio rond) ^{68}Ni verder te onderzoeken.

Contents

1 | Nuclear Structure

As a motivation for the study of the two-neutron transfer reaction ^{66}Ni(t,p)^{68}Ni presented in this work, the structure of the atomic nucleus will be discussed within the concept of the nuclear shell model. Further, an overview of the experimental and theoretical knowledge of the region around ^{68}Ni will be given. The two-neutron transfer reaction is performed in order to disentangle the structure of the 0^+ and 2^+ states in ^{68}Ni. Also, an overview of the other (t,p) reactions in the lighter nickel isotopes and to other (doubly-) magic nuclei will be given.

1.1 Introduction

The atomic nucleus consists of positively charged protons and neutral neutrons, together they are referred to as nucleons. The number of protons Z, which equals the number of electrons in an atom, defines the chemical element and thus its place in the Periodic Table of Elements. A certain element can have a variable amount of neutrons N. Elements with the same proton number, but different neutron number are called isotopes. Therefore a nucleus is characterized by its charge Z and its mass number A ($=$ N $+$Z), and is typically denoted by ^{A}X, where X is the chemical element.

Since the electromagnetic interaction causes a repulsion between the positively charged protons, another force has to exist to keep the nucleons bound together. This is the strong interaction, which has a very short range ($\sim 10^{-15}$m). Through these interactions, the nucleons can bind with each other in many different configurations, of which not all of them are stable. The latter are called radioactive nuclei and can decay to a more stable configuration, e. g. through α decay, β decay (which is governed by the weak interaction), electron capture or spontaneous fission. Next to these three mentioned interactions, the

gravitational interaction is the fourth fundamental force in nature. This force is however too weak to play any considerable role in the nucleus.

The exact nature of the strong nucleon-nucleon interaction is not yet known and thus it is not possible to describe the interaction between the different nucleons in a nucleus in an exact way. However, data from nucleon-nucleon scattering have been used to deduce phenomenological properties of the strong interaction [1, 2]. Realistic nucleon-nucleon and even three-nucleon interaction potentials can be determined from these properties, which in turn can be used to perform 'ab-initio' calculations to reproduce the level structure and properties of nuclei. This has been done for nuclei up to A = 13 [3, 4]. These calculations are limited by the current computer capacities as the number of nucleon-nucleon interactions increases quickly when more nucleons are added to the nucleus. Therefore to describe heavier nuclei, it is necessary to use nuclear models, e. g. the nuclear shell model.

1.2 The Nuclear Shell Model

The Hamiltonian describing a system of A nucleons has the general form:

$$H = \sum_{i=1}^{A} T_i + \frac{1}{2} \sum_{i,j=1}^{A} V(i,j) \tag{1.1}$$

where T_i is the kinetic energy of the nucleons and $V(i,j)$ is the two-nucleon interaction between nucleon i and j. To find the nuclear structure it suffices to solve the Schrödinger equation with this Hamiltonian. However, as already mentioned above, the exact potential of the strong interaction is not known, and thus the Schrödinger equation cannot be solved. Instead certain models have to be suggested from which the nuclear structure can be deduced. The most used model is the single-particle or shell model in which it is assumed that the nucleons move independently in an average central potential caused by all the other nucleons. This approach is called a *mean field approximation*. The Hamiltonian can then be rewritten as

$$H = \underbrace{\sum_{i=1}^{A} (T_i + U(r_i))}_{H_0} + \underbrace{\frac{1}{2} \sum_{i,j=1}^{A} V(i,j) - \sum_{i=1}^{A} U(r_i)}_{H_1} \tag{1.2}$$

where $U(r_i)$ is the mean one-body potential [5]. H_0 describes the movement of a single particle in the central potential $U(r)$, independent of the other particles. The term H_1 takes the nucleon-nucleon interaction into account and is treated as a residual interaction. The Schrödinger equation can now be solved for H_0 by taking a certain shape for the potential $U(r)$. This potential has to be determined as close to the real one as possible such that H_1 can indeed be treated as a small perturbation. Most often $U(r)$ is approximated by a harmonic oscillator, extended by an l^2-term, which makes the original (parabolic) potential resemble more a Woods-Saxon potential, and a spin-orbit $\vec{l}\cdot\vec{s}$-term [2, 5, 6]. Solving the Schrödinger equation for this potential will result in discrete energy levels or *orbitals*. These orbitals are shown in Fig. 1.1 as a function of energy. Each orbital is characterized by three quantum numbers, the shell number N, the angular momentum l ($l = 0$, 1, 2, 3... for s, p, d, f ...) and the spin $j = l \pm 1/2$. The maximum number of nucleons (of the same type) in one orbital is $2j + 1$. The latter follows from the Pauli principle. Since the nucleons are fermions, a certain quantum state can only be occupied by one nucleon. Consequently, only a number of nucleons can fill a certain orbital. By filling the successive orbitals for the protons and neutrons separately, the ground state of a nucleus can be constructed. Nuclei can then be excited by moving one ore more nucleons to an orbital that is higher in energy than their ground state orbital.

As Fig. 1.1 shows, the orbitals will be grouped in certain shells, with a rather large energy difference between the shells. This results in the so-called shell structure of the nuclei. At specific proton or neutron numbers (2, 8, 20, 28, 50, 82...), the so-called *magic numbers*, a shell is completely filled and is then referred to as a closed shell. If the nucleus is magic in both proton and neutron number, it is called a doubly-magic nucleus. Non-magic nuclei can then be considered as consisting of a closed core plus a number of *valence nucleons*. These valence nucleons can be particles and/or holes (i. e. the difference between the maximum number of particles that one orbital can contain and the number of particles in this orbital). Holes and particles are equivalent in the shell model.

1.2.1 Shell Model Calculations

As already noted it is not possible to make a calculation taking all the nucleon-nucleon interactions into account. Therefore, shell model calculations use the presence of the nearest inert core, which can be chosen freely, but most often a doubly-magic nucleus is taken. In this way only the residual interactions between the valence nucleons (particles and/or holes) have to be considered. This assumption of an inert core with valence nucleons outside this core is called

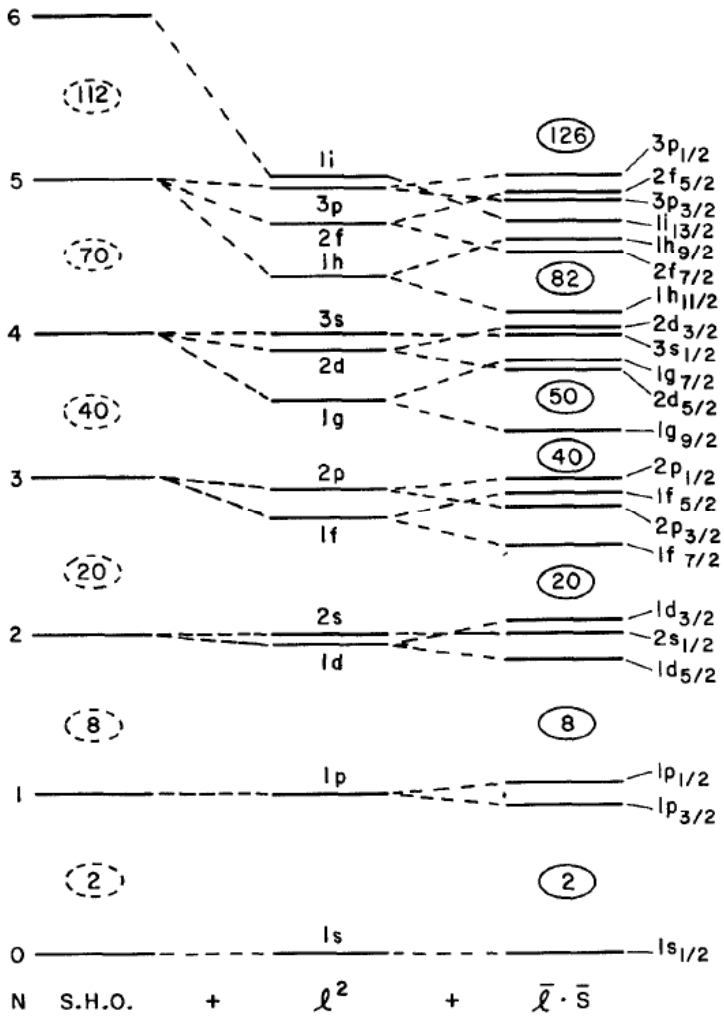

Figure 1.1: Energy states for a simple harmonic oscillator (SHO), an extended harmonic oscillator with an l^2-term and a realistic potential with l^2 and spin-orbit ($\vec{l} \cdot \vec{s}$) term (figure taken from Ref. [2]).

a *truncation*. The interactions between the valence nucleons are then described by the term H_1 in eq. (1.2). The core however is never fully inert and still interacts with the valence nucleons. This is taken into account by using *effective* two-body interactions. The choice of these residual two-body interactions is

not unique, several approaches exist, namely microscopic (uses the Bruecker G-matrix), phenomenological (deduced from experimental results) and schematic (uses a schematic analytical form for the two-body matrix elements) effective interactions can be used. These will not be described here, details can be found in Ref. [5, 7, 8, 9] and references therein.

1.2.2 Residual Nucleon-Nucleon Interaction

The Hamiltonian describing the two-body nucleon-nucleon interaction can be decomposed in a multipole expansion[1] [10, 11, 12] as

$$H = H_{monopole} + H_{multipole} \tag{1.3}$$

The monopole term is responsible for the change in energy of the proton and neutron orbitals due to the residual nucleon-nucleon interaction. The multipole term describes the correlations between the valence nucleons. The most important parts of the multipole term are the pairing and quadrupole interaction. Further, this term also causes *configuration mixing* between levels with a given state and parity. Such states can be formed by different configurations of protons and neutrons in their respective orbitals. All these different configurations will mix under influence of the residual interaction. When configuration mixing occurs, the wave function of a certain excited state will not be composed of only a single pure configuration, but will consist of a linear combination of multiple components representing different configurations. A consequence of this configuration mixing is that two mixed states with the same spin and parity will be pushed apart. A more detailed description can be found in Ref. [2, 5].

The Monopole Term

The monopole term describes the evolution of the energies of the different orbitals throughout a major shell and is defined by

$$V_{jj'}^{m} = \sum_{J}(2J+1)\langle jj'J|V|jj'J\rangle / \sum_{J}(2J+1) \tag{1.4}$$

[1] Any interaction that depends on the separation of two particles can be expanded in a multipole expansion. This is a series expansion where in general only the first components are important, such that the series can be truncated after the first few terms. Such an expansion consists of a monopole, dipole, quadrupole, octupole and higher order terms.

for a specific multiplet [7, 11, 12]. In this notation j and j' are short for the radial, orbital angular momentum, spin and isospin quantum numbers of the nucleons and the sum runs over all orbitals in the major shell [7]. The monopole term thus corresponds to a mean energy that is not dependent on the relative orientation of the involved orbits. The monopole interaction changes the separation in energy between two orbitals j_1 and j_2 when filling an orbital j' as follows

$$\Delta_{j_1,j_2} = V^m_{j_1,j'}(2j'+1-\delta_{j_1j'}) - V^m_{j_2,j'}(2j'+1-\delta_{j_2j'}). \tag{1.5}$$

The Kronecker delta is included to obey the Pauli principle for identical nucleons. The monopole term can thus cause a large shift in e. g. the energies of the neutron orbitals when e. g. protons are added to an inert core, and vice versa. In this way, the monopole term can cause the disappearance of known shell gaps and the appearance of new shell gaps when moving away from stability. A consequence of the Pauli principle is that the effect of the monopole interaction between identical particles (proton-proton or neutron-neutron) is about two times smaller than that between protons and neutrons. Further, the monopole energy of the proton-neutron interaction decreases strongly with mass number, and thus the largest effects are expected for the lighter nuclei [11]. Finally, it is noted that the inclusion of three-body forces in the monopole term optimizes the calculations to explain certain features [13, 14], such as e. g. the correct experimentally observed neutron dripline in the oxygen isotopic chain [15].

The monopole term can be subdivided in a central, spin-orbit and tensor part [11]. It seems that the central part is the strongest term. The tensor term causes a strong interaction when the involved proton and neutron orbitals have the same angular momentum ($\Delta l = 0$) or are different by one unit ($\Delta l = 1$). In this case it can cause a strong deviation in the spin-orbit splittings, and thus can change the shell gap significantly for magic numbers that stem from the spin-orbit force. The tensor term is repulsive when the proton and neutron orbitals have the same spin-orbit coupling (both aligned or anti-aligned) and attractive when the spin-orbit coupling is opposite [16].

The effect of the monopole component on the energies of the proton orbitals in the nickel isotopic chain from N = 40 to N = 50 (thus filling the $g_{9/2}$ orbital) was calculated by Otsuka *et al.* [16, 17] and is shown in Fig. 1.2. The dashed lines show the calculations including only the central force, the full lines also include the tensor force. It is clear that the tensor force has a strong influence on the Z = 28 shell closure at ^{78}Ni (N = 50). The $f_{7/2}$ - $f_{5/2}$ splitting is reduced by $\sim$ 2 MeV going from N = 40 to N = 50. This is due to the attractive (repulsive) tensor interaction between the $\pi f_{5/2}$ ($\pi f_{7/2}$) and $\nu g_{9/2}$ orbitals.

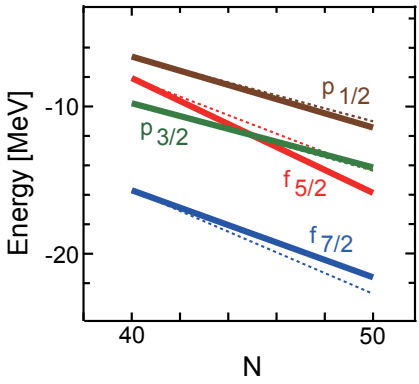

Figure 1.2: Calculated effect of the monopole term on the energies of the proton orbitals in the nickel isotopic chain when the $g_{9/2}$ orbital is filled (going from N = 40 to N = 50). The dashed line includes only the central force, the full line also includes the tensor part (figure adjusted from Ref. [17]).

The Pairing Interaction

The ground state spin of all even-even nuclei is 0^+. This is a consequence of the pairing interaction. This attractive interaction ensures that two identical nucleons will couple to a pair with total spin zero. The pairing interaction is defined as [2]:

$$\langle j_1 j_2 J | V_{pair} | j_3 j_4 J' \rangle = -G \left(j_1 + \frac{1}{2} \right) \left(j_3 + \frac{1}{2} \right) \delta_{j_1 j_2} \delta_{j_3 j_4} \delta_{J0J'0} \qquad (1.6)$$

where G is the strength of the interaction ($G_p = 17/A$ for protons and $G_n = 23/A$ MeV for neutrons). This interaction is restricted to 0^+ states (J = 0), but is not limited to diagonal matrix elements. It allows for nondiagonal scattering of the pair from one orbital, e. g. j_1, to another, j_3. However, this scattering can only occur near the Fermi level (i. e. the last orbital occupied by nucleons), since the Pauli principle inhibits scattering of deeply bound nucleons. The pairing interaction leads to partial occupancies near the Fermi level, this is illustrated in Fig. 1.3. Further, all these 0^+ states will coherently mix, which will lower the energy of the lowest 0^+ state and introduce a 'pairing' gap between this state and the other (noncollective) states.

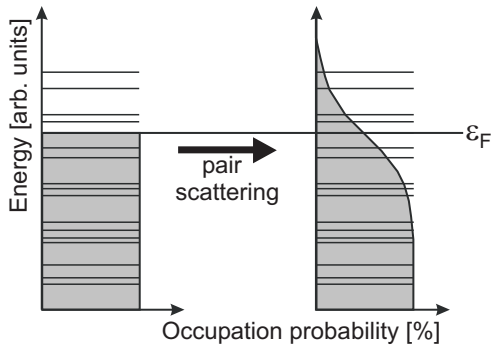

Figure 1.3: Distribution of the nucleon pairs (gray area). Left: In the absence of pairing the levels are filled up to the Fermi level, ϵ_F. Right: When the pairing interaction is introduced, nucleon pairs are scattered above the Fermi level.

The Quadrupole Term

The dominant term of the higher multipole order terms is the quadrupole part. The motivation for this interaction lies in the fact that certain properties of almost all nuclei that are more than a few mass numbers away from closed shells can be described by quadrupole deformation, e. g. almost all even-even nuclei have a 2^+ state as first excited state [2]. The quadrupole energy increases with increasing amount of valence nucleons, therefore it is expected to be largest at mid-shell [12, 18].

The residual interaction can cause a strong increase in correlation energy, hereby reducing the excitation energy of multiple particle-hole excitations across closed (sub)shells. For example, in some (doubly-magic) nuclei (e. g. ^{40}Ca) an excited 0^+ state (or more than one) is present at much lower excitation energy than expected from the energy necessary to promote two nucleons across a closed shell. These are also called *intruder* states. These states often stem from what is called the *collective* behavior of the nucleons. These multiple particle-hole excitations thus cause collective excitations, that can lead to e. g. deformed bands [12].

1.3 The Region Around Z = 28 and N = 40: ^{68}Ni

The nickel isotopes have a shell closure for their protons at Z = 28 and exhibit a wide diversity in the possible number of neutrons from N = 20 up to N = 50. This range contains the (semi-)magic numbers 20 (^{48}Ni), 28 (^{56}Ni), 40 (^{68}Ni) and 50 (^{78}Ni) and thus the nickel isotopic chain is very well suited to study the evolution of the magic numbers away from the valley of stability.

The two nickel isotopes that are known with the most extreme N/Z-ratios are ^{48}Ni and ^{78}Ni. Not much information is known about these nuclei. ^{48}Ni has only been observed two times, by which its half life and two-proton radioactivity were reported [19, 20]. Also for ^{78}Ni only the half life is known [21, 22]. This nucleus, however, has gained a lot of attention since ^{78}Ni is a waiting point in the r-process[2]. It is not certain that ^{78}Ni can be considered as a doubly-magic nucleus, since strong proton-neutron interactions exist between the protons in the $\pi f_{7/2}$ and the $\pi f_{5/2}$ orbitals and the neutrons in the $\nu g_{9/2}$ orbital. The proton-neutron interactions are not precisely known, but they can alter the Z = 28 and N = 50 gap significantly (see e. g. the shell model calculations in Ref. [17, 24]).

The isotope ^{56}Ni has some properties that are typical for a doubly-magic nucleus, as becomes clear when looking at the systematics of the nickel isotopes as shown in Fig. 1.4. This figure shows the observed excitation energies of the first excited 2^+ state, the B($E2{:}0^+ \rightarrow 2_1^+$) reduced transition probabilities[3] and the two-neutron separation energy differences δ_{2n}[4] for the nickel isotopes between N = 26 and N = 50. ^{56}Ni clearly shows a local maximum for the first excited 2^+ energy, a (albeit weak) minimum for the B($E2$) value and a deviation from the trend for the two-neutron separation energy differences. These three properties are all consistent with a doubly-magic character of the ^{56}Ni nucleus. The B($E2$)-value is however higher than expected and within error bars equal with the value for ^{54}Ni and ^{58}Ni [33]. This has been explained by full pf-shell model calculations using the Quantum Monte Carlo Diagonalization method [34]. The result of this calculation shows that only 49 % of the ground state wave function has the doubly closed shell configuration. This is attributed to strong proton-neutron correlations characterizing N = Z nuclei [35] and to extended possibilities to create a 2^+ excitation across N, Z = 28 by 1p-1h excitations [33]. More recent calculations have shown a closed shell configuration for the ground state of about 60 % [24].

[2] More information on the r-process can be found in Ref. [23]

[3] The B($E2$) value is a measure for the $E2$ transition strength and is defined as: $B(E2{:}J_i \rightarrow J_f) = \frac{1}{2J_i+1}\langle\psi_f\|\mathbf{E2}\|\psi_i\rangle$, with $\langle\psi_f\|\mathbf{E2}\|\psi_i\rangle$ the reduced $E2$ matrix element between the initial state with spin J_i and final state with spin J_f [2].

[4] $\delta_{2n} = S_{2n}(Z=28,N) - S_{2n}(Z=28,N+2)$ with S_{2n} the two-neutron separation energy.

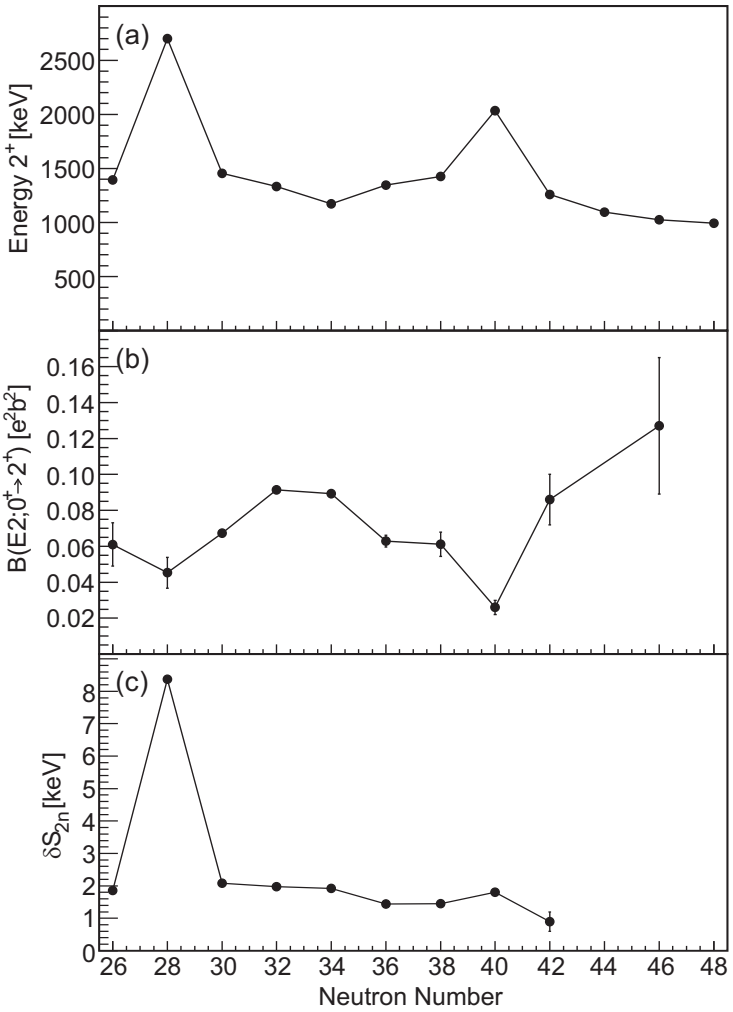

Figure 1.4: Systematics of (a) the first excited 2_1^+ energies, (b) the B($E2{:}0^+ \rightarrow 2_1^+$) reduced transition probabilities and (c) the two-neutron separation energy differences δ_{2n}. Data are taken from Ref. [25, 26, 27, 28, 29, 30, 31, 32].

The final intriguing nucleus in the nickel isotopic chain is ^{68}Ni. As can be seen in Fig. 1.4, the first 2^+ excitation energy peaks at ^{68}Ni [36] and the B($E2$) value reaches a minimum [26, 31]. These observations together with the fact that the first excited state in ^{68}Ni is a 0^+ state [37], led to the conclusion that the N = 40

forms a substantial harmonic oscillator shell closure in ^{68}Ni. However, mass measurements, which are known to be a good probe for shell closures, do not show a clear shell gap at N = 40 [30, 38]. If N = 40 would form a pronounced shell gap, the δ_{2n} would show a clear deviation from the general trend. This is not the case for ^{68}Ni, as can be seen in Fig. 1.4.c, this in contrast to the shell closure at N = 28. This paradox has been explained by the change in parity going from the pf-orbitals to the $\nu g_{9/2}$ orbital (see Fig. 1.5). Introducing a 1p-1h excitation into the $\nu g_{9/2}$ orbital would result in negative parity states. Thus, in order to create a 2^+ state at least two neutrons have to be excited, which increases the energy of the first excited 2^+_1 state compared to the other nickel isotopes [26, 39, 40].

Further, the measured small B($E2$) value for ^{68}Ni is also not necessarily a signature of a shell closure at N = 40. This because the chargeless neutrons cannot contribute directly to the B($E2$) value and, thus, if the 2^+ state was produced purely by a neutron 2p-2h excitation, the measured B($E2$) value should even be smaller. However, when the neutron shell gap at N = 40 is of the order of the pairing energy [41], there will be strong pair-scattering from the pf-shell to the $\nu g_{9/2}$ orbital [42]. This pair-scattering can induce core-polarization which enhances proton excitations across the Z = 28 gap. These proton excitations do contribute to the measured B($E2$) value, and, in fact, it has been calculated that 80 % of the measured B($E2$) value stems from proton core excitations of the $\pi f_{7/2}$ orbital [26]. It follows that the ground state wave function of ^{68}Ni consists of a hybrid structure, partly a closed shell (counting for approximately 40 % [42] or 50 % [43]) configuration and partly a superfluid nucleus (2p-2h neutron excitation of 25 % [42], 35 % [44]) [26, 42]. Finally, calculations in Ref. [44] point out that most of the total low-energy B($E2$) strength comes from 2^+ states lying above 4 MeV. This is in contrast to ^{56}Ni, where the total low B($E2$) strength can be almost completely explained by the transition to the first excited 2^+ state [44].

1.3.1 0^+ States in ^{68}Ni

Three low-lying 0^+ states are currently known in ^{68}Ni, one of them is of course the ground state, the other two have an energy of respectively 1604 keV [45] and 2511 keV [46, 47] (see Fig. 1.6). Until very recently the energy of the first excited 0^+ state was measured at 1770(30) keV [37]. Its half life has been measured in a ^{70}Zn(^{14}C,^{16}O) reaction as $t_{1/2} = 211^{+60}_{-40}$ ns [48, 49], in a reaction where ^{86}Kr collided with a natural nickel target as $t_{1/2} = 340(30)$ ns [50], in a reaction with a ^{70}Zn beam and a ^{58}Ni target as $t_{1/2} = 270(5)$ns [26] and a recent β-decay study reported 237(24) ns [51]. The configuration of this 0^+_2 state has been calculated to consist primarily of neutron 2p-2h excitations from the pf-shell

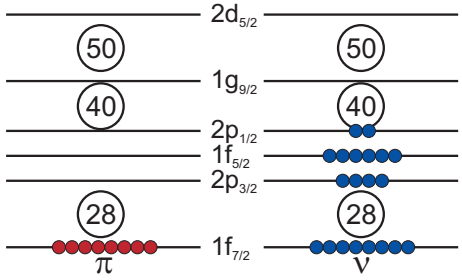

Figure 1.5: Schematic representation of the occupation of proton π and neutron ν orbitals for ^{68}Ni in its ground state. No residual interactions are taken into account.

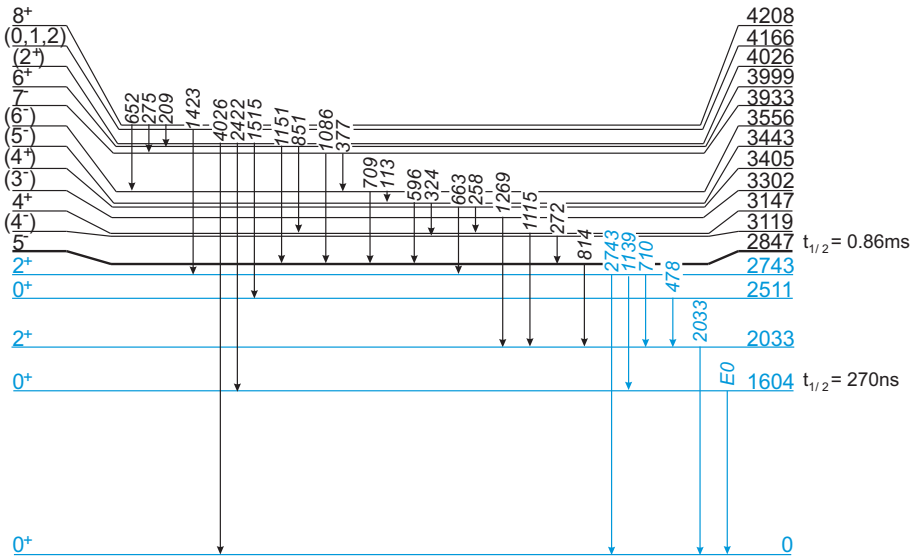

Figure 1.6: Level scheme of ^{68}Ni, all known levels up to the first 8^+ state are shown. The known 0^+ and 2^+ states are indicated in blue. Data are taken from Ref. [25, 53, 45].

to the $\nu g_{9/2}$ orbital [40]. Its low excitation energy can be explained by a strong gain in pairing energy, which is about 1.65 MeV larger than the shell gap at N = 40 [52].

The third 0^+ state at 2511 keV has first been observed in a β-delayed γ decay

experiment [46]. The tentative 0^+ assignment has recently been confirmed by Chiara *et al.* [47]. It was first suggested that this state is the result of collective excitations, which was based on the fact that Hartree-Fock-Bogoliubov calculations predicted a 0^+_3 state at ≈ 2.3 MeV. This is close to the measured energy of 2511 keV [46, 49]. More recently, it has been suggested that this 0^+_3 state is a good candidate for the π(2p-2h) excitation across the Z = 28 shell gap. This was the conclusion after calculations showed that the estimated energy for the π(2p-2h) excitation lies at 2202 keV [52, 54]. Such a low excitation energy for the π(2p-2h) state, while Z = 28 is a good shell closure, can only be obtained by a strong gain in binding energy from proton-neutron residual interactions. In order for these interactions to be strong, many valence neutrons need to be available. Hence, this is another indication that the N = 40 does not behave as a firm shell closure [52]. The authors of a recent experiment Ref. [55], where a ^{238}U beam of 6.33 A MeV bombarded a ^{70}Zn target, claimed to have observed a 0^+_3 state at 2202(1) keV with a half life of $t_{1/2} = 216^{66}_{50}$ ns. They interpreted this state as the π(2p-2h) state across the Z = 28 shell gap [55]. The energy of this state thus coincides with the estimated energy of 2202 keV. However, Chiara *et al.* [47] did not observe this state, while the experimental conditions were similar to those used in Ref. [55], namely in this experiment a ^{70}Zn beam of 430 and 440 MeV (the latter equals 6.3 A MeV) was directed onto a ^{238}U, ^{208}Pb and ^{197}Au target. If this state existed, it should have been observed by Chiara *et al.* [47].

In conclusion, current experimental and theoretical work suggest that the structure of ^{68}Ni at low energies is dominated by excitations across the N = 40 (mainly 0^+_2 state at 1604 keV) and the Z = 28 (mainly 0^+_3 state at 2511 keV) (sub)shell gap.

Very recently, the low-lying states in the exotic nickel isotopes have been calculated in the framework of Monte Carlo shell model and could be interpreted in the framework of shape coexistence [56]. In these calculations, the ground state of ^{68}Ni would have a spherical shape, while the 0^+_2 and 0^+_3 states would be the bandheads of a modestly-oblate and strong-prolate deformed band, respectively. The authors of this work Ref. [56] state that ^{68}Ni comes the closest to being a doubly-magic nucleus among the three possible doubly magic nickel isotopes, ^{56,68,78}Ni. The existence of a band built on top of the 0^+_2 was actually previously predicted by the authors of Ref. [40].

As is clear from this whole discussion, the structure of ^{68}Ni and especially the specific role of the N = 40 is still, after decades of research, not yet fully understood. Therefore, this thesis will focus on a new experimental approach to study ^{68}Ni, namely via a two-neutron transfer reaction on ^{66}Ni, the ^{66}Ni(t,p)^{68}Ni reaction in inverse kinematics. The main purpose of this experiment is to study and characterize the known 0^+ states in ^{68}Ni. It is

the aim to disentangle the structure and mixing of the 0^+ states using the relative population in the two-neutron transfer reaction. A two-neutron transfer reaction is especially sensitive to two-neutron correlations in the final nucleus. Therefore, if the ground state and first excited 0^+ state are strongly mixed (as is suggested in Fig. 1.7), it is expected that these states will be quite strongly populated in this experiment. This in contrast to the 0^+_3 state, since it is predicted to consist primarily of proton excitations.

1.3.2 Previous (t,p) and (p,t) Experiments

It will be useful to review the results from previous two-neutron transfer reactions in order to be able to make a comparison with our results. While a proper comparison can only be made based on spectroscopic factors obtained after a proper and consistent analysis of the reaction data, we restrict the discussion in this paragraph to a general comparison of the relative intensities as the details to make a full analysis are not available. On the one hand a comparison can be made with the lighter nickel isotopes and on the other hand one can compare the results from two-neutron transfer reactions to other (doubly)-magic nuclei.

Stable Nickel Isotopes

In the seventies and early eighties the nickel isotopic chain has already been studied by performing (t,p) and (p,t) reactions using enriched targets of stable ^{58,60,62,64}Ni isotopes. The first (t,p) experiment was performed by Darcey *et al.* [57] in direct kinematics with a beam energy of 12 MeV. They reported that the cross section to the ground states in ^{60,62,64,66}Ni is larger by a factor of at least four than the population to any of the excited states. Further, the cross section to excited 0^+ states is always very small, at most 6 % of the ground state yield (in ^{66}Ni). This was interpreted as the consequence of a strong pairing interaction which would lead to an enhancement of the ground state cross section. In the lighter nuclei of the stable nickel isotopes the first 2^+ and 3^- states are quite strongly populated (see Fig. 1.8).

Also in the (p,t) reactions on the stable nickel isotopes the strongest feeding goes to the ground state with also a substantial feeding to the first excited 2^+ state [58, 59, 60]. The dominant feeding of the ground state hints to a strong configuration mixing in the pf-shell [58, 61]. A summary of the most strongly fed states in the (t,p) and (p,t) reactions on the stable nickel isotopes is shown in Fig. 1.8.

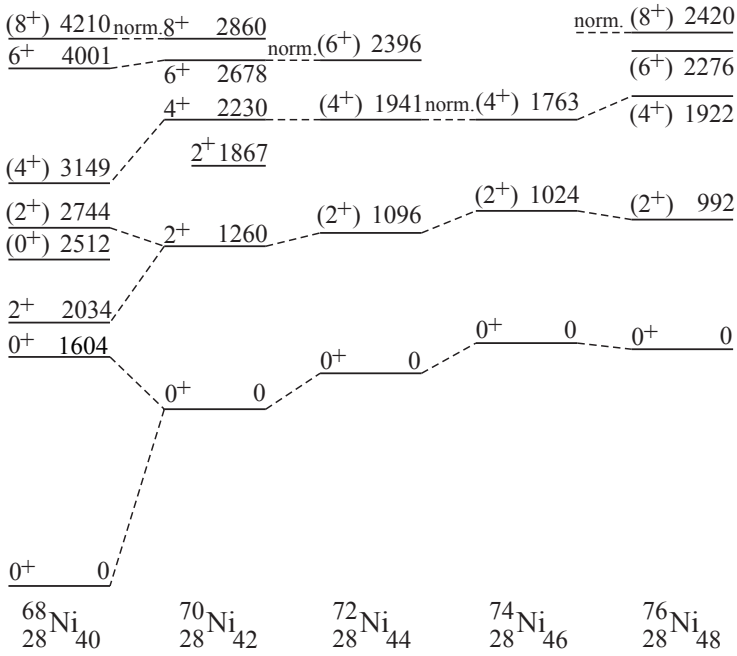

Figure 1.7: Systematics of the low-lying positive-parity states in $^{68-76}$Ni shown relative to the 8^+ states, except for ^{72,74}Ni where other states are used to normalize the spectra. The pattern seems to suggest that the 0_2^+ in ^{68}Ni is the result of a strong mixing between different configurations involving neutron pair occupancies of the $p_{3/2}$, $f_{5/2}$, $p_{1/2}$ and $g_{9/2}$ orbitals (see Fig. 1.5). Figure taken from Ref. [12].

In a paper by Alford *et al.* [62] the influence of the sequential transfer[5] on the (t,p) cross sections was investigated in the nickel chain. Their analysis showed that the two-step transfer process can cause large deviations in the predicted cross sections.

(Doubly)-Magic Nuclei

The first (t,p) experiment to a doubly-magic nucleus was performed by Bjerregaard *et al.* [64], who studied the even calcium isotopes $^{42-50}$Ca, thus including the doubly-magic nucleus ^{48}Ca. In ^{48}Ca the second excited 0^+ state

[5]Here the two-neutron transfer does not occur in a direct way, but in two steps, namely by a (t,d)- followed by a (d,p)- reaction. Details are given in Chapter 2 of this thesis.

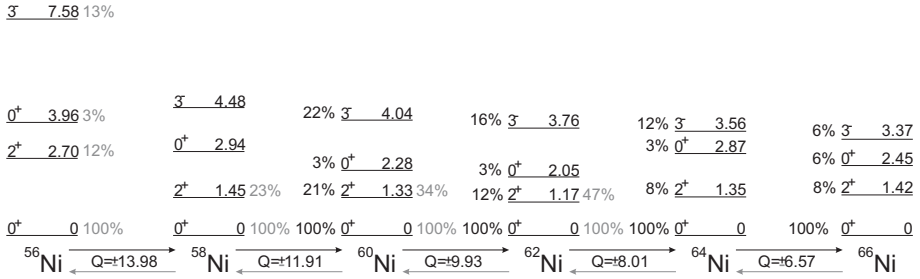

Figure 1.8: Summary of the feeding in the (t,p) (black) and (p,t) (gray) reaction on the stable nickel isotopes relative to the ground state feeding (given in %), only the most strongly fed levels are shown. Level energies are given in MeV. Data are taken from Ref. [57, 58, 60, 63]. For the (t,p) reactions the used beam energy was 4 MeV/u, while for the (p,t) reactions it was 40 MeV/u, except for the ^{58}Ni(p,t) reaction where it was 45 MeV/u.

at 5.46 MeV is populated the strongest, 160(5) % compared to 100(5) % ground state feeding. The first excited 0^+ state at 4.28 MeV has a yield of 60(30) %. This strong feeding to an excited 0^+ state is in agreement with a general trend in (t,p) reactions, where for nuclei with $N \leq 28$ always a strongly populated excited 0^+ state is observed, while for $N > 28$ the $l = 0$ cross section to the ground state is always largest [65]. Three 2^+ states and a 3^- state are also fed with a relatively strong intensity (43(15) % for the 2^+_1 at 3.83 MeV, 170(5) % for the 2^+_2 at 6.34 MeV, 98(5) % for the 2^+_3 at 6.81 MeV and 26(15) % for the 3^-_1 at 4.51 MeV). The 0^+ states in the even calcium isotopes are interpreted as the consequence of configuration mixing [64]. ^{48}Ca has not been studied yet through a (p,t) reaction, since the initial nucleus ^{50}Ca is radioactive.

For the doubly-magic nucleus ^{40}Ca it is the other way around, it has been studied through (p,t) reactions [66, 67, 68] but not through (t,p). In this transfer reaction the ground state receives the strongest feeding, the first excited 0^+ state is weakly excited ($\approx$13 % [66]) and the lowest 3^- state is populated quite strongly [67]. The authors of Ref. [68] also report the population of a 0^+ level at 9.30 MeV.

The only doubly-magic nucleus that was already studied through both a (t,p) and a (p,t) reaction is ^{208}Pb. The ^{206}Pb(t,p) reaction was first studied by Bjerregaard *et al.* [69], who observed a strong feeding to the ground state, to the 3^-_1 state at 2.61 MeV and to the 5^-_1 state at 3.20 MeV. They identified one excited 0^+ state at 4.87 MeV which was also quite strongly populated (45(3) % relative to the ground state). This state has been interpreted as a pairing

vibration state or a neutron 2p-2h state across the N = 126 shell closure [70]. The ^{210}Pb(p,t) reaction, together with the ^{206}Pb(t,p), has been studied by Igo *et al.* [70, 71]. In the (p,t) reaction, the cross section to the excited 0^+ state at 4.87 MeV is considerably larger than the cross section to the ground state [71]. Also a small population of the 0^+ state at 5.24 MeV is observed. For both the (t,p) and (p,t) reaction, the authors of Ref. [70] report the population of a number of 2^+, 3^- and 5^- states.

2 | Transfer Reaction Theory

In this chapter, a short description is given of the theory of transfer reactions. No equations will be deduced, only the results will be given, to finally come to the Distorted Wave Born Approximation (DWBA), which is used in the calculations performed in this thesis. The chapter is based on the book of I. J. Thompson and F. M. Nunes [72], in which a more elaborate discussion can be found. In the last section predictions for the cross section of the ^{66}Ni(t,p)^{68}Ni reaction will be shown.

2.1 Scattering Theory

In general the two-body scattering problem, for the motion of two particles A and B with total energy E_{tot} is described by the following Schrödinger equation

$$\left[-\frac{\hbar^2}{2m_A}\nabla^2_{\mathbf{r}_A} - \frac{\hbar^2}{2m_B}\nabla^2_{\mathbf{r}_B} + V(\mathbf{r}_A - \mathbf{r}_B) - E_{\text{tot}}\right]\Psi(\mathbf{r}_A, \mathbf{r}_B) = 0 \qquad (2.1)$$

where $V(\mathbf{r}_A - \mathbf{r}_B)$ is the potential acting between the two particles. The internal structure of the particles is not considered at this point, it will be explicitly taken into account in section 2.1.2. Eq. (2.1) can be rewritten in terms of the center of mass, $\mathbf{S} = (\mathrm{m}_A\mathbf{r}_A + \mathrm{m}_B\mathbf{r}_B)/(\mathrm{m}_A + \mathrm{m}_B)$, and relative, $\mathbf{R} = \mathbf{r}_A - \mathbf{r}_B$, coordinates as

$$\left[-\frac{\hbar^2}{2m_{AB}}\nabla^2_{\mathbf{S}} - \frac{\hbar^2}{2\mu}\nabla^2_{\mathbf{R}} + V(\mathbf{R}) - E_{\text{tot}}\right]\Psi(\mathbf{S}, \mathbf{R}) = 0, \qquad (2.2)$$

with $m_{AB} = m_A + m_B$ and μ is the reduced mass of particles A and B. One can now look for separable solutions of the form $\Psi(\mathbf{S},\mathbf{R}) = \Phi(\mathbf{S})\psi(\mathbf{R})$. Eq. (2.2) can then be rewritten as two separate equations

$$-\frac{\hbar^2}{2m_{AB}}\nabla^2_{\mathbf{S}}\Phi(\mathbf{S}) \;=\; (E_{\text{tot}} - E)\Phi(\mathbf{S}) \tag{2.3}$$

$$\left[-\frac{\hbar^2}{2\mu}\nabla^2_{\mathbf{R}} + V(\mathbf{R})\right]\psi(\mathbf{R}) = E\psi(\mathbf{R}), \tag{2.4}$$

where E is the energy of relative motion. Eq. (2.3) describes the center of mass motion and its solution is given by a simple plane wave. This means the interesting physics is contained in eq. (2.4), which describes the relative motion of the two particles. It is the aim to solve this equation, which will not be straightforward since the scattering potential $V(\mathbf{R})$ does not always has a simple form.

The wave function $\psi(\mathbf{R}) = \psi(R,\theta,\phi)$, with θ the polar and ϕ the azimuthal angle, can be separated in two parts, the incoming and the scattered beam. If the z-axis is taken as the beam direction, the incoming beam can be described by a plane wave $\psi^{beam} = Ae^{ik_i z}$, for some amplitude A and wave number k_i. Considering a certain channel, the outgoing scattered wave will behave asymptotically as a spherical wave and can be written as $\psi^{scat} = Af(\theta,\phi)\frac{e^{ik_f R}}{R}$, where $f(\theta,\phi)$ is called the *scattering amplitude*. The total asymptotic wave function can thus be described as

$$\psi^{asym} = A\left[e^{ik_i z} + f(\theta,\phi)\frac{e^{ik_f R}}{R}\right] \tag{2.5}$$

The differential cross section is defined as the ratio of scattered flux to incident flux[1], therefore

$$\frac{\mathrm{d}\sigma(\theta,\phi)}{\mathrm{d}\Omega} = \frac{v_f}{v_i}|f(\theta,\phi)|^2 \tag{2.6}$$

where, $v_{i,f}$ is the initial and final velocity. It is the aim of many theories to solve eq. (2.4) in order to find $f(\theta,\phi)$ and thus $\mathrm{d}\sigma/\mathrm{d}\Omega$.

[1]The flux $\mathbf{j}$ gives the number of particles per second per unit area. This is equivalent to the probability density of particles $|\psi|^2$, for a wave function ψ, multiplied by the velocity $\mathbf{v}$ of the particles, thus $\mathbf{j} = \mathbf{v}|\psi|^2$

2.1.1 One-Channel Scattering

In order to solve eq. (2.4), first the one-channel (elastic) problem will be addressed. Later on, the Coulomb potential will be added, and finally multi-channel scattering will be considered.

Finite Spherical Potentials

If now a spherical potential is considered, that is, $V(\mathbf{R})$ in eq. (2.4) does not depend on the direction of the vector between the two particles or on the angles θ and ϕ, then this potential cannot break the cylindrical symmetry of the incoming wave. Therefore the wave function $\psi(R,\theta)$ and the scattering amplitude $f(\theta,\phi) = f(\theta)$ will not depend on ϕ.

Using Legendre polynomials $P_L(\cos\theta)$, the wave function $\psi(R,\theta)$ can be expanded into partial waves as follows

$$\psi(R,\theta) = \sum_{L=0}^{\infty} (2L+1)\, i^L P_L(\cos\theta) \frac{\chi_L(R)}{kR} \tag{2.7}$$

The functions $\chi_L(R)$ still have to be determined and L is the angular momentum. By substituting this partial wave expansion into eq. (2.4), it turns out that for each angular momentum value L there is a separate partial-wave equation

$$\left[-\frac{\hbar^2}{2\mu}\left(\frac{\mathrm{d}^2}{\mathrm{d}R^2} - \frac{L(L+1)}{R^2}\right) + V(R) - E\right] \chi_L(R) = 0 \tag{2.8}$$

This separation for each L value is possible because of the potential being spherical. Therefore, the angular momentum L is conserved when the potential is spherical.

To find a solution of eq. (2.8), it is easiest to first look at the external wave function $\chi_L^{ext}(R)$, outside the range R_n of a finite range potential, such as a nuclear potential. The free-field partial-wave equation can be simplified and rewritten using the dimensionless radius $\rho \equiv kR$ as

$$\left[\frac{\mathrm{d}^2}{\mathrm{d}\rho^2} - \frac{L(L+1)}{\rho^2} + 1\right] \chi_L^{ext}(\rho/k) = 0 \tag{2.9}$$

This equation is a special form ($\eta = 0$[2]) of the *Coulomb wave function* which has two well-known linearly independent solutions, namely the regular function $F_L(\eta, \rho)$ and the irregular function $G_L(\eta, \rho)$ (for a definition see Box 3.1 in Ref. [72]). From these functions, two linearly independent solutions can be constructed as $H_L^{\pm} = G_L \pm iF_L$, which are the Coulomb Hankel functions (see Ref. [72]). H_L^+ represents a radially outgoing wave and H_L^- an incoming wave. The incoming plane wave can now be expanded as

$$e^{ikz} = \sum_{L=0}^{\infty} (2L+1)\, i^L P_L(\cos\theta) \frac{i}{2kR} \left[H_L^-(0, kR) - H_L^+(0, kR)\right]. \tag{2.10}$$

Outside the range ($R > R_n$) of the finite-range potential the wave function is given by eq. (2.5). It turns out that the partial wave expansion of the external full wave function can be written as

$$\psi(R, \theta) \xrightarrow{R>R_n} \frac{1}{kR} \sum_{L=0}^{\infty} (2L+1)\, i^L P_L(\cos\theta) A_L \left[H_L^-(0, kR) - \mathbf{S}_L H_L^+(0, kR)\right] \tag{2.11}$$

where A_L and $\mathbf{S}_L$ are complex values. $\mathbf{S}_L$ is called the *partial-wave S-matrix element*[3] and is uniquely determined by the potential. Since the wave function $\chi_L(R)$ in eq. (2.7) is not known inside the range where the potential is present, a trial solution $u_L(R)$ is used and eq. (2.8) is then solved using numerical methods. To determine $\mathbf{S}_L$, $u_L(R)$ and its derivative are matched to the external wave function eq. (2.11) at a matching radius $R = a$ outside the nuclear range R_n. This is done by constructing the *inverse logarithmic derivative*, which is also called the *R-matrix element*

$$\mathbf{R}_L = \frac{1}{a} \frac{\chi_L(a)}{\chi'_L(a)} = \frac{1}{a} \frac{u_L(a)}{u'_L(a)} \tag{2.12}$$

$$= \frac{1}{a} \frac{H_L^- - \mathbf{S}_L H_L^+}{H_L'^- - \mathbf{S}_L H_L'^+} \tag{2.13}$$

Since $\mathbf{R}_L$ is uniquely determined by $u_L(R)$, $\mathbf{S}_L$ can be uniquely deduced from eq. (2.13).

[2] The parameter η is the *Sommerfeld parameter* which will be defined in eq. (2.16).

[3] $\mathbf{S}$ is a matrix because there are different possible outgoing channels, each element in the matrix represents one channel.

Eq. (2.11) can now be used to find $f(\theta)$ in eq. (2.5) in terms of $\mathbf{S}_L$:

$$f(\theta) = \frac{1}{2ik} \sum_{L=0}^{\infty} (2L+1)\, P_L(\cos\theta)\, (\mathbf{S}_L - 1)\,. \tag{2.14}$$

Each matrix element $\mathbf{S}_L$ can also be described by a phase shift δ_L as $\mathbf{S}_L = e^{2i\delta_L}$. For attractive (repulsive) potentials δ_L is positive (negative). Also the *partial wave T-matrix element* is used, which is defined as $\mathbf{S}_L = 1 + 2\mathrm{i}\mathbf{T}_L$. In terms of $\mathbf{T}_L$ the scattering amplitude becomes

$$f(\theta) = \frac{1}{k} \sum_{L=0}^{\infty} (2L+1)\, P_L(\cos\theta)\mathbf{T}_L. \tag{2.15}$$

This equation shows that $\mathbf{T}_L$ represents only the outgoing wave, while $\mathbf{S}_L$ is the total amplitude containing also the incoming wave (which is represented by the -1 factor in eq. (2.14)).

Coulomb and Nuclear Potentials

Besides a short-range attractive nuclear potential, interacting nuclei also suffer from a long-range Coulomb repulsion between them. The point-Coulomb potential $V_c(R) = Z_1 Z_2 e^2/R$, with $Z_{1,2}$ the nuclear charges and e the unit charge, has an infinite range, and thus the results obtained above are not valid. However, the Schrödinger equation eq. (2.4) can be solved analytically for the pure Coulomb potential. Introducing the *Sommerfeld parameter* η for scattering with relative velocity v

$$\eta = \frac{Z_1 Z_2 e^2}{\hbar v}, \tag{2.16}$$

the partial wave expansion of the plane wave in the presence of the Coulomb potential is given by

$$\psi_c(k\hat{\mathbf{z}}, \mathbf{R}) = \sum_{L=0}^{\infty} (2L+1)\, i^L P_L(\cos\theta) \frac{1}{kr} F_L(\eta, kR). \tag{2.17}$$

The asymptotic form of $F_L(\eta, kR)$ is

$$F_L(\eta, kR) \sim \sin(kR - L\pi/2 + \sigma_L(\eta) - \eta \ln(2kR)) \tag{2.18}$$

where $\sigma_L(\eta)$ is the Coulomb phase shift. From this asymptotic form of the Coulomb wave function, the asymptotic scattering amplitude $f_c(\theta)$, summed over all partial waves, can be found:

$$f_c(\theta) = -\frac{\eta}{2k\sin^2(\theta/2)} \exp\left[-i\eta \ln(\sin^2(\theta/2)) + 2i\sigma_0(\eta)\right]. \tag{2.19}$$

This leads to the *point-Coulomb scattering amplitude*, which is called the *Rutherford cross section*,

$$\left(\frac{\mathrm{d}\sigma(\theta)}{\mathrm{d}\Omega}\right)_{Ruth} = |f_c(\theta)|^2 = \frac{\eta^2}{4k^2\sin^4(\theta/2)}. \tag{2.20}$$

The next step is to include the nuclear potential as well as a deviation of the Coulomb potential from the $1/R$ form at short distances. The scattering potential now is $V_{nc}(R) = V_c(R) + V_n(R)$, with $V_n(R)$ a finite-range spherical potential. The phase shift from the potential $V_{nc}(R)$ is given by $\delta_L = \sigma_L(\eta) + \delta_L^n$, introducing the additional Coulomb-distorted nuclear phase shift δ_L^n or $\mathbf{S}_L^n = e^{2i\delta_L^n}$. The asymptotic form of the wave function is similar to the external wave function for the pure finite range (nuclear) potential eq. (2.11),

$$\chi_L^{ext}(R) = \frac{i}{2}\left[H_L^-(\eta, kR) - \mathbf{S}_L^n H_L^+(\eta, kR)\right]. \tag{2.21}$$

The scattering amplitude $f_{nc}(\theta)$ will now be a combination of the point-Coulomb scattering amplitude eq. (2.19) and a Coulomb-distorted nuclear amplitude $f_n(\theta)$, $f_{nc}(\theta) = f_c(\theta) + f_n(\theta)$, where $f_n(\theta)$ is given by

$$f_n(\theta) = \frac{1}{2ik}\sum_{L=0}^{\infty}(2L+1)\,P_L(\cos\theta)e^{2i\sigma_L(\eta)}\,(\mathbf{S}_L^n - 1). \tag{2.22}$$

Complex Potentials

In scattering reactions often other reaction channels than elastic scattering are open, that can remove flux from the initial channel. The next section will show how to deal with the existence of multiple channels. The removal of flux from the entrance channel can be described by complex potentials, such as $V(R) + \mathrm{i}W(R)$. If the imaginary part W is negative, it is an absorptive potential and there is a loss of flux. Potentials that consist of both real

and imaginary parts are called *optical potentials*, due to the similarity of light incident on a somewhat opaque refractive medium.

The scattering theory described above remains valid for complex potentials, however the fase shift δ_L now also becomes complex. As a consequence, the moduli $|\mathbf{S}_L|$ will no longer be equal to one. For absorptive potentials $|\mathbf{S}_L|$ will be smaller than one.

2.1.2 Multi-Channel Scattering

The above results are deduced for elastic scattering, however, depending on the energy of the incoming particle, other reaction channels may be open, such as inelastic excitations, nucleon or cluster transfer reactions... Each of these different *mass partitions* is labeled by x. The partitions are limited to two particles, one projectile-like and one target-like particle. Their relative position is indicated by $\mathbf{R}_x$. p (for projectile) and t (for target) will label their energy level, $I_{p,t}$ their spin, $\pi_{p,t}$ their parity and $\xi_{p,t}$ their internal coordinates. $\phi^{xi}_{I_i\mu_i}(\xi_i)$, with $i=p,\ t$ is used to refer to the wave function of the projectile and target. These internal-structure wave functions now have to be specified, since they can change in the reaction process. If $\mathbf{L}$ is their relative angular momentum, $\mathbf{L}$, $\mathbf{I}_p$ and $\mathbf{I}_t$ can be coupled in two ways to a total angular momentum $\mathbf{J}_{tot}$. In the so-called *S basis*, $\mathbf{I}_p$ and $\mathbf{I}_t$ are first coupled to $\mathbf{S}$, in the *J basis*, $\mathbf{L}$ and $\mathbf{I}_p$ are first coupled to $\mathbf{J}_p$. For a given J_{tot}, $\alpha=\{xpt, LI_pJ_pI_t\}$ denotes a *partial-wave channel* in the J basis. The radial wave function is now denoted by $\psi_\alpha(R_x)$ instead of $\chi_L(R)$, while the total wave function is written as $\Psi(\mathbf{R}_x,\xi_p,\xi_t)$. $\Psi(\mathbf{R}_x,\xi_p,\xi_t)$ contains a sum over all the partitions, which are represented by the product of the internal states and a wave function for their relative orbital motion. In the J basis, for a certain partition x, where the two particles are in relative motion with total angular momentum J_{tot} and projection M_{tot}, the basis set of wave functions is given by

$$\begin{aligned}\Psi^{M_{tot}}_{xJ_{tot}}(\mathbf{R}_x,\xi_p,\xi_t) &= \sum_\alpha \left[\left[i^L Y_L(\hat{\mathbf{R}}_x)\otimes\phi^{xp}_{I_p}(\xi_p)\right]_{J_p}\otimes\phi^{xt}_{I_t}(\xi_t)\right]_{J_{tot}M_{tot}}\frac{\psi^{J_{tot}}_\alpha(R_x)}{R_x}\\ &= \sum_\alpha |\alpha; J_{tot}M_{tot}\rangle\frac{\psi^{J_{tot}}_\alpha(R_x)}{R_x},\end{aligned} \tag{2.23}$$

where the sum over α is restricted to those with the same partition as x. The total system wave function is given by a superposition of all the partitions, and

thus the sum over α is then unrestricted. It follows that the $|\alpha\rangle$ states form a complete set of basis states.

Eq. (2.21) can now be generalized to also depend on the entrance channel α_i:

$$\begin{aligned} \psi^{J_{tot}\pi}_{\alpha\alpha_i}(R_x) &= \tfrac{i}{2}\left[H^-_{L_i}(\eta_\alpha, k_\alpha R_x)\delta_{\alpha\alpha_i} - H^+_L(\eta_\alpha, k_\alpha R_x)\mathbf{S}^{J_{tot}\pi}_{\alpha\alpha_i}\right] \\ &= F_{L_i}(\eta_\alpha, k_\alpha R_x)\delta_{\alpha\alpha_i} + H^+_L(\eta_\alpha, k_\alpha R_x)\mathbf{T}^{J_{tot}\pi}_{\alpha\alpha_i}. \end{aligned} \tag{2.24}$$

for $R_x > R_n$. $\pi = (-1)^L \pi_{xp}\pi_{xt}$ is the total parity of the partial-wave channel. The amplitude of an outgoing wave in channel α that results from an incoming plane wave in channel α_i is given by the S matrix $\mathbf{S}^{J_{tot}\pi}_{\alpha\alpha_i}$.

2.1.3 Coupled Equations

Eq. (2.23) contains the channel wave functions $\psi_\alpha(R_x)$. In order to find these wave functions, one has to solve the Schrödinger equation for the whole system: $[H - E]\,\Psi^{M_{tot}}_{J_{tot}\pi} = 0$, for total energy E and total Hamiltonian H,

$$H = H_x + \hat{T}_x(R_x) + V_x(R_x, \xi_p, \xi_t), \tag{2.25}$$

where $\hat{T}_x$ is the kinetic energy, V_x is the finite interaction potential and $H_x = H_{xp} + H_{xt}$ is the partition's internal Hamiltonian, which determines the internal wave function $\phi^{xpt} = \phi^{xp}_{I_p}\phi^{xt}_{I_t}$ with eigenvalue $\epsilon_{xpt} = \epsilon_{xp} + \epsilon_{xt}$ (and $H_{xi}(\xi_i)\phi^{xi}_{I_i}(\xi_i) = \epsilon_{xi}\phi^{xi}_{I_i}(\xi_i)$, for $i = p,\, t$).

In the J basis the Schrödinger equation reads

$$\sum_\alpha [H - E]\,|\alpha; J_{tot}\pi\rangle \frac{\psi_\alpha(R_x)}{R_x} = 0. \tag{2.26}$$

One can project onto one of the basis states by operating on the left by $R_{x'}\langle\alpha'|$:

$$\begin{aligned} \sum_\alpha R_{x'}\langle\alpha'|H - E|\alpha\rangle R_x^{-1}\psi_\alpha(R_x) &= 0 \\ \sum_\alpha (H - E)_{\alpha'\alpha}\psi_\alpha(R_x) &= 0 \end{aligned} \tag{2.27}$$

This gives for each α' combination a separate equation. This set of equations is called the *set of coupled-channels equations*.

The matrix element $\langle\alpha'|H-E|\alpha\rangle$ can now be written by either replacing H by $\hat{T}_x + H_x + V_x$, to act on the right side of the matrix element, which is the *prior* form, or by $\hat{T}_{x'} + H_{x'} + V_{x'}$ to act on the left side, which is the *post* form. The use of the prior or post form should lead to the same results. If the prior form is considered the matrix element becomes

$$\begin{aligned}(H-E)_{\alpha'\alpha} &= R_{x'}\langle\alpha'|\hat{T}_x + V_x - E_{xpt}|\alpha\rangle R_x^{-1} \\ &= R_{x'}\langle\alpha'|\alpha\rangle R_x^{-1}\left[\hat{T}_{xL} - E_{xpt}\right] + R_{x'}\langle\alpha'|V_x|\alpha\rangle R_x^{-1} \\ &\equiv \hat{N}_{\alpha'\alpha}\left[\hat{T}_{xL}(R_x) - E_{xpt}\right] + \hat{V}^{prior}_{\alpha'\alpha},\end{aligned} \tag{2.28}$$

where $E_{xpt} = E$ - ϵ_{xp} - ϵ_{xt} and $\hat{N}_{\alpha\alpha'}$ are the norm overlap operators between the partial-wave basis states α and α'. The norm overlaps are diagonal, $\hat{N}_{\alpha'\alpha} = \delta_{\alpha'\alpha}$, for reactions within the same mass partition $x' = x$. Eq. (2.27) can now be rewritten as

$$\begin{aligned}&\left[\hat{T}_{xL}(R_x) - E_{xpt}\right]\psi_\alpha(R_x) + \sum_{\alpha'}\hat{V}^{prior}_{\alpha\alpha'}\psi_{\alpha'}(R_{x'}) \\ &+ \sum_{\alpha',x'\neq x}\hat{N}_{\alpha\alpha'}\left[\hat{T}_{x'L'} - E_{x'p't'}\right]\psi_{\alpha'}(R'_x) = 0.\end{aligned} \tag{2.29}$$

The last term in this equation is called the non-orthogonality term since it involves the overlap $\langle\alpha'|\alpha\rangle$ between different mass partitions. These terms will thus be important in transfer reactions.

2.1.4 Integral Forms

The description of the scattering cross section in terms of the S- or T-matrix elements can also be done by using the integral forms, instead of the definition through the boundary conditions of the differential equations. By rewriting the coupled equations, i. e. separating the point-Coulomb potential from all other couplings, one arrives at the inhomogeneous Schrödinger equation,

$$[E_{xpt} - T_{xL}(R) - V_c(R)]\,\psi_\alpha(R) = \sum_{\alpha'}\langle\alpha|V|\alpha'\rangle\psi_{\alpha'}(R') \equiv \Omega_\alpha(R), \qquad (2.30)$$

where $\Omega_\alpha(R)$ is called the source term. The wave function $\psi_\alpha(R)$ can be found by using the *Green's function method*:

$$\psi_\alpha(R) = \delta_{\alpha\alpha_i}F_\alpha(R) + \frac{2\mu_x}{\hbar^2}\int G^+(R,R')\Omega_\alpha(R')dR' \qquad (2.31)$$

where $G^+(R,R')$ is the Green's function and $F_\alpha(R)$ is the regular Coulomb function (see Box 3.1 in Ref. [72]). This equation can be more compactly written using the Green's operator $\hat{G}^+ = [E - \hat{T} - U_c]^{-1}$, with $\hat{T}$ the kinetic energy operator and U_c the Coulomb potential. $\hat{G}^+$ has the kernel function $2\mu_x/\hbar^2 G^+(R,R')$. In the operator notation eq. (2.31) can be written as

$$\begin{aligned}\psi &= \phi + \hat{G}^+\Omega \\ &= \phi + \hat{G}^+V\psi\end{aligned} \qquad (2.32)$$

where ϕ represents the homogeneous solution (no source term) and is only present in the elastic channel. Eq. (2.32) is called a partial-wave *Lippmann-Schwinger equation*. In this notation the T-matrix in eq. (2.24) can be written as

$$\mathbf{T} = -\frac{2\mu}{\hbar^2 k}\langle\phi^{(-)}|V|\psi\rangle \equiv -\frac{2\mu}{\hbar^2 k}\int\phi(R)V(R)\psi(R)dR. \qquad (2.33)$$

where (-) is used to indicate the complex conjugation.

Two-Potential Formula

If the potential can be decomposed in two parts $V(R) = U_1(R) + U_2(R)$, with U_1 the distorting potential and U_2 the remaining interaction, then eq. (2.33) can also be described with two terms. In Table 2.1 the corresponding Lippmann-Schwinger equations are given, where ϕ is the solution for the free field, χ for U_1 only and ψ gives the full solution.

The T-matrix integral $\mathbf{T}^{(1)} = -\frac{2\mu}{\hbar^2 k}\langle\phi^{(-)}|U_1|\chi\rangle$ (see eq. (2.33)) describes only the scattering from the potential U_1. The T matrix for the full potential can be written as

Table 2.1: Lippmann-Schwinger equations for the two-potential formula.

	Schrödinger eq.	Lippmann-Schwinger	Asymptotic Solution
Free	$[E-T]\phi = 0$	$\hat{G}_0^+ = [E-T]^{-1}$	$\phi = F$
Distorted	$[E-T-U_1]\chi = 0$	$\chi = \phi + \hat{G}_0^+ U_1 \chi$	$\chi \to \phi + \mathbf{T}^{(1)} H^+$
Full	$[E-T-U_1-U_2]\psi = 0$	$\psi = \phi + \hat{G}_0^+ (U_1+U_2)\psi$	$\psi \to \phi + \mathbf{T}^{(1+2)} H^+$

$$-\frac{\hbar^2 k}{2\mu}\mathbf{T}^{(1+2)} = \int \phi(U_1+U_2)dR$$
$$= \langle \phi^{(-)}|U_1|\chi\rangle + \langle \chi^{(-)}|U_2|\psi\rangle. \tag{2.34}$$

Eq. (2.34) is called the *two-potential formula* and is for both real and complex potentials U_1 and U_2 an exact solution.

2.1.5 Born Approximation

The Lippmann-Schwinger equation $\chi = \phi + \hat{G}_0^+ U\chi$ is an implicit equation, since the wave function χ appears on both sides. In order to find the wave function the equation can be iterated, i. e. one can build the *Born series*:

$$\chi = \phi + \hat{G}_0^+ U[\phi + \hat{G}_0^+ U[\phi + \hat{G}_0^+ U[...]]]$$
$$= \phi + \hat{G}_0^+ U\phi + \hat{G}_0^+ U\hat{G}_0^+ U\phi + \hat{G}_0^+ U\hat{G}_0^+ U\hat{G}_0^+ U\phi + ... \tag{2.35}$$

Also the T-matrix can be constructed in a similar way,

$$\mathbf{T} = -\frac{2\mu}{\hbar^2 k}\langle \phi^{(-)}|U|\chi\rangle$$
$$= -\frac{2\mu}{\hbar^2 k}\left[\langle \phi^{(-)}|U|\phi\rangle + \langle \phi^{(-)}|U\hat{G}_0^+ U|\phi\rangle + ...\right] \tag{2.36}$$

If the potential $U(R)$ can be treated as a perturbation, then the Born series can be truncated after the first term. This is called the *plane-wave Born Approximation* (PWBA):

$$\mathbf{T}^{\mathrm{PWBA}} = -\frac{2\mu}{\hbar^2 k}\langle\phi^{(-)}|U|\phi\rangle. \tag{2.37}$$

In this approximation also the scattering amplitude can be determined:

$$f^{\mathrm{PWBA}}(\theta) = -\frac{\mu}{2\pi\hbar^2}\int d\mathbf{R}e^{-i\mathbf{q}\cdot\mathbf{R}}U(\mathbf{R}), \tag{2.38}$$

where $\mathbf{q} = \mathbf{k}\text{-}\mathbf{k}_i$ is the momentum transfer. This equation shows that the PWBA scattering amplitude is proportional to the Fourier transform of the potential. The PWBA is most accurate at very high energies, when the potentials are weak (e. g. in electron-nucleus scattering).

Distorted-Wave Born Approximation

For the two-potential formula the Born series can also be constructed

$$\mathbf{T}^{(1+2)} = \mathbf{T}^{(1)} - \frac{2\mu}{\hbar^2 k}\left[\langle\chi^{(-)}|U_2|\chi\rangle + \langle\chi^{(-)}|U_2\hat{G}_1U_2|\chi\rangle + ...\right]. \tag{2.39}$$

This series will converge if U_2 is weak, while there is not such a requirement on U_1. Again this series can be truncated after the first term which leads to the *distorted-wave Born approximation* (DWBA)

$$\mathbf{T}^{\mathrm{DWBA}} = \mathbf{T}^{(1)} - \frac{2\mu}{\hbar^2 k}\langle\chi^{(-)}|U_2|\chi\rangle. \tag{2.40}$$

It is called distorted, since the wave functions $\chi(R)$ are deduced from the distorting potential U_1. This first order DWBA is very useful when U_1 is a central potential that cannot cause transitions (i. e. $\mathbf{T}^{(1)} = 0$) to a certain exit channel. The T matrix from the incoming channel α_i to the outgoing channel α then becomes

$$\mathbf{T}^{\mathrm{DWBA}}_{\alpha\alpha_i} = -\frac{2\mu_\alpha}{\hbar^2 k_\alpha}\langle\chi^{(-)}_\alpha|U_2|\chi_{\alpha_i}\rangle. \tag{2.41}$$

Using the formalism for multiple mass partitions developed in section 2.1.3, a DWBA expression can be obtained that can be used for transfer reactions involving different mass partitions:

$$\mathbf{T}^{\mathrm{DWBA}}_{\alpha\alpha_i} = -\frac{2\mu_\alpha}{\hbar^2 k_\alpha}\left\langle \chi^{(-)}_\alpha \left| R_x \langle \alpha | H - E | \alpha_i \rangle R^{-1}_{x_i} \right| \chi_{\alpha_i} \right\rangle, \tag{2.42}$$

where the inner matrix element $\langle \alpha | H - E | \alpha_i \rangle$ is integrated over the internal coordinates ξ. The Hamiltonian H can be written in prior or post form, the T matrix then yields:

$$\begin{aligned}
\mathbf{T}^{\mathrm{DWBA,prior}}_{\alpha\alpha_i} &= -\frac{2\mu_\alpha}{\hbar^2 k_\alpha}\left\langle \chi^{(-)}_\alpha \left| \hat{N}_{\alpha\alpha_i}\left[T_{x_i L_i} + U_{\alpha_i} - E_{x_i p_i t_i}\right] + \hat{V}^{x_i}_{\alpha\alpha_i} \right| \chi_{\alpha_i} \right\rangle \\
&= -\frac{2\mu_\alpha}{\hbar^2 k_\alpha}\langle \chi^{(-)}_\alpha | \hat{V}^{x_i}_{\alpha\alpha_i} | \chi_{\alpha_i} \rangle \qquad (2.43) \\
\mathbf{T}^{\mathrm{DWBA,post}}_{\alpha\alpha_i} &= -\frac{2\mu_\alpha}{\hbar^2 k_\alpha}\langle \chi^{(-)}_\alpha | \hat{V}^{x}_{\alpha\alpha_i} | \chi_{\alpha_i} \rangle \qquad (2.44)
\end{aligned}$$

Since the non-orthogonality terms $\hat{N}_{\alpha\alpha_i}$ disappear in first order DWBA, because $\left[T_{x_i L_i} + U_{\alpha_i} - E_{x_i p_i t_i}\right] \chi_{\alpha_i} = 0$, this becomes a simple expression.

2.2 Optical Potentials

To describe the scattering between two particles, a potential model is necessary. The interaction potential between two nuclei is usually described by an attractive *Woods-Saxon* potential,

$$V(R) = -\frac{V_v}{1 + \exp\left(\frac{R - R_v}{a_v}\right)} \tag{2.45}$$

with V_v the depth of the potential, which is typically 40-50 MeV for nucleon scattering, $\approx$100 MeV for deuterons and $\approx$150 MeV for tritons, a_v is a measure for the diffuseness and is typically about 0.6 fm. The radius R_v is proportional to the sum of the radii of the two nuclei involved, $R_v = r_v(A_1^{1/3} + A_2^{1/3})$, with $r_v \approx 1.2$ fm. In general, the depth of this real potential gets shallower with increasing laboratory energy, with about $\partial V_v / \partial E \approx$ -0.3 for energies op to about 20 MeV and slower at higher energies.

The real nuclear potential is often extended with an imaginary and spin-orbit part. The imaginary part also has a Woods-Saxon form, with similar radius

$R_{iv} \approx R_v$ and diffuseness $a_{iv} \approx a_v$, but with a smaller depth, W_v is typically between 10-20 MeV depending on the energy. Also a surface-peaked imaginary part can be included (W_s), which has a shape like the derivative of eq. (2.45). Since absorption occurs at the nuclear surface, the radii of the imaginary parts are most often a little larger than those of the real potential.

The spin-orbit potential couples the relative angular momentum to the spin of the nucleus and has the form

$$V_{so} = \mathcal{F}_1^{so}(R) 2\mathbf{L} \cdot \mathbf{s} \tag{2.46}$$

The factor $\mathcal{F}_1^{so}$ is deduced from the form of the spin-orbit potential for electrons in atoms

$$\mathcal{F}_1^{so}(R) = \left(\frac{\hbar}{m_\pi c}\right)^2 \frac{1}{R} \frac{d}{dR} \frac{V_{so}}{1 + \exp\left(\frac{R - R_{so}}{a_{so}}\right)} \tag{2.47}$$

with $\hbar^2/(m_\pi c)^2 = 2.00\,\mathrm{fm}^2$. The depth of the potential V_{so} is typically about 5-8 MeV for nucleons.

Finally, a Coulomb potential has to be added, which will be different from the point-Coulomb potential $V_c(R)$ defined in section 2.1, for small radii when the projectiles penetrate the nucleus:

$$V_c(R) = Z_p Z_t e^2 \times \begin{cases} \left(\frac{3}{2} - \frac{R^2}{2R_c^2}\right) \frac{1}{R_c} & \text{for } R \le R_c \\ \frac{1}{R} & \text{for } R \ge R_c \end{cases} \tag{2.48}$$

with $R_c = r_c A^{1/3}$ the Coulomb radius.

The parameters in eq. (2.45) through eq. (2.48) have to come from some model, or from fitting the angular distributions of elastic scattering.

Global Optical Potentials

The optical potential parameters can be fitted to experimental data for a specific projectile and for a large range of target nuclei and incident energies. In this way a *global optical potential* can be found. The coefficients will normally vary slowly with mass number and energy, and thus such a global optical potential can be used for interpolation and extrapolation to new reactions and

energies. Global optical model parameters that were used in this work can be found in Ref. [73, 74, 75, 76]. As an example, the global optical potential parameters from Ref. [73] for tritons are:

$$V_v = 165.0 - 0.17E - 6.4(N-Z)/A, \qquad R_v = 1.20, \qquad a_v = 0.72$$

$$W_{iv} = 46.0 - 0.33E - 110(N-Z)/A, \qquad R_{iv} = 1.40, \qquad a_{iv} = 0.84$$

$$V_{so} = 2.5, \qquad R_{so} = 1.20, \qquad a_{so} = 0.72$$

$$R_c = 1.30.$$

2.3 Transfer Reactions

All the ingredients are now available to deduce the transition amplitude for transfer reactions. In a transfer reaction a nucleon or a cluster is transferred from the projectile to the target, or vice versa.

Fig. 2.1 shows a schematic representation of the A(a,b)B transfer reaction, with $\mathrm{a} = \mathrm{b} + \mathrm{n}$ and $\mathrm{B} = \mathrm{A} + \mathrm{n}$. The different coordinates that will be used are indicated. **R** (**R'**) refers to the difference in position between the projectile a and target A (ejectile b and recoil B), **r** and **r'** are the relative coordinates of the valence cluster n to its core b and A, and $\mathbf{R}_c$ is the distance between the two cores A and b.

The initial bound state of the projectile $\phi_{\mathrm{a}}(\mathbf{r})$ and the final bound state of the residual nucleus $\phi_{\mathrm{B}}(\mathbf{r}')$ are described by

$$\begin{aligned} [H_{\mathrm{a}} - \epsilon_{\mathrm{a}}]\,\phi_{\mathrm{a}}(\mathbf{r}) &= [T_{\mathbf{r}} + V_{\mathrm{a}}(\mathbf{r}) - \epsilon_{\mathrm{a}}]\,\phi_{\mathrm{a}}(\mathbf{r}) = 0 \\ [H_{\mathrm{B}} - \epsilon_{\mathrm{B}}]\,\phi_{\mathrm{B}}(\mathbf{r}') &= [T_{\mathbf{r}'} + V_{\mathrm{B}}(\mathbf{r}') - \epsilon_{\mathrm{B}}]\,\phi_{\mathrm{B}}(\mathbf{r}') = 0 \end{aligned} \tag{2.49}$$

with $V_{\mathrm{a}} = V_{\mathrm{nb}}$ and $V_{\mathrm{B}} = V_{\mathrm{nA}}$. The total Hamiltonian describing the transfer reactions involves the three bodies, the initial and final cores and the transferred cluster or nucleon, and can be written as

$$H = T_{\mathbf{r}} + T_{\mathbf{R}} + V_{\mathrm{nb}}(\mathbf{r}) + V_{\mathrm{nA}}(\mathbf{r}') + U_{\mathrm{bA}}(\mathbf{R}_c), \tag{2.50}$$

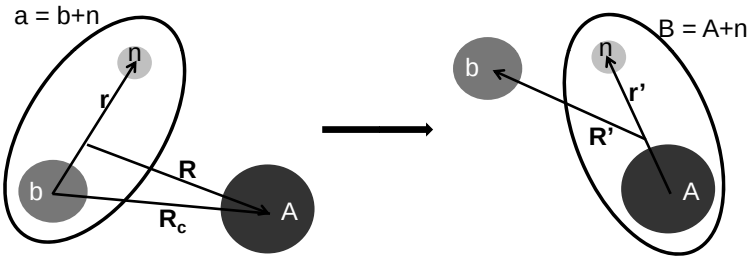

Figure 2.1: Schematic representation of the transfer reaction A(a,b)B. The different used coordinates are indicated.

where $U_{\mathrm{bA}}(\mathbf{R}_c)$ is the core-core potential. As was already shown in section 2.1.3 this Hamiltonian can be expanded in the post or prior form,

$$\begin{aligned} H &= H_{\mathrm{prior}} = T_{\mathbf{R}} + U_i(R) + H_{\mathrm{a}}(\mathbf{r}) + V_i(\mathbf{R},\mathbf{r}) \\ &= H_{\mathrm{post}} = T_{\mathbf{R}'} + U_f(R') + H_{\mathrm{B}}(\mathbf{r}') + V_f(\mathbf{R}',\mathbf{r}') \end{aligned} \tag{2.51}$$

where $U_{i,f}$ are the diagonal potentials for the entrance and exit channels (U_1 in section 2.1.4), while $V_{i,f}$ are the *interaction terms* that cause transitions from one channel to another. They satisfy

$$\begin{aligned} V_i(\mathbf{R},\mathbf{r}) &= V_{\mathrm{nA}}(\mathbf{r}') + U_{\mathrm{bA}}(\mathbf{R}_c) - U_i(R) \\ V_f(\mathbf{R}',\mathbf{r}') &= V_{\mathrm{nb}}(\mathbf{r}) + U_{\mathrm{bA}}(\mathbf{R}_c) - U_f(R'). \end{aligned} \tag{2.52}$$

The first part of these interactions are the binding potentials $V_{\mathrm{a,B}}$. The last two terms are called the *remnant terms*, which are often similar in magnitude and contain complex potentials and are therefore sometimes neglected.

2.3.1 Transfer Matrix Element

The exact transfer matrix element can be written in post or prior form, which yields

$$\mathbf{T}_{\text{prior}}^{\text{exact}} = \langle \Psi^{(-)\text{exact}} | V_{nA} + U_{bA} - U_i | \Phi_{I_b:I_a}(\mathbf{r}) \chi_{\mathbf{k}_i}(\mathbf{R}) \rangle \tag{2.53}$$

$$\mathbf{T}_{\text{post}}^{\text{exact}} = \langle \Phi_{I_A:I_B}(\mathbf{r}') \chi_{\mathbf{k}_f}^{(-)}(\mathbf{R}') | V_{nb} + U_{bA} - U_f | \Psi^{\text{exact}} \rangle. \tag{2.54}$$

In the DWBA theory one of the exact solutions $\Psi^{(\pm)\text{exact}}$ is replaced by a distorted wave multiplied by a corresponding bound state, $\Phi(\mathbf{r})\chi(\mathbf{R})$. The T matrix then becomes:

$$\mathbf{T}_{fi}^{\text{DWBA}} = \langle \chi_f^{(-)}(\mathbf{R}') \Phi_{I_A:I_B}(\mathbf{r}') | \mathcal{V} | \Phi_{I_b:I_a}(\mathbf{r}) \chi_i(\mathbf{R}) \rangle, \tag{2.55}$$

where $\mathcal{V} = V_{\text{nA}} + U_{\text{bA}} + U_i$ in the prior form and $\mathcal{V} = V_{\text{nb}} + U_{\text{bA}} + U_f$ in the post form. The potentials $U_{i,f}$ are the incoming and outgoing optical potentials used to obtain the distorted wave functions $\chi_{i,f}$. The functions $\Phi_{I_b:I_a}(\mathbf{r})$ and $\Phi_{I_A:I_B}(\mathbf{r}')$ are overlap functions. The magnitude of e. g. the overlap function $\Phi_{I_A:I_B}(\mathbf{r}')$ gives the amplitude for removing a nucleon or cluster at $\mathbf{r}'$ from the composite nucleus B in state I_{B} and leaving the core A in state I_{A}. They are often described by single-particle states using a Woods-Saxon potential. The depth of this potential is fitted to reproduce the correct binding energy and nlj quantum numbers of the state.

All the ingredients to calculate a transfer cross section have now been introduced. This calculation contains three steps:

(i) Either extract the optical potentials from fitting elastic scattering data for the correct nucleus and at the right incident energy, or use global optical potential parameters.

(ii) Use these potentials to calculate the distorted waves and also the single-particle orbitals. Most often the standard values for the radius and diffuseness ($r \approx 1.2\,\text{fm}$ and $a \approx 0.65$) are taken and the depth of the potential is fitted in order to reproduce the right binding energies.

(iii) Compute the differential cross sections using the DWBA theory. These cross sections can be compared with experimentally measured angular distributions.

The theoretical calculations of cross sections that will be shown in this work are performed with the computer code FRESCO [77].

2.3.2 Dependencies

In general, the transfer cross section will depend strongly on the amount of transferred angular momentum, on the Q-value of the reaction and on the beam energy. Additionally, when calculating the cross section using DWBA the choice of optical potential parameters is important.

Angular Momentum

Transfer reactions are very dependent on the transferred angular momentum. It is easiest to show this by considering a A(d,p)B reaction to a specific state with angular momentum l. The remnant term is neglected, thus $\mathcal{V} = V_{np}(r)$ and the *zero-range approximation* is used, $V_{np}\phi_d(\mathbf{r}) = D_0\delta(\mathbf{R}' - \mathbf{R})$, with $D_0 \simeq$ -122.5 MeV fm$^{3/2}$. Further, a plane-wave approximation for the incoming and outgoing channel is assumed, i. e. $U_i = U_f = 0$. The T matrix then becomes

$$\begin{aligned} \mathbf{T}_{fi}^{\mathrm{DWBA}} &= D_0 \int e^{i\mathbf{q}\cdot\mathbf{R}} \Phi_{I_A:I_B}(\mathbf{R}) \mathrm{d}\mathbf{R} \\ &= \sum_{l=0}^{\infty} i^l (2l+1) \int F_l(0, qR)/(qR) P_L(\cos\theta) \Phi_{I_A:I_B}(\mathbf{R}) \mathrm{d}\mathbf{R}. \end{aligned} \tag{2.56}$$

Here, $\mathbf{q}$ is the momentum transfer that increases with the scattering angle according to $q^2 = p_i^2 + p_f^2 - 2p_i p_f \cos\theta$, where $p_{i,f}$ are the momenta of the incoming and outgoing particles and θ is the scattering angle. The angular part in the integral picks out only those angular momenta l that also appear in the overlap function $\Phi_{I_A:I_B}(\mathbf{R})$. Thus, for a single l value, the cross section is, as a function of $q(\theta)$, proportional to $|F_l(0, qr)|^2$, which shows an oscillatory behavior. In general for larger angular momentum the first maximum in the cross section shifts to larger angles, and the magnitude of the cross section gets smaller. These observations remain valid when more complicated distorted optical potentials are included. This dependency of the cross section on the angular momentum is e. g. illustrated below in Fig. 2.6, where the gray and blue lines indicate an $l = 0$ transfer, while the green lines indicate an $l = 2$ transfer.

Q-Value Matching

The magnitude of the transfer cross section depends strongly on the Q-value of the reaction. For the transfer of a neutral particle, the cross section will be

largest when $Q = 0$. This Q-value matching ensures that the cross section to a certain excited state can be enhanced by using different reaction types. E. g. the (p,d) reaction ($Q = 2.2\,\text{MeV}$) and (^{3}He,α) reaction ($Q = 19.8\,\text{MeV}$) will populate completely different states due to their big difference in Q-value. Also within a certain type of reaction, there can be an enhancement to a certain excited state. This was e. g. observed in the ^{66}Ni(d,p)^{67}Ni reaction. The Q-value of this reaction is $Q = 3.583\,\text{MeV}$ [27] and the strongest population observed was to a state at 3.621 MeV [78, 79].

The Q-value of the ^{66}Ni(t,p)^{68}Ni reaction is $Q = 5.118\,\text{MeV}$ [27], and thus a strong population of states around an excitation energy of $\sim 5\,\text{MeV}$ is expected. However, the density of states in this region becomes quite large, and thus it is not sure that separate levels can be distinguished. Further, at these high excitation energies, the oscillatory behavior of the cross section is fading. Therefore it will become more difficult to assign a certain l-transfer to a populated level.

Energy Dependence

The transfer cross section depends on the center of mass energy. If the beam energy increases, the center of mass energy will of course also increase. The magnitude and the shape of the angular distribution will change with changing beam energy. As the available energy increases, more angular momentum can be transferred. As such, reactions with higher angular momentum transfer will be favorable as the beam energy rises.

Optical Potential Parameters

The angular distributions calculated with the DWBA theory can depend strongly on the chosen optical potential parameters. This will be illustrated in section 2.4, where the theoretically predicted cross sections for the ^{66}Ni(t,p)^{68}Ni reactions will be shown.

2.3.3 Spectroscopic Factors

In eq. (2.55) the overlap functions are present. Thus in order to calculate the transfer amplitude or T matrix the overlap function $\phi_{I_A:I_B}(\mathbf{r}) = \langle \Phi^A_{I_A}(\xi_A) | \Phi^B_{I_B}(\xi_B) \rangle$ of core A with wave function $\Phi^A_{I_A}(\xi_A)$ and of composite nucleus B with wave function $\Phi^B_{I_B}(\xi_B)$ has to be known. The composite state I_B can be decomposed in a superposition of all the orthogonal core states

$$\Phi^B_{I_B}(\xi_A, \mathbf{r}) = \sum_{I_A} \phi_{I_A:I_B}(\mathbf{r}) \Phi^A_{I_A}(\xi_A). \tag{2.57}$$

Let s be the spin of the transferred particle n and choose the coupling order $|(ls)j, I_A; I_B\rangle$. The overlap function eq. (2.57) can then be expanded in partial waves as a composition in terms of the core A and valence particle n:

$$\Phi^B_{I_B}(\xi_A, \mathbf{r}) = \sum_{I_A, lsj} u^{jI_AI_B}_{lsj}(r)/r \left[[Y_l(\hat{\mathbf{r}}) \otimes \chi_s]_j \otimes \Phi^A_{I_A}(\xi_A) \right]_{I_B} \tag{2.58}$$

$$= \sum_{I_A, lsj} A^{jI_AI_B}_{lsj} v^{jI_AI_B}_{lsj}(r)/r \left[[Y_l(\hat{\mathbf{r}}) \otimes \chi_s]_j \otimes \Phi^A_{I_A}(\xi_A) \right]_{I_B}. \tag{2.59}$$

$u^{jI_AI_B}_{lsj}(r)$ are single-particle radial wave functions that are not normalized. Therefore they can be written as a product of normalized wave functions $v^{jI_AI_B}_{lsj}$ and an amplitude $A^{jI_AI_B}_{lsj}$. The latter are called the *coefficients of fractional parentage*. They are linked to the *spectroscopic factors* as follows

$$S^{jI_AI_B}_{lsj} = |A^{jI_AI_B}_{lsj}|^2 \tag{2.60}$$

Since

$$\sum_{lsjI} |A^{jI_AI_B}_{lsj}|^2 = \sum_{lsjI} S^{jI_AI_B}_{lsj} = 1, \tag{2.61}$$

the spectroscopic factor can be thought of as the probability of finding core state I_A in the composite state I_B when a nucleon in partial-wave state lsj is removed.

The DWBA calculations are usually performed assuming a pure single-particle state, while the populated level in a transfer experiment is almost never a pure configuration due to e. g. configuration mixing. The spectroscopic factor can then be deduced from the experimental data as the scaling factor between the measured and calculated cross section:

$$\frac{\mathrm{d}\sigma^{\mathrm{exp}}}{\mathrm{d}\Omega} = S^{\mathrm{exp}} \frac{\mathrm{d}\sigma^{\mathrm{DWBA}}}{\mathrm{d}\Omega} \tag{2.62}$$

The spectroscopic factor is therefore a measure for the single-particle purity of a state and can be compared to theoretical structure calculations.

However, due to the low beam energy of the current ^{66}Ni(t,p) experiment, the transfer reaction is mostly peripheral and thus it only probes the tail of the wave functions. Therefore the spectroscopic factors should not be extracted. Only relative spectroscopic factors can be deduced, as in this case also the dependency on the optical potential parameters is removed. Further, if a state is not a single-particle state, but consists of multiple configurations, the extraction of spectroscopic factors is not so straightforward. The contributions from all orbitals involved in the formation of that state need to be taken into account and have to be added coherently, since they can interfere. One can take predictions for the spectroscopic amplitudes from some model (e. g. the shell model) and form the transition amplitude or cross section by the coherent sum of the different components. This last option will be used to compare the theoretical angular distributions to the experimentally deduced cross sections in the case of the ^{66}Ni(t,p)^{68}Ni reaction.

2.3.4 Higher-Order Corrections

There are two types of higher order reactions, namely distortions and/or breakup of bound states and excitations of collective states, e. g. there can be states that can be reached directly or by an excitation of the core nucleons before or after the transfer. In the latter case the transfer would include two steps, namely the transfer of a particle and the excitation of the core nucleons. When any of these couplings are strong, multi-step reactions have to be taken into account. This can be done through the *coupled reaction channel* theory. In the case of multi-step transfer the dependency of the cross section on the spectroscopic factor is not straightforward anymore. Again, it is best to predict the transition amplitudes with some reaction model and compare the calculated cross section directly to the experimental data.

This multi-step transfer will have to be taken into account in a two-neutron transfer reaction, such as the ^{66}Ni(t,p)^{68}Ni reaction. The two neutrons can be transferred in a single step (direct transfer) or in two steps (sequential transfer), by passing through the intermediate nucleus, ^{67}Ni in our case. The differential cross section will be given by the coherent sum of both processes

$$\left(\frac{\mathrm{d}\sigma}{\mathrm{d}\Omega}\right) = |f_{direct}(\theta) + f_{seq}(\theta)|^2. \tag{2.63}$$

Both transfer processes, direct and sequential, can interfere with each other and lead to constructive or destructive interference for the population of a certain state. The influence of the sequential transfer on the cross sections of the ^{66}Ni(t,p)^{68}Ni reaction will be discussed in the next section.

2.4 Theoretical Calculations for ^{66}Ni(t,p)^{68}Ni Cross Sections

From the shape of the angular distribution of a one-nucleon transfer reaction, the orbital angular momentum of the state to which the nucleon is transferred can be deduced. A one-nucleon transfer reaction thus investigates the single-particle structure of the states of the nucleus of interest. Also for a two-nucleon transfer reaction the transferred angular momentum can be deduced from the cross section. However, this transferred angular momentum does not reflect the single-particle states to which the two nucleons are transferred. This is because in the case of two-nucleon transfer the angular momentum is shared between the two nucleons and only the sum of their separate angular momenta has to equal the transferred angular momentum. There are many different ways how the angular momentum can be shared between them and they all sum up coherently. Depending on the correlation between the two nucleons, i. e. the similarity between the correlation in both nuclear states between which the nucleons are transferred, constructive or destructive interference can occur for the cross sections. The strength of the reaction is also determined by the amount that the state in the final nucleus can be described as the ground state of the initial nucleus with two added nucleons. Since, as already mentioned above, it is anyway difficult to extract spectroscopic factors from a two-nucleon transfer reaction, these reactions can be performed in order to test predictions from a certain nuclear model (see Chapter 15 of Ref. [80]). This is the strategy followed in the analysis of the ^{66}Ni(t,p)^{68}Ni reaction.

To determine the cross sections for the two-neutron transfer to ^{68}Ni, input from the shell model calculation code NUSHELL [81] was used. The neutron $f_{5/2}p_{3/2}p_{1/2}g_{9/2}$ model space (thus ^{56}Ni was used as a core and no proton excitations are possible) together with the jj44pna interaction from Ref. [82] was used to calculate the two-nucleon transfer amplitudes (TNA's). These TNA's could then be inserted in the input of FRESCO. The resulting theoretically calculated cross sections can then be directly compared to the experimental data.

First, the contribution of the sequential transfer to the total cross section as well as the dependency of the cross section on the choice of potential parameters

will be discussed without going into the details of the NUSHELL calculations. Thereafter, the details on the influence of the different orbitals included in the NUSHELL calculations will be explained.

2.4.1 Direct and Sequential Transfer

The Q-value of the ^{66}Ni(t,d) reaction to the intermediate nucleus ^{67}Ni is Q = -0.450 MeV [27]. Since this Q-value is close to zero, it is expected that the sequential transfer will have a strong influence on the two-neutron transfer to ^{68}Ni ($Q_{direct} = 5.118$ MeV [27]). This is indeed what is shown in Fig. 2.2. This figure shows the calculated cross section for transfer to the ground state of ^{68}Ni, where the black line shows the contribution from the direct transfer process, the blue line that of the sequential transfer and the green line is the coherent sum of both. It is clear that the contribution of the sequential transfer is rather important.

2.4.2 Dependence On Optical Potential Parameters

The calculated cross section will depend on the choice of global optical model parameters. In the two-neutron transfer reaction there are three channels in which the global optical model parameters can be varied, the incoming channel, $^{66}\mathrm{Ni} + {}^{3}\mathrm{H}$ ($E_{cm} = 7.2$ MeV), the intermediate channel, $^{67}\mathrm{Ni} + {}^{2}\mathrm{H}$ ($E_{cm} = 7.0$ MeV) and the outgoing channel, $^{68}\mathrm{Ni} + {}^{1}\mathrm{H}$ ($E_{cm} = 12.5$ MeV). The given center-of-mass energies are calculated for the energy of the beam in the middle of the target.

Incoming Channel

For incident tritons two global optical potentials are available, that of Becchetti and Greenlees [73] and that of Li *et al.* [74]. The difference in both sets of parameters is tested by keeping the optical parameters of the other two channels constant. Both resulting cross sections for transfer to the ground state of ^{68}Ni are shown in Fig. 2.3. Only a small difference in cross section is present when using the two different optical potential parameters. The global optical model parameters of Becchetti and Greenlees are used in the following discussions, since these gave the best fit for the angular distribution of elastically scattered tritons, as will be shown in section 4.3.2.

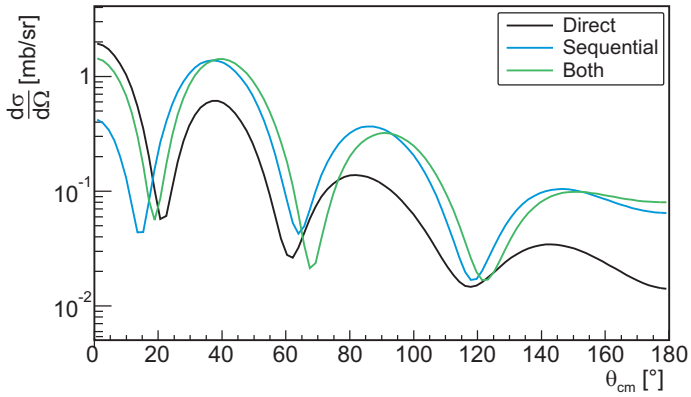

Figure 2.2: Theoretically calculated cross section to the ground state of ^{68}Ni. The black line shows the contribution of the direct transfer and the blue line that of the sequential transfer. The cross section when both transfer processes are included is shown by the green line.

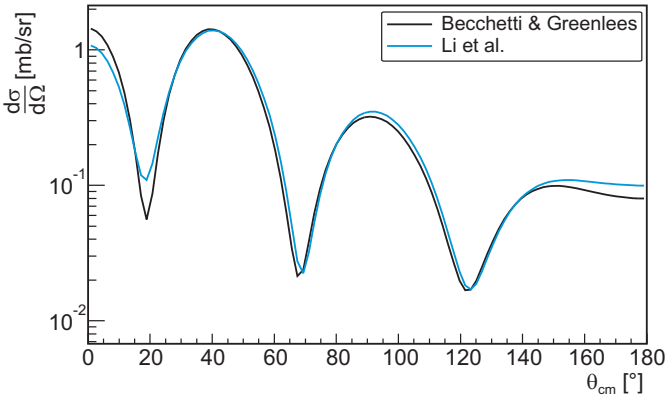

Figure 2.3: Theoretically calculated cross section to the ground state of ^{68}Ni, where both direct and sequential transfer are taken into account. The black line shows the cross section when the optical potential parameters of Becchetti and Greenlees [73] are used for the incoming channel, while for the blue line those of Li *et al.* [74] are used.

Intermediate Channel

For the intermediate channel three global optical model parameters, that were deduced for the correct energy range, are available, namely those of Han *et*

al. [76], those of Lohr and Haeberli [83] and those of An and Cai [84]. The calculated cross sections to the ground state of ^{68}Ni are shown in Fig. 2.4. Again, no huge differences are observed between the different calculations. The first maximum and minimum lie at the same position for all three calculations. In the current analysis, the optical potential parameters of Han *et al.* were used, since these gave the best results in the previously analyzed ^{66}Ni(d,p)^{67}Ni experiment [78].

Outgoing Channel

The calculated cross sections for the different global optical potentials available for the outgoing channel are shown in Fig. 2.5. The available parameters are those of Perey [85], Becchetti and Greenlees [86], Walter and Guss [87] and Koning and Delaroche [75]. Also here, there is not much difference in the cross sections when using the different optical potential parameters. In the current DWBA analysis the most recently deduced parameters of Koning and Delaroche are used.

The global optical potential parameters that are used in this work are summarized in Table 2.2.

2.4.3 Predicted Cross Sections

In the beginning of this section it was already mentioned that NUSHELL calculations were performed in order to get two-nucleon transfer amplitudes (TNA's) for the transition from ^{66}Ni to ^{68}Ni. These NUSHELL calculations used the neutron $f_{5/2}p_{3/2}p_{1/2}g_{9/2}$ model space together with the jj44pna interaction [82]. It follows that the nucleus ^{56}Ni was used as a core, and thus the model assumes there are no proton excitations. This is to a certain extent justified because Z = 28 is a good shell closure, thus neutron excitations should be much more important, at least for the lowest excited states. The NUSHELL calculations were performed by B. A. Brown [88], who also provided a method to link the TNA's to the spectroscopic amplitudes that need to be given as part of the input in FRESCO. Two examples of FRESCO input files can be found in Appendix A. In the FRESCO input the two-nucleon bound states are constructed out of sums of one-nucleon bound states. This is described by the TNA's that always link two single-particle orbitals. The TNA's resulting from the NUSHELL calculation are shown in Table 2.3 for the ground state, second 0_2^+ state and first excited 2_1^+ state in ^{68}Ni. Also the predicted excitation energy of these states is given. These are in good agreement with the experimental values of $E(0_2^+) = 1604$ keV [45] and $E(2_1^+) = 2033$ keV [25].

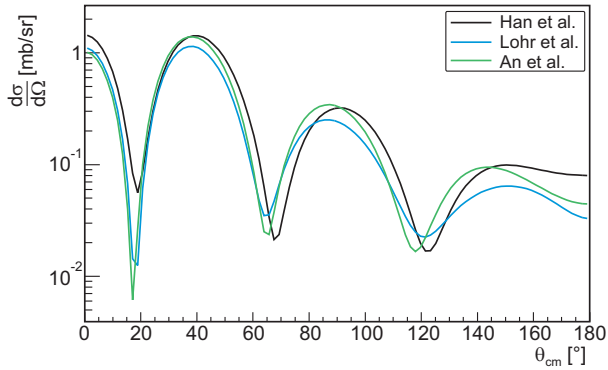

Figure 2.4: Theoretically calculated cross section to the ground state of ^{68}Ni, where both direct and sequential transfer are taken into account. The black line shows the cross section when the optical potential parameters of Han *et al.* [76] for the intermediate channel are used, for the blue line those of Lohr and Haeberli [83] are used, and for the green line those of An and Cai [84].

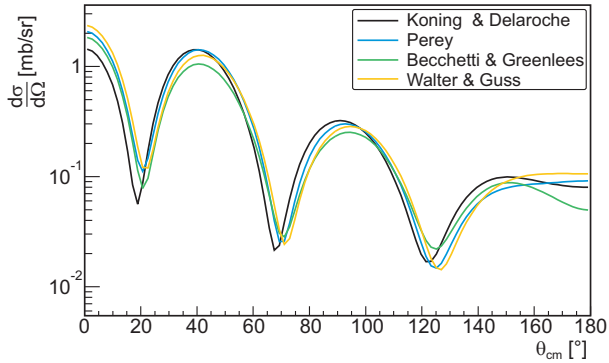

Figure 2.5: Theoretically calculated cross section to the ground state of ^{68}Ni, taking into account both direct and sequential transfer. The black line shows the cross section when the optical potential parameters of Koning and Delaroche [75] for the outgoing channel are used, for the blue line the parameters from Perey [85], for the green line those of Becchetti and Greenlees [86] and for the yellow line those of Walter and Guss [87] are used.

The resulting angular distribution for these states is shown in Fig. 2.6. For a certain state, the dark line shows the contribution of the direct transfer, while the lighter line shows the total cross section, including the sequential transfer.

Table 2.2: Global optical potential parameters used in the current DWBA analysis. The subscript 'v' stands for the volume part, 's' for the surface part and 'so' for the spin-orbit part of the optical potential.

	^{66}Ni + ^{3}H [73] ($E_{cm} = 7.2$ MeV)	^{67}Ni + ^{2}H [76] ($E_{cm} = 7.0$ MeV)	^{68}Ni + ^{1}H [75] ($E_{cm} = 12.5$ MeV)
V_v [MeV]	162.8	82.7	59.6
r_v [fm]	1.200	1.174	1.205
a_v [fm]	0.720	0.809	0.668
W_{iv} [MeV]	27.0	1.2	0.9
r_{iv} [fm]	1.400	1.563	1.204
a_{iv} [fm]	0.840	0.883	0.668
W_s [MeV]	/	13.3	9.1
r_s [fm]	/	1.328	1.278
a_s [fm]	/	0.648	0.554
V_{so} [MeV]	2.5	3.7	5.7
r_{so} [fm]	1.200	1.234	1.027
a_{so} [fm]	0.720	0.813	0.590
R_c	1.300	1.698	1.251

No experimental information for the intermediate nucleus ^{67}Ni was used in the calculations, i. e. the binding energy of ^{67}Ni is taken as the mean of the binding energies of ^{66}Ni and ^{68}Ni and the excitation energies of the states in ^{67}Ni are put to zero. By comparing the angular distributions for the different states in Fig. 2.6 it is immediately clear that the predicted cross section for transfer to the first excited 0^+ and 2^+ state is much smaller than that to the ground state. According to the calculation the population of the 0_2^+ (2_1^+) state amounts to $\approx 3\,\%$ ($\approx 5\,\%$) relative to 100 % ground state feeding.

Including Experimental Knowledge

Despite the fact that the binding energy and the excitation energies of the $p_{1/2}$, $p_{3/2}$, $f_{5/2}$ and $g_{9/2}$ states in ^{67}Ni are known, no experimental information on the intermediate ^{67}Ni was included in all the previous calculations. This experimental knowledge can now be taken into account, and the result is shown in Fig. 2.7. The black line shows the calculation that is the same as in all the previous plots, were no experimental information of ^{67}Ni is included. The experimental knowledge is incorporated in several steps in the colored lines. First the experimental binding energy was included, while keeping

Table 2.3: TNA's for the ground state, 0_2^+ and 2_1^+ state of ^{68}Ni calculated with NUSHELL, using the $f_{5/2}p_{3/2}p_{1/2}g_{9/2}$ model space together with the jj44pna interaction [82]. The given energies are the predicted excitation energies resulting also from the NUSHELL calculation.

Ground State			$\mathbf{0_2^+}$		$E^* = 1.593\,\text{MeV}$
orbital 1	orbital 2	TNA	orbital 1	orbital 2	TNA
$f_{5/2}$	$f_{5/2}$	0.73320	$f_{5/2}$	$f_{5/2}$	0.15932
$p_{3/2}$	$p_{3/2}$	0.48149	$p_{3/2}$	$p_{3/2}$	0.09490
$p_{1/2}$	$p_{1/2}$	0.62529	$p_{1/2}$	$p_{1/2}$	-0.06370
$g_{9/2}$	$g_{9/2}$	-0.70477	$g_{9/2}$	$g_{9/2}$	-0.70792
$\mathbf{2_1^+}$		$E^* = 2.077\,\text{MeV}$			
orbital 1	orbital 2	TNA			
$f_{5/2}$	$f_{5/2}$	-0.03332			
$f_{5/2}$	$p_{3/2}$	0.07957			
$f_{5/2}$	$p_{1/2}$	-0.10751			
$p_{3/2}$	$p_{3/2}$	-0.03696			
$p_{3/2}$	$p_{1/2}$	-0.02882			
$g_{9/2}$	$g_{9/2}$	0.65702			

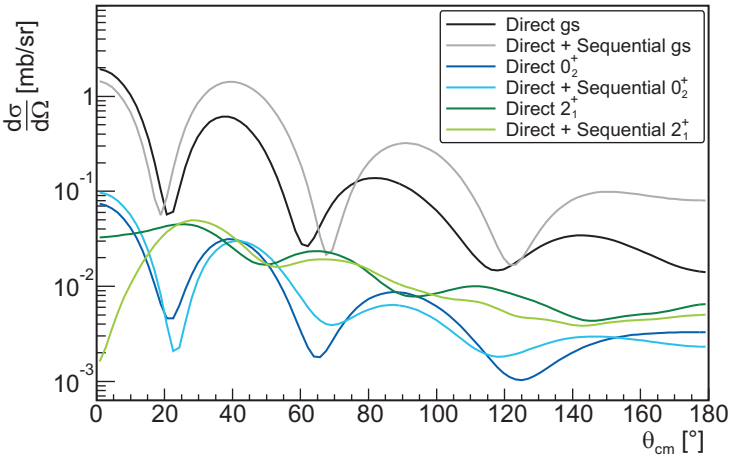

Figure 2.6: Theoretically calculated cross section to the ground state (gray), 0_2^+ (blue) and 2_1^+ state (green) of ^{68}Ni. For a certain state, the dark line only takes the direct transfer into account, while the lighter line is the total cross section, including sequential transfer. No experimental information for the intermediate nucleus ^{67}Ni was used in the calculation.

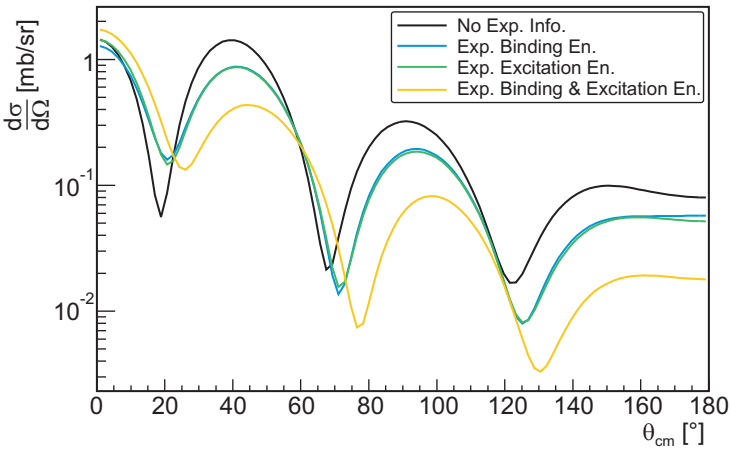

Figure 2.7: Theoretically calculated cross section to the ground state of ^{68}Ni where both direct and sequential transfer is taken into account. For the colored lines the known experimental information of ^{67}Ni is brought into the FRESCO calculation (see text for details).

the excitation energies still at zero (blue line). The second one includes the excitation energies, but keeps the value of the binding energy at the mean of the binding energies of ^{66}Ni and ^{68}Ni (green line). Finally, both the binding energy and the excitation energies are included (yellow line). One can observe that the calculations change considerably when including the experimental information. In principle, the calculation that takes into account the real binding energy and experimental excitation energies of ^{67}Ni (yellow line) should be the most correct. However, the shape of the calculated angular distributions for the sequential transfer depends strongly on the spectroscopic amplitudes of the ^{66}Ni(t,d)^{67}Ni and ^{67}Ni(d,p)^{68}Ni reactions. Unfortunately, these are not known from experiment. Therefore it is not guaranteed that the calculation including the most experimental knowledge would indeed give the most correct calculation for the two-neutron transfer to ^{68}Ni.

For small center of mass angles ($<15°$) the four calculations however do not differ much. This conclusion will be important when the calculations are compared to the experimental data in Chapter 5.

Contribution From Different Orbitals

A final interesting aspect that can be looked at is the separate contribution of the different involved orbitals ($f_{5/2}$, $p_{3/2}$, $p_{1/2}$ and $g_{9/2}$) to the total cross section. For clarity, this is shown for the direct transfer only in Fig. 2.8 for transfer to the ground state, second 0^+ and 2_1^+ state in ^{68}Ni. The calculations were done by always taking only one configuration, e. g. the coupling of two neutrons in the $f_{5/2}$ orbital (the red line in the figure), into consideration, but still using their calculated TNA value (see Table 2.3), while the TNA value of the other configurations was put to zero. It is clear from the figure that the transfer to the ground state seems to be dominated by the p orbitals, while the 0_2^+ and 2_1^+ are dominated by the $g_{9/2}$ orbital. This is also reflected in the structure of these states. From the NUSHELL calculations it follows that only 13.6 % of the wave function of the second 0^+ state of ^{68}Ni contains no neutrons in the $g_{9/2}$ orbital, while for the ground state 41.7 % of the wave function has no neutrons in this orbital. The 2_1^+ state can only be formed by promoting at least two neutrons to the $g_{9/2}$ orbital. This can be compared to the structure of the ground state of ^{66}Ni, of which 54.6 % of the wave function contains no neutrons in the $g_{9/2}$ orbital. The same orbitals are dominant, although less obvious, when also the sequential transfer is taken into account, which is shown in Fig. 2.9.

The calculated average number of neutrons in the active orbitals are shown in Table 2.4 for the ground state of ^{64}Ni and for the ground, 0_2^+ and 2_1^+ state of ^{66}Ni and ^{68}Ni. It is clear from this table that the calculations for ^{68}Ni predict a larger amount of neutrons in the $g_{9/2}$ orbital for the first excited 0^+ and 2^+ state than for the ground state, even though the ground state already has a considerable amount of neutrons in the $g_{9/2}$ orbital. These calculated occupation numbers for ^{68}Ni are in good agreement with other shell model calculations of e. g. Ref. [56]. The calculated occupation numbers of ^{64}Ni can be compared to a recent measurement performed by Schiffer *et al.* [89]. They deduced the neutron occupancies for the stable nickel isotopes out of neutron-adding and neutron-removal reactions on these isotopes. For ^{64}Ni they deduced a neutron occupancy of 3.41 for the $f_{5/2}$ orbital, 3.17 for the $p_{3/2}$ orbital, 1.07 for the $p_{1/2}$ orbital and 0.66 for the $g_{9/2}$ orbital, which are in good agreement with the NUSHELL calculations (see Table 2.4). We will come back to the, with NUSHELL, calculated neutron occupation numbers in Chapter 6.

One could also remove the predictions of the structure model, to see which orbitals are favored by the reaction mechanism. This can be done by calculating the cross sections for the different possible pure configurations in our model space, i. e. TNA = 1 for each separate configuration. This is shown for the ground state in Fig. 2.10. It is clear that the p orbitals are dominant. This also

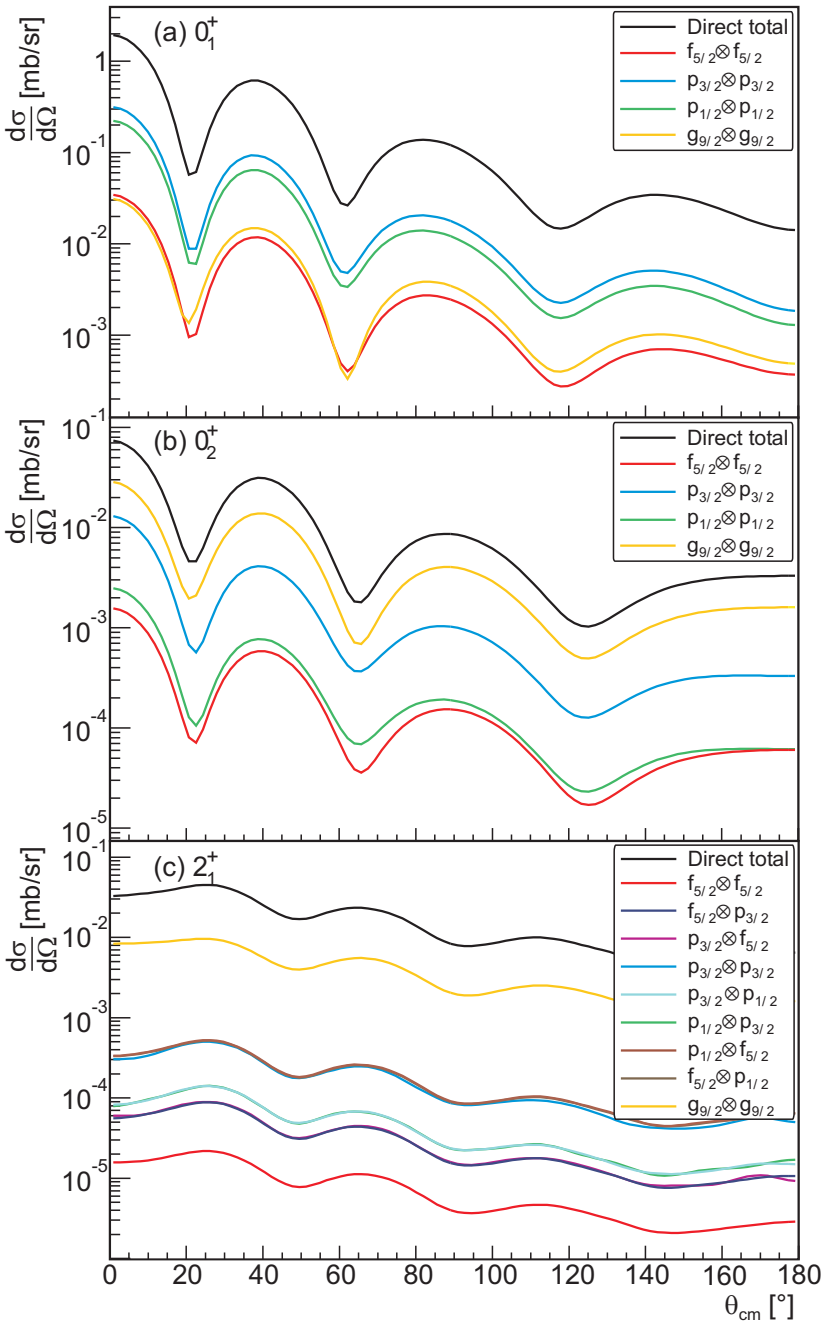

Figure 2.8: Calculated cross section to the (a) ground, (b) second 0^+ and (c) first excited 2^+ state in ^{68}Ni, only direct transfer is taken into account. The colored lines show the separate contribution to the total angular distribution of every possible combination of the involved orbitals.

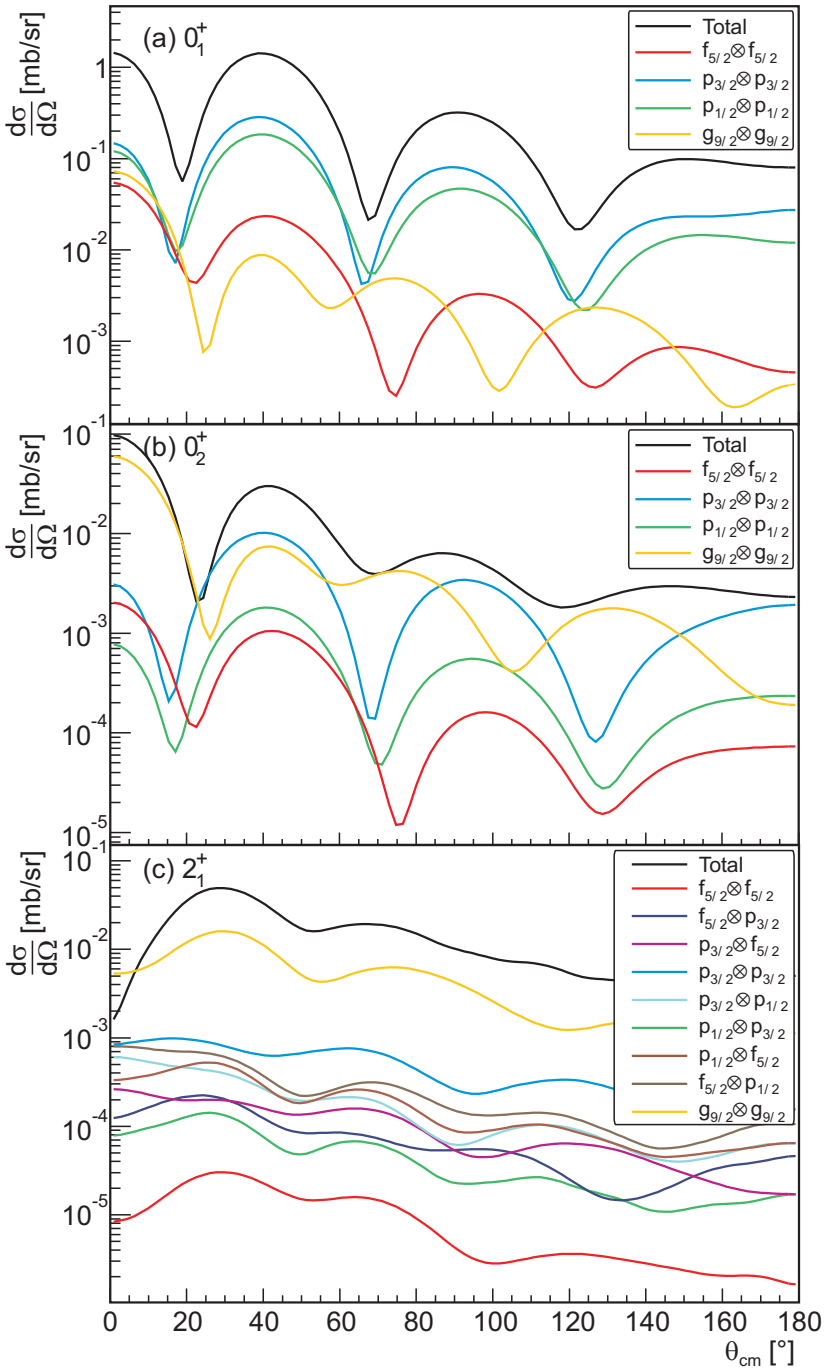

Figure 2.9: Calculated cross section to the (a) ground, (b) second 0^+ and (c) first excited 2^+_1 state in ^{68}Ni, taking both the direct and sequential transfer into account. The colored lines show the separate contribution to the total angular distribution of every possible combination of the involved orbitals.

Table 2.4: Calculated average number of neutrons in the ground state (gs) of ^{64}Ni and in the ground, 0_2^+ and 2_1^+ state of ^{66}Ni and ^{68}Ni using the NUSHELL results [88].

	$f_{5/2}$	$p_{3/2}$	$p_{1/2}$	$g_{9/2}$
^{64}Ni gs	3.57	3.04	0.74	0.65
^{66}Ni gs	4.53	3.34	1.07	1.06
^{66}Ni 0_2^+	4.35	3.69	1.18	0.78
^{66}Ni 2_1^+	4.50	3.45	1.16	0.89
^{68}Ni gs	5.19	3.59	1.73	1.49
^{68}Ni 0_2^+	5.01	3.44	1.14	2.41
^{68}Ni 2_1^+	4.76	3.43	1.13	2.68

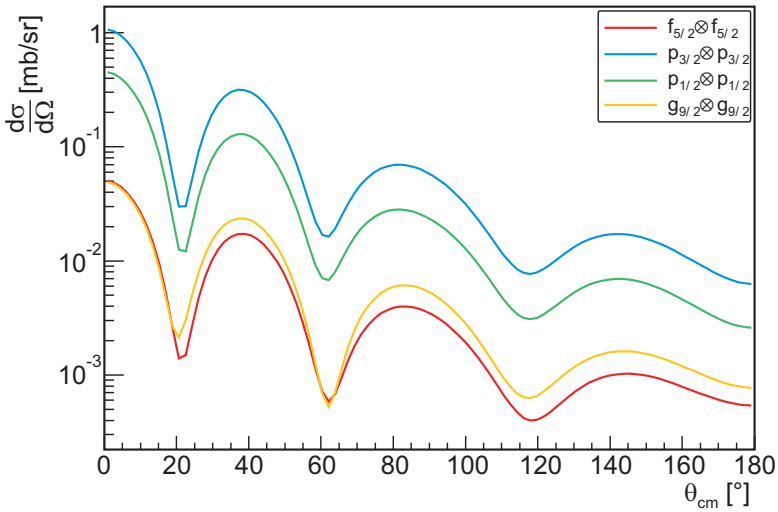

Figure 2.10: Each colored line represents the calculated cross section to the ground state, taking only direct transfer into account, for a different pure configuration (TNA = 1) possible in our used model space.

follows when taking pure configurations for transfer to the 0_2^+ and 2_1^+ states. The dominance of the p orbitals could be due to the low energy of the current experiment, which favors low angular momentum transfer. This was however checked by increasing the beam energy to 10 MeV/u and looking again to the angular distributions for the pure configurations. Even at this high energy the p orbitals are still favored. Of course the dominance of a certain orbital will also

depend on other kinematic properties like e. g. the Q-value. Another reason for the dominance of the p orbitals could be sought in the overlap between the wave functions of the neutron pair in the triton and the orbitals in ^{68}Ni. The neutrons in the triton are occupying a $0s$ state for their relative motion. It could be that this overlap between the wave functions is larger for the p orbitals in ^{68}Ni than for e. g. the $g_{9/2}$ orbital.

3 | Experimental Setup

The experimental campaign discussed in this work was performed at the ISOLDE facility located at CERN (European Organization for Nuclear Research). This chapter will give an overview of the ISOLDE facility, and more specifically of the REX-ISOLDE accelerator and the T-REX setup.

3.1 The ISOLDE Facility

There exist two general ways to produce short-lived radioactive beams of exotic nuclei, namely the In-Flight (IF) Fragmentation and the Isotope Separation On Line (ISOL) method. In the first method a high energy heavy ion beam is fragmented by impinging on a thin target, hereby producing a strongly forward focused radioactive beam, consisting of a whole range of different isotopes. The isotopes of interest are then selected using magnetic and electric deflectors. The ISOLDE facility however is an ISOL facility in which the radioactive isotopes are typically produced through fission, fragmentation and spallation reactions by impingement of a high energy beam of light particles, such as protons, on a thick target. The reaction products are produced inside the target and have to be extracted from the target by other methods. This makes the ISOL method slower than the In-Flight method.

At ISOLDE [91] (see Fig. 3.1) the radioactive nuclei of interest are produced by proton induced nuclear reactions. The protons have an energy of 1.4 GeV and the proton beam has an average intensity of 2.1 μA. They are delivered by the Proton-Synchrotron-Booster, which is formed by four small synchrotrons. The proton beam consists of pulses that are 2.4 μs in length and have a period of 1.2 s. 12 to 48 of such proton pulses are grouped into a so-called supercycle. The different pulses are distributed among the different facilities of CERN.

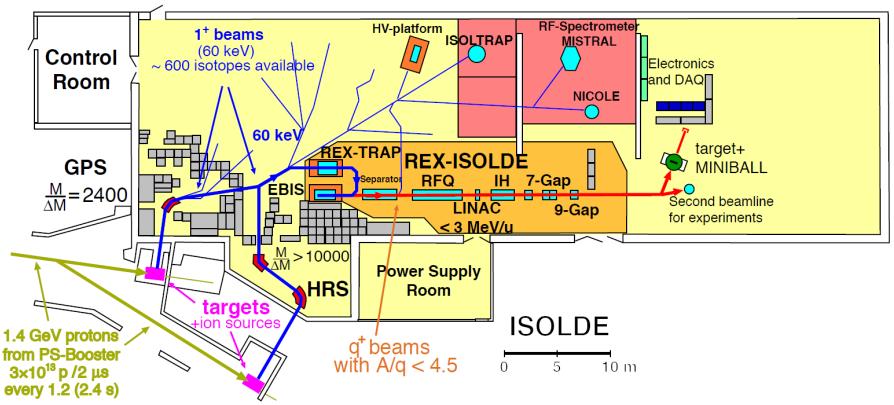

Figure 3.1: Overview of the ISOLDE facility. Figure taken from Ref. [90].

Protons arriving at ISOLDE impinge on a hot, thick target which in the case of nickel beams, and also in most cases, is a uranium-carbide ($^{238}UC_x$) target ($\sim 50\,mg/cm^2$). After production, the radioactive nuclei diffuse through and effuse out of the target material and drift towards an ion source through a heated transfer line. To reduce the diffusion, desorption (e. g. from the walls of the target chamber) and effusion times, the target-ion source is kept at a high temperature of $\sim$2300 K.

Apart from the (exotic) radioactive nuclei of interest, a whole range of other nuclei will be produced. Therefore, it is essential to have an as selective as possible ionization process. At ISOLDE three kinds of ionization methods are used

- surface ionization, which is suitable for elements with a low ionization potential
- ionization by electron impact, which can be used for elements with a high ionization potential
- resonant laser ionization

In this experiment the latter method was used, namely Resonant Laser Ionization Ion-Source (RILIS) [92, 93]. Lasers of different wavelength are used to stepwise excite and eventually ionize a specific element by using different atomic transitions. These transitions are unique for a certain element, therefore only the element of interest will be ionized. The ionization scheme for nickel is shown in Fig. 3.2 [94, 95]. A RILIS ionization efficiency of about 6 % can be

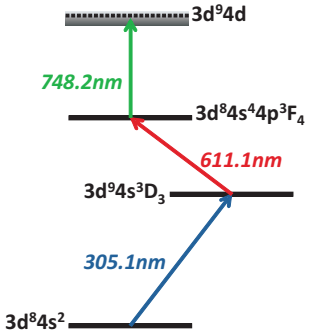

Figure 3.2: Resonant Laser Ionization of nickel.

reached for nickel [95]. Due to the high temperature of the target-ion source, also elements with a low ionization potential can be ionized through surface ionization, which can lead to contamination of the beam. The only element which can be surface ionized in the neighborhood of the nickel isotopes is gallium, with an ionization potential $V_{ion} = 6\,eV$.

The amount of gallium contamination can be measured by comparing Laser-on (where the lasers are tuned to ionize nickel) and Laser-off (where the lasers are blocked, only surface ionized contaminants are present) measurements. In the Laser-off measurements almost no particles were detected, from which it could be deduced that the gallium contamination in the beam was $< 1\,\%$.

After ionization the radioactive isotopes are extracted from the target-ion source using extraction electrodes. These electrodes are kept at ground potential, while the ion source is at a high voltage of 30-60 kV, as such the ion beam can be accelerated up to an energy of 60 keV. In the current experiment the voltage on the ion source was 30 kV.

After the ionization process and acceleration, the ions are mass separated using the High Resolution Separator (HRS) or the General Purpose Separator (GPS). The latter was used in the nickel experiment and has a mass resolving power $m/\Delta m$ of 2400.

3.2 REX-ISOLDE

After mass separation the ion beam is guided towards the REX-accelerator (Radioactive beam EXperiment) [96, 97, 98, 99, 100]. This post-accelerator was

built because the low energy beams provided by ISOLDE are not suitable to do Coulomb excitation and/or transfer reactions, which need higher beam energies. In order to be able to accelerate ions efficiently to higher energy in the linear accelerator, they need to be brought to a higher charge state. This is done with EBIS (Electron-Beam Ion Source). First, the ions are bunched, accumulated and cooled. This is done with REXTRAP, a Penning trap. The 30-60 keV ion beam is slowed down to some eV by a high voltage retardation potential and further cooled by an argon or neon buffer gas. In order to synchronize the system the cooling time must be related to the breeding time, which was fixed to 48 ms. Since some extra time is needed for the transportation from REXTRAP to EBIS and extraction from EBIS, the total trapping time amounted to 51 ms in the case of the ^{66}Ni beam.

After this process, the bunches are reaccelerated to 30-60 keV and transported to EBIS. EBIS is a charge breeding system that uses electron impact ionization to bring the 1^+ ion beam to a higher charge state, which in the case of the ^{66}Ni ions was a 17^+ charge state. Since the ^{66}Ni beam was quite intense, the method of slow extraction was used to extract the nickel ions from EBIS. This method increases the length of an ion bunch to ≈ 1 ms instead of ≈ 150 µs.

Since also residual gases, from e. g. REXTRAP, can penetrate in the EBIS, the ion bunches have to pass an A/q-separator. This separator has an S-shaped configuration, in which the beam first passes through an electrostatic deflector, where the ions are separated according to their energy, and then through a bending magnet, where the beam is separated according to mass. The charge state of the beam is chosen in such a way that the separator can be set to the desired $A/q < 4.5$ value, so that most of the residual gas contaminants are eliminated.

After this mass separation the bunches are injected into the REX linear accelerator (linac). This linac consists of a RFQ[1]-accelerator, an IH[2]-structure, three 7-gap resonators and one 9-gap resonator and can accelerate the ion beam up to 2.85 MeV/u. However, in the case of this experiment the beam energy had to be reduced to 2.6 MeV/u to avoid fusion of nickel with the titanium in the target (see section 3.3.1). After post-acceleration the beam can be delivered to the T-REX setup. The transmission efficiency of the ^{66}Ni beam from the ion source to the T-REX setup was measured to be about 7 %.

[1] Radio Frequency Quadrupole
[2] Interdigital H-type

3.2.1 Time Structure

Timing information is very important for the data acquisition and analysis of the experiment. Unfortunately, during the present campaign no time information on the arrival of the proton pulse at ISOLDE was collected. Due to the long half life of ^{66}Ni and the slow release of nickel from the target-ion source system, the ^{66}Ni beam current supplied to REX trap varied only little in time relative to the proton impact. A second important signal is the EBIS signal, which registers the time when the ions are released from the EBIS (every 51 ms in our case). With this trigger a so-called On-Beam window of about 1 ms is opened. During this time ions arrive at the T-REX setup, and thus data are accumulated. After this window the data are read out, which takes a few milliseconds. After this read-out, an Off-Beam window is opened of the same length as the On-Beam window. During this time, no ions arrive at the setup, so only background is registered. These Off-Beam windows can be used for background subtraction in the analysis.

3.3 T-REX

The T-REX setup is especially designed for nucleon transfer reaction experiments in inverse kinematics and is based on an array of ΔE-E$_{\mathrm{rest}}$ telescopes for particle detection [101, 102]. It consists of two double sided segmented annular strip detectors, the CD detectors [103], and eight position sensitive silicon strip detectors, the barrel. Together they have an angular coverage of about 66 % of 4π. Since each detector stack consists of two layers, particle identification can be done through their specific energy loss in the first layer. The T-REX setup is shown in Fig. 3.3. A detailed description of T-REX can be found in Ref. [101, 102, 104]. Here, only a brief description of the detectors will be given.

The barrel detector stacks in forward and backward direction consist of a 140-µm thick ΔE detector and a 1000-µm thick E$_{\mathrm{rest}}$ or also called pad detector with an active area of $50 \times 50\,\mathrm{mm}^2$. The latter is positioned at a distance of 2.2 mm from the ΔE detector. The ΔE detectors are segmented in 16 strips perpendicular to the beam direction. These are resistive strips, such that position information along each strip can be obtained. The energy deposited in one strip, thus the charge created, is split in two parts which are collected at opposite sides of the strip. The charge that is collected at one end of the strip is approximately linearly dependent on the position of the hit. Further, a mylar foil of 12 µm thickness was placed 2 mm in front of the forward barrel detectors. This to reduce background from elastically scattered titanium coming from the target (see section 3.3.1). The ΔE detectors are produced by

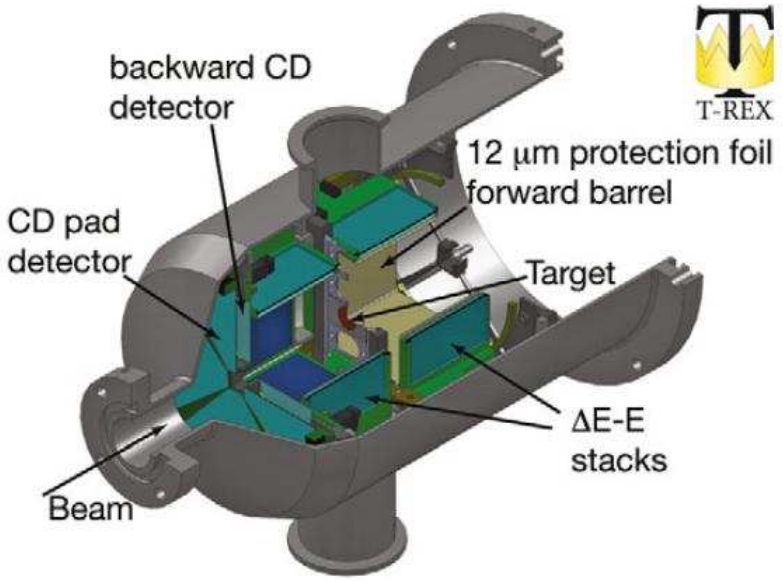

(a)

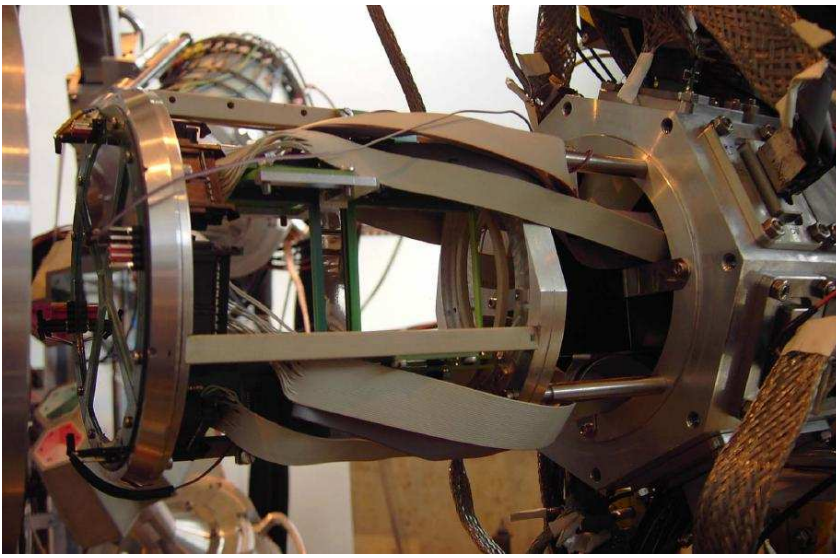

(b)

Figure 3.3: (a) Drawing of the T-REX setup. The CD detector in forward direction is not shown [102]. (b) Photo of the barrel detector, mounted on the beamline [104]. The beam is coming from the left.

Micron Semiconductors (type X1) [105] and the E_{rest} detectors by Canberra (type RF) [106].

In backward direction, with respect to the beam axis, the CD detector stack consists of two layers, each consisting of four quadrants. Both ΔE and E_{rest} detectors have a thickness of 500 µm. The ΔE detectors are segmented in 16 annular rings on the front side and 24 radial strips on the back. Thus, for each hit θ_{lab} and ϕ_{lab} are registered. To reduce the number of needed electronic channels the number of radial strips was reduced to 16 by connecting the inner strips in pairs [104]. The quadrants of the CD detector are in the outer regions partially covered by the barrel detectors. The CD detector in forward direction was mounted but not used in our experimental campaign. The CD detectors are produced by Micron Semiconductors [105] (types QQQ1 (ΔE) and QQQ2 (E_{rest})).

3.3.1 Tritium Target

To perform (t,p) reactions with radioactive beams a radioactive tritium target is needed. In this case the target consisted of a tritium-loaded titanium foil[3] with a total thickness of 500 µg/cm^2 (the dimensions are 4.5×12 mm^2 and about 1 µm thickness). The atomic ratio of tritium to titanium was ^{3}H/Ti = 1.5 resulting in an effective target thickness of tritium of about 40 µg/cm^2. At the time of production the activity of the target was about 10 GBq [90, 107]. This target was mounted on a target ladder together with three other targets. The target ladder was inserted in the reaction chamber through a hole in the bottom, so that the target was positioned in the center between the forward and backward barrel detectors. Further, the target ladder was put at a high voltage of +2000 V in order to reduce the background from δ-electrons. These δ-electrons are the result from the electromagnetic interaction of the high energy beam with the target material, resulting in an ionization of the target particles [108, 109].

The beam energy had to be lowered to 2.6 MeV/u instead of the maximum 2.85 MeV/u to avoid fusion of the ^{66}Ni beam with ^{48}Ti in the target. The fusion barrier for this reaction is $B_{fus}^{cm} = 77.3$ MeV, which would correspond to a beam energy of about 2.78 MeV/u. To be well below the fusion barrier, the beam energy was chosen to be 2.6 MeV/u.

[3] produced by EADS SODERN, 94451 Limeil-Brévannes Cedex, France

3.4 The Miniball Array

Since the intensities of radioactive beams for transfer (and Coulomb) experiments are typically quite low, a gamma ray detection system is needed that can detect gamma rays with a high efficiency and that has a large solid angle coverage. Further, the resulting nuclei of interest in the transfer reactions have a high velocity ($v/c \approx 0.07$ for ^{68}Ni in our experiment). Hence, the gamma rays resulting from the decay of populated excited states in these nuclei will in general be emitted 'in-flight', and thus their energies will suffer from a significant Doppler broadening. To be able to correct for these Doppler shifts, it is necessary to know the angle between the gamma ray and the direction of the nucleus emitting the radiation. All these requirements are met by using the Miniball detector array (details can be found in Ref. [110]).

This detector array consists of eight clusters of three Hyper Pure Germanium (HPGe) crystals each. These crystals are further divided in six segments by electronically segmenting the outer electrode of the crystal. The central electrode is referred to as the 'core' and registers the full energy that was deposited in the crystal, while the outer electrodes register only that part of the energy that was deposited in the corresponding segment. Through this segmentation (144 segments in total), a high granularity and thus position sensitivity is achieved. The typical energy resolution for the core and the segments is 2-3 keV. The core signal is used for energy determination and timing, while the segments are used for position information.

The high voltage (4000-5000 V) is applied to the central electrode. Further, the crystals are cooled through contact with a cold finger that is kept at liquid nitrogen (LN_2) temperature by connecting it with a dewar filled with LN_2. The clusters can be mounted on four flexible aluminum arms, which make it possible to vary the angle, orientation and distance of the clusters with respect to the target. To get the largest solid angle coverage, the clusters are mounted as close as possible to the reaction chamber.

Due to Compton scattering or pair production of a gamma ray in the detector material, it could be that the full energy of the gamma ray is deposited in several segments and/or crystals of the clusters. To be able to apply a Doppler correction, the first interaction point of the gamma ray with the detector has to be known, which cannot be determined. To overcome this problem, it is assumed that the first interaction point is the segment where the most energy is deposited. If Compton scattering occurs, it could be that the gamma energy is deposited in different crystals of the same cluster. Therefore, the principle of *addback* is applied, in which the energy of gamma rays detected in different crystals of the same cluster is added together if they are detected within 200 ns

of each other.

3.5 Data Acquisition

The signal processing is done with digital electronics for Miniball while T-REX uses analog electronics.

Miniball

The preamplified signals coming from the cores and the segments ($8\times3\times7=168$ channels in total) are sent to the 'Digital Gamma Finder with 4 Channels' (DGF-4C) modules from the X-ray Instruments Associates company [111]. Two modules per crystal are used, one for the core and two segments (leaving one channel empty), the other for the remaining four segments, thus in total 48 DGF-4C modules are used for Miniball. The core signal is used as a trigger to read out the other 7 channels. To keep the DGF-4C modules synchronous an external 40 MHz timing reference is used. The data are buffered until a forced read-out occurs (which happens after each On- and Off-Beam window). One other DGF-4C module was used, to register the supercycle time, the T1 signal and the EBIS time stamp.

T-REX

For the signals coming from particle detection, different types of Mesytec [112] modules are used. After preamplification and shaping all the signals are sent to Mesytec MADC-32 modules. The particle detectors modules use the same 40 MHz timing reference as the DGF-4C modules. The four quadrants of the barrel and CD detectors are arranged in two independent trigger groups, the top and left quadrant are put together and bottom and right. This to reduce the dead time, while keeping the amount of necessary MADC modules low. A schematic overview of the used electronics is shown in Fig. 3.4.

To reduce the number of output channels, Mesytec multiplexers (MUX-32) are used for the CD detectors. These modules have 32 input channels and only 5 output channels, two for energy and two to identify the corresponding channel where the energy was deposited, and one global trigger. The rings and strips of the trigger groups are connected to two different multiplexers, and thus two simultaneous events can be recorded. The output channels then give the energy and position signal (indicating which strip/ring is hit) for the first and second

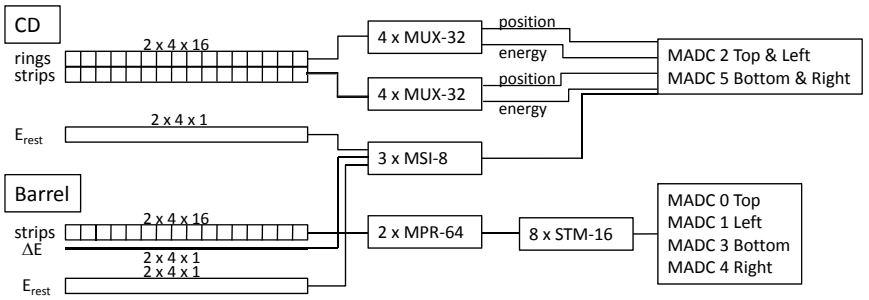

Figure 3.4: Schematic overview of the electronics used for T-REX, for details see text.

hit. If more than two simultaneous hits are registered the event is rejected. The output signals of a MUX-32 module are sent to an MADC module. The signals recorded by the E_{rest} detector are sent to a Mesytec MSI-8 module to preamplify and shape the signal, and are then also sent to the MADC corresponding to the same trigger group.

For the strips of the barrel detectors this multiplexing is not possible, since the different strips will not give a position signal that is unique for each strip. This is due to the read-out of the resistive strips. The strips are read out on one side only. By comparing the amount of charge collected on this side of the strip with the amount collected on the rear side of the detector (the ΔE detector), which is the total deposited energy, the position of the hit in the strip can be determined. Therefore the signal from every strip is separately recorded and sent to a Mesytec MPR-64 module (one for each trigger group) for preamplication and to a Mesytec STM-16 module (one for each quadrant and direction) for shaping. Finally, the signals from the strips of one quadrant (backward and forward direction) are sent to one MADC-32 module. The signals from the rear (ΔE) and E_{rest} detectors of the barrel are sent to two MSI-8 modules, before being sent to the corresponding MADC-32 module of the same trigger group.

The collection of data starts from the moment when particles are ejected from EBIS (in the case of the On-Beam window) and, as with the DGF-4C modules used for Miniball, the particle events are written to a buffer until a forced read-out occurs, which, as already mentioned, happens after each On- and Off-Beam window. The read-out is done with the MARABOU Data Acquisition software [113, 114] and is stored in *.med*-files [115].

4 | Data Analysis

In order to be able to analyze the data, the events that have been recorded by the MARABOU software [113, 114] have to be unpacked and transformed to ROOT [116] files. After unpacking, the data have to be calibrated. Finally, a kinematic reconstruction is done by converting recorded events to particles and gamma rays.

4.1 Unpacking and Event Building

In a first step MADC and DGF subevents are put together in one event, a so-called built event, if they are in coincidence with each other within 1 µs. These built events are stored as separate entries in a ROOT-tree. This unpacking of the data results in different *.root*-files. If data are taken with the beam, there is a root file that contains the Off-beam window data and two that contain the On-beam window data. The On-beam window is split in two files, one containing the events that are registered within 125-900 µs after the timestamp of the EBIS pulse and one containing events measured outside this window. The latter is called the On-beam background window and counts in this window stem mostly from β decay. The time window is depicted in Fig. 4.1. Since the length of one On-beam window is 1 ms (see section 3.2.1), the read-out stops after 1 ms, as can be seen in the figure. If data are taken with calibration sources, no distinction is made between an On- and Off-beam windows.

4.2 Calibration

The raw DGF and MADC data are then calibrated and linked to the different detectors. The built event is transformed into a so-called calibrated event

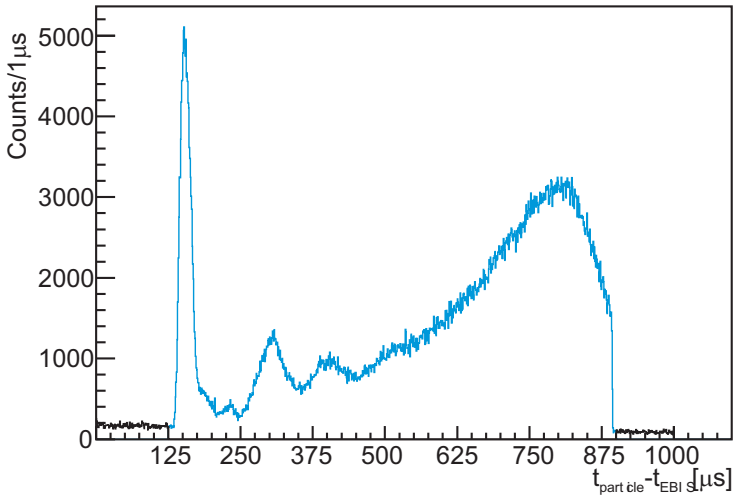

Figure 4.1: Time structure of one EBIS pulse. The blue spectrum marks the time window used in the analysis, the black the On-beam background window[1].

where the signals are calibrated, containing information on energy, timing and the detector in which the signal was registered.

4.2.1 ΔE Detectors Barrel

For the calibration of the ΔE detectors of the barrel and CD detector a quadruple alpha source, consisting of ^{148}Gd, ^{239}Pu, ^{241}Am and ^{244}Cm, was used.

In order to be able to determine the position of a particle detected in a strip, the strip signals of the different quadrants have to be calibrated. In a first step the pedestals or noise peaks of the strips of the different quadrants are determined. These noise peaks are subtracted by putting a different threshold for each strip of each quadrant. The threshold is determined as the maximum value of the noise peak (see Fig. 4.2)

To get an energy independent measurement of the position of a particle hit along a strip, the strip signal is divided by the total energy deposited in the

[1]This figure is constructed for data taken before the beam tuning in the middle of the experiment took place (see below section 4.3.1).

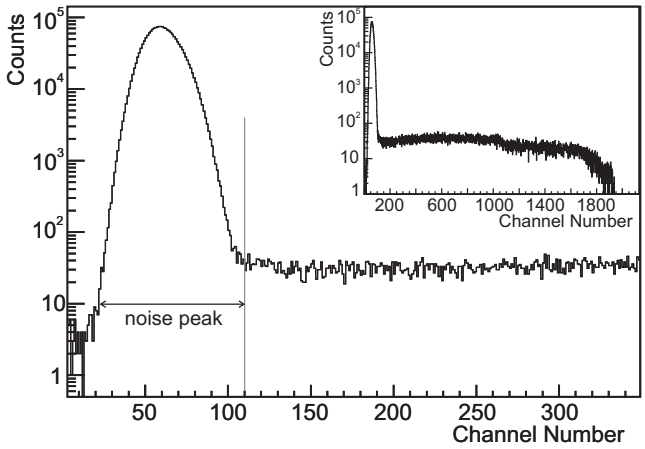

Figure 4.2: An example of the uncalibrated strip signal when data were taken with the alpha source. The threshold is indicated by the gray line. The inset shows the full spectrum registered by the strip. The maximal channel number were hits are registered corresponds to the maximal strip position and the alpha particle with maximal energy, which is about 6 MeV.

ΔE detector. An example of such an uncalibrated position signal is shown in Fig. 4.3. This position signal is calibrated such that the position along a strip lies between 0 and 1, instead of between 0 and $x_{\max}$. Later in the analysis, namely in the kinematical reconstruction, this position is converted to the real position ranging from -25 to 25 mm along a strip. The gain by which the position has to be multiplied in order to lie between 0 and 1, is determined by $1/x_{\max}$. To find $x_{\max}$ the step in Fig. 4.3 is fitted with a Fermi distribution (as shown by the blue line in the figure).

The energy measured at the rear of the ΔE detector depends on the position of the hit along the strip. This effect is shown in Fig. 4.4, which shows the uncalibrated rear signal as a function of the position along the strip. The measured rear signal is clearly larger for particle hits near a position along the strip equal to 1, which corresponds to the side of the strips that is read out. The energy can be corrected by using the following position dependent function

$$E_{corr} = \frac{E(x)}{1 - a(0.5 - x)}$$

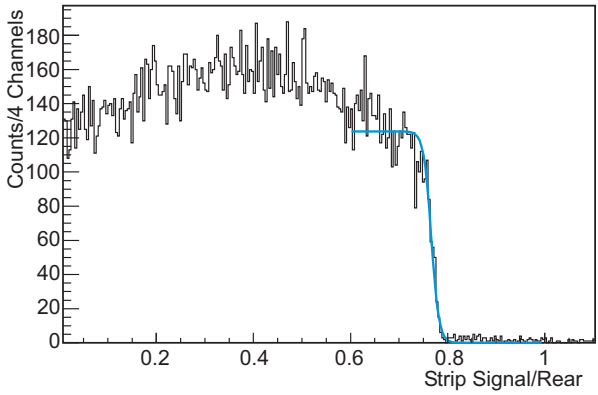

Figure 4.3: An example of the uncalibrated position signal along a strip, which is determined by dividing the strip signal by the full energy deposited in the ΔE detector (i. e. the rear signal). A fit with a Fermi distribution to determine the maximum position $x_{\max}$ that is needed to perform the position calibration is shown as a blue line.

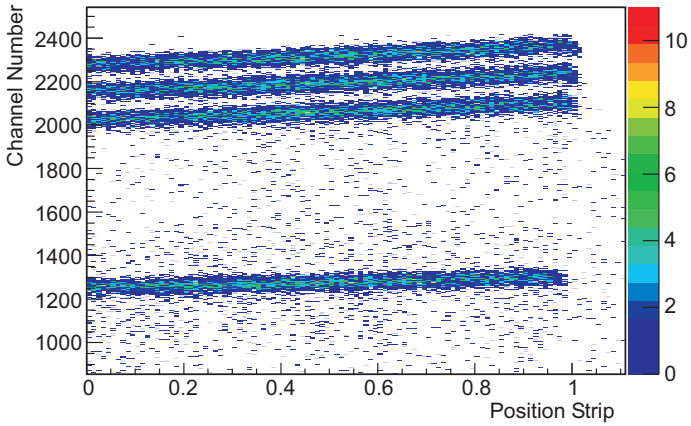

Figure 4.4: Uncalibrated rear signal as a function of the calibrated position signal for one strip. It is clear that the energy detected in the rear of the ΔE detector depends on the position along the strip.

in which $E(x)$ is the measured energy at position x along the strip and a is called the tilt correction factor.

This tilt correction can only be done for detectors without a (mylar) foil in front of them, since the foil causes such a large energy spread for the alpha particles, that the resolution to detect the alpha particles is too bad. Thus, in this case it is only applicable to the backward barrel detectors. It is assumed that the forward barrel detectors need the same tilt correction as the backward barrel.

As a final step, the rear of the ΔE detector can be calibrated in energy. The four alpha lines are fitted with four Gaussians and a linear fit is performed as follows

$$E_{cal} = a \cdot (E - b) \tag{4.1}$$

where E is the channel number. This can easily be done for the backward barrel ΔE detectors. In forward direction however, there is a mylar foil in front of the detectors. The energy loss of the alpha particles in this mylar foil has to be taken into account. These energy losses were calculated with SRIM2008 [117]. Since with increasing strip number the effective thickness of the foil increases, the four alpha lines cannot be distinguished anymore after strip number 4. Also, the foil is thick enough to stop the alpha particles with lowest energy. Further, the effective foil thickness depends not only on the strip number (which gives the polar θ-direction), but also on the position along the strip (azimuthal ϕ-direction). Therefore, only the middle of the strip ($x = 0.500(25)$) is taken into account in the calibration, since in this case $\phi = 0$. As the energy loss of the alpha particles is thus strip dependent, this gives $4 \cdot 3 = 12$ calibration points for the rear side of the forward ΔE detectors.

4.2.2 Pad Detectors Barrel

For the calibration of the E_{rest} or pad detectors of the barrel (and CD) the alpha source cannot be used, since the alpha particles are all stopped in the ΔE detectors. There are two methods used to calibrate the pad detectors. One uses the Compton scattering of gamma rays from a ^{152}Eu source, the other uses the known kinematics of a transfer reaction using a stable beam.

Low Energy Calibration

The first method to calibrate the pad detectors of the barrel uses the Compton scattering of gamma rays coming from the decay of ^{152}Eu. Gamma rays can pass the ΔE detectors without interaction, then undergo a Compton scattering

in one of the pad detectors and finally be detected by Miniball. A plot of the gamma energy detected by Miniball versus the uncalibrated pad energy is shown in Fig. 4.5. This plot also shows the Compton scattered line of the 1408 KeV gamma ray (indicated by the black line). Since the Miniball detectors can easily be calibrated (see section 4.2.4) and the total energy of the gamma ray is known, the pad detector can be calibrated by determining the linear function through the Compton scattered line. When a projection is made along the black line in the figure a peak will result. This projection is made for different gains of the pad detector, the gain that results in the largest area underneath the peak provides the correct gain for the calibration of the pad detector.

One drawback of this method is the fact that the (intense) gamma line with highest energy coming from the decay of ^{152}Eu has an energy of only 1408 keV. Since the energy deposited by protons in the pad detectors of the forward barrel can go up to about 18 MeV, this calibration procedure will not be very precise for these higher energies. This calibration method is therefore usually combined with the one described below. In contrast, in backward direction the deposited energy of the protons is maximum only 5 MeV, it is thus safe to use this method for the backward barrel pad detectors. However, the gamma rays do not lose any energy in the dead layer of the detector, while the protons do. The results of this low energy method were therefore also for the backward barrel checked with calibration method described below.

High Energy Calibration

The method to calibrate higher energies uses the known kinematics from the transfer reaction ^{22}Ne(d,p)^{23}Ne. A beam of ^{22}Ne of high intensity can easily be produced, since ^{22}Ne is a buffer gas of the REX-ISOLDE system. This beam then impinges on a deuterated polyethelene target. The calibrated measured ΔE energy is used to find a calibration for the pad detector. The ΔE energy versus the uncalibrated pad energy for one strip of one quadrant of the forward barrel detector stack is shown in Fig. 4.6. Protons result from the (d,p)-reaction while deuterons result from the elastic scattering of the beam on the target. If the effective thickness of the ΔE detector and the energy loss in this detector is known, the full energy of the protons/deuterons can be reconstructed, by using e. g. the stopping and range tables of SRIM2008 [117]. The ΔE-E_{rest} histogram is divided in different ΔE energy bins. For each of these energy bins, the channel number of the pad detector is determined and the full energy is reconstructed. From this reconstructed energy, the energy deposited in the pad detector can be determined. By performing a linear fit (of the form eq. (4.1)) between the

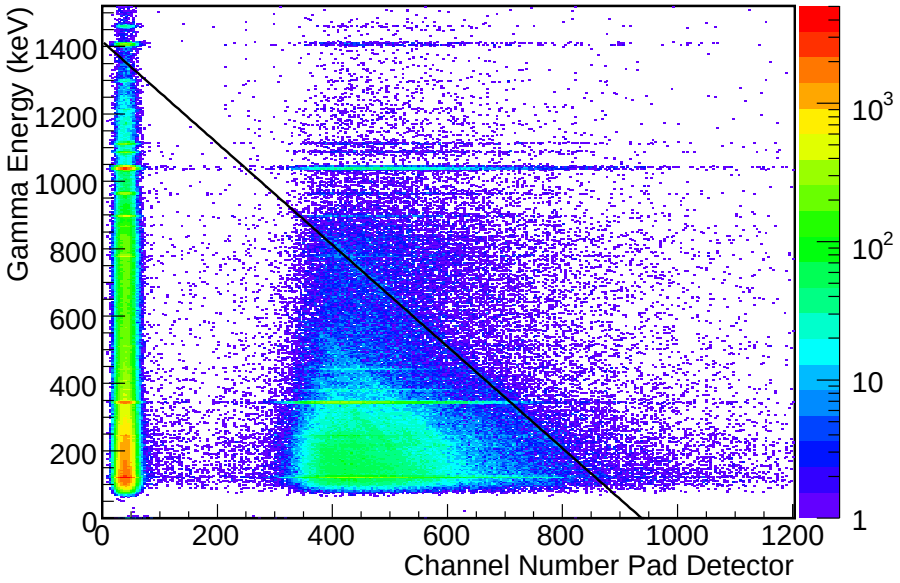

Figure 4.5: Gamma energy detected in Miniball versus the uncalibrated pad detector. The black line indicates the Compton scattered line originating from the 1408 keV gamma line of the decay of ^{152}Eu.

real energy deposited in the pad detector and the channel number, the pad calibration can be obtained.

4.2.3 ΔE Detectors CD

Since for the CD detectors Mesytec multiplexers were used (see section 3.5), the signals coming from this modules have to be 'de-multiplexed', which means it is necessary to determine in which ring and strip of the ΔE detector of the CD a certain hit was registered. The strip or ring number is saved as a position or ID. Each strip/ring has a different ID. The ID's for the rings of the Top and Left quadrant of the backward CD are shown in Fig. 4.7. The left group belongs to the Top quadrant, the right to the Left quadrant.

If the de-multiplexing is done, all the registered energy signals can be linked with a certain ring and/or strip. The detectors can then easily be calibrated

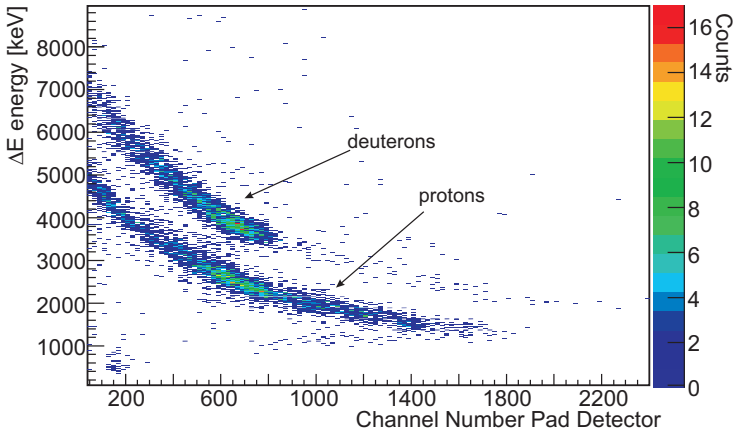

Figure 4.6: Calibrated ΔE energy versus the uncalibrated pad detector for the reaction ^{22}Ne(d,p)^{23}Ne.

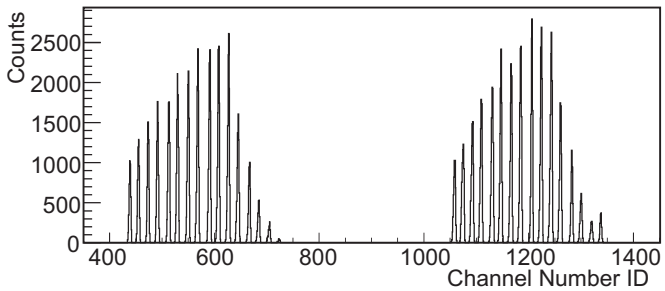

Figure 4.7: ID of the rings of the Top and Left quadrant of the backward CD detector. Each position peak corresponds to one ring.

with the quadruple alpha source, by performing again a linear fit eq. (4.1) through the peak positions of the alpha lines.

Since all interesting particles are stopped in the ΔE detector of the backward CD detector, no pad calibration was done for the CD detector.

4.2.4 Miniball Detectors

The Miniball detectors need to be calibrated and their position needs to be determined in order to be able to perform a Doppler correction. Further, the detection efficiency of gamma rays as a function of their energy needs to be explained.

Energy Calibration

For the energy calibration of the Miniball cores and segments a ^{152}Eu and a ^{60}Co source were used. The strongest gamma lines are determined and are fitted with a linear fit as in eq. (4.1).

Doppler Correction

To be able to perform the necessary Doppler correction for the detected gamma rays resulting from a transfer reaction, where the gamma rays are emitted 'in-flight', the angles of the Miniball detectors have to be determined. To determine these angles again the well-known ^{22}Ne(d,p)^{23}Ne reaction is used. This reaction can populate the first excited state in ^{23}Ne at 1017 keV. The 1017 keV gamma ray resulting from the decay of this state suffers from a Doppler shift, since it is emitted 'in-flight'. The Doppler correction can be performed via

$$E_{corr} = \frac{E_{lab}}{\sqrt{1-\beta^2}}(1-\beta\cos\alpha) \tag{4.2}$$

in which $\beta = v/c$ and α is the angle between the gamma ray and the trajectory of the nucleus. Since, the maximum scattering angle of ^{23}Ne is $< 5°$, it can be assumed that its deflection from the beam axis is zero. In this case α is just the polar θ-angle, the angle between the beam axis and the Miniball detector, and does not depend on the azimuthal ϕ-angle anymore. For each segment the Doppler shifted line is determined and by using eq. (4.2), the angle of every segment of the Miniball detectors can be determined.

The relative resolution (FWHM divided by energy) obtained with the Doppler correction was about 1 %.

Efficiency Calibration

The determination of the efficiency curve for gamma rays is extensively discussed in Ref. [118, 119], no details will be given here. The efficiency curve presented in Fig. 4.8 is obtained using the addback method and using a ^{152}Eu and a ^{60}Co source.

The data points were fitted with a function of the form

$$\epsilon(E) = \exp\left[a_0 + a_1 \ln\left(\frac{E}{x}\right) + a_2 \left(\ln\left(\frac{E}{x}\right)\right)^2\right]. \tag{4.3}$$

where ϵ is the efficiency and E the energy of the gamma rays in keV. The parameter x is a scaling factor ($x = 600$ in the current experiment) that is introduced in order to reduce the error on the parameters a_i. By using this factor the intercept with the vertical axis is artificially brought closer to the data points, which will reduce the error on the fit parameters. The parameters resulting from a fit of this function through the data points (the gray line in Fig. 4.8) are given in Table 4.1.

Timing

Since the registered time signal for low energy gamma rays is slower than that for high energy gammas, there is an exponential tail visible for low energies when the time difference between protons and gamma rays is plotted versus the gamma energy. This is shown in Fig. 4.9.a. In order to reduce the background from random coincidences, this tail can be significantly reduced by fitting it with an exponential function of the form

$$f(E) = a_0 - a_1 \exp\left(\frac{a_2}{\sqrt{(E)}}\right). \tag{4.4}$$

where the energy E of the gamma rays is given in keV.

The result after this correction is shown in Fig. 4.9.b. The parameters for the fit are given in Table 4.2. This correction is referred to as the *walk correction*.

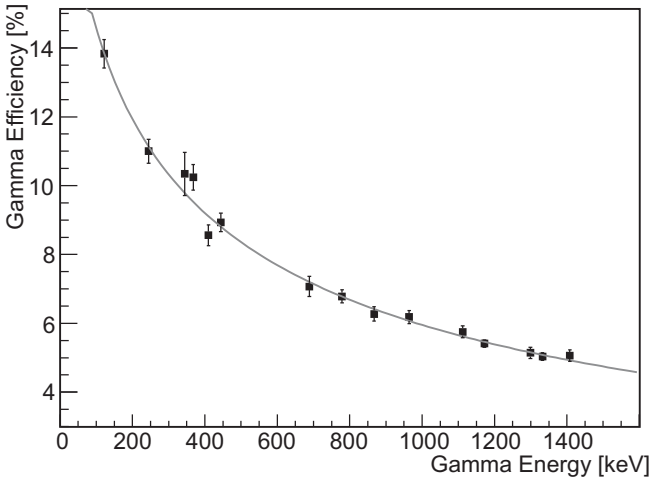

Figure 4.8: Efficiency curve for the Miniball cluster as a function of gamma energy. The gray line is a fit through the data points using eq. (4.3).

Parameter	Value
a_0	$-2.58(2)$
a_1	$-0.47(3)$
a_2	$-0.07(3)$

Table 4.1: Parameters resulting from a fit of the form eq. (4.3) through the data points in Fig. 4.8.

4.3 Kinematic Reconstruction

Once all the events are calibrated, their kinematical properties have to be reconstructed. For the particles this means that their direction has to be determined from their position in the detector, namely the polar θ and azimuthal ϕ angles have to be deduced. For the gamma rays, the direction was also determined and the addback procedure was applied (see section 3.4).

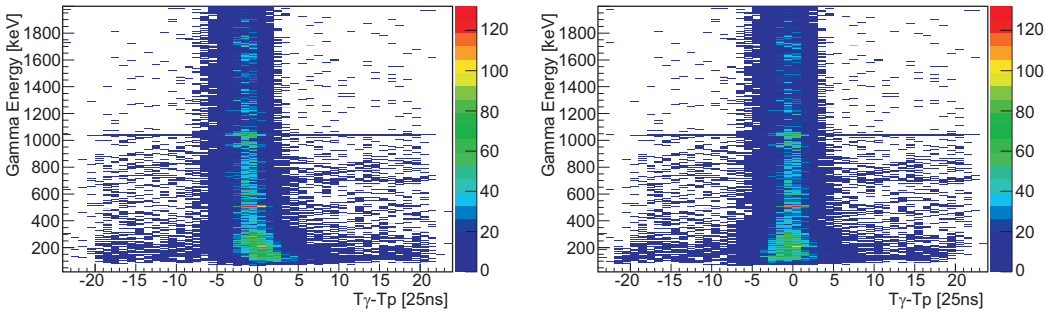

(a) (b)

Figure 4.9: Gamma energy versus time difference between a gamma ray and a proton. In (a) the uncorrected and in (b) the corrected spectrum is shown.

Parameter	Value
a_0	$-2.93(3)$
a_1	$-0.75(2)$
a_2	19.4(3)

Table 4.2: Parameters resulting from a fit of the form eq. (4.4) through the tail in Fig. 4.9.a.

4.3.1 Particle Identification

The particles are identified by looking at their ΔE-E_{rest} signature. This is possible, since particles with varying mass and energy will lose a different amount of energy in the ΔE detector, which is described by the Bethe-Bloch equation [120]. An example of all identified particles in one strip of the forward barrel detector is shown in Fig. 4.10. The tritons come from elastic scattering of the beam on the tritium in the target. The observed deuterons are the result of the (t,d) reaction with the ^{66}Ni beam. Since protons were also present in the target, elastically scattered protons are observed. The other protons are the interesting particles, they stem from the (t,p) reaction with the ^{66}Ni beam. There are also 'punch-trough' protons, their origin will be explained below. As can be seen in the figure, some of the particle identification lines overlap. Since we do not want to lose protons and tritons (to calculate the beam intensity, see below) in the analysis and the number of deuterons in the overlap regions is comparable to or less than that of the protons or tritons in these regions, the latter are chosen above the deuterons.

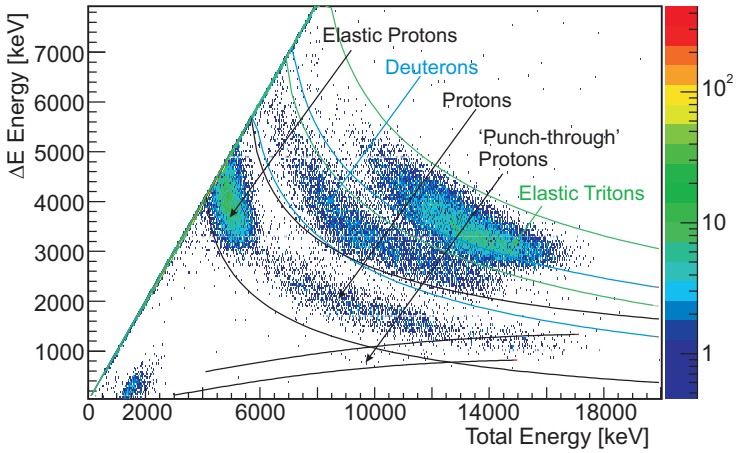

Figure 4.10: ΔE-E spectrum for one strip of the top forward barrel detector. All the identified particles are indicated.

In the backward direction it is more difficult to perform a particle identification, since most particles resulting from a transfer reaction are stopped in the ΔE detector. Not to lose any transfer protons, it was assumed that everything in backward direction is a proton if their energy loss in the ΔE detector is less than the maximum energy loss of a proton.

Punch-through Reconstruction

In forward direction, some protons resulting from the (t,p) reaction on ^{66}Ni have enough energy to punch through both the ΔE detector and the pad detector. These protons are referred to as 'punch-through' protons. Since they fly through both detectors, their full energy is not registered. Therefore a method was developed to reconstruct it. If the deposited energy and the effective detector thickness (ΔE + pad) is known, the energy of the particle can be reconstructed. The protons that punch through both detectors are indicated in Fig. 4.10. However, between the indicated lines in this figure lie also protons that are stopped in the detectors. Thus, another cut had to be made to separate the punch-through protons from the stopped protons. This is indicated in Fig. 4.11, all protons lying inside the dashed gray area (between the blue and green lines) are identified as punch-through protons. The blue line was determined by sight, to include as much as possible punch-through protons and as few as possible stopped protons. Fig. 4.11 was obtained by performing a

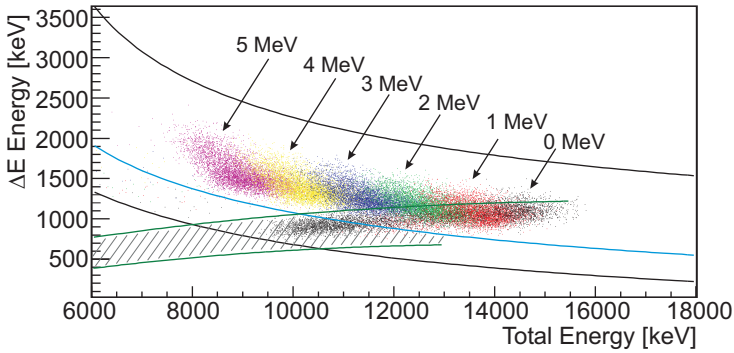

Figure 4.11: Simulation of a ΔE-E spectrum for one strip of the top forward barrel detector, in which every color is a simulation to another excited state in ^{68}Ni (from the ground state up to 5 MeV in steps of 1 MeV). The dashed gray area indicates the events that are identified as punch-through protons.

GEANT4 simulation [121], since in this case the number of events can be freely chosen and the punch-through protons are more clearly visible. The different colored groups indicate a simulation to a different excited state in ^{68}Ni, namely states from 0 MeV, the ground state, up to 5 MeV in steps of 1 MeV. It is clear that the cut is far from perfect, but it is not possible to improve it, since in that case a lot of stopped protons would also be identified as punch-through protons.

After particle identification the original energy of the particles can be reconstructed, by taking into account the energy losses in the target and in the mylar foil in front of the forward barrel detector.

Particle Energy Versus Lab Angle

In Fig. 4.12.a all the detected particles as a function of their lab angle are shown. The indicated lines show the expected kinematical curves for the different identified particles. For clarity, these plots are shown separately for the identified protons, deuterons and tritons in Fig. 4.13. Immediately, by looking at Fig. 4.12.a and Fig. 4.13.a, it is clear that in backward direction (lab angles $> 90°$) a lot of noise is present. This is due to a bad beam tuning in the middle of the experiment. This is clear from Fig. 4.12.b, which shows the detected

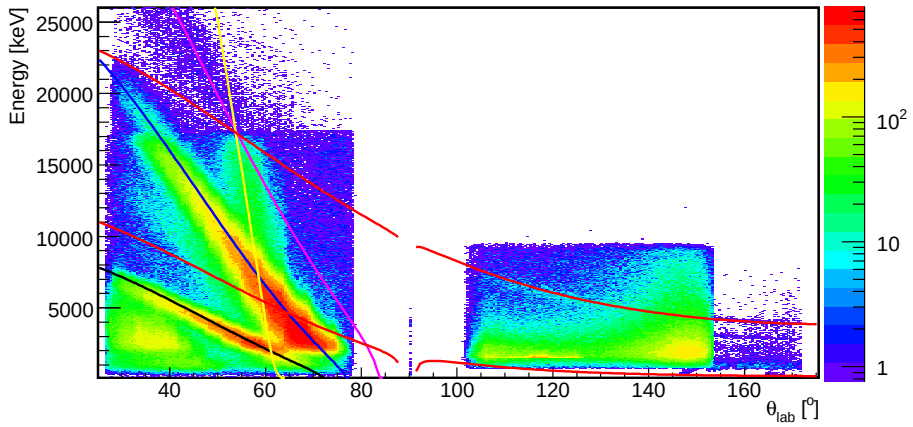

(a)

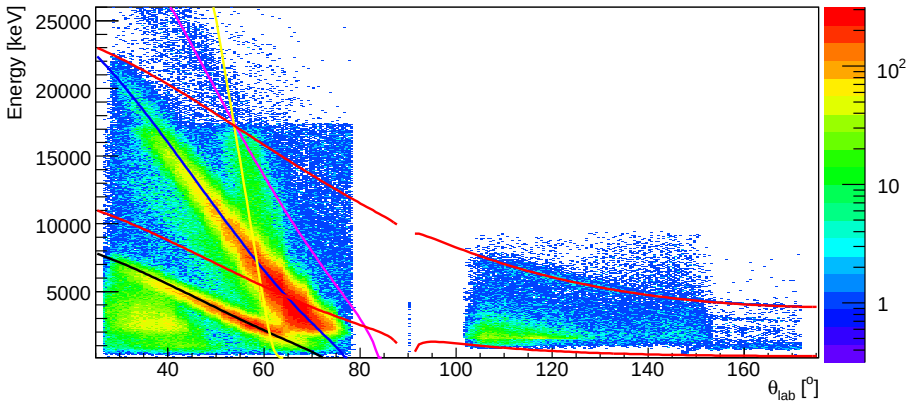

(b)

Figure 4.12: Total energy versus lab angle for all detected particles. (a) Full statistics (105 h), (b) only the first part of the run (43 h). The elastic protons (black), tritons (blue) and oxygen nuclei (yellow) are indicated. Particles resulting from a transfer reaction are also shown, in pink alpha particles resulting from the ^{66}Ni(t,α)^{65}Co reaction (to the ground state in ^{65}Co) and in red protons from the ^{66}Ni(t,p)^{68}Ni reaction (the top line indicates a transfer to the ground state in ^{68}Ni, the bottom line transfer to a state at 8 MeV).

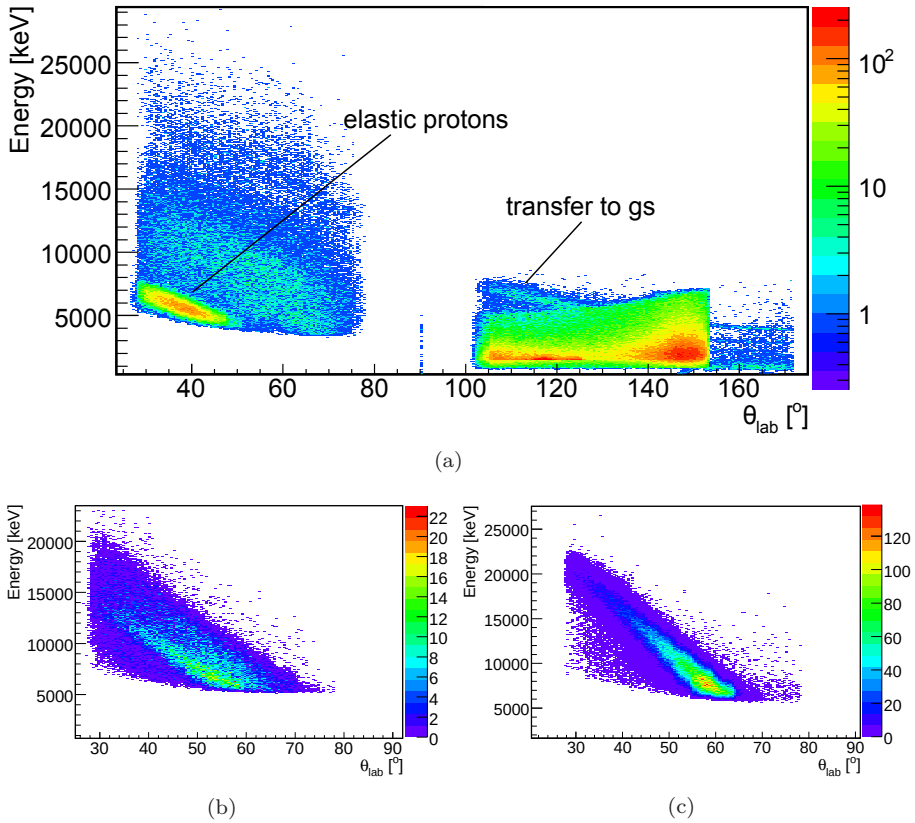

Figure 4.13: Total energy versus lab angle for identified (a) protons, (b) deuterons and (c) tritons (full statistics is shown). Transfer to the ground state of ^{68}Ni and the elastically scattered protons are indicated in (a).

particles before this beam tuning took place. The total time of measurement in the experiment was about 105 h, of which about 43 h was measured before the beam tuning. For this reason the analysis of the experiment was divided in a 'first part' (first 43 h) and a 'second part'. The noise in the backward barrel is not coincident with prompt gamma rays, therefore when looking to proton-gamma coincidences, this noise does not cause a problem. However, in certain cases information is required, without the ability to look for proton-gamma coincidences. When this occurs it is only possible to look at the first part of the run. It is further important to note that only three out of four quadrants of the forward barrel were working, the right quadrant broke down

in the beginning of the experiment.

Particle Detection Efficiency

The particle detection efficiency can be determined by using a GEANT4 simulation [121]. An isotropic angular distribution of protons is simulated and two sets of data are registered, all *simulated* events and all *detected* events. The latter events are analyzed in the same way the real data events from the experiment are analyzed. In this way the thresholds in the detectors and the losses due to e. g. wrong particle identification are taken into account. The simulated events are used as a reference, to register the number of emitted protons at a certain angle. To get the detection efficiency, the ratio between the analyzed, detected events and the simulated events is taken for every angle. These simulations have to be performed separately for every excitation energy in ^{68}Ni, since the detection efficiency can change for different excitation energies, as is shown in the example below.

The detection efficiency for protons transferred to the ground state (black dots) and to an excited state at 8 MeV (gray dots) in ^{68}Ni is shown in Fig. 4.14. For the ground state the detection efficiency of the protons is rather constant in backward direction, except for the change from the barrel to the CD detector. In forward direction the detection efficiency for the ground state protons has quite a strange shape, which can be explained by the fact that most of the protons transferred to the ground state are punch-through protons. It shows again that the punch-through reconstruction is far from perfect. A lot of punch-through protons are not identified correctly, and thus their reconstructed energy is also not correct. This reduces the detection efficiency to the ground state. Near 70° the detection efficiency rises again, reflecting the fact that the protons do not punch through both the ΔE and pad detector anymore, and thus are identified correctly.

The detection efficiency for protons transferred to a state at 8 MeV in ^{68}Ni show a different result. In forward direction the detection efficiency is rather constant, up to the angles where the protons do not reach the pad detector anymore and are thus stopped in the ΔE detector. In this case they are not identified and thus not taken into account. In backward direction the protons have an energy below the threshold of the barrel detectors (see also Fig. 4.12) and thus cannot be identified, reducing the detection efficiency to zero. In the CD detector part of the protons can still be identified, resulting again in a higher detection efficiency.

The maximum efficiency in both the forward and backward barrel is quite low (60-70 %), this is due to the fact that only three out of four quadrants are

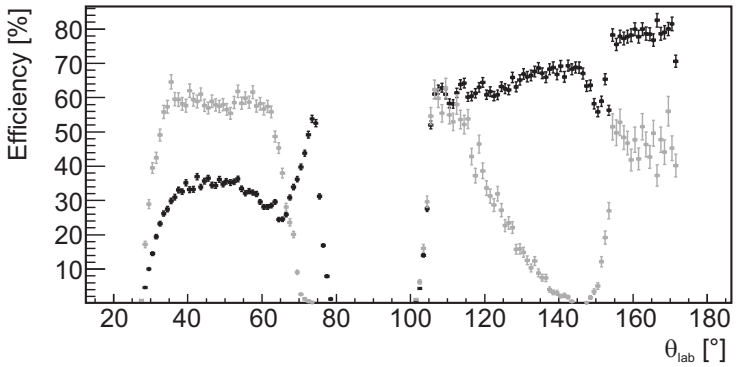

Figure 4.14: Detection efficiency for protons transferred to the ground state (black dots) and to an excited state at 8 MeV (gray dots) in ^{68}Ni. See text for details.

taken into account in the efficiency calculation. The bottom quadrant in the backward barrel had a very bad energy resolution and, as already mentioned above, the right quadrant of the forward barrel was not working.

4.3.2 Beam Intensity

From the elastic scattering of the ^{66}Ni beam on the tritium in the target, the beam intensity can be determined. This can be done by scaling the differential cross section, resulting from a DWBA calculation, to the experimental data. The number of detected particles R can be related to the differential cross section $d\sigma/d\Omega$ through

$$R = t \cdot I \cdot N \cdot \frac{d\sigma}{d\Omega} \cdot \Delta\Omega \tag{4.5}$$

where t is the time of measurement, which is known from the data files, N is the target thickness, I is the beam intensity and $\Delta\Omega$ is the solid angle factor, which is proportional to $\sin\theta_{lab}$. If the differential cross section $d\sigma/d\Omega$ is known from a DWBA calculation it can be scaled to the angular distribution of the elastically scattered tritons (after correction for the particle detection efficiency), as is shown in Fig. 4.15. In this figure two DWBA calculations are shown, one using the global optical parameters from Becchetti and Greenlees [73] (black line) and one using those of Li *et al.* [74] (blue line). The best reduced χ^2 value is obtained from the fit using the paramters from Becchetti and Greenlees (black

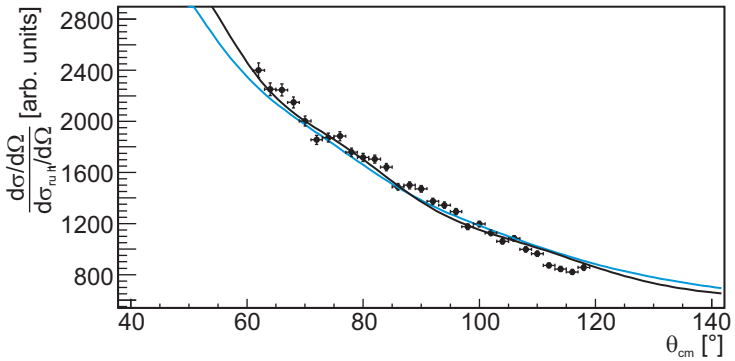

Figure 4.15: Differential cross section of elastically scattered tritons, normalized to the Rutherford cross section. Two DWBA calculations that are fitted to the data are also shown. For the calculations global optical model parameters from Becchetti and Greenlees [73] (black line) and Li *et al.* [74] (blue line) are used.

line). Therefore this calculation is used to deduce the beam intensity. As in Chapter 2, these DWBA calculations were obtained by using the computer code FRESCO [77]. From the scaling factor of the calculations to the data an average beam intensity of $2.4(3) \cdot 10^6$ pps was deduced. The main error stems from the large uncertainty in the target thickness, the error on the tritium content in the target amounts to about 10 %. Further, since tritium is radioactive and the target was already approximately three years old at the time of measurement, only about 84 % of the original tritium still remained.

^{1}H/^{3}H Ratio in Target

Fig. 4.12 shows that also elastically scattered protons are observed, thus it is clear that there were also protons present in the target. However, since the energy of the elastically scattered protons is low, they can only be identified unambiguously for a very limited angular range (from $\sim 30°$ to $\sim 42°$ lab angle). Therefore the DWBA calculations cannot be scaled in a reliable way to the angular distribution of the elastically scattered protons. However, to get an estimate of the ratio of protons to tritons in the target, the differential cross section, from a DWBA calculation using global optical model parameters from Koning and Delaroche [75] for protons and Becchetti and Greenlees [73] for tritons, was integrated over the angular range from 30° to 40°. The ratio was then calculated as follows

$$\frac{N_{1H}}{N_{3H}} = \frac{R_{1H} \cdot \sigma_{3H}}{R_{3H} \cdot \sigma_{1H}} \tag{4.6}$$

where the symbols have the same meaning as in eq. (4.5), but are now integrated from 30° to 40° lab angle. A ratio of $N_{1H}/N_{3H} = 5.46(3)\,\%$ was obtained.

4.3.3 Coincidence Gates

All particles and gamma rays coincident within 1 µs are put together in one event. However, this coincidence window is too broad to only contain real *prompt* coincidences between particles and gamma rays. The time difference between a proton and a gamma ray (in one event) is shown in Fig. 4.16.a. One can clearly distinguish a prompt coincidence peak, which contains the real coincidences, and a background caused by random coincidences. These prompt and random windows can be used to subtract random background from the prompt, real coincidences. One can also notice that there are events outside the 1 µs window (outside the -20 to 20 timestamps in the figures). This is due to events with multiplicity higher than one and due to shifts caused by the applied walk correction.

Fig. 4.16.b shows the same plot, but now for the time difference between two gamma rays, when they are in coincidence with a proton, i. e. it shows proton-gamma-gamma coincidences.

In the analysis a problem with the timing of the gamma rays was identified for the first 14 h of the run. Some gamma rays did not receive the correct time stamp. As a consequence, when investigating the proton-gamma coincidences, these files cannot be used.

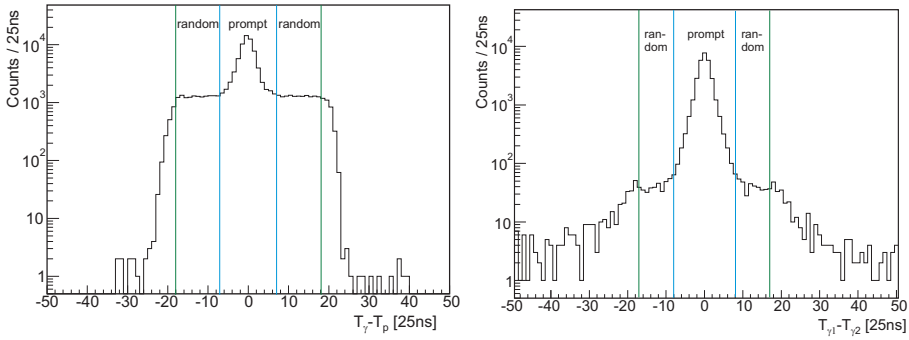

(a) (b)

Figure 4.16: (a) Time difference between protons (T_p) and gamma rays (T_γ) and (b) time difference between two gamma rays when they are in coincidence with a proton, in units of 25 ns. The prompt and random coincidence windows are indicated.

5 | Results

In this chapter the results from the ^{66}Ni(t,p) experiment will be reported. The proton-gamma coincidences and excitation energy spectrum of ^{68}Ni will be discussed. The chapter will close with a comparison of the angular distributions for a few states with calculations using FRESCO [77].

5.1 Proton-Gamma Coincidences

In Fig. 5.1 the Doppler corrected gamma spectrum in coincidence with protons is shown. The black spectrum shows the prompt coincidences and the gray spectrum shows the random coincidences (constructed according to the gates in Fig. 4.16.a). The most intense random coincidence line arises from the β decay of ^{66}Cu, β-decay daughter of ^{66}Ni. The β decay of ^{66}Cu results in a strong gamma line at 1039.231(6) keV [25]. This line is broadened and shifted in energy in the Doppler corrected proton-gamma spectrum, and thus two broad lines or bumps are observed around an energy of 1039 keV, which are indicated in gray in Fig. 5.1. The reason that one of these bumps is more intense than the other, lies in the fact that in the second part of the run, probably part of the beam was stopped in the back of the particle detection chamber (see also section 4.3.1). For this reason, the 1039 keV line is dominantly detected in the backward oriented Miniball detectors. The Doppler correction for the backward oriented clusters is always in the same direction (to higher energy), and thus the bump, due to the broadened and shifted 1039 keV line, that corresponds to detection in the backward oriented Miniball clusters, will be more intense than the other one.

The most intense observed gamma lines in ^{68}Ni stemming from the (t,p) reaction are indicated in Fig. 5.1 in black. All the observed gamma transitions, together with their intensities are given in Table 5.1. The intensities are all

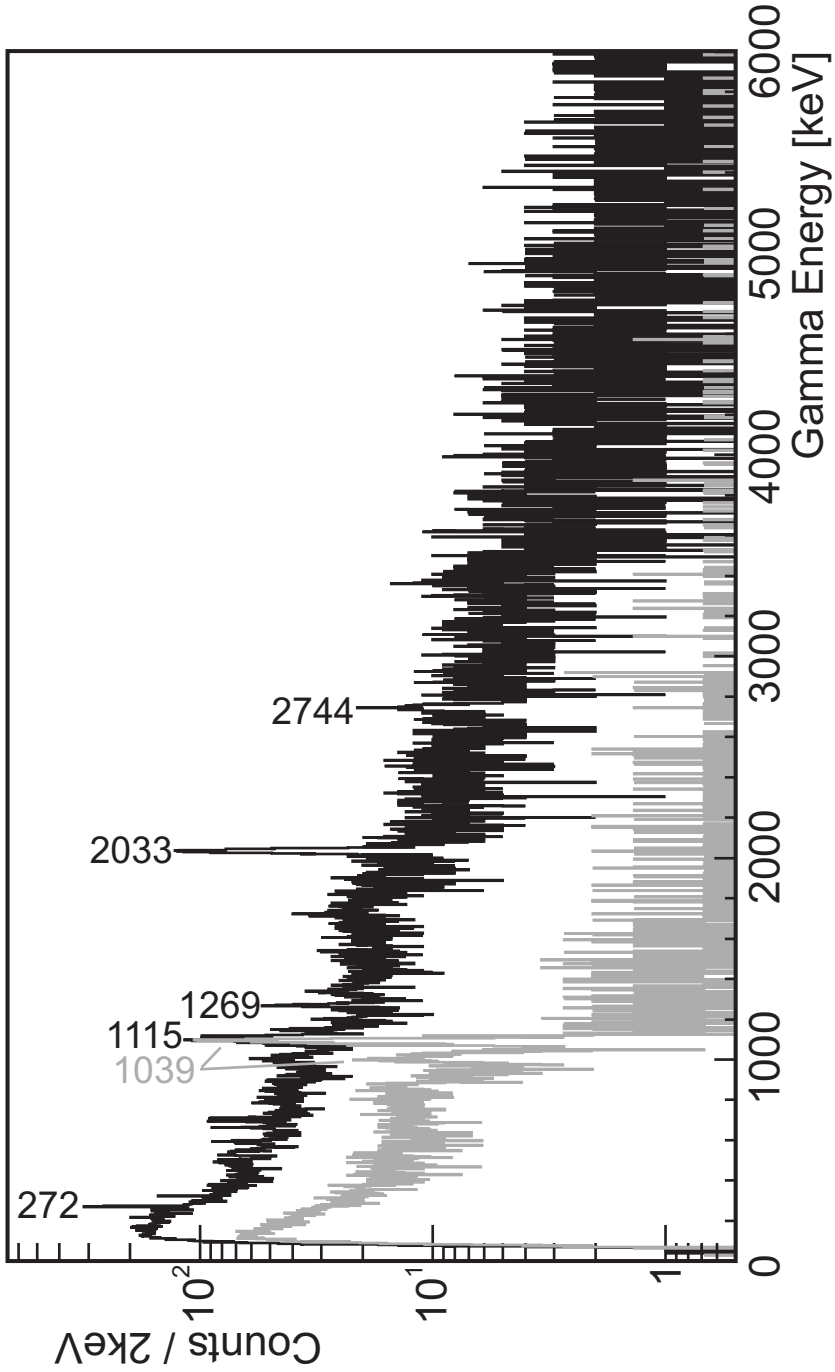

Figure 5.1: Doppler corrected gamma spectrum in coincidence with all protons (no energy conditions were set on the detected protons). The black spectrum shows the prompt coincidences, the gray the random coincidences.

Table 5.1: Observed gammas in the ^{66}Ni(t,p) reaction. Total counts and intensities relative to the 2033 keV transition are given. ⋆ indicates gammas that are unknown in ^{68}Ni, • indicates doublets and ◇ indicates lines in ^{67}Ni (see text for details).

E_γ (keV)	Counts	Rel. Int. (%)
217.6(6)⋆	112(36)	3.4(12)
271.8(2)	418(41)	13.9(18)
323.3(3)	96(20)	3.4(8))
378.3(6)	62(20)	2.4(8)
592.1(13)	194(47)	8.9(23)
663.3(4)	100(27)	4.9(14)
694.6(4)◇	179(25)	8.9(14)
709.2(4)	191(24)	9.6(14)
1115.4(4)	334(36)	21.3(29)
1144.5(15)•	153(47)	9.9(32)
1202.6(15)◇	48(20)	3.2(13)
1268.5(7)	189(23)	12.9(19)
1338.2(18)⋆	96(25)	6.8(19)
2034.2(3)	1099(41)	100.0(105)
2744.3(18)	135(19)	15.0(27)

corrected for gamma detection efficiency and are given relative to the intensity of the 2033 keV transition[1]. This line stems from the gamma decay of the first excited 2^+ state at 2032.9(2)keV [53] (see Fig. 5.4 below). There are only two gamma transitions, with an energy of 217.7(6) keV and 1338.2(18) keV, that have not been observed before in ^{68}Ni. An attempt to place these gamma transitions in the level scheme of ^{68}Ni by investigating proton-gamma-gamma coincidences fails due to the lack of statistics. Two pairs of gamma rays show clear coincidences, namely the 272-324 keV and the 1115-2033 keV pair, which are shown in Fig. 5.2. These gamma cascades confirm previous experiments and supports their identification as belonging to ^{68}Ni. Fig. 5.2 also shows the gamma rays in coincidence with the unknown 218 keV and 1338 keV transitions. No transitions are observed in coincidence with these two lines and as a consequence these transitions cannot be placed in the level scheme of ^{68}Ni.

[1] We quote here the value of 2033 keV throughout the text, instead of 2034 keV measured in our experiment, since the energy of this state has been measured more precisely in a recent deep-inelastic reaction experiment [53]. The same applies to the 323 keV transition which is quoted as 324 keV.

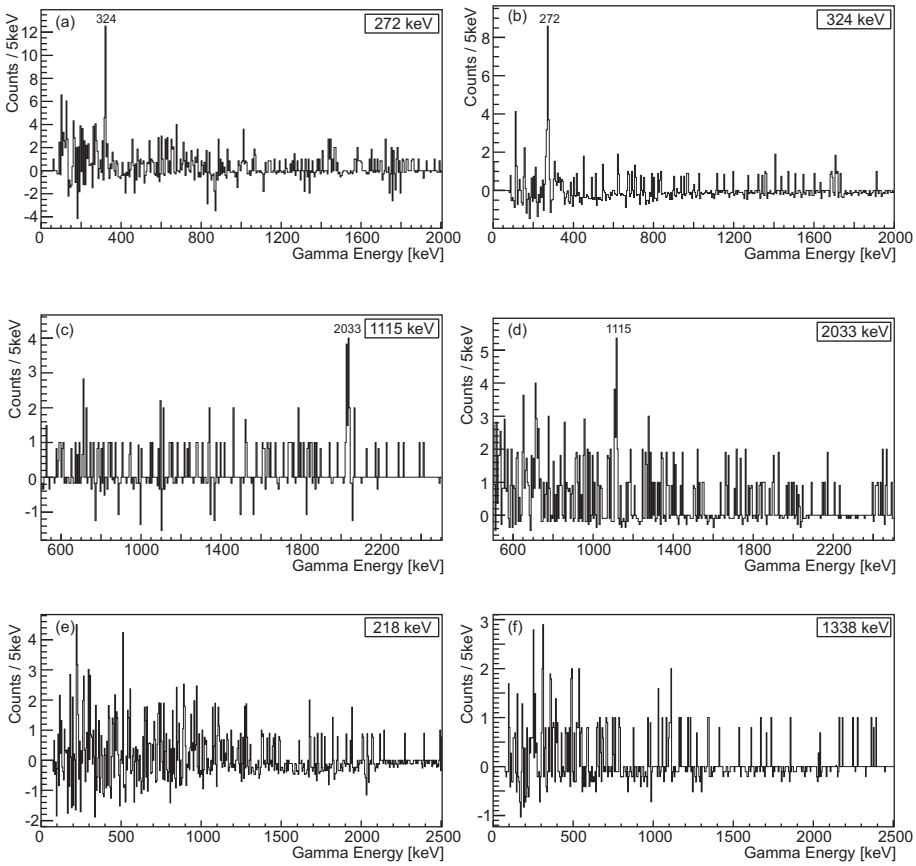

Figure 5.2: Random subtracted gamma spectra from proton-gamma-gamma events. The coincidence gates were put at a gamma energy of (a) 272 keV, (b) 324 keV, (c) 1115 keV, (d) 2033 keV, (e) 218 keV and (f) 1338 keV.

Table 5.1 also shows that one doublet was observed at 1144.5(14) keV. Part of the gamma spectrum in coincidence with protons (Fig. 5.1) around the energy region of the 1145 keV line is shown in Fig. 5.3 . The observed gamma transitions in this energy region are indicated. The measured FWHM of the 1145 keV line is larger than the FWHM of the surrounding observed gamma transitions. Therefore the 1145 keV line is interpreted as a doublet consisting of the known 1139 keV and 1151 keV transitions (see Fig. 5.4 below). The 1139 keV is the transition from the 2_2^+ to the 0_2^+ state, which makes it an interesting transition in the current experiment. However, it cannot be separated from the

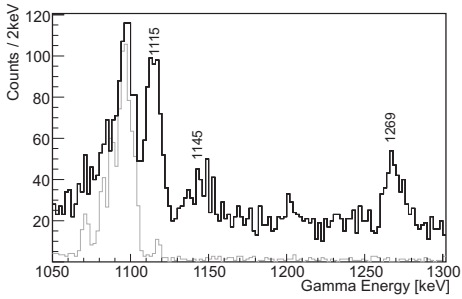

Figure 5.3: Part of the Doppler corrected gamma spectrum in coincidence with all protons (no energy conditions were set on the detected protons). The black spectrum shows the prompt coincidences, the gray the random coincidences.

1151 keV transition, and thus its individual intensity cannot be determined.

Two gamma lines belonging to ^{67}Ni are also observed, the 694.6(4) keV and 1202.6(15) keV line. The 1203 keV line is most probably due to a wrong particle identification. This identification process is not perfect and some deuterons are identified as protons. Further, the intensity of the 1203 keV is very low, while it is the strongest transition observed in the (t,d)-reaction to ^{67}Ni [118]. The 695 keV line however is a quite intense line. It results from neutron emission in ^{68}Ni after the (t,p) reaction took place. If a state is populated above or near the neutron separation energy of ^{68}Ni ($S_n = 7.792(4)$ MeV [27]), there is a finite possibility that a neutron will be emitted. A state in ^{67}Ni will then be populated, that can further gamma decay to the ground state. Since the total available energy in the (t,p) reaction is $\sim$12.6 MeV ($= E_{CM} + Q$), it is possible to populate states above the neutron separation energy. It will be shown below (section 5.2) that the excitation energy of ^{68}Ni, that is related to the 695 keV line, is indeed consistent with an excitation above the neutron separation energy.

Eventually, all the important, intense transitions could be placed in the known level scheme of ^{68}Ni, part of which is shown in Fig. 5.4. The observed transitions in the present experiment are indicated in blue.

The intensities reported in Table 5.1 are not directly related to the feeding of a certain level. This is illustrated in Fig. 5.5, where the excitation energy, as deduced from the proton energy, of states in ^{68}Ni populated in the (t,p) reaction are shown as a function of the gamma energies in prompt coincidence with the protons. This figure shows, first of all, that most of the feeding goes to high energy states in ^{68}Ni. Further, almost no ground state transitions are observed

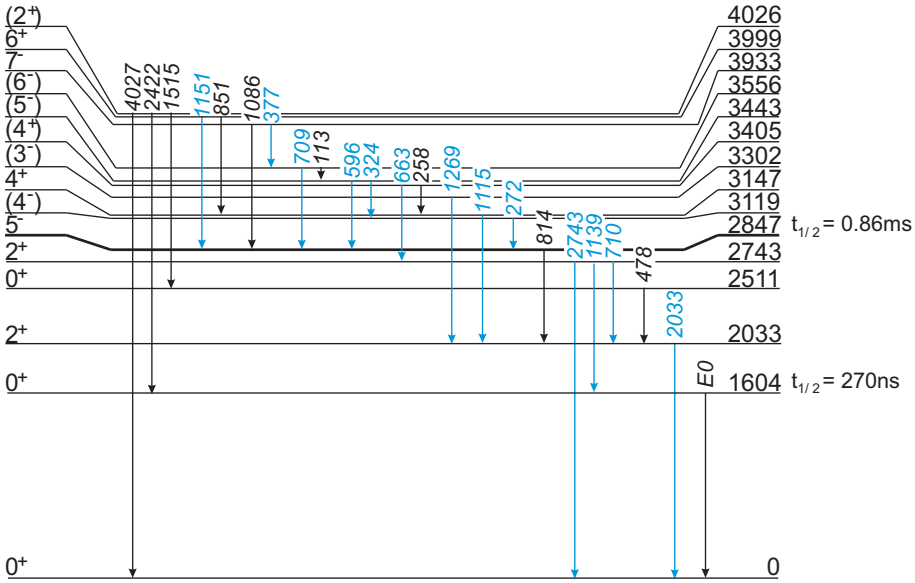

Figure 5.4: Part of the level scheme of ^{68}Ni. Observed transitions are indicated in blue.

in the (t,p) reaction. The only ground state transition that can be identified is that of the first excited 2^+ state at 2033 keV (number 1 in the figure). In the figure also the 694 keV transition is indicated (number 2), which shows that the excitation energy of ^{68}Ni corresponding to this transition lies around 8-10 MeV, which is indeed above the neutron separation energy of ^{68}Ni. Finally, also the broadened and shifted 1039 keV transition due to the β decay of ^{66}Cu is indicated (number 3). It is clear that this is a background line, since it is in coincidence with every excitation energy of ^{68}Ni. Note that in this matrix the random coincidence are not subtracted.

5.2 Excitation Energy Spectrum

From the detected proton energy, the excitation energy of the state populated in ^{68}Ni can be calculated. The deduced excitation energy spectrum of ^{68}Ni is shown in Fig. 5.6 separately for (a) the forward and (b) the backward barrel. The spectrum for the forward barrel shows all the available data, while the spectrum for the backward barrel only shows the data from the first part of

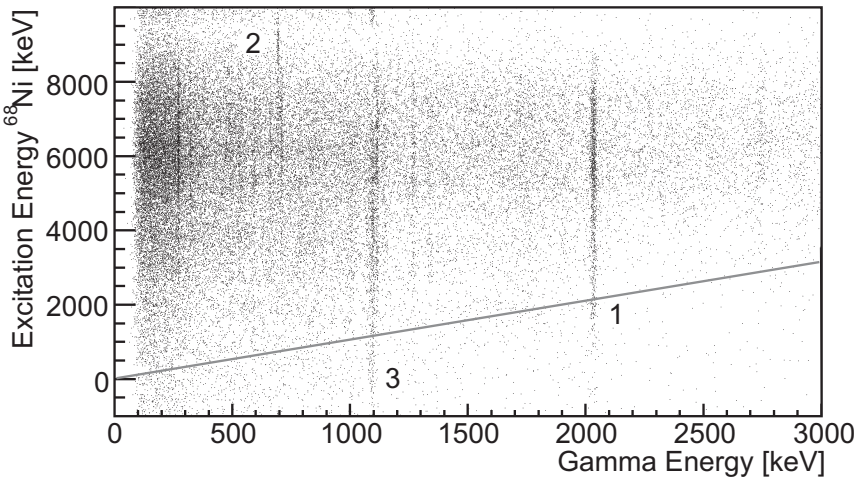

Figure 5.5: A coincidence matrix between the gamma-ray energy (horizontal axis) versus the excitation energy in ^{68}Ni (vertical axis) is shown. The latter is deduced from the energy of the identified protons. Excited states populated in ^{68}Ni that are followed by a ground-state gamma transition should be positioned on the gray line. The numbers indicate (1) the ground state transition from the first excited 2^+ state, (2) the excitation energy corresponding to the 694 keV transition and (3) the broadened and shifted 1039 keV transition due to the β decay of ^{66}Cu.

the run. This, because of the noise problem that occurred during the second part of the run (see section 4.3.1). As can be seen from Fig. 5.6, the particle detection resolution is not good enough to separate the population of closely spaced levels. Therefore, to be able to deduce which levels were populated, information from proton-gamma coincidences has to be combined with these excitation energy spectra.

Further, the spectra show that most of the feeding goes to high energy states between 5-9 MeV, as was already clear from Fig. 5.5. The density of states in this region is probably too large, to be able to identify individual levels. The fact that the excitation energy spectrum in the backward barrel only goes up to 8 MeV, is due to the thresholds of the detectors and the low proton energy for these excitation energies. To further illustrate that most of the feeding goes to high energy states, a few excitation energy spectra, constructed for protons in coincidence with a certain gamma ray are shown in Fig. 5.7 (these figures

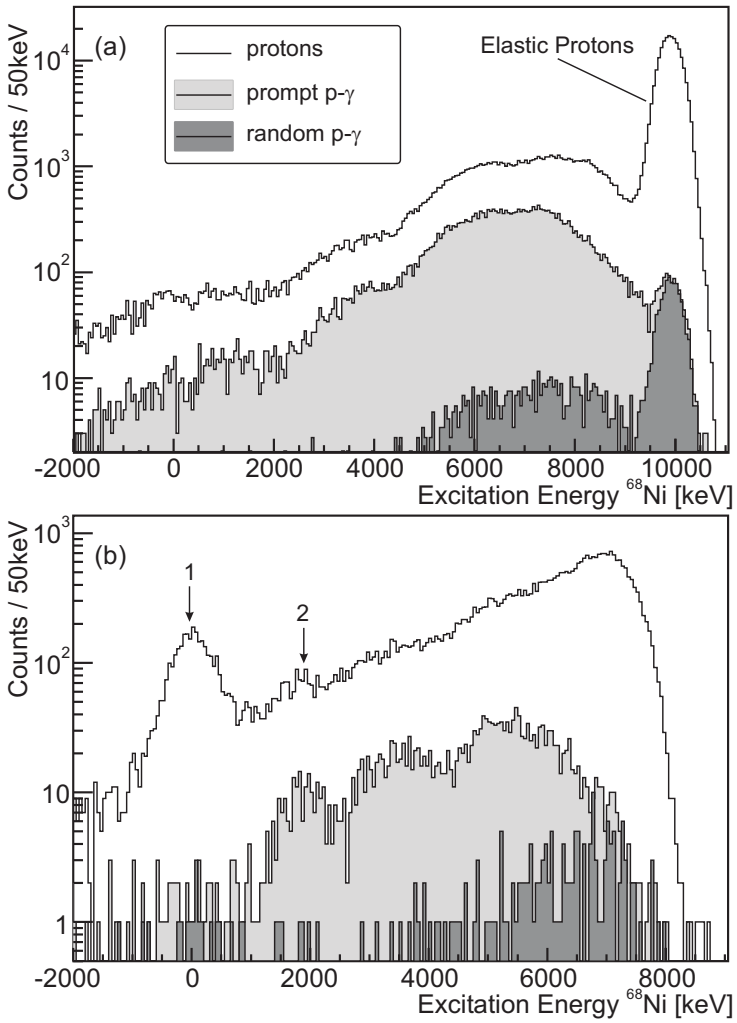

Figure 5.6: Excitation energy spectrum of ^{68}Ni, (a) for the forward barrel (all data) and (b) for the backward barrel (only data from the first part of the run (see section 4.3.1)). The not shaded part of the spectrum shows the data from all the protons, the light gray part shows data from prompt proton-gamma coincidences and the dark gray part shows data from random proton-gamma coincidences. The numbers indicate feeding to the ground state (1) and to the second excited state at 2033 keV (2).

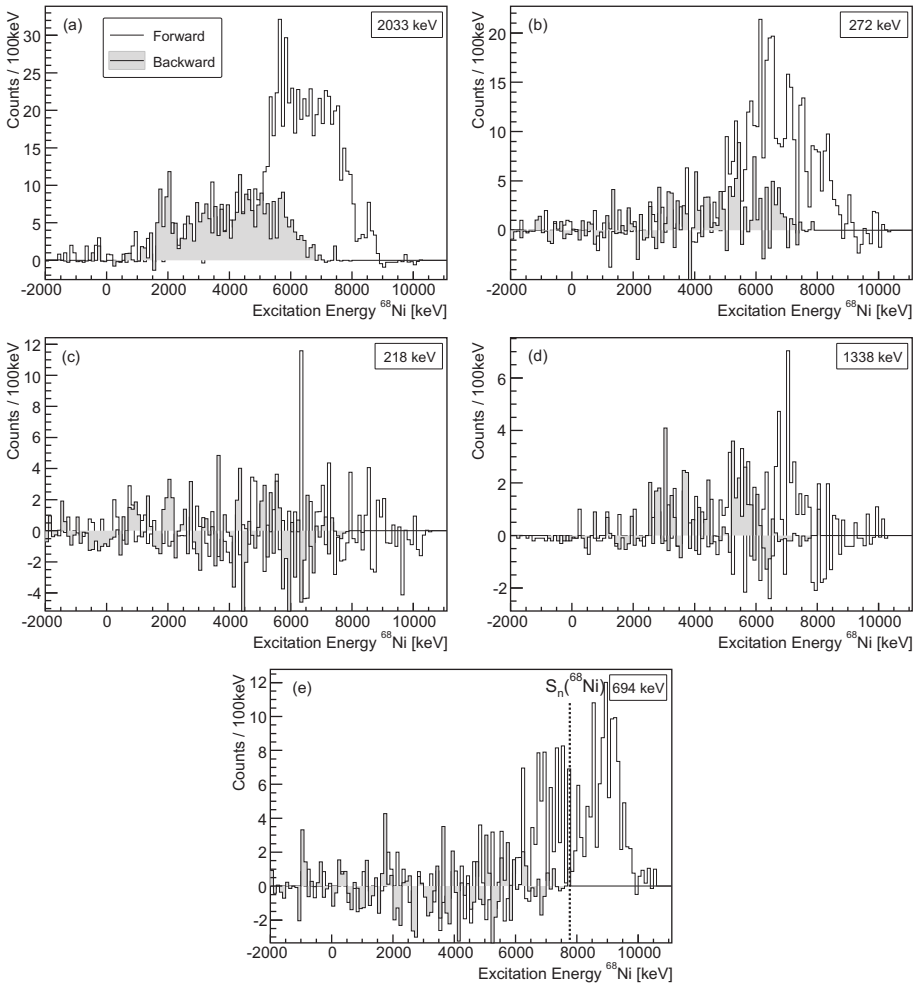

Figure 5.7: Excitation energy spectra of ^{68}Ni deduced for protons in coincidence with (a) 2033 keV, (b) 272 keV, (c) 218 keV, (d) 1338 keV and (e) 694 keV, random subtracted. The not shaded part of the spectrum is constructed with protons detected in the forward direction (forward barrel), the gray part with protons detected in backward direction (backward barrel and CD detector). In spectrum (e) the neutron separation energy of ^{68}Ni is indicated, $S_n = 7.792(4)$ MeV [27], by the black dotted line.

correspond to taking a vertical slice in Fig. 5.5 and subtracting left and right background and random coincidences). The first spectrum shows the excitation energy spectra for the coincidence with the 2033 keV line. One can observe that there is a small direct feeding to the first excited 2^+ state, but that most of the intensity of the 2033 keV gamma ray originates from feeding to high energy levels. The same can be observed for Fig. 5.7.b. The 272 keV gamma ray results from the gamma decay of a state at 3119 keV (see Fig. 5.4). In this case the direct feeding is even smaller.

Fig. 5.7.c and d show the excitation energy spectra for coincidences with the two observed unknown gammas in ^{68}Ni at 218 keV and 1338 keV (see Table 5.1). Unfortunately, no information can be extracted about the levels from which these gamma rays would originate. Finally, Fig. 5.7.e shows the excitation energy spectrum for coincidences with the 694 keV line, claimed to be a gamma transition in ^{67}Ni. One can observe that the excitation energy of ^{68}Ni for this gamma transition is indeed in agreement with an excitation energy close to or above the neutron separation energy of $S_n(^{68}\text{Ni}) = 7.792(4)$ MeV [27]. Therefore, our conclusion that the 694 keV line is a transition in ^{67}Ni, that originates from neutron emission of the ^{68}Ni nucleus seems solid.

In Fig 5.6, a strong population to the ground state is also observed for the backward barrel (number 1 in Fig. 5.6.b). This is less clear for the forward barrel, due to the punch-through protons (see section 4.3.1). Direct population to one or more states around 2 MeV is also observed (number 2 in Fig. 5.6.b). To be able to deduce which states around 2 MeV are populated, it is more instructive to look at the excitation energy spectrum constructed for protons that were detected in the CD detector only, see Fig. 5.8. The particle detection resolution for the CD detector is clearly much better than for the barrel detectors. Fig. 5.8.a shows all available data, while Fig. 5.8.b shows only the data of the first part of the run. One can again observe a strong direct population of the ground state (number 1 in the figures). Further, it is clear that most of the feeding to states around 2 MeV, that was observed in the backward barrel, comes from direct population of the first excited 2^+ state at 2033 keV (number 2). However, to the left of this peak, also a small bump is observed, which is more clear in Fig. 5.8.b, since the noise level is lower in this spectrum. This is the direct population of the 0_2^+ state (number 3 in the figures). The energy of this state can be deduced from this excitation energy spectrum and is equal to $E(0_2^+) = 1621(28)$ keV, which is in agreement with the recent measurement of 1604 keV [45]. If this state is indeed the 0_2^+ state, it can only decay by an $E0$ transition to the 0_1^+ ground state, through 1.595 MeV conversion electrons (55 %) or pair creation. The latter can give rise to 511 keV gamma radiation. Because of the 270(5) ns [26] half life and the fact that the ^{68}Ni recoiling ions are flying out of the reaction chamber (about 6 m during

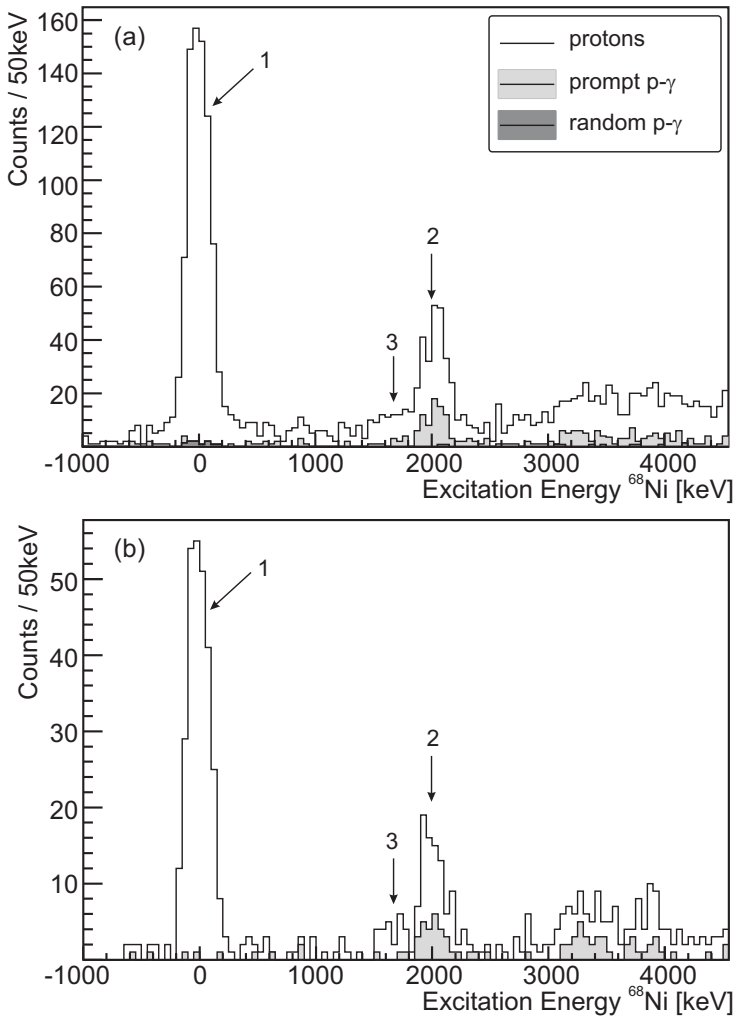

Figure 5.8: Excitation energy spectrum of ^{68}Ni for the CD detector, (a) all data and (b) only data from the first part of the run. The data from the first 14 h of the run are not included in the spectra, due to the problem with the timing of the gamma rays (see section 4.3.3). The not shaded part of the spectrum shows the data from all the protons, the light gray part shows data from prompt proton-gamma coincidences and the dark gray part shows data from random proton-gamma coincidences (no condition on the gamma-ray energy). The numbers indicate the ground state feeding (1) and direct feeding to the first excited 2^+ (2) and 0^+ (3) state.

one half life time), coincidences cannot be observed. To verify the fact that the population of the level at 1604 keV is not followed by gamma emission, the ratio of proton-gamma coincidences and proton singles (the ratio of the gray and not shaded spectra in Fig. 5.8) can be taken. This ratio for protons corresponding to the 0_2^+ state is 9(3) %. The same ratio for the first excited 2_1^+ state is 29(5) %. The non zero ratio for the state at 1604 keV can be explained as due to tailing from the feeding to the 2_1^+ state. In fact, it turns out that all gamma rays in coincidence with the peak corresponding to the the 0_2^+ state can be explained by Compton scattering of the 2033 keV gamma ray.

5.3 Feeding to Low Lying 0^+ and 2^+ States

The next step is to determine the feeding to the states in ^{68}Ni, especially the feeding to the 0^+ and 2^+ states will be interesting, as this could help disentangling their structure. ^{68}Ni has three known 0^+ states, the ground state, one at 1604 keV and one at 2511 keV, and two 2^+ states, at 2033 keV and at 2743 keV (see Fig. 5.4 or Fig. 1.6). The feeding to the different states will be given, where possible, relative to 100 % ground state feeding, as it is clear from Fig. 5.6.b and Fig. 5.8 that the ground state is the most strongly populated.

Feeding to the 0_2^+ and 2_1^+ can be deduced from the ratios between the number of protons populating each state. For the CD detector, this can be obtained from Fig. 5.8.a by fitting the peaks of the ground state, 0_2^+ and 2_1^+ state with a Gaussian. The fit for the 0_2^+ and 2_1^+ state is shown in Fig. 5.9. This resulted in a feeding of 4.2(16) % for the 0_2^+ state and 29.3(29) % for the 2_1^+ state, relative to 100 % ground state feeding. This deduced feeding intensity can be verified by determining the integral of the peaks directly from Fig. 5.8.b (only data from the first part of the run are used, since these data contain much less noise). This is not so straightforward, since there is an overlap between the tails of the peaks of the 0_2^+ and 2_1^+ state. Therefore GEANT4 [121] was used to simulate a population of the ground, 0_2^+ and 2_1^+ state. The shape and width of the simulated peak for the ground state were validated by comparing it to the ground state peak in Fig. 5.8.a. From this simulation a pure peak for both the 0_2^+ state and 2_1^+ state was determined, by selecting only that part of the peak where the contamination of the tails of the other peak is neglegible. The deduced integral for both peaks was then correct for the limited width of the peak that was taken into account. The feeding determined by this method was 4.8(16) % and 28.0(36) % for respectively the 0_2^+ state and the 2_1^+ state. These are, within error bars, in agreement with the feeding intensities deduced from the fit in Fig. 5.9.

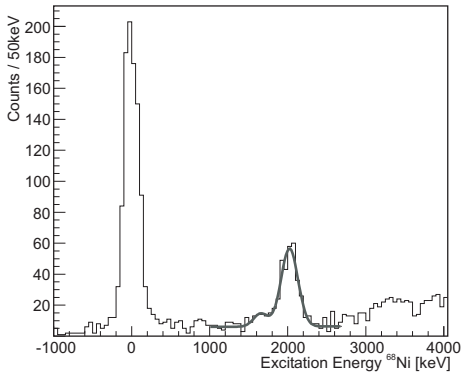

Figure 5.9: Excitation energy spectrum of ^{68}Ni for the CD detector. The fit from which the feeding to the 0_2^+ state and 2_1^+ state is deduced is shown by the gray line.

One has to bear in mind that these feeding percentages were deduced only for data in the CD detector, which represents the most forward center of mass angles ($\approx$4-16°). Nothing can be said of the feeding to the 0_2^+ and 2_1^+ over the full range (0-180°). A theoretical calculation of the angular distribution is needed, as such that the ratio of the cross section of the most forward center of mass angles can be compared to the total integrated cross section.

For the 0_3^+ at 2511 keV and 2_2^+ state at 2743 keV only an upper limit can be determined. This is clear from Fig. 5.8, as no clear peak is seen at these energies. Since these states lie close in energy in comparison with the obtained proton detection resolution, they cannot be treated separately. Further, also the 5^- isomer at 2847 keV (see Fig. 5.4) is too close in energy and cannot be excluded from the gate. Thus, an upper limit can only be determined by taking these three states together. A pure energy range (2.31-2.71 MeV) was selected where the 2_1^+ level at 2033 keV and the (4^-) level at 3119 keV (Fig. 5.4) do not intrude. Again only the data from the first part of the run are used, due to the increased noise level in the second part of the run (see section 4.3.1). The strategy to determine upper limits outlined in Ref. [122] is followed and the obtained feeding was corrected for the limited energy range that was taken into account. Within a 95 % confidence level an upper limit for the feeding of < 3.8 % was obtained (< 2.3 % within a confidence level of 1σ) for the 0_3^+, 2_2^+ and 5^- state, taken together.

Above an excitation energy of about 2.5 MeV the energy levels in ^{68}Ni lie very close in energy (see Fig. 5.4) compared to our detection resolution (see Fig. 5.6

and Fig. 5.8). Therefore the population intensity for these higher lying levels cannot be determined from the excitation energy spectrum of ^{68}Ni deduced for protons detected in the CD detector (Fig. 5.8). However, the population of a certain state can also be deduced by looking at their gamma decay. By gating on the excitation energy of the state of interest, the number of counts in the corresponding gamma ray can be determined (taking the left and right background and random coincidences into account). Since the ground state does not decay by gamma rays, the deduced number of counts cannot be directly related to the feeding relative to the ground state. Therefore the 2_1^+ state, which decays by a 2033 keV gamma ray was taken as reference. In order to avoid intrusion from other excited states, a narrow gate on the excitation energy has to be selected. Fig. 5.7.a shows that the 2033 keV line is in coincidence with excitation energies from about 1 MeV up to about 8 MeV. It is thus not straightforward to select a width of the gate on the excitation energy that contains only the direct population of the 2_1^+ state. In the determination of this gate, it was assumed that the 0_3^+ state at 2511 keV and the 2_2^+ state at 2743 keV were not directly fed, which is a reasonable assumption regarding our deduction of their upper limit above. The state that is closest in energy that could cause a contamination is the 4^+ state at 3147 keV (see Fig. 5.4). To exclude intrusion from this state a width of the gate on the excitation energy of the 2_1^+ state of 1.13-2.25 MeV was deduced. Since the 2_1^+ state is used as a reference, the width of the gates on the other states, for which the feeding is deduced, have to be the same.

Further, in forward direction a considerable amount of protons that correspond to a population of the 2_1^+ state fly through the ΔE and E_{rest} detector of the forward barrel (see section 4.3.1 about the punch-through protons). Thus, when gating on the excitation energy of the 2_1^+ state, an important fraction of the protons that are actually related to the population of this state are not taken into account, since their full energy is not registered. Therefore only the backward direction can be used, but this reduces the statistics significantly.

A direct population of 38(14) % to the 4^+ state at 3147 keV and 41(15) % to the (3^-) state at 3302 keV (see Fig 5.4) could be determined. The gamma ray spectra when gating on these excitation energies are shown in Fig. 5.10. These feeding intensities are corrected for the gamma detection efficiency and the gamma branching ratio. One has to bear in mind that these feeding intensities are relative to the 2_1^+ state and that they are only deduced for the range of the backward direction. In Fig. 5.8 a peak structure around 3.3 MeV is observed, which corresponds to the feeding that was deduced for these two levels. Since the feeding of the 2_1^+ state relative to the ground state is only known for the range of the CD detector, it is not possible to convert these deduced feeding intensities to a population relative to the ground state. From a theoretical

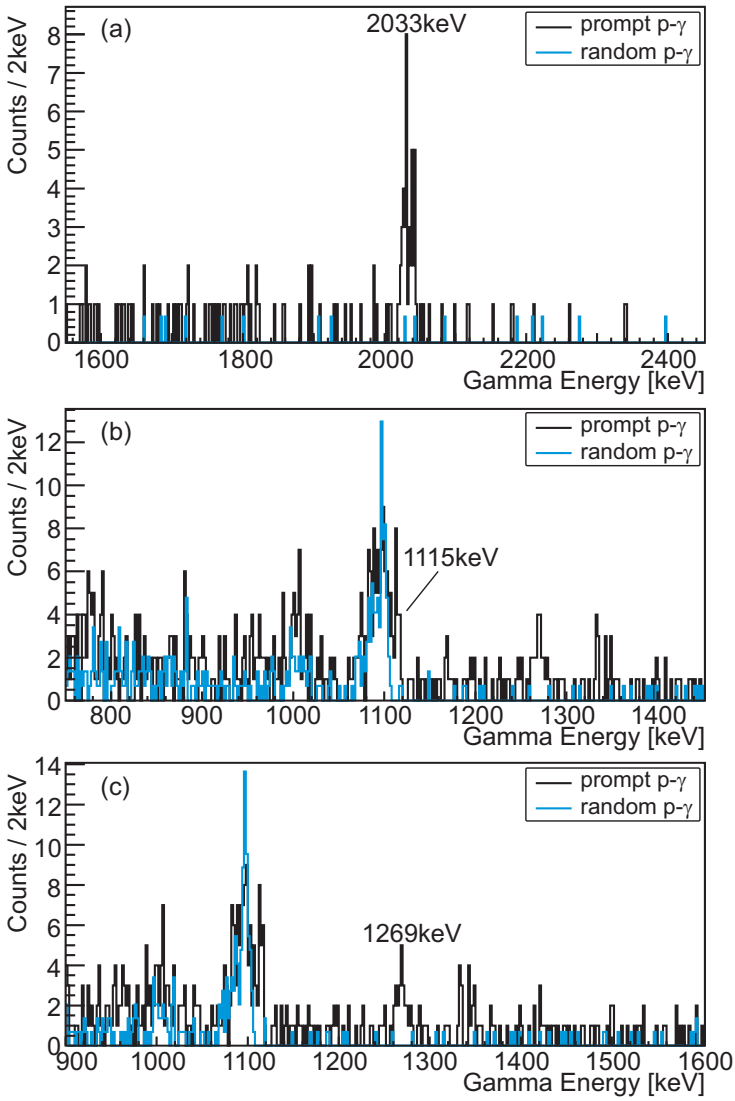

Figure 5.10: Gamma spectra when gated on the excitation energy of ^{68}Ni of (a) 2033 keV (gate 1.13-2.25 MeV), (b) 3147 keV (2.25-3.37 MeV) and (c) 3302 keV (2.40-3.52 MeV). The energy of the gamma rays that follow from the decay of these excited levels are indicated. The black spectrum shows the prompt proton-gamma coincidences, the blue are the random coincidences.

calculated angular distribution the deduced feeding of the 2_1^+ state for the range of the CD detector could be converted to a feeding intensity for the range of the full backward direction. However, as will be shown below, the theoretical calculations for the cross section of the 2_1^+ do not agree with the experimental data (see section 5.4). Therefore this conversion cannot be performed.

A summary of the feeding intensities is given in Table 5.2.

5.4 Angular Distributions

The experimental angular distributions can now be compared to the cross section calculations presented in section 2.4.3. The strategy to construct angular distributions starts with putting a gate on the desired excitation energy of ^{68}Ni and storing the number of protons observed at each θ_{lab}-angle (in units of one degree). These number of counts are then corrected for particle detection efficiency, the scaling factor deduced from triton elastic scattering (see section 4.3.2) and the solid angle in order to deduce the differential cross section. To limit statistical fluctuations in the constructed angular distributions five θ_{lab}-angles are taken together. Finally, the angular distributions are converted from laboratory angles to center of mass angles and can then be compared to the theoretically calculated cross sections.

The gates that were put on the excitation energy in order to construct the angular distribution of the ground state are -1600 keV to 300 keV for the forward barrel, $\pm$ 650 keV for the backward barrel and $\pm$ 350 keV for the CD detector. That the width of the gates is different for the different detectors is first of all due to their different proton detection resolution. Secondly, the gates are chosen as pure as possible, without intrusion of other excited states into the gates. All the deduced angular distributions are corrected for the proton detection efficiency (see e. g. Fig. 4.14) and for the limited width of the excitation energy peak that was taken into account. The angular distribution for the ground state of ^{68}Ni is shown in Fig. 5.11. The black line shows the calculation for the direct transfer only, the blue line shows the coherent sum of the direct and sequential transfer, the red line is the calculation where the known binding energy of ^{67}Ni is taken into account, the green line takes into account the experimental excitation energies of ^{67}Ni and finally, the yellow line shows the calculation were both the binding energy and experimental excitation energies of ^{67}Ni are taken into account. These calculations were already shown in Fig. 2.7.

For small center of mass angles, all the calculations are in agreement with the data. For larger angles a deviation is present. As already mentioned in section 2.4.3, in principle the calculation that takes into account all the

Table 5.2: Feeding to the different states in ^{68}Ni.

Feeding relative to 100 % ground state feeding [%]	
0_2^+ at 1604 keV	4.2(16)
2_1^+ at 2033 keV	29.3(29)
0_3^+ at 2511 keV 2_2^+ at 2743 keV	<3.9
Feeding relative to the 2_1^+ state [%]	
4_1^+ at 3147 keV	38(14)
(3_1^-) at 3302 keV	41(15)

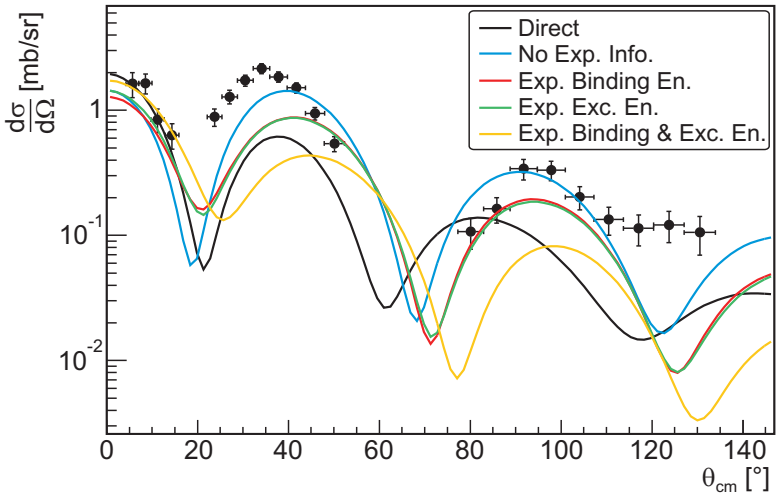

Figure 5.11: Angular distribution for transfer to the ground state of ^{68}Ni. DWBA calculations, that were already described in section 2.4.3, are also shown (see text for details).

experimental knowledge of ^{67}Ni (yellow line) should be the most correct. However, since the spectroscopic factors of the ^{66}Ni(t,d)^{67}Ni and ^{67}Ni(d,p)^{68}Ni reactions are not known from experiment, it is not sure that the yellow calculation indeed results in the most correct shape for the angular distribution of the two neutron-transfer to ^{68}Ni. Therefore, in the following calculation, no experimental information on ^{67}Ni was included, its binding energy is taken as the mean of the binding energies of ^{66}Ni and ^{68}Ni and its experimental energies are put to zero.

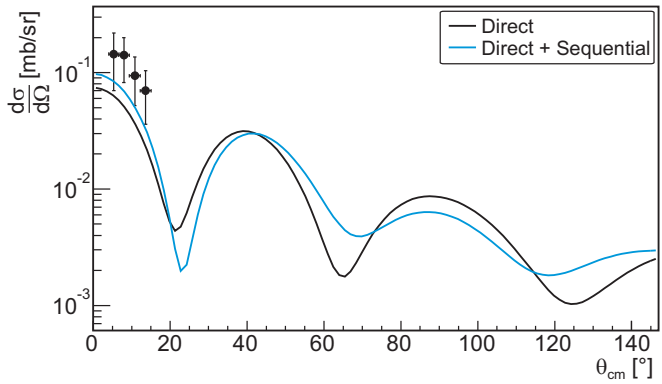

Figure 5.12: Angular distribution for transfer to the second 0^+ state at 1604 keV in ^{68}Ni. The black line shows the DWBA calculation for only the direct transfer, while the blue line takes into account both direct and sequential transfer.

The angular distribution for the 0_2^+ state at 1604 keV can only be deduced for the most forward center of mass angles, i. e. the angles of the CD detector, and is shown in Fig. 5.12. The gate on the excitation energy was taken to be $\pm$ 180 keV, in order to exclude intrusion from the first excited 2_1^+ state. The calculations for this state are also in good agreement with the data for the most forward center of mass angles.

The calculated cross section to the first excited 2^+ state at 2033 keV, is however an order of magnitude smaller than the angular distribution deduced from the data, as is shown in Fig. 5.13. This disagreement with the data will be discussed in the next chapter. In this case, a gate on the excitation energy of $\pm$ 400 keV for the forward barrel, $\pm$ 300 keV for the backward barrel and $\pm$ 250 keV for the CD detector was taken.

The numerical values for the cross section as a function of angle for the ground, 0_2^+ and 2_1^+ state in ^{68}Ni are given in Appendix B.

5.4.1 High Excitation Energies

As is shown in Fig. 5.6, most of the feeding in the two-neutron transfer to ^{68}Ni goes to high excitation energies. Fig. 5.6.b shows in the prompt gamma gate (light gray spectrum) two bumps around 3.5 MeV and 5.5 MeV. The angular

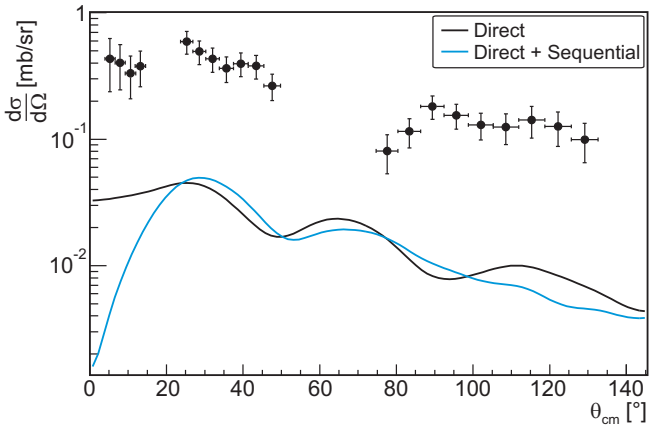

Figure 5.13: Angular distribution for transfer to the first excited 2^+ state at 2033 keV in ^{68}Ni. The black line shows the DWBA calculation for only the direct transfer, while the blue line takes into account both direct and sequential transfer.

distributions for an excitation energy of 3.5(5) MeV and 5.5(10) MeV were constructed and shown in Fig. 5.14. These cross sections were determined by defining a double gate, namely next to a gate on the excitation energy, also a gate on prompt gamma coincidences was applied. Random proton-gamma events were subtracted. The limited statistics did not allow gates on individual gamma ray transitions and thus proper corrections for the different gamma ray efficiencies could not be applied. Therefore the differential cross section is given in arbitrary units only. Both angular distributions do not show a clear shape and cannot be directly linked to a certain angular momentum transfer.

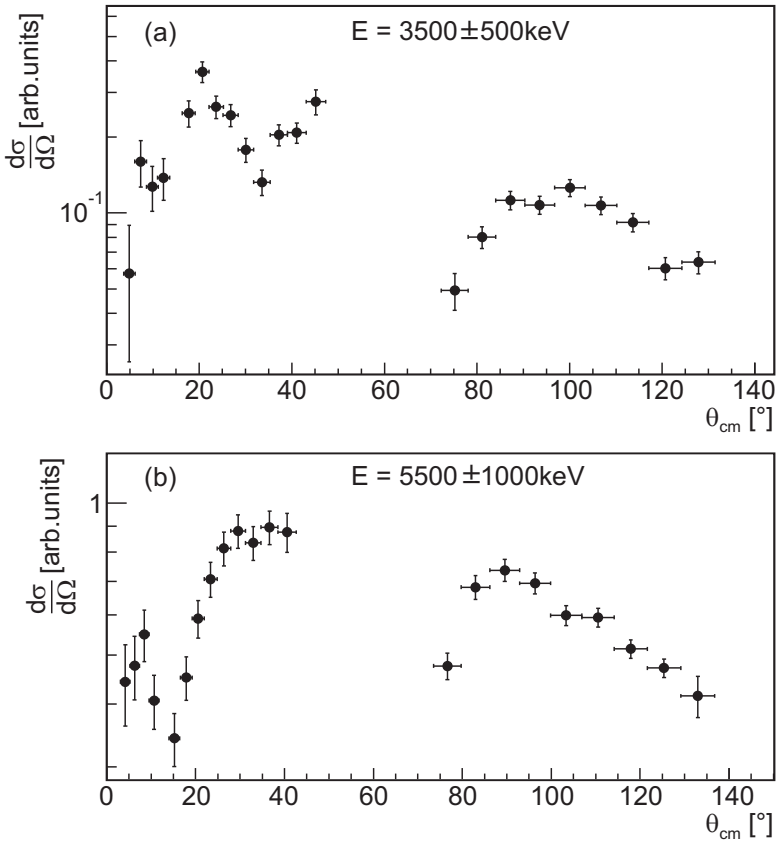

Figure 5.14: Angular distribution to high excitation energies in ^{68}Ni. The cross section to states with an excitation energies within 3500 ± 500 keV is shown in (a) and within 5500 ± 1000 keV is shown in (b).

6 | Discussion

In this chapter, the measured angular distributions will be interpreted in terms of the structure of the different states in ^{68}Ni. The obtained results will be compared to other (t,p) reactions on lighter nickel isotopes as well as to (t,p) reactions that populate a (doubly-)magic nucleus. Finally, the results for ^{68}Ni will be compared to the region around its valence mirror nucleus ^{90}Zr (Z = 40, N = 50).

6.1 Structure of Low-Lying States in ^{68}Ni

The DWBA calculations presented in Chapter 2 were obtained by taking into account the full neutron pf-shell and the $\nu g_{9/2}$ orbital. The calculations are thus the result of a coherent combination of these orbitals. The measured angular distributions can also be compared to a calculation for a pure configuration (which means that the two-nucleon spectroscopic amplitude (TNA) is put to one), the one that is expected from a simple shell model picture and some simple assumptions. This would yield for the ground state of ^{68}Ni two neutrons in the $p_{1/2}$ orbital and an empty $g_{9/2}$ orbital. The 0_2^+ and 2_1^+ could then be assumed to have two neutrons in the $g_{9/2}$ orbital (^{66}Ni is assumed to have an empty $p_{1/2}$ and $g_{9/2}$ orbital for its neutrons). The comparison between the full calculation and the pure configuration is shown, together with the data, in Fig. 6.1 for these three states in ^{68}Ni.

For the 0_2^+ and 2_1^+ states the pure and full calculation do not show much difference in magnitude, which means that the NUSHELL calculations predict that the wave functions of these two states will consist of a predominant configuration of two neutrons in the $g_{9/2}$ orbital (see Fig. 6.1.b and c). This is also what emerged from the calculations in Chapter 2. In Fig. 2.8 and Fig. 2.9 it was shown that the $g_{9/2}$ orbital is the dominant orbital for these two states

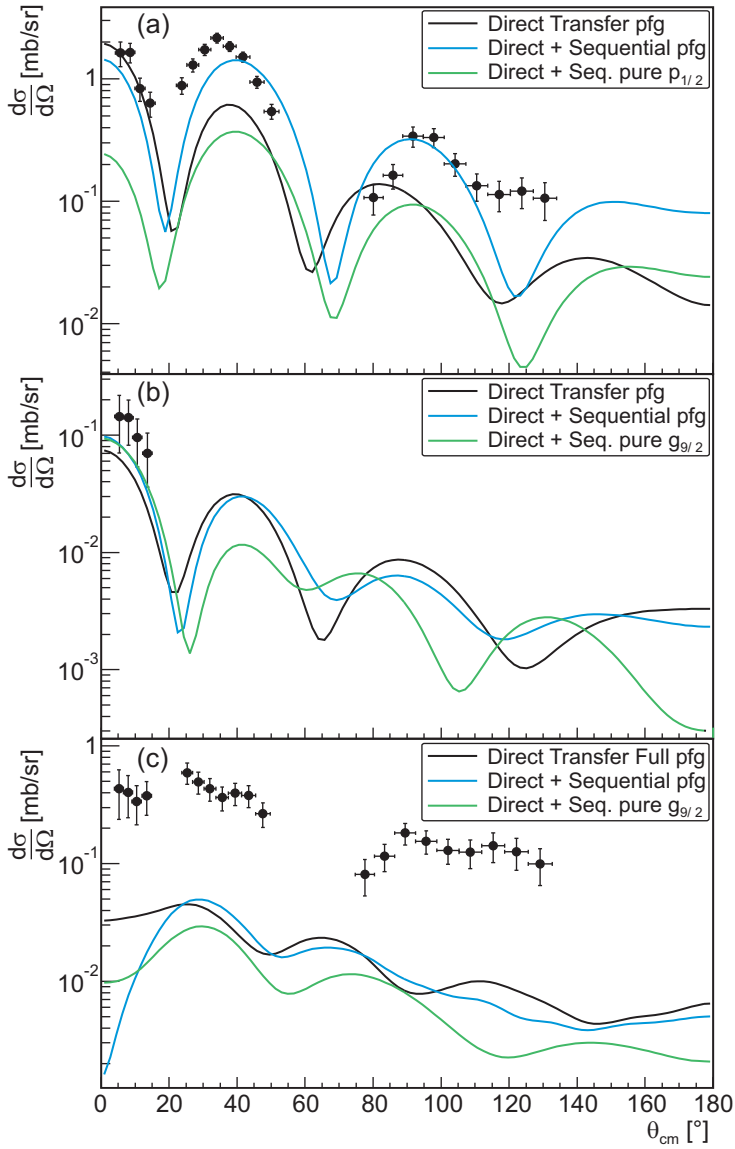

Figure 6.1: Angular distributions together with the DWBA calculations for the (a) ground state, (b) 0_2^+ and (c) 2_1^+ state in ^{68}Ni. The black and blue calculations are done taking the full neutron pf-shell and $g_{9/2}$ orbital into account, while the green calculation only takes a pure configuration, expected from a simple shell model picture and some simplified considerations, into account. The black calculation considers only the direct transfer, while the blue and green considers both the direct and sequential transfer.

when the calculated TNA values are taken into account. From Fig. 5.13 and Fig. 6.1.c it is however clear that the NUSHELL calculations do not agree at all with the measured magnitude of the cross section to the 2_1^+ state. This will be discussed below. For the ground state, one observes that the coherent combination of all orbitals is necessary in order to explain the magnitude of the measured cross section (see Fig. 6.1.a). This is due to coherent pairing. Further, it is clear that the sequential transfer has to be taken into account in order to reproduce the right magnitude of the cross section, especially at higher angles.

The magnitude of the calculated angular distributions is in good agreement with the measured one for the ground state and the 0_2^+ state. This means that the used model space, including the neutron $f_{5/2}$, $p_{3/2}$, $p_{1/2}$ and $g_{9/2}$ orbital, and interaction (Ref. [82]) is able to predict the structure of these states quite well. The calculated neutron occupation numbers of the different involved orbitals used in the present calculations (see Table 2.4) are in good agreement with the calculations of Tsunoda *et al.* [56], who used a much larger model space, including also the $f_{7/2}$ and $d_{5/2}$ orbital for both protons and neutrons. The authors of this paper Ref. [56] describe the structure of ^{68}Ni in terms of shape-coexistence. They predict the existence of a modestly-oblate deformed band built on top of the 0_2^+ state. Since the occupation numbers of the neutron orbitals used in our calculations are similar to their predicted occupation numbers and our calculations reproduce the data reasonably well, one might conclude that our experimental results also support their findings, at least for the ground and 0_2^+ state.

Another recent theoretical calculation involving the ground and first excited 0^+ state in ^{68}Ni was performed by Lay *et al.* [123], who performed a zero-range DWBA calculation. They assume a mixing for the ground and 0_2^+ state involving neutron 0p-0h excitations and 2p-2h excitation from the $p_{1/2}$ orbital into the $g_{9/2}$ orbital. The ground and 0_2^+ state are then represented by $0_{gs}^+ = \alpha|0\rangle + \beta|(g_{9/2})^2(p_{1/2})^{-2}\rangle$ and $0_{exc}^+ = -\beta|0\rangle + \alpha|(g_{9/2})^2(p_{1/2})^{-2}\rangle$, where $\alpha^2 + \beta^2 = 1$. From the ratio of the cross section between the 0_2^+ and the ground state they can deduce α^2, see Fig. 6.2. However, as is shown in Fig.6.2.a, for our measured ratio of 4.2(16) %, there are two possible mixing parameters α^2 and thus the authors of Ref. [123] cannot draw a firm conclusion about the mixing of the ground and 0_2^+ state in ^{68}Ni from this comparison, although a value for $\alpha^2 > 0.7$ would result. Therefore they propose the study of a new reaction, the ^{66}Ni(^{14}C,^{12}C)^{68}Ni reaction, as in this case the ratio of cross sections as a function of α^2 would result in a monotone increasing curve (see Fig. 6.2.b), and thus the mixing could unambiguously be determined, albeit in a model dependent way.

Contrary to the ground and 0_2^+ state, the magnitude of the measured cross

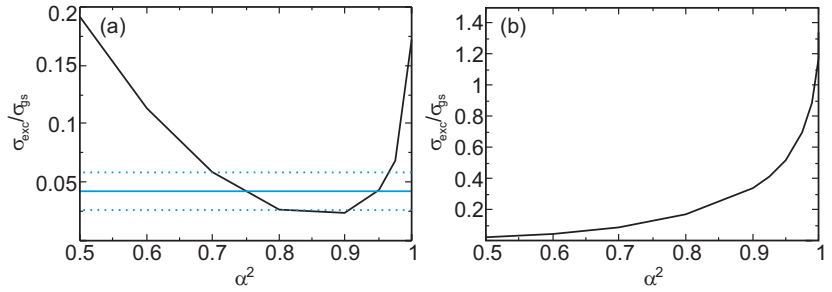

Figure 6.2: Ratio of cross sections of the 0_2^+ state to the ground state as a function of the mixing probability parameter α^2 for (a) the ^{66}Ni(t,p)^{68}Ni and (b) the ^{66}Ni(^{14}C,^{12}C)^{68}Ni reaction. The horizontal blue line shows the experimental result for the ratio of cross sections, the dotted blue lines indicate the error on this result. Figure adjusted from Ref. [123].

section to the 2_1^+ is not reproduced by the NUSHELL calculations, i. e. the magnitude of the calculated angular distribution is an order of magnitude too small (see Fig. 6.1.c). One of the reasons might be that the model space used for the present calculation (neutron $p_{1/2}$,$p_{3/2}$,$f_{5/2}$ and $g_{9/2}$ orbital) does not take into account the correct active orbitals. This was examined by also including the $d_{5/2}$ orbital in our FRESCO calculations. Only pure configurations were considered, i. e. TNA = 1. In Fig. 6.3 the calculated angular distributions for a few possible pure configurations are shown. To show the influence of all the separate orbitals, only the pure configurations that can couple two neutrons in the same orbital to a 2^+ state are shown, except for the $p_{1/2}$ orbital, as it is not possible to construct a 2^+ state by coupling two neutrons in this orbital. Therefore, the two configurations that can couple to a 2^+ state and that involve the $p_{1/2}$ orbital are also shown. It is clear from the figure that including the $d_{5/2}$ orbital cannot increase the calculated cross section substantially in order to reproduce the experimental data. As TNA values resulting from a realistic shell model calculation are always smaller than one, the calculated cross section, including the $d_{5/2}$ orbitals, would be smaller than that calculated for a pure configuration. Only a pure configuration involving the p orbitals (blue and green lines) can reproduce the measured magnitude of the cross section.

The reason for the discrepancy between the measured and calculated cross section to the 2_1^+ state, thus has to be sought elsewhere. From the calculations in section 2.4.3 it followed that transfer including the p orbitals is favored by our two-neutron transfer reaction, which is also clear from Fig. 6.3. From these calculations it followed that, when looking to a pure configuration, the calculated cross section involving the p orbitals is an order of magnitude

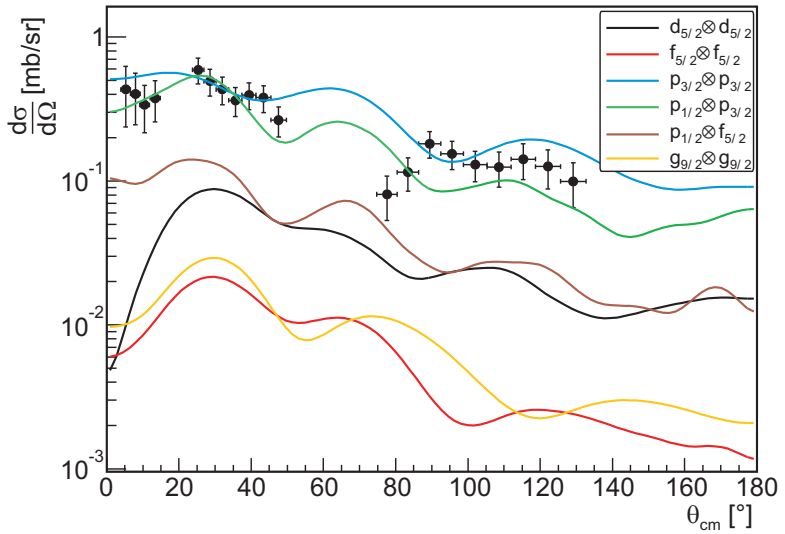

Figure 6.3: Calculated angular distributions, including both direct and sequential transfer, to the first excited 2^+ state for a few possible pure configurations (TNA = 1). The dots represent the experimentally measured angular distribution.

larger than the calculated angular distributions involving the $f_{5/2}$ and $g_{9/2}$ orbitals (see also e. g. Fig. 2.10 or Fig. 6.3). This means that, within the current calculation framework, only by increasing the contribution from the p orbitals, thus increasing their TNA's, the calculated cross section could be enhanced enough to reproduce the magnitude of the measured cross section.

It can be concluded that the used model space and interaction (jj44pna from Ref. [82]) do reproduce the observed cross sections for populating the ground state and 0_2^+ state, however fail to reproduce the cross section populating the 2_1^+ state. It thus appears that the calculated neutron occupation numbers (see Table. 2.4) for the 0_1^+ and 0_2^+ states, that are similar to the occupation numbers of other shell-model calculations (e. g. Ref. [56]), produce reliable cross sections for the two-neutron transfer reaction. The large discrepancy for the population of the 2_1^+ state might indicate a deficiency in the neutron occupancy for this state in contrast to all current shell-model calculations. Probably, the p orbitals are more important than what was assumed in our calculations. Also in the recently measured ^{30}Mg(t,p)^{32}Mg two-neutron transfer reaction, the $p_{3/2}$ orbital plays an important role. The measured magnitude of the cross section to the ground and 0_2^+ state can only be explained by including a contribution

of the $p_{3/2}$ orbital [90, 107].

Finally, the low upper limit for the population of the 0_3^+ state, is not in conflict with the prediction that this state would include an important component of proton 2p-2h excitations. The two-neutron transfer reaction is not directly sensitive to proton correlations and thus is not expected to populate a state consisting dominantly of proton 2p-2h excitations.

6.2 Comparison to Other (t,p) Reactions

A comparison of the feeding in the (t,p) reaction to the first excited 0^+ and 2^+ state in the nickel isotopes is shown in Fig. 6.4. It shows that the feeding to the 0_2^+ state is rather constant, while the population of the 2_1^+ changes considerably over the isotopic chain. One has to take into account however, that the feeding intensities for ^{68}Ni are only deduced for the most forward center of mass angles (approximately between 4-16°, see section 5.3), while for the lighter isotopes the feeding was deduced for angles $< 90°$ [57]. Nevertheless, the general trend should not change when all center of mass angles are taken into account. Further, the feeding may depend on the Q-value of the reaction and on the beam energy. The beam energy of the previous (t,p) reaction experiment on the lighter nickel isotopes was 4 MeV/u [57], which is not that different from the energy of 2.6 MeV/u used in the present experiment. The influence of the Q-value was examined by calculating the cross section to a certain fictitious state at different excitation energies. The difference in cross section for the forward center of mass angles ($< 90°$) was at most about a factor of two for a difference in Q-value of 5 MeV.

The general trend for the population of the first excited 2^+ state shows a decreasing intensity towards ^{68}Ni. The reason for the strong population of the 2_1^+ state in the ^{66}Ni(t,p) reaction is still a puzzle, since also the performed NUSHELL calculations predict a much smaller cross section than the one that was measured. In order to check the DWBA calculations, using NUSHELL, the neutron *fpg* model space and the jj44pna interaction [82], and FRESCO, the cross section to the first excited 0^+ and 2^+ state for e. g. the ^{64}Ni(t,p) reaction can be calculated. The ratio of integrated cross sections yields $\approx 9\,\%$ for the 0_2^+ state and $\approx 4\,\%$ for the 2_1^+ state, which is within a factor of two in agreement with the data (see Fig. 6.4). Thus, for ^{66}Ni the structure of the 0_2^+ and 2_1^+ state seems to be rather well predicted by NUSHELL. In this case the small calculated cross section to the 0_2^+ and 2_1^+ state however does not seem to be determined by the $g_{9/2}$ orbital. This is clear from the neutron occupancies that were shown in Table 2.4, as in the case of ^{66}Ni the occupancy of the $g_{9/2}$ orbital gets even

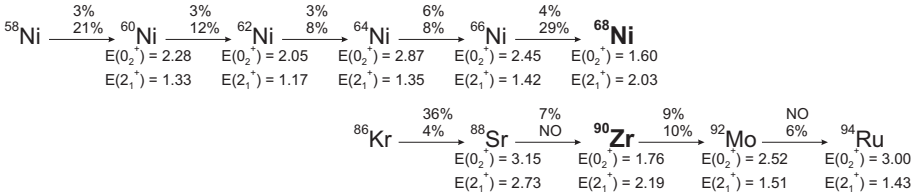

Figure 6.4: Systematics of the two-neutron (t,p) transfer reaction in the even nickel isotopes and of the two-proton (^{3}He,n) transfer reaction for the N = 50 isotones around ^{90}Zr. The percentages give the observed feeding to the 0_2^+ (top number) and 2_1^+ state (lower number) relative to 100 % ground state feeding. The energies of these levels are given in MeV. For the N = 50 isotones the given percentage is the ratio of the cross sections at the angle where the cross section is maximal. 'NO' stands for 'not observed', meaning the transition was not detected with a reasonable amount of strength. The data are taken from [25, 57, 124, 125, 126].

smaller for the first excited 0^+ and 2^+ state. This means that although the feeding intensity to a certain state can be more or less the same over part of the isotopic chain, as is the case for the 0_2^+ state in the nickel isotopes (see Fig. 6.4), the structure of this state does not have to be the same. For the 0_2^+ state this is clear from the occupation numbers, as the calculated amount of neutrons in the $g_{9/2}$ orbital for the 0_2^+ state is much larger in ^{68}Ni compared to the lighter nickel isotopes, while their feeding intensities are more or less the same.

When comparing the ^{66}Ni(t,p) reaction to other (t,p) reactions to (doubly)-magic nuclei (see section 1.3.2), the general trend for nuclei with N > 28, i. e. that the ground state receives the strongest feeding, is continued in ^{68}Ni. A quite strong excitation to at least one 2^+ state was also observed in ^{48}Ca and ^{208}Pb. In ^{208}Pb a quite strong population (45(3) % relative to the ground state) to the first excited 0^+ state at 4.87 MeV was observed [69]. This state is interpreted as a neutron 2p-2h state across N = 126 [70]. This strong population is in contrast to the intensity of the feeding to the 0_2^+ state in ^{68}Ni, which is only 4.2(16) % of the ground state feeding, although this state is also interpreted as a neutron 2p-2h excitation.

6.3 Comparison with ^{90}Zr

The structure of ^{68}Ni can be compared to its valence mirror nucleus ^{90}Zr, which has a good shell closure for its neutrons (N = 50) and a harmonic oscillator shell closure for its protons (Z = 40). Since this is a stable nucleus, it has been investigated much more extensively than ^{68}Ni and its structure is better known. The low lying structure of ^{90}Zr resembles that of ^{68}Ni, with the second 0^+ state at an energy of 1761 keV (compared to 1604 keV) and the first excited 2_1^+ state at 2186 keV (compared to 2033 keV) [25, 45], see Fig. 6.5. ^{90}Zr also shows the same 'magic' properties as ^{68}Ni, namely a high excitation energy for the first excited 2_1^+ state and a small B($E2{:}0_1^+ \rightarrow 2_1^+$) value, however no deviation in the two-proton separation energy is observed [25, 40]. Further, the authors of Ref. [40] predict also for ^{90}Zr an excited band on top of the 0_2^+ state, that is dominated by proton 2p-2h excitation from the pf-shell to the $g_{9/2}$ orbital. Nevertheless, differences are also present in the structure of ^{90}Zr and ^{68}Ni. In Ref. [52] it was shown that the Z = 40 in ^{90}Zr behaves as a closed shell, while the N = 40 in ^{68}Ni behaves more as an open-shell configuration. As a consequence, there will be much more pair scattering of neutrons across N = 40 than of protons across Z = 40. This was deduced from the fact that the energy of the 0_3^+ state in ^{90}Zr is much higher than that in ^{68}Ni (4126 keV versus 2511 keV [25]). To explain the low excitation energy of the 0_3^+ state in ^{68}Ni a strong gain in binding energy from residual proton-neutron interactions is required, which means that many valence neutrons have to be available.

It is interesting to look at the results of the complementary transfer (t,p) reaction to ^{68}Ni, which is the ^{88}Sr(^{3}He,n) two-proton transfer reaction to ^{90}Zr with a Q-value of Q = 7.712(2) MeV [27]. Two experiments studying this reaction have been performed in the seventies [124, 126]. In the most recent experiment Ref. [124], with a beam energy of E(^{3}He) = 25.4 MeV, only a strong transition to the ground state in ^{90}Zr was observed. In the first experiment Ref. [126], where E(^{3}He) = 20.59 MeV, also a small feeding of 6.6(36) %, relative to 100 % ground state feeding, to the second 0^+ state at 1.76 MeV was observed. This feeding ratio was deduced at 0°. Further, the authors of Ref. [124] note that the strength of the transition to the ground state can only be explained when the full pf-shell and $g_{9/2}$ orbital are taken into account in the calculations, with a strong admixture of the $p_{1/2}$ and $g_{9/2}$ orbitals. In the two-neutron transfer to ^{68}Ni also the full neutron pfg space has to be taken into account, as was shown in Fig. 6.1.a. The results for the transfer to the ground state are thus similar in ^{90}Zr and ^{68}Ni. In ^{68}Ni however also a strong transition to the first excited 2_1^+ state is observed, which is absent in the transfer to ^{90}Zr.

Just as it was done for the even nickel isotopes, the systematics of the feeding

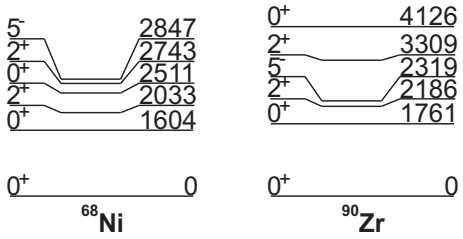

Figure 6.5: Comparison of the low lying levels in ^{68}Ni and ^{90}Zr [25, 45].

to the 0_2^+ and 2_1^+ state can be compared in the N = 50 isotones. This is shown in Fig. 6.4 for data taken from Ref [124, 125]. In general, the feeding to these two states is small or even not observed, except in one case, the feeding to the 0_2^+ state in ^{88}Sr reaches 36 % of the ground state feeding. These systematics can be compared to the systematics of the (t,p) reaction in the nickel isotopes, which is also shown in Fig. 6.4. In this figure the corresponding nuclei in the nickel chain and in the N = 50 isotones are put in the same column. Since ^{90}Zr is a stable nucleus, the systematics could be extended to heavier masses. Even though in principle the systematics in the N = 50 isotones could be used to predict the analog feedings in the heavier nickel isotopes, one notices that the patterns in the two chains are quite different. Hence, such a correspondence cannot be drawn.

7 | Conclusion

In this thesis we presented a study of the ^{66}Ni(t,p)^{68}Ni two-neutron transfer reaction, performed in inverse kinematics. The aim of the experiment was to characterize and disentangle the structure of the 0^+ and 2^+ states in ^{68}Ni, through the relative population of these states in the transfer reaction.

The experiment was performed at the ISOLDE facility in CERN. The T-REX setup together with the Miniball array were used to detect the resulting particles and gamma rays from the two-neutron transfer reaction. The ^{66}Ni beam was ionized by RILIS and post-accelerated to 2.6 MeV/u by REX. A beam intensity of $2.4(3) \cdot 10^6$ pps and beam purity $> 99\,\%$ were achieved.

From the detected proton energy the excitation energy of ^{68}Ni could be deduced. The excitation energy spectra of ^{68}Ni showed that the ground state was the most strongly fed in the ^{66}Ni(t,p) reaction with also a strong feeding to the first excited 2_1^+ state at 2033 keV, namely 29.3(29) % relative to 100 % ground state feeding. A direct small population of several other states in ^{68}Ni was also observed, of which the most important is the first excited 0^+ state at 1604 keV that received a feeding of 4.2(16) % of the ground state feeding. The recently measured energy [45] of this 0_2^+ state was confirmed in the present experiment, an energy of 1621(28) keV was deduced. A population of other 0^+ and 2^+ states was not directly observed, only an upper limit could be deduced for these states.

As a second step in the analysis, the angular distribution for the ground, 0_2^+ and 2_1^+ state was constructed and compared to DWBA calculations performed with FRESCO, using input from NUSHELL calculations. The neutron $f_{7/2}p_{3/2}p_{1/2}g_{9/2}$ model space was considered, proton excitations were not allowed, together with the jj44pna interaction [82]. The magnitude of the cross section of the ground and 0_2^+ state was well reproduced by the calculations. From the calculations it can be concluded that the transfer to the ground state is dominated by the p orbitals, but the coherent combination of all possible configurations is needed to explain the magnitude of the cross section. The transfer to the 0_2^+ state is

dominated by the $g_{9/2}$ orbital (see also Fig. 2.9.b).

The calculated cross section to the 2_1^+ state is an order of magnitude too small, the reason for this discrepancy is not clear. The influence of the $d_{5/2}$ orbital on the cross section was investigated, but the exclusion of this orbital from our used model space does not explain the discrepancy between the data and the calculations. By performing model calculations, however, we showed that especially the population of the p orbitals is favored by the reaction mechanism. By artificially increasing the influence of these orbitals in the transfer to the 2_1^+ state, it was possible to increase the calculated cross section to the right order of magnitude. Preliminary one might conclude that the p orbitals are more active in the transfer to the 2_1^+ state than predicted by the NUSHELL calculations.

Finally the feeding to the first excited 0^+ and 2^+ state in ^{68}Ni was compared to the results of (t,p) reactions on the lighter, stable nickel isotopes. The measured feeding to the 0_2^+ state is consistent with the systematics in the lighter nickel isotopes, although the predicted structure of the 0_2^+ state in the lighter isotopes is not the same as that in ^{68}Ni, especially the predicted neutron occupancy of the $g_{9/2}$ orbital is different. The feeding to the 2_1^+ state in the stable nickel isotopes shows a decreasing trend towards ^{66}Ni, in contrast with the strong population observed for the 2_1^+ state in ^{68}Ni. The strong population of the 2_1^+ state in ^{68}Ni is currently not understood.

Outlook

One way to try and clarify the nature of 0^+ states in ^{68}Ni is to look for possible 4p-4h configurations. This can be done via alpha-transfer reactions. Such 4p-4h states have been found in a number of other (doubly)-magic nuclei. The first excited 0^+ state at 3.35 MeV in ^{40}Ca is interpreted as a 4p-4h state and is strongly populated in the ^{36}Ar(^{6}Li,d)-reaction (82 % of the ground state) and in the ^{32}S(^{12}C,α)-reaction (1220 % of the ground state) (see Fig. 2.9 in Ref [127]). Such a 4p-4h state has also been observed in ^{16}O at 6.05 MeV through a ^{12}C(^{7}Li,t)-reaction [128]. Possible reactions to search for these 4p-4h states in ^{68}Ni at ISOLDE are the ^{72}Zn(d,^{6}Li) ($t_{1/2}(^{70}\mathrm{Zn}) = 46.5(1)$ h [25]) and ^{64}Fe(^{6}Li,d) ($t_{1/2}(^{64}\mathrm{Fe}) = 2.0(2)$ s [25]) reaction. The latter reaction with $Q = 9.445(6)$ MeV [25] will be hard to perform since it is very difficult to produce a short-living iron beam at ISOLDE. Iron is an element whose extraction from the target source is very slow. Radioactive iron beams with a short half-life thus cannot be directly produced at ISOLDE. The only method to produce an iron beam at ISOLDE is through in-trap decay of a manganese beam in

REX, but this method is still in its testing phase. The proof of principle of this method was demonstrated in a Coulomb excitation experiment of ^{61}Mn and ^{61}Fe [129].

The other possible reaction, ^{72}Zn(d,^{6}Li)^{68}Ni, has a large negative Q-value of Q = -5.633(4) MeV [25] and thus the beam energy should be high enough to overcome the threshold for the reaction. This requirement can be met by the HIE-ISOLDE project [130, 131], which is an upgrade of the present ISOLDE facility with the goal to be able to deliver post-accelerated beams with an energy up to 10 MeV/u. A lot of transfer reactions will benefit from this higher energy, e. g. the oscillatory behavior in the angular distribution can become more pronounced, which will facilitate spin assignments.

Further, information about how the 0^+ and 2^+ states in ^{68}Ni interact with each other can be obtained through Coulomb excitation (Coulex) [132]. Through the transition probabilities or B($E2$)-values the structure of the different 0^+ and 2^+ states could be deduced. A proposal to study Coulex of ^{68}Ni at HIE-ISOLDE has been submitted to the INTC of CERN in September 2013 [133]. Another proposal Ref. [134] aims to characterize the 0^+ and 2^+ states in ^{68}Ni through the study of the β decay of ^{68}Mn using γ and electron spectroscopy. Among others, their aim is to measure the lifetime of the 0_3^+ state and its $E0$ transition strength to the ground and 0_2^+ state.

A final interesting reaction that could be considered is the ^{67}Ni(d,p)^{68}Ni one-neutron transfer reaction, with Q = 5.568 MeV [25]. This reaction will lead to states that are composed of a neutron plus the ^{67}Ni ground state. The results of this reaction could be compared to the analogue ^{89}Y(^{3}He,d)^{90}Zr reaction [135].

A last subject is the search for improvements of the detector setup. The T-REX setup could be improved by coupling it to a recoil detector (a ΔE-E$_{\text{rest}}$ detector or mass spectrometer), in order to be able to link the light emitted ejectiles one-to-one to the recoils. Further, there is currently an interest in studying Coulex and transfer reactions simultaneously, as is also proposed in the previously mentioned proposal Ref. [133]. Therefore the T-REX setup was modified by removing the forward barrel detectors, while the detectors in backward direction are not changed. In this way the forward CD detector can be placed closer to the target. The optimal distance between the CD detector and the target can be determined for every experiment separately. This altered setup was used for the first time in a successful Coulex experiment on ^{72}Zn [136].

Of course, also different detection setups that could be used to study transfer reactions at (HIE)-ISOLDE can be developed. Two possible options are presently under consideration, namely HELIOS [137, 138, 139, 140] and ACTAR [141]. HELIOS or Helical Orbit Spectrometer consists of a

superconducting solenoid, that creates a magnetic field that is aligned with the beam axis. The target is placed on this axis and the emitted light particles are, following a helical trajectory, transported back to the magnetic axis and detected by position-sensitive silicon detectors, which measure the deposited energy, time-of-flight and distance from the target. The advantage of HELIOS is that, when looking at a fixed distance from the target, the kinematic compression is removed. This will enhance the Q-value resolution considerably [138, 139]. HELIOS has been used successfully in a few experiments [138, 140]. The downside of HELIOS is its size, which does not allow a close geometry for gamma ray detectors, such as the Miniball array, and thus gamma rays cannot be detected with a high efficiency. However, since a very good particle detection resolution is expected, this may not be a problem.

ACTAR consists of an ACtive TARget detector to study transfer reactions. It is based on a gaseous ionization detector where the nuclei of the gas atoms are also the target nuclei [141]. By using a gaseous target, utilization of a thick target is possible without losing energy resolution. The detector uses the principle of a time projection chamber. Hereby, a three-dimensional reconstruction of the tracks of the charged particles in the gas volume is possible. The active target is designed for use with the weakest beams (down to 10^3 pps). The proof of principle of using an active target at ISOLDE was successfully shown in a recent experiment using the Maya active target [142].

A | Fresco Input

Two input files for FRESCO are given as an example. Both inputs are for a DWBA calculation of the cross section to the ground state in ^{68}Ni. The first one, given in Box A.1 does not use experimental input for the intermediate nucleus ^{67}Ni, while the second one, given in Box A.2 uses all the available experimental information, i. e. binding energies and excitation energies, of ^{67}Ni.

Box A.1: Input for FRESCO for a calculation of the two-neutron transfer cross section to the ground state of ^{68}Ni. No experimental information for the intermediate nucleus ^{67}Ni is used in this input.

```
Ni 66(t,p) Ni 68 @ 7.559 MeV Q = 5.12 MeV Ex = 0.00 MeV
NAMELIST
&FRESCO hcm=0.05 rmatch=30.00 rintp=0.20 hnl=0.1
   rnl=16.00 centre=-1.2 hnn=0.300 rnn=10.00 rmin=0.30
   jtmin=0.0 jtmax=20 absend=-1.0
   thmin=0.00 thmax=180.00 thinc=1.00
   iter=2 nnu=36  chans=1 xstabl=1 smats=2
   elab= 7.559 /

&PARTITION
 namep='t3'  massp=3.016 zp=1
 namet='Ni 66' masst=66.000 zt=28 nex=1  /
&STATES jp=0.5 bandp=1 ep=0.0
        cpot=1 jt=0.00 bandt=1 et=0.00 /


&PARTITION
 namep='p1' massp=1.0078 zp=1
 namet='Ni 68' masst=68.000 zt=28 qval=5.117 nex=1 /
&STATES jp=0.5 bandp=1 ep=0.0
        cpot=2 jt=0.0 bandt=1 et=0.00 / #p+T=T+p
```

```
&PARTITION
 namep='d2' massp=2.0141 zp=1
 namet='Ni 67' masst=67.000 zt=28
 nex=-4 qval=0.542 / #pn+(T-n)=T+p
&STATES jp=1.0 bandp=1 ep=0.0
                cpot=9 jt=2.5 bandt=-1 et=0.000 /
&STATES copyp=1 cpot=9 jt=1.5 bandt=-1 et=0.000 /
&STATES copyp=1 cpot=9 jt=0.5 bandt=-1 et=0.000 /
&STATES copyp=1 cpot=9 jt=4.5 bandt= 1 et=0.000 /
&partition /

&POT kp=1 at=66.000 rc=1.300  / #triton optical
&POT kp=1 type=1 p1=162.801 p2=1.200 p3=0.720
                 p4=26.947 p5=1.400 p6=0.840 /
&POT kp=1 type=2 p1=0.000   p2=0.000 p3=0.000
                 p4=0.000  p5=1.400 p6=0.840 /
&POT kp=1 type=3 p1=2.500   p2=1.200 p3=0.720
                 p4=0.000  p5=0.000 p6=0.000 /

&POT kp=2 at=68.000 rc=1.251  / #proton optical
&POT kp=2 type=1 p1=59.600 p2=1.205 p3=0.668
                 p4=0.900 p5=1.204 p6=0.668 /
&POT kp=2 type=2 p1=0.000  p2=0.000 p3=0.000
                 p4=9.100 p5=1.278 p6=0.554 /
&POT kp=2 type=3 p1=5.700  p2=1.027 p3=0.590
                 p4=0.000 p5=1.027 p6=0.590 /

&POT kp=4 at=1.000 rc=1.28  /
&POT kp=4 type=1 p1=100. p2=0.95 p3=0.65
                 p4=0. p5=0. p6=0. / #triton p+n pot

&POT kp=5 at=66.000 rc=1.251  / #proton optical
&POT kp=5 type=1 p1=59.600 p2=1.205 p3=0.668
                 p4=0.900 p5=1.204 p6=0.668 /
&POT kp=5 type=2 p1=0.000  p2=0.000 p3=0.000
                 p4=9.100 p5=1.278 p6=0.554 /
&POT kp=5 type=3 p1=5.700  p2=1.027 p3=0.590
                 p4=0.000 p5=1.027 p6=0.590 /

&POT kp=6 at=66.000 rc=1.250/ #neutron bound state pot
&POT kp=6 type=1 p1=50.000 p2=1.250 p3=0.650 /
```

```
&POT kp=6 type=3 p1=6.500  p2=1.250 p3=0.650 /

&POT kp=9 at=67.000 rc=1.698  / #deuteron optical
&POT kp=9 type=1 p1=82.682 p2=1.174 p3=0.809
                 p4=1.220  p5=1.563 p6=0.883 /
&POT kp=9 type=2 p1=0.000  p2=0.000 p3=0.000
                 p4=13.289 p5=1.328 p6=0.648 /
&POT kp=9 type=3 p1=3.703  p2=1.234 p3=0.813
                 p4=0.000  p5=1.234 p6=0.813 /

&pot kp=11 type= 1 p(1:7)= 100.000 0.4000 0.6000
     0.0000 0.0000 0.0000 1.0000 /# n+p=d simple gs
&pot kp=12 type= 1 p(1:7)= 100.000 0.9500 0.6500
     0.0000 0.0000 0.0000 1.0000 / # d+n=t simple gs
&pot /

&OVERLAP kn1=1 ic1=1 ic2=3 in=1 kind=0 nn=1 l=0 sn=0.5
         j=0.5 kbpot=12 be=6.2570 isc=1 ipc=0 / #<d|t>
&OVERLAP kn1=2 ic1=2 ic2=3 in=1 kind=0 nn=1 l=0 sn=0.5
         j=0.5 kbpot=11 be=2.2245 isc=1 ipc=0 / #<p|d>

&Overlap kn1=3 ic1=1 ic2=3 in=1 kind=0 nn=1 l=0 sn=0.5
         j=0.5 kbpot=4 be=4.2409 isc=1 ipc=0 /
&Overlap kn1=30 kn2=60 ic1=1 ic2=2 in=1 kind=6 nn=1
         l=0 lmax=0 sn=0.0 ia=1 j=0.0 ib=1
         kbpot=1 be=0.1000 isc=0 ipc=1 / #projectile
&twont
         tnt(1,1)=3 tnt(2,1)=3 coef(1)=1.00000 /

&Overlap kn1=13 ic1=3 ic2=1 in=2 kind=0 nn=1 l=3 sn=0.5
         j=2.50 kbpot=6 be=6.800 isc=1 ipc=0 /
&Overlap kn1=14 ic1=3 ic2=1 in=2 kind=0 nn=2 l=1 sn=0.5
         j=1.50 kbpot=6 be=6.800 isc=1 ipc=0 /
&Overlap kn1=15 ic1=3 ic2=1 in=2 kind=0 nn=2 l=1 sn=0.5
         j=0.50 kbpot=6 be=6.800 isc=1 ipc=0 /
&Overlap kn1=16 ic1=3 ic2=1 in=2 kind=0 nn=1 l=4 sn=0.5
         j=4.50 kbpot=6 be=6.800 isc=1 ipc=0 /


&Overlap kn1=200 kn2=270 ic1=2 ic2=1 in=2 kind=6 nn=4
         l=0 lmax=0 sn=0.0 ia=1 j=0.0 ib=1
         kbpot=1 be=0.1000 isc=0 ipc=2 /
```

```
&twont
          tnt(1,  1)=13 tnt(2,  1)=13 coef( 1)=0.8262
          tnt(1,  2)=14 tnt(2,  2)=14 coef( 2)=0.5426
          tnt(1,  3)=15 tnt(2,  3)=15 coef( 3)=0.7046
          tnt(1,  4)=16 tnt(2,  4)=16 coef( 4)=-0.7942
        /
&overlap /

&Coupling icto=-2 icfrom=1 kind=7 ip1=0 ip2=-1 ip3=5/
&CFP in=1 ib=1 ia=1 kn=30 a=1.00  /
&CFP in=-2 ib=1 ia=1 kn=200 a=1.00  /
&COUPLING icto=-3 icfrom=1 kind=7 ip1=1
           ip2=-1 ip3=0  / # transfer (t3,d)
  &cfp in=1 ib=1 ia=1 kn=1  a=1.176  /
  &cfp in=2 ib=1 ia=1 kn=13 a=1.4142 /
  &cfp in=2 ib=2 ia=1 kn=14 a=1.4142 /
  &cfp in=2 ib=3 ia=1 kn=15 a=1.4142 /
  &cfp in=2 ib=4 ia=1 kn=16 a=1.4142 /
  &cfp /
&COUPLING icto=-2 icfrom=3 kind=7 ip1=0
           ip2=-1 ip3=0  / # transfer (d,p)
  &cfp in=1 ib=1 ia=1 kn=2  a=1.000   /
  &cfp in=2 ib=1 ia=1 kn=13 a=0.8262  /
  &cfp in=2 ib=1 ia=2 kn=14 a=0.5426  /
  &cfp in=2 ib=1 ia=3 kn=15 a=0.7046  /
  &cfp in=2 ib=1 ia=4 kn=16 a=-0.7942  /
  &cfp /
&coupling /
```

Box A.2: FRESCO input file for a calculation of the two-neutron transfer cross section to the ground state of ^{68}Ni. The binding energy and experimental excitation energies of the intermediate nucleus ^{67}Ni are included in the calculation.

```
Ni 66(t,p) Ni 68 @ 7.559 MeV Q = 5.12 MeV Ex = 0.00 MeV
NAMELIST
&FRESCO hcm=0.05 rmatch=  30.00 rintp=0.20 hnl=0.1
   rnl=16.00 centre=-1.2 hnn=0.300 rnn=10.00 rmin=0.30
   jtmin=0.0  jtmax=20 absend=-1.0
   thmin=0.00 thmax=180.00 thinc=1.00
   iter=2 nnu=36  chans=1 xstabl=1 smats=2
   elab= 7.559 /
```

```
&PARTITION
 namep='t3'  massp=3.016 zp=1
 namet='Ni 66' masst=66.000 zt=28 nex=1  /
&STATES jp=0.5 bandp=1 ep=0.0
  cpot=1 jt= 0.00 bandt=1 et=0.0000  /

&PARTITION
 namep='p1' massp=1.0078 zp=1
 namet='Ni 68' masst=68.000 zt=28 qval=5.117 nex=1 /
&STATES jp=0.5 bandp=1 ep=0.0
  cpot=2 jt= 0.0 bandt=1 et=   0.000 / #p+T=T+p

&PARTITION
 namep='d2' massp=2.0141 zp=1
 namet='Ni 67' masst=67.000 zt=28
 nex=-4 qval=-0.45 / #pn+(T-n)=T+p
&STATES jp=1.0 bandp=1 ep=0.0
                cpot=9 jt=2.5 bandt=-1 et=0.6940 /
&STATES copyp=1 cpot=9 jt=1.5 bandt=-1 et=1.7243 /
&STATES copyp=1 cpot=9 jt=0.5 bandt=-1 et=0.0000 /
&STATES copyp=1 cpot=9 jt=4.5 bandt= 1 et=1.0066 /
&partition /

&POT kp=1 at=66.000 rc=1.300 / #triton optical
&POT kp=1 type=1 p1=162.801 p2=1.200 p3=0.720
                 p4=26.947 p5=1.400 p6=0.840 /
&POT kp=1 type=2 p1=0.000   p2=0.000 p3=0.000
                 p4=0.000  p5=1.400 p6=0.840 /
&POT kp=1 type=3 p1=2.500   p2=1.200 p3=0.720
                 p4=0.000  p5=0.000 p6=0.000 /

&POT kp=2 at=68.000 rc=1.251 / #proton optical
&POT kp=2 type=1 p1=59.600 p2=1.205 p3=0.668
                 p4=0.900 p5=1.204 p6=0.668 /
&POT kp=2 type=2 p1=0.000  p2=0.000 p3=0.000
                 p4=9.100 p5=1.278 p6=0.554 /
&POT kp=2 type=3 p1=5.700  p2=1.027 p3=0.590
                 p4=0.000 p5=1.027 p6=0.590 /

&POT kp=4 at=1.000 rc=1.28 /
&POT kp=4 type=1 p1=100. p2=0.95 p3=0.65
                 p4=0. p5=0. p6=0. / #triton p+n pot
```

```
&POT kp=5 at=66.000 rc=1.251 / #proton optical
&POT kp=5 type=1 p1=59.600 p2=1.205 p3=0.668
                 p4=0.900 p5=1.204 p6=0.668 /
&POT kp=5 type=2 p1=0.000  p2=0.000 p3=0.000
                 p4=9.100 p5=1.278 p6=0.554 /
&POT kp=5 type=3 p1=5.700  p2=1.027 p3=0.590
                 p4=0.000 p5=1.027 p6=0.590 /

&POT kp=6 at=66.000 rc=1.250/ #neutron bound state pot
&POT kp=6 type=1 p1=50.000 p2=1.250 p3=0.650 /
&POT kp=6 type=3 p1=6.500  p2=1.250 p3=0.650 /

&POT kp=9 at=67.000 rc=1.698  / #deuteron optical
&POT kp=9 type=1 p1=82.682 p2=1.174 p3=0.809
                 p4=1.220  p5=1.563 p6=0.883 /
&POT kp=9 type=2 p1=0.000  p2=0.000 p3=0.000
                 p4=13.289 p5=1.328 p6=0.648 /
&POT kp=9 type=3 p1=3.703  p2=1.234 p3=0.813
                 p4=0.000  p5=1.234 p6=0.813 /

&pot kp=11 type=1 p(1:7)= 100.000 0.4000 0.6000
     0.0000 0.0000 0.0000 1.0000 /# n+p=d simple gs
&pot kp=12 type=1 p(1:7)= 100.000 0.9500 0.6500
     0.0000 0.0000 0.0000 1.0000 / # d+n=t simple gs
&pot /

&OVERLAP kn1=1 ic1=1 ic2=3 in=1 kind=0 nn=1 l=0 sn=0.5
         j=0.5 kbpot=12 be=6.2570 isc=1 ipc=0 / #<d|t>
&OVERLAP kn1=2 ic1=2 ic2=3 in=1 kind=0 nn=1 l=0 sn=0.5
         j=0.5 kbpot=11 be=2.2245 isc=1 ipc=0 / #<p|d>

&Overlap kn1=3 ic1=1 ic2=3 in=1 kind=0 nn=1 l=0 sn=0.5
         j=0.5 kbpot=4 be=4.2409 isc=1 ipc=0 /
&Overlap kn1=60 kn2=90 ic1=1 ic2=2 in=1 kind=6 nn=1
         l=0 lmax=0 sn=0.0 ia=1 j=0.0 ib=1
         kbpot=1 be=0.1000 isc=0 ipc=1 / #projectile
&twont
         tnt(1,1)=3 tnt(2,1)=3 coef(1)=1.00000 /

&Overlap kn1=13 ic1=3 ic2=1 in=2 kind=0 nn=1 l=3 sn=0.5
         j=2.50 kbpot=6 be=6.8002 isc=1 ipc=0 /
```

```
&Overlap kn1=14 ic1=3 ic2=1 in=2 kind=0 nn=2 l=1 sn=0.5
         j=1.50 kbpot=6 be=6.8002 isc=1 ipc=0 /
&Overlap kn1=15 ic1=3 ic2=1 in=2 kind=0 nn=2 l=1 sn=0.5
         j=0.50 kbpot=6 be=6.8002 isc=1 ipc=0 /
&Overlap kn1=16 ic1=3 ic2=1 in=2 kind=0 nn=1 l=4 sn=0.5
         j=4.50 kbpot=6 be=6.8002 isc=1 ipc=0 /


&Overlap kn1=23 ic1=3 ic2=1 in=2 kind=0 nn=1 l=3 sn=0.5
         j=2.50 kbpot=6 be=5.1138 isc=1 ipc=0 /!<66|67>
&Overlap kn1=24 ic1=3 ic2=1 in=2 kind=0 nn=2 l=1 sn=0.5
         j=1.50 kbpot=6 be=4.0835 isc=1 ipc=0 /
&Overlap kn1=25 ic1=3 ic2=1 in=2 kind=0 nn=2 l=1 sn=0.5
         j=0.50 kbpot=6 be=5.8078 isc=1 ipc=0 /
&Overlap kn1=26 ic1=3 ic2=1 in=2 kind=0 nn=1 l=4 sn=0.5
         j=4.50 kbpot=6 be=4.8016 isc=1 ipc=0 /

&Overlap kn1=33 ic1=3 ic2=2 in=2 kind=0 nn=1 l=3 sn=0.5
         j=2.50 kbpot=6 be=8.4867 isc=1 ipc=0 /!<67|68>
&Overlap kn1=34 ic1=3 ic2=2 in=2 kind=0 nn=2 l=1 sn=0.5
         j=1.50 kbpot=6 be=9.5170 isc=1 ipc=0 /
&Overlap kn1=35 ic1=3 ic2=2 in=2 kind=0 nn=2 l=1 sn=0.5
         j=0.50 kbpot=6 be=7.7927 isc=1 ipc=0 /
&Overlap kn1=36 ic1=3 ic2=2 in=2 kind=0 nn=1 l=4 sn=0.5
         j=4.50 kbpot=6 be=8.7989 isc=1 ipc=0 /


&Overlap kn1=200 kn2=270 ic1=2 ic2=1 in=2 kind=6 nn=4
         l=0 lmax=0 sn=0.0 ia=1 j=0.0 ib=1
         kbpot=1 be=0.1000  isc=0 ipc=2 /
&twont
         tnt(1, 1)=13 tnt(2, 1)=13 coef( 1)=0.8262
         tnt(1, 2)=14 tnt(2, 2)=14 coef( 2)=0.5426
         tnt(1, 3)=15 tnt(2, 3)=15 coef( 3)=0.7046
         tnt(1, 4)=16 tnt(2, 4)=16 coef( 4)=-0.7942
       /
&overlap /

&Coupling icto=-2 icfrom=1 kind=7 ip1=0 ip2=-1 ip3=5/
&CFP in=1 ib=1 ia=1 kn=60 a=1.00  /
&CFP in=-2 ib=1 ia=1 kn=200 a=1.00  /
&COUPLING icto=-3 icfrom=1 kind=7 ip1=1
```

```
          ip2=-1 ip3=0  / #transfer (t3,d)
  &cfp in=1 ib=1 ia=1 kn=1  a=1.176  /
  &cfp in=2 ib=1 ia=1 kn=23 a=1.4142 /
  &cfp in=2 ib=2 ia=1 kn=24 a=1.4142 /
  &cfp in=2 ib=3 ia=1 kn=25 a=1.4142 /
  &cfp in=2 ib=4 ia=1 kn=26 a=1.4142 /
  &cfp /
&COUPLING icto=-2 icfrom=3 kind=7 ip1=0
          ip2=-1 ip3=0  / #transfer (d,p)
  &cfp in=1 ib=1 ia=1 kn=2  a=1.000   /
  &cfp in=2 ib=1 ia=1 kn=33 a=0.8262  /
  &cfp in=2 ib=1 ia=2 kn=34 a=0.5426  /
  &cfp in=2 ib=1 ia=3 kn=35 a=0.7046  /
  &cfp in=2 ib=1 ia=4 kn=36 a=-0.7942  /
  &cfp /
&coupling /
```

B | Tables Cross Section

In this appendix the numerical values for the cross section to the ground state and first excited 0^+ and 2^+ state in ^{68}Ni are given.

Table B.1: Differential cross section to the ground state in ^{68}Ni.

θ_{CM}	$\frac{\mathrm{d}\sigma}{\mathrm{d}\Omega}$ [mb/srad]	$\delta\frac{\mathrm{d}\sigma}{\mathrm{d}\Omega}$ [mb/srad]
5.7	1.63	0.37
8.5	1.65	0.30
11.4	0.84	0.18
14.4	0.63	0.15
23.7	0.88	0.14
27.1	1.28	0.16
30.5	1.73	0.18
34.1	2.16	0.20
37.8	1.85	0.17
41.7	1.51	0.15
45.8	0.94	0.11
50.1	0.54	0.08
80.1	0.11	0.03
85.8	0.16	0.04
91.7	0.34	0.06
97.8	0.33	0.06
104.1	0.20	0.04
110.5	0.13	0.03
117.1	0.11	0.03
123.7	0.12	0.03
130.5	0.11	0.04

Table B.2: Differential cross section to the 0_2^+ state at 1604 keV in ^{68}Ni.

θ_{CM}	$\frac{d\sigma}{d\Omega}$ [mb/srad]	$\delta\frac{d\sigma}{d\Omega}$ [mb/srad]
5.4	0.14	0.07
8.1	0.14	0.06
10.8	0.09	0.04
13.6	0.07	0.03

Table B.3: Differential cross section to the 2_1^+ state at 2033 keV in ^{68}Ni.

θ_{CM}	$\frac{d\sigma}{d\Omega}$ [mb/srad]	$\delta\frac{d\sigma}{d\Omega}$ [mb/srad]
5.3	0.43	0.19
7.9	0.40	0.16
10.6	0.33	0.12
13.4	0.38	0.12
25.3	0.59	0.12
28.6	0.49	0.10
32.0	0.43	0.09
35.6	0.36	0.08
39.4	0.40	0.08
43.4	0.38	0.08
47.6	0.26	0.06
77.6	0.08	0.03
83.4	0.12	0.03
89.4	0.18	0.04
95.6	0.15	0.03
102.0	0.13	0.03
108.6	0.12	0.03
115.3	0.14	0.04
122.2	0.13	0.04
129.1	0.10	0.03

C | Papers: β decay and β-delayed fission of ^{180}Tl

Paper I:
Shape coexistence in ^{180}Hg studied through the β decay of ^{180}Tl

PHYSICAL REVIEW C **84**, 034307 (2011)

Shape coexistence in ^{180}Hg studied through the β decay of ^{180}Tl

J. Elseviers[1], A. N. Andreyev1, 2, S. Antalic[3], A. Barzakh[4], N. Bree[1], T. E. Cocolios[1,5], V. F. Comas[6], J. Diriken[1], D. Fedorov[4], V. N. Fedosseev[7], S. Franchoo[8], J. A. Heredia[6], M. Huyse[1], O. Ivanov[1], U. Köster[9], B. A. Marsh[7], R. D. Page[10], N. Patronis[1,11], M. D. Seliverstov[1,5], I. Tsekhanovich[12], P. Van den Bergh[1], J. Van De Walle[5], P. Van Duppen[1], M. Venhart[1,13], S. Vermote[14], M. Veselský[15] and C. Wagemans[14]

[1] *Instituut voor Kern-en Stralingsfysica, K. U. Leuven, University of Leuven, BE-3001 Leuven, Belgium*
[2] *School of Engineering and Science, University of the West of Scotland, Paisley, PA1 2BE, UK and the Scottish Universities Alliance (SUPA)*
[3] *Department of Nuclear Physics and Biophysics, Comenius University, 84248 Bratislava, Slovakia*
[4] *Petersburg Nuclear Physics Institute, 188350 Gatchina, Russia*
[5] *ISOLDE, CERN, CH-1211 Geneve 23, Switzerland*
[6] *Gesellschaft für Schwerionenforschung, Planckstrasse 1, D-64291 Darmstadt, Germany*
[7] *EN Department, CERN, CH-1211 Geneve 23, Switzerland*
[8] *Institut de Physique Nucléaire, IN2P3-CNRS/Université Paris-Sud, F-91406 Orsay Cedex, France*
[9] *Institut Laue Langevin, 6 rue Jules Horowitz, F-38042 Grenoble Cedex 9*
[10] *Department of Physics, Oliver Lodge Laboratory, University of Liverpool, Liverpool L69 7ZE, United Kingdom*
[11] *Department of Physics, University of Ioannina, GR-45110 Ioannina, Greece*
[12] *CENBG, CNRS IN2P3, Univ. Bordeaux 1, FR-33175 Gradignan, France*
[13] *Slovak Academy of Sciences, Bratislava, SK-84511 Slovakia*
[14] *Department of Physics and Astronomy, University of Gent, Proeftuinstraat 86, B-9000 Gent, Belgium*

(Received 23 June 2011; published 7 September 2011)

Abstract

The β^+/EC decay of ^{180}Tl and excited states in the daughter nucleus ^{180}Hg have been investigated at ISOLDE, CERN. Many new low-lying energy levels were observed in ^{180}Hg, of which the most significant are the 0_2^+ at 419.6 keV and the 2_2^+ at 601.3 keV. The former is the bandhead of an excited band in ^{180}Hg assumed originally to be of prolate nature. From the β feeding to the different states in ^{180}Hg, the ground state spin of ^{180}Tl was deduced to be $(4^-,5^-)$.

PACS numbers: 21.10.Re,23.20.Lv,27.70.+q,29.38.-c

I. INTRODUCTION

Even-even mercury isotopes have been found to be a prolific testing ground for the phenomenon of shape coexistence [1-3], whereby different types of deformation coexist at low excitation energy within the same nucleus. Shape coexistence in the neutron-deficient mercury nuclei was observed by using different techniques, ranging from optical [4] and laser spectroscopy [5,6] to in-beam spectroscopy [7,8] and decay spectroscopy [9,10]. A wealth of new data has become available, recently through lifetime measurements [11,12] and by using new techniques such as Coulomb excitation of post-accelerated radioactive beams [13].

The excitation energies of the yrast-band members of the even-even mercury isotopes between A = 190 and 198 (see Fig. C.1) show an almost constant behavior and are believed to be associated with the weakly deformed oblate ground state ($\beta_2 \sim$ - 0.15). This pattern is distorted in the lighter mercury isotopes through the intrusion of a strongly deformed prolate band ($\beta_2 \sim 0.25$) as discussed in Ref. [2,3]. This band is built on top of a deformed excited 0_2^+ state, which is interpreted as resulting from proton excitations across the Z = 82 closed shell [14]. Such intruder states have been found to be a widely occurring structural feature of nuclei at and near closed shells. The emerging picture for the intruder states' behavior in the mercury isotopes is the parabolic trend of the excitation energy of states in the prolate band as a function of the neutron number N. Studies of the lightest even-even isotopes $^{174-180}$Hg [3,15-18], showed that the minimum of the energy of the intruder structure was probably reached in ^{182}Hg (N = 102), although the 0_2^+ bandhead had not been observed in ^{180}Hg before the present work. Also the 2_2^+ state in ^{180}Hg was not firmly established; a state at 797 keV was proposed in Ref. [18] as the 2^+ member of the prolate band, but this is not validated in the present study.

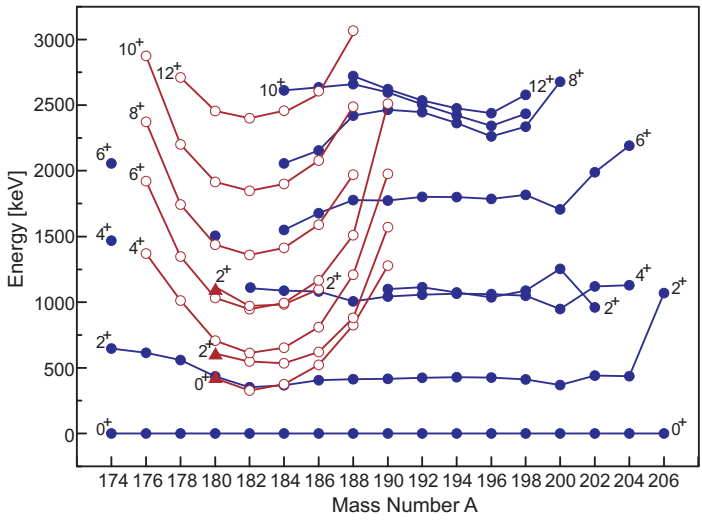

Figure C.1: (Color online) Energy systematics of excited states of even-even neutron-deficient mercury isotopes. The energies are taken from Refs. [3,12,20-22]. The filled triangles show the states identified in this work. The full dots are the level energies associated with the weakly oblate ground state band, the open dots are those related to the excited prolate band. However, at low spin states, strong mixing can occur [23].

Furthermore, theoretical predictions [14] suggest a transition from a weakly oblate to a spherical ground state of the even-even mercury isotopes with $N < 96$. Indeed, the observed evolution of the ground-state band properties, i.e. the high excitation energy of the first 2^+ and 4^+ states in ^{174,176}Hg [3], supports this prediction.

Shape coexistence is not the only reason to study ^{180}Tl decay. The main aim of the present experiment was the study of the β-delayed fission of ^{180}Tl [19]. To investigate the β-delayed fission probability, the β branching ratio of ^{180}Tl has to be known precisely. This can be determined by investigating the β decay of ^{180}Tl. Furthermore, the heavier odd-odd thallium isotopes with $A = 188$-196 have typically two β-decaying isomers [20]. If ^{180}Tl has also more than one β-decaying isomer, it is important to know through which isomer the β-delayed fission occurs. The existence of isomerism in ^{180}Tl could possibly be verified via a β-γ study.

The present paper reports on the results of an experiment carried out to study low-lying excited states of ^{180}Hg through the EC/β^+ decay of ^{180}Tl. Prior

to this study, the states of ^{180}Hg have only been investigated by using the technique of in-beam γ-ray spectroscopy in conjunction with the recoil-decay tagging technique [11,12,17,18]. These experiments show three excited bands, up to spin $I = (22)$. In contrast with in-beam spectroscopy, which dominantly reveals yrast states, the β-decay spectroscopy allows deeper insight into low-lying non-yrast coexisting states.

II. EXPERIMENTAL SETUP

The experiment was performed at the CERN-ISOLDE facility [24] and is part of a systematic α, β and β-delayed fission study of neutron-deficient thallium isotopes. Protons from the PS-Booster with an energy of 1.4 GeV and an average intensity of 2.1 μA impinged on a 50 g·cm^{-2} UC_x target, producing a wide variety of nuclei through fission, spallation or fragmentation. The thallium isotopes were predominantly formed through spallation. The proton beam consisted of pulses that had a length of 2.4 μs and a period of 1.2 s. During the experiment, a sequence of 21 pulses was grouped into a so-called *supercycle* with a total length of 25.2 s. The amount of proton pulses that ISOLDE received changed throughout the experiment from four to ten pulses per supercycle.

After the proton impact, the produced radioactive isotopes diffused across and effused from the target material towards an ion source through a heated transfer line. To reduce the release time the target-ion source was kept at a high temperature of $\approx$ 2300 K. The desired thallium isotopes were subsequently ionized with the resonant laser ionization technique [25]. The ionized thallium isotopes were extracted from the target-ion source using extraction electrodes and were accelerated to 30 keV. The High Resolution Separator [26] was used to separate the isotopes according to their mass to charge ratio. As a result, a high-purity beam of ^{180}Tl nuclei was obtained. By comparing the ratio of the number of thallium nuclei in spectra taken with the lasers tuned to the ionization of thallium to spectra taken without lasers, a fraction of only 1.4(1) % of surface-ionized ^{180}Tl was observed.

The decay of ^{180}Tl was observed using the so-called Windmill system [19]. After mass separation, the incident thallium beam of $\sim$ 150 atoms/s was implanted in one of ten 20 μg·cm^{-2} thick carbon foils mounted on a wheel. Any long-living radioactivity was removed from the implantation position by rotating the wheel after every supercycle. The proton pulses of the supercycle were chosen in such way that two consecutive proton pulses were taken followed by a period without proton pulses (see Fig. C.2). The separator gate was opened from the moment the first proton pulse arrived until 1.2 s after the second proton pulse.

Two Si detectors were placed at the implantation position in close geometry. An annular detector having an active area of 450 mm^2, thickness of 300 μm and

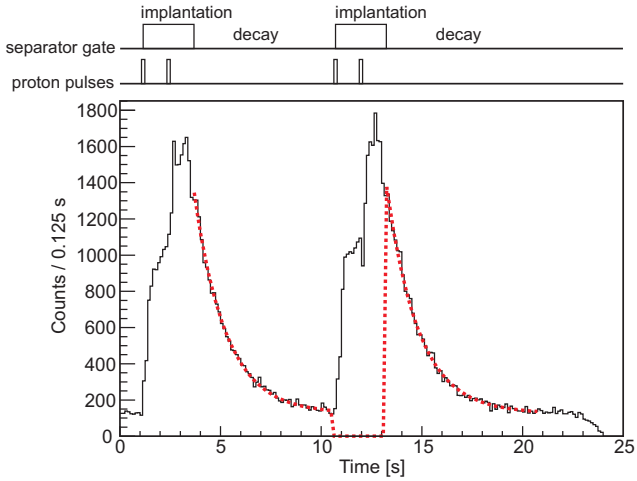

Figure C.2: (Color online) Time behavior for the $2_1^+ \rightarrow 0_1^+$ (434 keV) transition in ^{180}Hg as a function of the implantation and decay periods within one supercycle, defined by the proton pulses and the separator gate, which determines the implantation period. The red dotted line is the exponential fit of the 'decay' intervals.

a central hole with a diameter of 6 mm was positioned in front of the foil, so that the ion beam could pass through the hole. A circular detector of active area 300 mm^2 and thickness 300 μm was placed behind the foil. Both detectors together covered a solid angle of 66 % of 4π. The energy resolution (FWHM) of these detectors for α decays in the range of 5000-7000 keV was $\sim$35 keV. As the primary aim of these experiments was the detection of β-delayed fission, the energy range was set to 200 keV-100 MeV to record events from electrons, positrons, α particles and fission fragments. Outside the vacuum chamber, at $\sim$2 cm from the implantation point, a Miniball Ge cluster detector was placed, which consisted of three Hyper Pure Germanium (HPGe) crystals [27]. The typical energy resolution (FWHM) of each crystal of the cluster for 1.3 MeV γ radiation was $\sim$3.1 keV. The absolute photo-peak efficiency of the whole cluster for the 434 keV line, the strongest transition in ^{180}Hg, was determined to be 7.3(1)%. The $\gamma\gamma$ coincidences used in the analysis of the experiment were those between the three crystals of the cluster. In the detection setup digital electronics [digital gamma finder (DGF) modules [28]] were used to acquire the data.

III. RESULTS

The half-life of ^{180}Tl can be determined from its α decay or β-delayed γ decay. The α-decay spectrum can be found in Ref. [19] and the time behavior after β decay is illustrated in Fig. C.2, which shows the time behavior for the $2_1^+ \rightarrow 0_1^+$ (434 keV) transition in ^{180}Hg. The half-life of ^{180}Tl was determined by fitting the 'decay' intervals between proton implantations with an exponential (see Fig. C.2). This results in a half-life of $t_{1/2} = 1.09(1)$ s for the α and β decay of ^{180}Tl. Except for several unresolved and/or weak lines, most of the γ transitions attributed to ^{180}Hg (see Table C.1) have a time behavior that within uncertainty is consistent with this half-life. Although isomerism is observed in the heavier thallium isotopes, no evidence for the presence of an isomer could be extracted from the half-life behavior of ^{180}Tl β-delayed γ decays.

A β branching ratio of 94(4)% for ^{180}Tl was determined from a comparison of the number of α and β decays (for more details, see Ref. [19]).

Figure C.3 shows a γ-ray energy spectrum measured at A = 180 with the Miniball Ge cluster, in which transitions belonging to the decay of ^{180}Tl are indicated. The assignment of γ lines to the β decay of ^{180}Tl is based on $\gamma\gamma$ coincidences and on previously known transitions in ^{180}Hg [17,18]. Other strong lines in Fig. C.3 that do not originate from the decay of ^{180}Tl come from the decay of beam contaminants. These mainly consist of ^{38,39,40}Cl, ^{140,142}La and ^{141,142}Ba. It is believed that molecules of mass 180 are formed between the chlorine isotopes and the barium or lanthanum isotopes, which are not fully suppressed by the High Resolution Separator. One of the strongest lines in the spectrum is the 511 keV γ ray, originating mainly from the annihilation of the positron resulting from the β^+ decay of ^{180}Tl or from pair production of high energy γ rays.

An example of a $\gamma\gamma$ coincidence spectrum is shown in Fig. C.4, with a coincidence gate on the strongest transition in ^{180}Hg, namely the 434 keV ($2_1^+ \rightarrow 0_1^+$) transition. In this spectrum the background is subtracted by also taking $\gamma\gamma$ coincidence spectra with a gate on the left and right hand sides of the 434 keV peak in the energy spectrum, and normalizing to the peak-to-background ratio. This method results in the appearance of artificial peaks (denoted as AP in the figure) in the $\gamma\gamma$ coincidence spectrum. The two artificial peaks in Fig. C.4 are due to the strong peaks at 827 keV and 1460 keV in the γ-ray energy spectrum, Fig. C.3. This is due to Compton scattering between the crystals of the Miniball Ge cluster. Due to this Compton scattering, these artificial peaks are broader than real transitions and they can be identified in the background subtracted $\gamma\gamma$ coincidence spectrum by the large drops on the the left and right side of the artificial peak.

Table C.1 gives the energy and γ intensity, relative to the 434 keV transition, of all the transitions in ^{180}Hg identified in the present study, as well as the

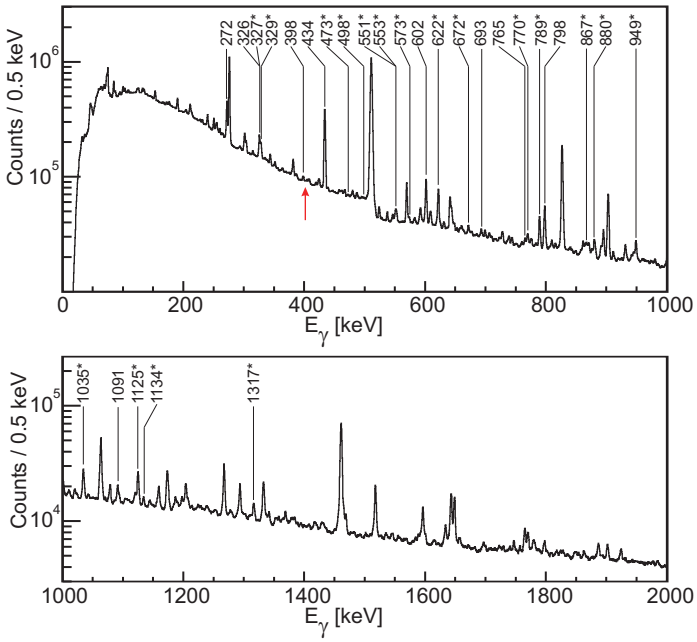

Figure C.3: (Color online) A γ-ray energy spectrum detected by the Miniball Ge cluster for mass 180. Transitions associated with the decay of ^{180}Tl are indicated (energies are in keV). New transitions, which were observed for the first time in the present study, are shown with '*'. Note that the 405 keV γ-ray (indicated by the red arrow), that deexcites the known 8^+ state in ^{180}Hg [18] is not observed. The other lines are due to room background and through the presence in the A = 180 beam of molecules with mass 180 (see text for details).

energy of the initial state and the γ rays with which the specific transition is coincident. Due to the close distance of the Miniball Ge cluster to the implantation point, summing between γ rays in a cascade can occur. Note that no correction for this summing was made in the determination of the γ intensities. The resulting level scheme of ^{180}Hg is shown in Fig. C.5. The spins of the levels at 434 keV (2^+), 706 keV (4^+), 1032 keV (6^+), 1399 keV (3^-), 1504 keV (6^+) and 1797 keV (5^-) are taken from Ref. [18]. Note that the known 8^+ level at 1437 keV, deexciting with a 405 keV γ line [18] is not observed in this decay study. The β-feeding intensities are based on the intensities from Table C.1 using the internal conversion coefficients for transitions where the multipolarity is known. The internal conversion coefficients are taken from Ref. [30]. However, due to the Pandemonium effect [31], only upper limits of

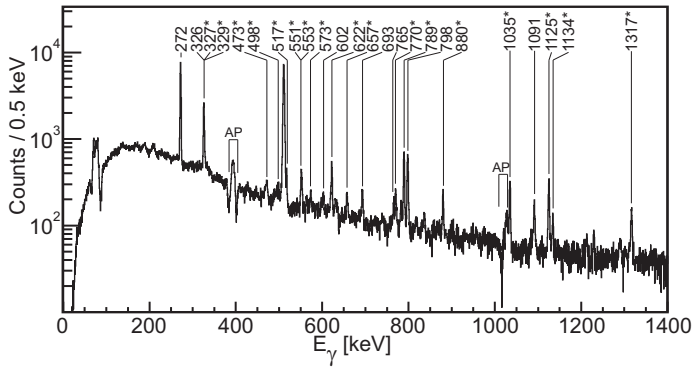

Figure C.4: A $\gamma\gamma$ coincidence spectrum with gate on the 434 keV transition. AP stands for artificial peak, see text for details. New transitions are indicated by '*'and γ-ray energies are in keV.

the β-feeding intensities can be given. From the β-feeding intensities and the Q_{EC} value to

Table C.1: The energy, γ-ray intensity (without correction for summing) relative to the transition at 434 keV, energy of the initial state and observed coincident γ rays for the transitions belonging to the decay of ^{180}Tl. The γ-ray intensities are determined from the γ-ray singles spectrum, unless otherwise indicated. Due to the occurrence of doublets and triplets, a number of observed coincident γ rays could not be uniquely assigned to one particular transition and are therefore grouped and indicated by an accolade sign. New transitions, observed for the first time in the present study, are marked by '*'.

Energy[1] (keV)	Relative γ Intensity (%)	Initial Energy Level (keV)	Observed coincident γ-rays (keV)
104.7*	1.4(4)[2]	706.0	
167.0*	3.3(2)	601.3	
181.8*	0.16(1)[3]	601.3	
272.0	54.2(27)	706.0	326, 398, 434, 472, 498, 518, 574, 693, 765, 798, 1091, 1125, 1134 1317, 1456, 1782

325.8	15.3(10)[4]	1031.8	272, 434, 473, 552, 602, 621, 765, 790, 798, 1035, 1317, 1455
326.8*	5.6(9)[4]	2348.4	
328.6*	2.7(17)[4]	1797.1	
398.2	2.9(2)	1797.1	272, 551, 602, 693, 798
434.0	100	434.0	167, 272, 326, 472, 498, 518, 552, 574, 602, 622, 658, 693, 765, 770, 790, 798, 880, 949, 1035, 1091, 1125, 1134, 1229, 1456, 1781
472.5*	1.1(2)	1504.2	272, 326, 434
498.1*	1.3(2)[4]	1203.8	272, 434
517.4*	3.4(4)[4]	1223.4	272, 434, 798, 1125
551.1*	3.0(4)[4]	2348.4	327, 398, 434, 573, 602, 622, 765, 867, 1035, 1091
553.0*	2.9(4)[4]	2021.8	
573.4*	1.6(2)	1797.1	434, 517, 551, 602, 622, 790
601.6	24.3(12)[4]	601.3	327, 398, 434, 552, 573, 602, 622, 636, 798, 867, 949, 1125
602.4*	1.5(2)[4]	1203.8	
622.0*	18.5(9)	1223.4	327, 434, 551, 574, 602, 798, 1125
657.3*	1.0(2)	1091.3	434, 773
671.6*	0.79(4)[5]	1091.3	773
692.9	2.4(2)	1399.0	272, 398, 434, 949
765.4	1.5(1)	1797.1	272, 326, 434, 551
769.7*	3.5(2)	1203.8	434, 635
789.4*	10.4(12)	1223.4	327, 434, 551, 573, 798, 1125
797.7	4.5(17)[4]	1399.0	272, 327, 398, 434, 518, 602, 622, 789, 949
798.0	5.1(18)[4]	1504.2	
798.1*	9.2(6)[4]	2021.8	
867.1*	1.9(2)[4]	1468.5	434, 552, 602, 880
880.3*	5.0(4)	2348.4	434, 602, 867, 1035
948.9*	3.5(11)[4]	2348.4	272, 434, 602, 693, 798
1034.6*	7.5(8)	1468.5	327, 434, 553, 880
1091.2	2.3(1)	1797.1	272, 434, 551
1125.1*	9.7(5)	2348.4	272, 434, 518, 602, 622, 790
1134.2*	1.1(1)[4]	1840.0	272, 434
1228.9*	0.8(2)[4]	1662.9	434
1316.5*	3.9(2)	2021.8	272, 326, 434, 602
1455.4*	0.6(1)[4]	2487.4	272, 325, 434
1781.5*	1.6(3)[4]	2487.4	272, 434

[1] The uncertainty on the energies is 0.2 keV for the strong transitions, for the weak transitions ($I_\gamma \leq 1.5\%$) the error can rise up to 0.5 keV.
[2] Calculated from the intensity of the 272 keV transition, the relative branching ratio of the 272 keV and the 105 keV transition (89% and 11%, respectively, determined from $\gamma\gamma$ coincidences) and the theoretical total E2 conversion coefficient of the 105 keV transition (4.575 according to Ref. [30].

[3] Determined from the γ spectrum with a gate on the K electron of the $E0$ transition between the first two 0^+ states (see Fig. C.9).
[4] Determined from $\gamma\gamma$ coincidences.
[5] Determined from the number of $E0$ transitions observed and the efficiency to detect conversion electrons.

a specific level, the logft values can be deduced. Only the logft values for the energy levels with the strongest β-feeding intensities are given, because these will not change significantly, even if there is some unobserved γ-ray feeding.

Many new states have been observed in ^{180}Hg, of which the most significant are the 0_2^+ (420 keV) and the 2_2^+ (601 keV) states. The latter differs from the one suggested by Kondev *et al.* [18], namely a 2_2^+ state at 797.3 keV. In the current study, the 798 keV transition is placed on top of the 601 keV transition, and not vice-versa as proposed in Ref. [18]. Our assignment is based on unambiguous coincidence relations. The 601 keV state is a 2^+ state, since the 167 keV transition to the first excited 2^+ at 434 keV has an important $E0$ component. This is clear from investigating the $\gamma\gamma$ coincidence spectrum, with a gate on the 622 keV transition (see Fig. C.6), which is placed on top of the 601 keV state in the ^{180}Hg level scheme. This transition is both coincident with the 602 keV and the 434 keV line. From these coincidences the total relative intensity of the 167 keV transition between the 601 keV and the 434 keV states could be deduced, by comparing the number of counts in the 602 keV and 434 keV peaks in this coincidence spectrum. This gave a total relative intensity of $I_{tot} = 15(1)\%$, which is much larger than the observed relative γ intensity of this transition $I_\gamma = 3.3(2)\%$. From this the total internal conversion coefficient of the 167 keV transition $\alpha = 3.5(4)$ was deduced, indicating that this transition is dominated by a strong $E0$ component, as the theoretical total electron conversion coefficients for a 167 keV M1 and E2 transition are 1.83 and 0.74 respectively [30].

The 0_2^+ state at 420 keV has been identified by investigating Si-γ coincidences. Due to the limited thickness of the Si detectors (300 μm), they mainly acted as ΔE detectors for electrons and positrons coming from the β decay yielding a ΔE peak around $\sim$120 keV. However, due to the energy threshold, the efficiency dropped for electron energies below 400 keV to become zero around 200 keV (see Fig. C.7a). By gating on the $2_1^+ \rightarrow 0_1^+$ 434 keV, the $4_1^+ \rightarrow 2_1^+$ 272 keV and the $6_1^+ \rightarrow 4_1^+$ 326 keV γ-ray transitions, for which the conversion coefficients (E2 transitions) and the K- and L-electron energies are known, energy and efficiency calibrations for the Si detectors in the energy range between 300 and 500 keV was performed. This is illustrated in Fig. C.7a, which shows the Si spectrum with a gate on the 272 keV transition.

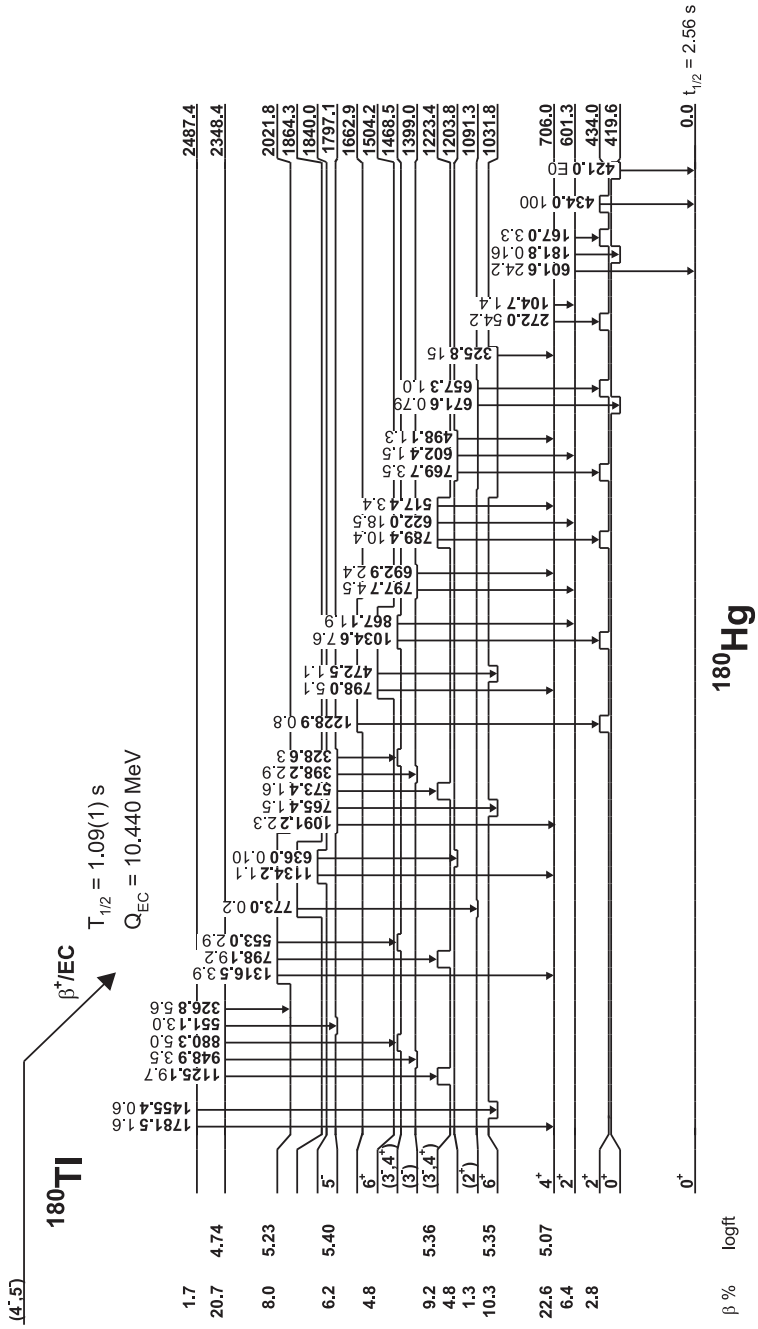

Figure C.5: Level scheme of ^{180}Hg deduced from the present work. γ-ray intensities are all normalized to the 434 keV transition (energies in keV). The given β-feeding intensities are upper limits. The calculated Q_{EC} value is taken from Ref. [29].

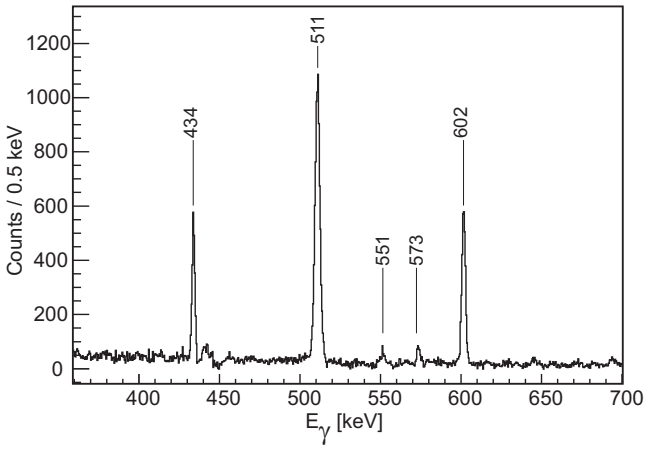

Figure C.6: Part of the $\gamma\gamma$ coincidence spectrum with a gate on the 622 keV transition (energies in keV).

In this figure, the background due to β particles, which is actually the ΔE spectrum of the β particles, is shown by the red lower curve. This background was deduced from Si spectra taken in a range between 5 and 11 s after the second proton pulse (see Fig C.2). These spectra are dominated by β decay of the daughter nuclei of ^{180}Tl as most of the ^{180}Tl has decayed away. The β background is normalized with the gated Si spectra in the energy range between 500 and 1000 keV. The $E0$ transition of the hitherto unobserved 0^+ prolate bandhead is expected in the range of 300 to 500 keV. By inspecting the γ rays coincident with electrons and positrons in this energy range, a new transition appeared at 672 keV (see Fig. C.8 and Fig. C.3). This transition does not belong to any of the daughter products of ^{180}Tl or to any of the known contaminants and is coincident with mercury X rays.

By looking at the events in the Si detector which are coincident with the 672 keV transition a strong peak appears, see Fig. C.7b. This is interpreted as the K-electron peak of the $E0$ transition between the 0_2^+ state and the ground state, placing the former at 421(20) keV. The fact that no γ rays of 421 keV are observed confirms that this is the 0_2^+ state. A small peak due to the electrons from all the other $E0$ (L, M, N,...) components can also be seen, indicated in the figure as the L-component, because this is the strongest of these transitions. The K-to-total ratio was deduced from this figure as K/tot = 0.85(18). This is consistent with the value for an $E0$ transition determined in Ref. [30] (K/tot = 0.8543), but other multipolarities cannot be excluded with the current precision.

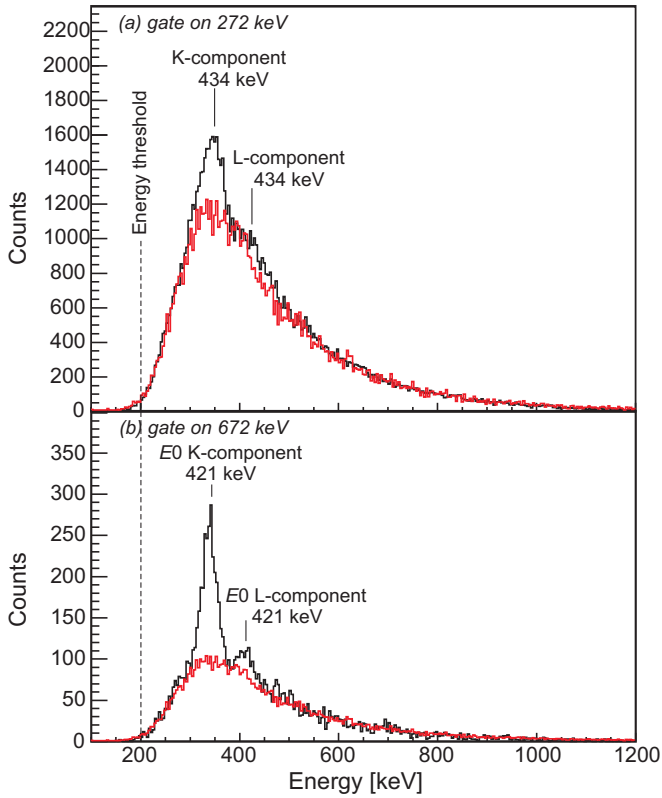

Figure C.7: (Color online) Si spectrum gated on (a) the 272 keV and (b) the 672 keV transition. The red lower curve is the ΔE spectrum due to β particles (see text for details).

Furthermore, in Fig. C.9 part of the background subtracted γ-ray spectrum with a gate on the K-electron energy of the $E0$ transition is shown. Next to mercury K X rays a new γ transition appears at 182 keV, which is equal, within error bars, to the difference between the 2_2^+ state and the 0_2^+ state. In this figure the 272 keV transition also appears. This is due to the fact that the K-electron energies of the internal conversion of the 434 keV transition and of the 420 keV transition are very close in energy. Finally, connecting γ rays and coincidence relations with the 672 keV and 182 keV transition fixes the energy of the 0_2^+ state at 419.6(4) keV and leads to the identification of the states at 1091 keV and at 1864 keV. Other new levels that have been observed are 1204 keV, 1223 keV, 1469 keV, 1663 keV, 1840 keV, 2022 keV, 2348 keV and 2487 keV. A unique spin

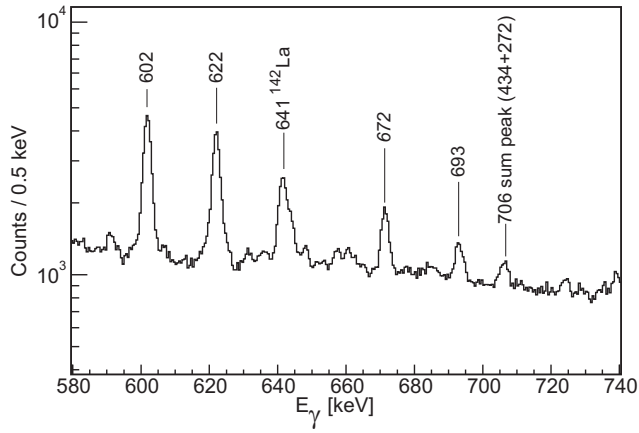

Figure C.8: Part of the γ spectrum with a gate on the Si events that have an energy between 200 and 1200 keV (energies in keV).

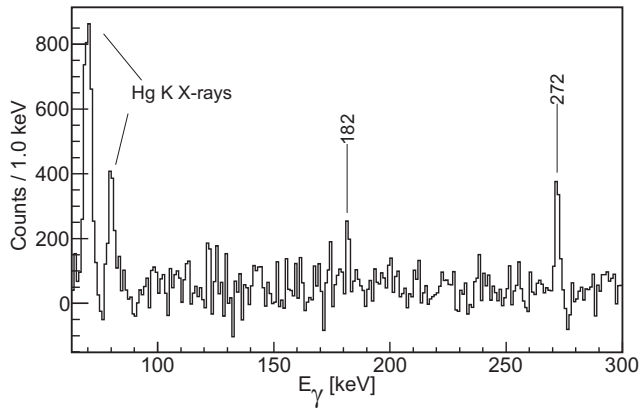

Figure C.9: Part of the background subtracted γ spectrum with gate on the K electron of the $E0$ transition between the first two 0^+ states (energies in keV).

assignment could not be deduced for any of these states.

We also note that an independent in-beam conversion electron study of ^{180}Hg using the SACRED spectrometer coupled to the RITU gas-filled recoil separator at the University of Jyväskylä [32], observed conversion electrons

that corroborates our assumption of the conversion of the $2_2^+ \rightarrow 2_1^+$ 167 keV transition and also contains a 420 keV electron line giving evidence that the 0_2^+ level is placed at the correct energy (see Fig. 2 of Ref. [32]).

IV. DISCUSSION

A. Ground state of ^{180}Tl

The β feeding of the different states of ^{180}Hg was calculated (see Fig. C.5) and used to deduce the most probable ground-state spin of ^{180}Tl, as β decay mainly populates states with a spin differing by $\Delta I = 0,1$. The heavier odd-odd thallium isotopes from $A = 184$ up to $A = 196$ are characterized by isomerism with two β-decaying states based on the coupling of the $3s_{1/2}$ proton with a $3p_{3/2}$ neutron, leading to a 2^- state, or with a $1i_{13/2}$ neutron leading to a 7^+ state. In ^{180}Tl with $N = 99$, however, the $1h_{9/2}$ neutron orbital has to be considered, leading to some differences compared with the heavier thallium isotopes. A robust feature in the β-decay pattern of the 7^+ isomer in the heavier thallium isotopes is the feeding of the 8^+ state in the mercury daughter. This is not the case for the decay of ^{180}Tl as the known 8^+ state in ^{180}Hg [18] is not fed; most of the feeding goes to the 4_1^+ state with feeding of 5^- and 6^+ states. From this it can be deduced that the β-decaying state in ^{180}Tl probably has spin 4 or 5. The coupling of the $3s_{1/2}$ proton to a $1h_{9/2}$ neutron can lead to a 4^- or 5^- state.

The observation in this study of the second 0^+ state and the associated low-spin transitions feeding it, is partly due to the feeding through (unobserved) γ-ray transitions. However, it is not clear yet if there is also direct feeding through a possible, but yet unobserved low-spin state in ^{180}Tl. Nevertheless, the half-life of ^{180}Tl obtained by gating on the 2_1^+ (434 keV) and 2_2^+ (601 keV) transitions in the present work agree with a half-life of $t_{1/2} = 1.09(1)$ s. Hence, based on this experimental fact, no conclusive evidence for the existence of the low-spin isomer in ^{180}Tl has been found. A possibility to settle this issue is expected from a recent in-source laser spectroscopy experiment at ISOLDE where spectra of the decay of ^{180}Tl were taken as a function of the frequency of the ionizing laser light. The analysis of these data is on-going [33].

B. Systematics of even mercury isotopes

In Fig. C.1, the newly observed 0_2^+ state at 420 keV, 2_2^+ state at 601 keV, and (2_3^+) state at 1091 keV in ^{180}Hg are shown. The 0_2^+ and 2_2^+ states follow well the general trend established in heavier mercury isotopes and confirm that the minimum of the parabolic behavior in excitation energy of the prolate band occurs in ^{182}Hg, i.e. at $N = 102$. These two states are the only new energy levels for which a firm spin assignment could be deduced, although it is believed that

the state at 1091 keV is the 2_3^+ state, which according to the systematics is expected to occur around $\sim$1 MeV (see Fig. C.1 and Fig. C.10). Furthermore, this state decays to the 0_2^+ and the 2_1^+ state via γ decay, so its spin should be 1 or 2. Also, in ^{182,184,186}Hg a similar 2_3^+ state has been observed, which decays similarly only to the 0_2^+ and the 2_1^+ states and not to the ground state (see Fig. C.10, the green dotted lines) [20]. This could be an indication that this is the bandhead of the γ vibrational band that is coupled to the prolate band. This assignment is also suggested for the corresponding 2^+ state in ^{184,186}Hg [10,34].

In Fig. C.10 the candidates for the 4_2^+ state are also indicated. The 1124 keV level in ^{182}Hg was suggested as a possible candidate for the 4_2^+ level in Ref. [12] and was also observed in Ref. [22,35]. In ^{180}Hg, two possible candidates for the 4_2^+ state are present, the 1203 keV and the 1223 keV levels. The latter is more strongly fed in the β decay of ^{180}Tl, suggesting that if the ground state spin of ^{180}Tl is indeed (4,5), this would have a higher probability of being the 4_2^+ state. However, by looking at the γ intensities of the transitions originating from these levels and comparing them with those of the 1080 keV level in ^{186}Hg, the 1203 keV level shows closer resemblance to the heavier mercury isotopes, and this would suggest this is the 4_2^+ level in ^{180}Hg.

V. CONCLUSION

The β decay of ^{180}Tl populating levels in ^{180}Hg was studied. As a result, many new low-lying energy states were observed in ^{180}Hg, of which the most significant are the 0_2^+ and 2_2^+ states, at energies of 420 keV and 601 keV, respectively. They confirm that the minimum of the prolate configuration in the chain of Hg isotopes occurs in ^{182}Hg, i.e. at N = 102. Moreover, the possible bandhead of the γ vibrational band built on the prolate deformed state was tentatively identified at 1091 keV.

Furthermore, from the β feeding of the different ^{180}Hg states, the ground state spin of ^{180}Tl was inferred to be $(4^-,5^-)$. A firmer assignment of the ground state spin will follow from a hyperfine interaction study [33]. This spin determination and the fact that only one β-decaying isomer is observed in ^{180}Tl is important for the understanding of the β-delayed fission study [19]. The identification of the lowest-energy states and their decays is important for the Coulomb excitation of ^{180}Hg, which has recently become possible. Finally, the ongoing analysis of the data from low-energy Coulomb excitation of $^{182-188}$Hg performed at the radioactive beam experiment (REX) at ISOLDE [13], of the lifetime measurements on $^{184-188}$Hg at the Argonne Tandem-Linac Accelerator System (ATLAS) [36] and of the recent β-decay studies of $^{182-184}$Tl [22] will complement the information on the different structures present in the even-

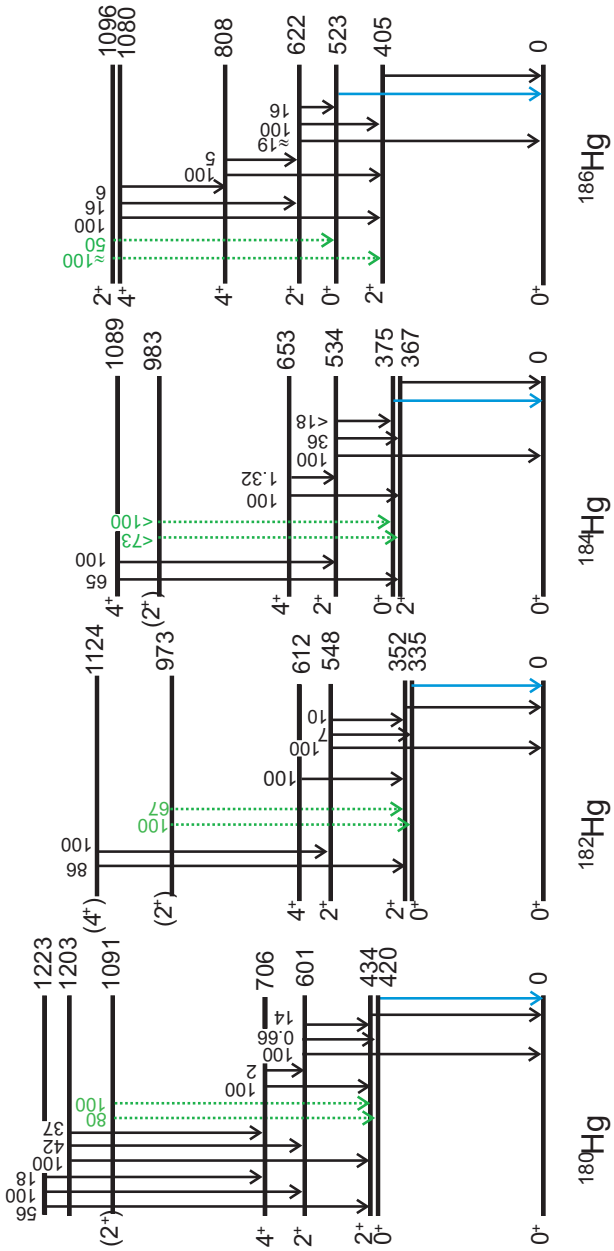

Figure C.10: (Color online) The systematics of the lowest positive-parity states and their transitions in the even-even $^{182-186}$Hg nuclei. The green dotted lines are the gamma-ray transitions of the possible γ-vibrational bandhead, i.e. the 2_3^+ state (see text for details). The relative γ-ray intensities are taken from the present work and Refs. [20,22] and level energies are given in keV.

even mercury nuclei near the neutron mid-shell. With all these observables a full theoretical description comes within reach.

ACKNOWLEDGEMENTS

We would like to thank J. L. Wood for fruitful discussions. We thank the ISOLDE collaboration for providing excellent beams and the GSI Target Group for manufacturing the carbon foils. This work was supported by FWO-Vlaanderen (Belgium), by GOA/2004/03 (BOFK.U.Leuven), by the IUAP - Belgian State Belgian Science Policy - (BriX network P6/23), by the European Commission within the Sixth Framework Programme through I3-EURONS (Contract RII3-CT-2004-506065), by the United Kingdom Science and Technology Facilities Council (STFC), and by the Slovak grant agency VEGA (Contract No. 2/0105/11 1/0091/10).

---

[1] K. Heyde *et al.* , Phys. Rep. **102**, 291 (1983), and references therein.

[2] J. L. Wood *et al.* , Phys. Rep. **215**, 101 (1992), and references therein.

[3] R. Julin *et al.* , J. Phys. G **27**, R109 (2001), and references therein.

[4] J. Bonn *et al.* , Phys. Lett. B **38**, 308 (1972).

[5] T. Kühl, P. Dabkiewicz, C. Duke, H. Fischer, H. -J. Kluge, H. Kremmling, and E. -W. Otten, Phys. Rev. Lett. **39**, 180 (1977).

[6] G. Ulm *et al.* , Z. Phys. A **325**, 247 (1986).

[7] D. Proetel *et al.* , Phys. Rev. Lett. **31**, 896 (1973).

[8] N. Rud *et al.* , Phys. Rev. Lett. **31**, 1421 (1973).

[9] J. H. Hamilton *et al.* , Phys. Rev. Lett. **35**, 562 (1975).

[10] J. D. Cole *et al.* , Phys. Rev. Lett. **37**, 1185 (1976).

[11] T. Grahn *et al.* , Phys. Rev. C **80**, 014324 (2009).

[12] M. Scheck *et al.* , Phys. Rev. C **81**, 014310 (2010).

[13] A. Petts *et al.* , in Conference Proceedings CP1090 Capture Gamma-Ray Spectroscopy and Related Topics, 13th International Symposium, 2009 (unpublished), p. 414.

[14] W. Nazarewicz, Phys. Lett. B **305**, 195 (1993).

[15] M. Muikku *et al.* , Phys. Rev. C **58**, R3033 (1998).

[16] M. P. Carpenter *et al.* , Phys. Rev. Lett. **78**, 3650 (1997).

[17] G. D. Dracoulis *et al.* , Phys. Lett. B **208**, 365 (1988).

[18] F. G. Kondev *et al.* , Phys. Rev. C **62**, 044305 (2000).

[19] A. N. Andreyev *et al.* , Phys. Rev. Lett. **105**, 252502 (2010).

[20] Evaluated Nuclear Structure Data File (ENSDF), [http://www. nndc. bnl. gov-/ensdf/].

[21] J. Wauters *et al.* , Phys. Rev. C **50**, 2768 (1994).

[22] E. Rapisarda *et al.* (unpublished).

[23] G. D. Dracoulis, Phys. Rev. C **49**, 3324 (1994).

[24] E. Kugler, Hyperfine Interact. **129**, 23 (2000).

[25] V. N. Fedoseyev *et al.* , Hyperfine Interact. **127**, 409 (2000).

[26] T. J. Giles *et al.* , Nucl. Instr. Meth. B **204**, 497 (2003).

[27] J. Eberth *et al.* , Progr. Part. Nucl. Phys. **46**, 389 (2001).

[28] X-ray Instruments Associates, [http://www. xia. com].

[29] P. Möller, A. J. Sierk, T. Ichikawa, A. Iwamoto, R. Bengtsson, H. Uhrenholt, and S. Aberg, Phys. Rev. C **79**, 064304 (2009).

[30] T. Kibédi *et al.* , Nucl. Instr. Meth. A **589**, 202 (2008).

[31] J. C. Hardy *et al.* , Phys. Lett. B **71**, 307 (1977).

[32] R. D. Page *et al.* , Phys. Rev. C **84**, 034308 (2011).

[33] V. Liberati *et al.* (unpublished).

[34] J. P. Delaroche *et al.* , Phys. Rev. C **50**, 2332 (1994).

[35] M. Keupers, MasterŠs thesis, University of Leuven, Faculteit Wetenschappen, 2010.

[36] L. Gaffney (unpublished).

Paper II:
β-delayed fission of ^{180}Tl

PHYSICAL REVIEW C **88**, 044321 (2013)

β-delayed fission of ^{180}Tl

J. Elseviers[1], A. N. Andreyev2, 3, M. Huyse[1], P. Van Duppen[1], S. Antalic[4], A. Barzakh[5], N. Bree[1], T. E. Cocolios[1,6], V. F. Comas[7], J. Diriken[1], D. Fedorov[5], V. N. Fedosseev[8], S. Franchoo[9], L. Ghys[1], J. A. Heredia[7], O. Ivanov[1], U. Köster[10], B. A. Marsh[8], K. Nishio[3]., R. D. Page[11], N. Patronis[1,12], M. D. Seliverstov[1,6], I. Tsekhanovich[13,14], P. Van den Bergh[1], J. Van De Walle[6], M. Venhart[1,15], S. Vermote[16], M. Veselský[15] and C. Wagemans[16]

[1]*Instituut voor Kern-en Stralingsfysica, KU Leuven, University of Leuven, B-3001 Leuven, Belgium*
[2]*Department of Physics, University of York, York, YO10 5DD, United Kingdom*
[3]*Advanced Science Research Center (ASRC), Japan Atomic Energy Agency (JAEA), Tokai-mura, Naka-gun, Ibaraki 319-1195, Japan*
[4]*Department of Nuclear Physics and Biophysics, Comenius University, 84248 Bratislava, Slovakia*
[5]*Petersburg Nuclear Physics Institute, 188350 Gatchina, Russia*
[6]*ISOLDE, CERN, CH-1211 Geneve 23, Switzerland*
[7]*Gesellschaft für Schwerionenforschung, Planckstrasse 1, D-64291 Darmstadt, Germany*
[8]*EN Department, CERN, CH-1211 Geneve 23, Switzerland*
[9]*Institut de Physique Nucléaire, IN2P3-CNRS/Université Paris-Sud, F-91406 Orsay Cedex, France*
[10]*Institut Laue Langevin, 6 rue Jules Horowitz, F-38042 Grenoble Cedex 9*
[11]*Department of Physics, Oliver Lodge Laboratory, University of Liverpool, Liverpool L69 7ZE, United Kingdom*
[12]*Department of Physics, University of Ioannina, GR-45110 Ioannina, Greece*
[13]*School of Physics and Astronomy, University of Manchester, Manchester M13 9PL, United Kingdom*
[14]*Centre d'Etudes Nucleaires de Bordeaux Gradignan, F-33175 Gradignan Cedex, France*
[15]*Slovak Academy of Sciences, Bratislava, SK-84511 Slovakia*
[16]*Department of Physics and Astronomy, University of Gent, Proeftuinstraat 86, B-9000 Gent, Belgium*

(Received 14 August 2012; revised manuscript received 3 September 2013; published 21 October 2013)

Abstract

The detailed analysis of the β-delayed fission data of ^{180}Tl is presented. The experiment was performed by producing a pure beam of ^{180}Tl by means of highly-selective resonance laser ionization followed by mass separation with the ISOLDE (CERN, Geneva) isotope separator. A surprising asymmetric mass distribution of fission fragments from ^{180}Hg, the daughter of ^{180}Tl β decays, was observed. Here, the energy calibration of the silicon detectors, which is crucial for a proper determination of the fission fragments' energy and mass split, is presented and the total kinetic energy and its dependence on the mass split ratio is discussed. A more precise β-delayed fission probability $P_{\beta DF}(^{180}\mathrm{Tl}) = 3.2(2)\times10^{-3}$ % was deduced.

PACS numbers: 23.40.-s, 24.75.+i, 25.85.-w,29.38.-c

I. INTRODUCTION

Studies of low-energy fission, in which the excitation energy E^* of the fissioning nucleus is lower than or comparable to the height of its fission barrier B_f, represent a very important branch of fission studies. At these low excitation energies the influence of shell effects is especially important, while these effects are expected to wash out as the excitation energy of the nucleus is increased [1]. Furthermore, the relatively low (or even zero) angular momentum of the fissioning nucleus simplifies the analysis and the interpretation of experimental data in most cases.

Low-energy fission has been quite extensively studied in a broad mass region of the nuclear chart using different approaches: spontaneous fission from the ground state [2] and from shape isomers [3], fission induced by thermal neutrons [1,4], Coulomb-excited fission [5,6] and β-delayed fission (βDF) [7,8]. Using the observed fission fragment mass distributions, one can distinguish two broad and actually adjacent regions of nuclei in the nuclear chart. In particular, the nuclei in the light thorium to gold region, having a typical neutron-to-proton ratio of $N/Z \sim 1.4$-1.5, show a symmetric fission fragment distribution (*symmetric* fission), which was demonstrated e.g. in the particle-induced fission studies of $A \sim 200$ nuclei in Ref. [9,10] and more recently by the pioneering experiments using Coulomb-excited fission of relativistic radioactive beams [5,6]. In contrast to this, fission of nuclei in the heavier actinides region, having a typical ratio of $N/Z \sim 1.55$, results in most cases in an asymmetric mass distribution of the fission fragments (*asymmetric* fission), as e.g. in the thermal neutron-induced fission of ^{235}U or in the majority of known cases of

spontaneous fission [1,2]. An elegant method of low-energy fission studies in this region is βDF [7,8] which was recently applied for e.g. neutron-deficient isotopes ^{242,244}Es and ^{238}Bk to study the mass distribution of their respective daughter (after β decay) isotopes ^{242,244}Cf [11,12] and ^{238}Cm [13].

In the βDF process, discovered in 1966 [7], the parent nucleus first undergoes β decay (β^- or β^+/EC), whereby it populates an excited state in the daughter nucleus. If this excited state has an energy comparable to or higher than the fission barrier of the daughter nucleus, it may fission with a finite probability. This decay mode will happen in competition with γ and/or particle (neutron or proton) decay. So far, this process was only observed in a dozen of very neutron-deficient nuclei in the trans-uranium region [8], in a few nuclei in the lead region [14-17] and in the neutron-rich region several cases of βDF are known [18]. The most recent review of βDF is given in Ref. [18]. In the heavy neutron-deficient nuclei, and especially when the beta decay populates high-lying levels close to and above the fission barrier, electron capture (EC) decay typically dominates over β^+ decay. Therefore in the literature this decay is often called EC-delayed fission ($ECDF$).

The maximum excitation energy of the daughter nucleus in this process is determined by the β decay Q-value, Q_{EC}, of the parent nucleus, which typically does not exceed 5-6 MeV in the uranium region and 11-12 MeV in the most neutron-deficient nuclei in the lead region. These values can be compared to the typical (*calculated*) values of the fission barriers in the respective regions, which are 3-7 MeV in the uranium nuclei of interest and 9-12 MeV in the lead region (see Table V of Ref. [19]). At this point we have to note that experimental masses (thus Q_{EC} values) and fission barriers are not available for these exotic nuclei. Values quoted throughout this paper are taken from the theoretical work by Möller *et al.* in Ref. [19]. The choice of theoretical model has negligible impact on the conclusions of this work.

Owing to relatively low Q_{EC}-values, the βDF can be classified as low-energy fission. Furthermore, the comparison of the above Q_{EC} and B_f values shows that fission in most known βDF cases is subbarrier, meaning that it proceeds from excited states below the fission barrier ($Q_{EC} - B_f \leq 0$). Additionally βDF allows low-energy fission studies of nuclei with very exotic N/Z ratios, which do not fission from their ground state, owing to their relatively high fission barrier.

Recently, we initiated an extensive campaign of βDF studies of nuclei in the neutron-deficient lead region, possessing a typical ratio of $N/Z = 1.25$-1.3, opening a new region in low-energy fission [16,17].

In particular, in our βDF study of ^{180}Tl [15] the fission fragments mass distribution from the fission of its daughter (after β decay) isotope ^{180}Hg ($N=100$, $Z=80$, $N/Z=1.25$) was measured for the first time. Before that study, symmetric fission of ^{180}Hg into two semi-magic nuclei ^{90}Zr ($N=50$, $Z=40$) was expected. In contrast to this, a surprising asymmetric mass split in nuclei in the vicinity of $A\approx 80$ and $A\approx 100$ was observed in Ref. [15]. This finding was discussed within the five-dimensional fission model developed by Möller *et al.* [19]. Following this discussion, the fission of even-A isotopes of mercury was analyzed within the Brownian Metropolis shape-motion treatment [20]. Further, the self-consistent nuclear density functional theory employing Skyrme SKM* and Gogny DIS energy density functionals was used to study the fission of ^{180}Hg and ^{198}Hg [21]. Two further approaches were inspired by the earlier scission-point model [22]. The authors of Ref. [23] use what they call the "improved scission-point" model and in Ref. [24] the recently developed microscopic scission-point model is used, whereby the individual potential of each fragment is derived in the framework of HFB microscopic calculations with the Gogny effective nucleon-nucleon force.

This experiment was performed at the on-line isotope separator ISOLDE (CERN, Geneva) [25] and was part of a systematic α, β and β-delayed fission study of a series of neutron-deficient thallium isotopes $^{178-182}$Tl. A dedicated β-decay study of ^{180}Tl has been described in our recent paper [26] and we concentrate here on the βDF results only. The present paper provides experimental details and improved analysis of the data reported in Ref. [15]. The βDF study of ^{178}Tl, resulting from the same set of experiments, is reported in the accompanying paper [27].

The structure of the paper is as follows: Section II gives the description of the experimental setup and measurement procedure, followed by the energy calibration of the silicon detectors in Sec. III. The obtained results, including the energy and mass distributions, are then discussed in Sec. IV.

II. EXPERIMENTAL SETUP

The thallium isotopes of interest were produced by proton-induced spallation reactions of a thick uranium target at ISOLDE. The proton beam from the PS-booster of CERN, having an energy of 1.4 GeV and an average intensity of 2.1 μA, impinged on a 50 g/cm^2 UC_x target, producing a wide variety of radioactive nuclei. The proton beam consisted of 2.4 μs proton bunches that had a period of 1.2 s or a multiple of 1.2 s. A sequence of 21 pulses was logically grouped into a so-called *supercycle* with a total length of 25.2 s. The number of proton pulses that ISOLDE received per supercycle was changed from four to ten pulses throughout the experiment, depending on the specific requirements,

as discussed further.

After production, the recoiling nuclei were stopped in the target material. The radioactive nuclei diffused out of the target matrix and effused towards the hot cavity where resonant laser ionization took place. In order to reduce the release time, the target-ion source was kept at a high temperature of ≈ 2300 K. In the Resonance Ionization Laser Ion Source (RILIS) [28] the desired thallium isotopes were resonantly excited from the atomic ground state to an intermediate electronic state by a frequency-doubled laser beam at 276.79 nm and subsequently ionized to a 1^+ charge state by a powerful 532.5 nm beam of 10 kHz pulsed Nd:YAG laser. The produced ions were extracted from RILIS, accelerated by a 30 keV electric field and separated according to their mass-to-charge ratio with the magnetic dipoles of the High Resolution Separator (HRS) of ISOLDE [29]. As a result of selective ionization with RILIS and subsequent mass analysis with HRS, a high-purity beam of ^{180}Tl nuclei was obtained.

To detect the radioactive decay of the ^{180}Tl nuclei, the Leuven windmill system was used, see Fig. C.11. After mass separation, the incident 30 keV Tl^+ ion beam of ~ 150 atoms/s was implanted in a 20 μg/cm^2 thick carbon foil. Ten of these carbon foils were mounted on a rotating wheel. The longer-living daughter products of ^{180}Tl were removed from the implantation position by rotating the wheel after each supercycle, which introduced the next foil to the implantation position. The time structure of the measurement is described in details in Fig. 2 of Ref. [26] and only the most relevant features are provided here. The time structure of the measurement was determined by the half-life of ^{180}Tl, which was known from literature to be 1.5(2) s [30]. Therefore, the proton pulses were chosen in such a way that two consecutive proton pulses with 1.2 s time between them were taken followed by a period without proton pulses. The opening of the separator gate, which allows the radioactive ions to pass towards the detection system, was synchronized with the proton pulse structure and was opened from the moment the first proton pulse arrived until 1.2 s after the second proton pulse (i.e. 2.4 s), after which the separator gate closed. Thus, during the first 2.4 seconds of the measurement, continuous implantation data were measured, followed by a period of pure decay, see Fig. 2 of Ref. [26]. Different groups of such two consecutive pulses were chosen during the experiment, depending on the specific type of measurements (α decay, β decay, βDF or half-life).

Two silicon detectors were placed in close geometry at the implantation position, as shown in Fig. C.11. An annular detector having an active area of 450 mm^2, thickness of 300 μm and a central hole with a diameter of 6 mm (Ortec Surface Barrier detector [31]) was positioned at a distance of ~ 7 mm upstream of the foil, so that the ion beam was passing through this hole before being implanted into the foil. A circular detector of active area 300 mm^2 and thickness 300 μm

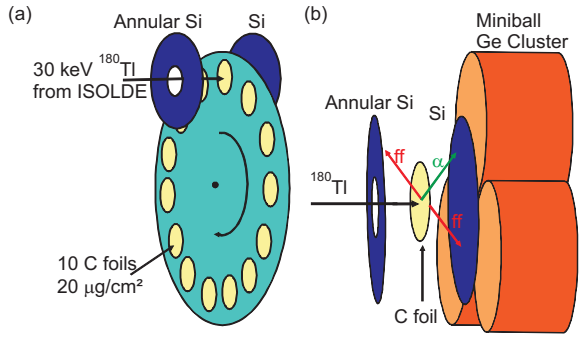

Figure C.11: (Color online) A schematic view of the windmill system is shown in (a) and a zoom of the detector arrangement in (b) [15].

(Canberra PIPS detector [32]) was placed $\sim$4 mm downstream of the foil. The use of two silicon detectors increases the geometrical efficiency and allows the measurement of double-fold fission fragments in coincidence. The total detection efficiency for an α particle or single fission fragment in any of the Si detectors was about 51 %, while coincident fission fragments were registered with an efficiency of about 16 %. These values are slightly lower than 66 % and 20 % given in our first paper [15]; this is attributable to a better estimation of the geometry of the setup, and relative positions between the foils and silicon detectors, made using GEANT4 simulations [33]. Note that this does not influence the determination of the βDF probability as it is normalized to the number of detected fission fragments and alphas detected in the same detector (see Sec. IV C). As the primary aim of this experiment was the detection of βDF, the energy range of the silicon-detector electronics was set to 200 keV-100 MeV to record events from electrons, positrons, α particles and fission fragments. The measured energy resolution (FWHM) for α decays in the range of 5000-7000 keV was $\sim$35 keV, which was mostly determined by the electronics owing to the necessity to cover a large energy range.

A Miniball germanium cluster detector, which consisted of three Hyper Pure Germanium (HPGe) crystals [34] and a planar germanium detector of the "low energy germanium (LeGe)" type [35] were placed in close geometry outside the vacuum chamber, to allow γ and K X-ray measurements in coincidence with α and β particles and fission fragments. The typical energy resolution (FWHM) of each crystal of the cluster and the LeGe detector for 1.3 MeV radiation was $\sim$3.1 keV. The analog signals from the preamplifiers were digitized using digital electronics (DGF-4C modules [36]) and for every decay event, the energy and time were recorded in the data system. One of the advantages of these

DGF modules is that the data can be stored in 64k channels, allowing a good resolution for the large energy range that should be covered.

III. ENERGY CALIBRATION PROCEDURE FOR SILICON DETECTORS

As a first step in the data analysis, a proper energy calibration of the silicon detectors in the fission fragment energy range of $\sim$40-100 MeV had to be performed. This calibration however is not straightforward, since semiconductor detectors suffer from what is known as the Pulse Height Defect (PHD). Owing to this effect, the total charge, which is proportional to the pulse height (PH), collected in the detector for a heavy ion is usually smaller than that of an α particle or a light ion for the same energy deposition inside the active volume of the silicon detector. Therefore, the measured pulse height is no longer strictly proportional to the energy of the incoming heavy ion, but will also depend on its mass [37,38]. The PHD is attributable to physical processes occurring in the detector's material, one of the most important being the increased recombination of charge carriers for the heavier ions, as they produce a denser ionization track in the silicon detector [39,40].

The importance of a proper account for the PHD effect for fission fragments with typical energies in the range of 30-120 MeV and masses of 40-150 amu is well-known, particularly in the experiments using silicon detectors. Specifically in the case of asymmetric fission, it is imperative to accurately account for different PHDs for the light and heavy masses. In the past, a special procedure to calibrate silicon detectors for such measurements was developed and by now became a well-accepted method [37,38].

For an incoming ion of a given mass, a linear relationship between pulse height x and energy E remains

$$E = C_1 x + C_2, \tag{C.1}$$

where C_1 and C_2 are constants. However, the PHD leads to a mass dependence of the coefficients C_1 and C_2. To study this effect, in their original work, Schmitt *et al.* [37] investigated the response of silicon detectors to ^{79,81}Br and ^{127}I ions that were accelerated in a Van de Graaff accelerator. Data were taken in the energy range between 30-120 MeV. They found that C_1 and C_2 are approximately linearly dependent on the ion mass:

$$E = (a + a'm)x + b + b'm, \tag{C.2}$$

where m is the mass of the incoming ion and a, a', b and b' are constants for a particular detector. Schmitt *et al.* [37] established a link between these constants and the mean pulse heights of the light and heavy fragment group of a reference fissioning isotope, e. g. ^{252}Cf, through universal constants for that specific fissioning isotope. Later these constants were improved by Weisenberger *et al.* [38]. However, these constants are not used in the current calibration, as the authors of Ref. [38] already pointed out that their constants are deduced for one specific type of detectors (i. e. ORTEC [31] F-series, active area 100 mm^2). It is not sure that they can also be used for other types of silicon detectors. Therefore a new calibration measurement was performed at the Lohengrin spectrometer of the Institut Laue-Langevin (ILL) in Grenoble. Fission fragments resulting from the ^{235}U(n,f) reaction can be separated according to their mass-to-charge A/q and energy-to-charge E/q ratio by two dipole bending magnets. Our silicon detector was placed behind the Lohengrin spectrometer on a rotating holder, as such that it was possible to also measure the fission fragments at a certain angle with respect to the beam axis. Further, a ^{241}Am source was used as a reference source and was mounted at the backside of the detector. Without breaking the vacuum, the detector could then be rotated over 180° to either face the ^{241}Am source or the fission fragment beam direction. As such, the masses and energies of the fission fragments were measured for all except one of the used detectors in the current experiment. The one detector that was not re-calibrated, did not work anymore at the time of measurement at ILL. Another detector of the same type was calibrated and possible differences in the calibration are taken into account in the systematic error discussed below.

From these measurements, it was possible to deduce an alpha calibration relation of the form Eq. (C.1) and a calibration for the fission fragments using Eq. (C.2). By assuming that the offset (b and b' in Eq. (C.2)) remains constant and by taking the ratio of the gain of the fission calibration (a and a' in Eq. (C.2)) to that of the alpha calibration ($c = a/C_1$ and $c' = a'/C_1$), new constants for a specific detector can be deduced, namely c, c', b and b'. To calibrate the same detector in a new experiment, only the alpha calibration needs to be known. This alpha calibration can be scaled to the constants for that detector, by multiplying the gain of this calibration with c and c' to get the parameters a and a' in Eq. (C.2), while b and b' remain constant. Specific details on how this calibration procedure was developed will not be discussed here, but will be reported in [41]. The deduced calibration constants for the current experiment are

$$\begin{array}{lcl|lcl} a_1 & = & 1.814(18)\times10^{-3} & a_2 & = & 1.707(17)\times10^{-3} \\ a_1' & = & 1.8946(2)\times10^{-6} & a_2' & = & 2.4191(2)\times10^{-6} \\ b_1 & = & -0.57(43) & b_2 & = & 0.94(51) \\ b_1' & = & 3.57(44)\times10^{-2} & b_2' & = & 2.23(52)\times10^{-2} \end{array} \quad \text{(C.3)}$$

The index 1 is used for the annular detector (referred to as detector 1), 2 is used for the detector downstream of the foil (detector 2). These constants also have a systematic error, which follows primarily from the fact that the constants, determined for one specific detector, were deduced from the ^{235}U(n,f) reaction. The fission fragments resulting from this reaction have a different N/Z ratio in comparison with the fission fragments from the βDF of ^{180}Tl. In, for example Ref.[42-44], they all assume a strong influence on the PHD of the stopping power or thus the energy loss in a detector. Since, according to the Bethe-Bloch equation the energy loss in a detector depends primarily on the velocity and effective charge of the ions, in addition to the mass and energy, which are taken into account in Eq. (C.2), it is plausible that different N/Z-values would also correspond to different calibration constants. To estimate the systematic error on the calibration constants, the PHDs of different isotopes measured at ILL were compared. From this comparison it is clear that the PHD increases with about 1 MeV when increasing simultaneously the mass A with ten and the charge Z with four units. This is true for the mass range that covers the fragment distribution from the βDF of ^{180}Tl. In the βDF of ^{180}Tl, the most probable isotopes are ^{80}Kr ($Z=36$) and ^{100}Ru ($Z=44$) (see Sec. IV A). In the ^{235}U(n,f) reaction the most probable isotopes for the masses $A=80$, 90 and 100 are (see e. g. [45]) ^{80}Ge ($Z=32$), ^{90}Kr ($Z=36$) and ^{100}Zr ($Z=40$). One notices that for the same mass A, the charge Z is always higher in the case of the fission fragments from the βDF of ^{180}Tl. It is clear that for e. g. ^{80}Kr the PHD should lie between the PHD of ^{80}Ge and ^{90}Kr. Therefore the calibrated energy of ^{80}Kr should be shifted with 0.5 MeV with a systematic error of 0.5 MeV. This argumentation holds for every fragment detected in the βDF of ^{180}Tl.

Figure C.12 shows the PH (uncalibrated) spectra obtained in the case of the βDF decay of ^{180}Tl. This figure alone clearly demonstrates the asymmetric mass split of ^{180}Hg. Eq. (C.2) along with the momentum and mass conservation laws can now be used to calibrate the fission spectra of ^{180}Hg according to this set of expressions:

$$\begin{cases} E_1 = (a_1 + a_1' m_1)x_1 + b_1 + b_1' m_1 \\ E_2 = (a_2 + a_2' m_2)x_2 + b_2 + b_2' m_2 \\ m_1^\star E_1^\star = m_2^\star E_2^\star \\ m_1^\star + m_2^\star = A_f = 180 \end{cases} \quad \text{(C.4)}$$

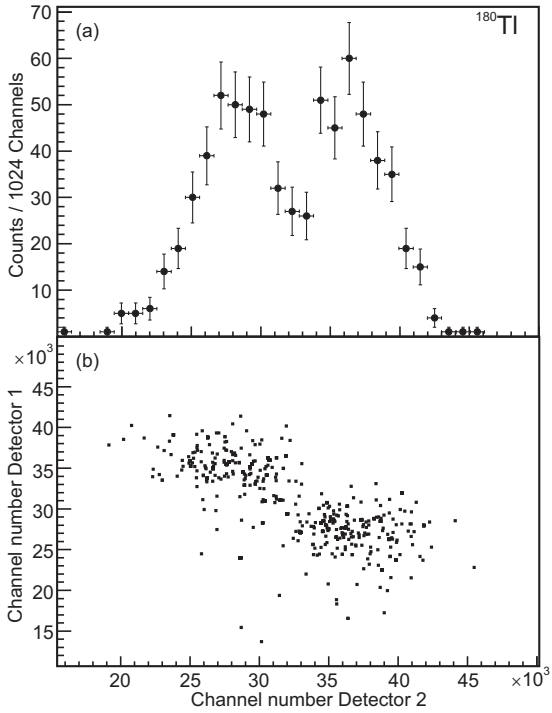

Figure C.12: (a) Uncalibrated energy spectrum of single fission events in the βDF of ^{180}Tl in detector 2. (b) Uncalibrated energy spectrum of coincident fission events in the βDF of ^{180}Tl (344 in total). Detector 1 is the annular detector located upstream and detector 2 is the one downstream of the carbon foil.

Here, x_i are the *measured* pulse heights of the fission fragments in the detector i ($i = 1, 2$) (see Fig. C.12), while E_i, m_i are their resulting energies and masses, which we aim to deduce. If neutron emission occurs in the fission process, E_i, m_i are the quantities after neutron emission (*post*-neutron quantities). $E_i^\star$ and $m_i^\star$ are the corresponding initial quantities, before neutron emission during fission, thus the *pre*-neutron quantities [46] and $A_f = 180$ is the mass number of the fissioning ^{180}Hg nucleus. By using this calibration procedure it is only possible to calibrate coincident fission events, since the measured pulse height of both fission fragments will have to be inserted simultaneously in the above equations.

We use $A_f = 180$ because the neutron separation energy $S_n(^{180}\mathrm{Hg}) = 11390(30)$ keV [47] is above the $Q_{EC}(^{180}Tl) = 10840(120)$ keV [47], thus preventing neutron emission from ^{180}Hg after the β decay of ^{180}Tl. The proton separation energy is $S_p(^{180}\mathrm{Hg}) = 2582(22)$ keV [47], but owing to the Coulomb barrier, the β-delayed proton emission probability is very small. Further, Hg K X rays in coincidence with fission fragments were observed and a half-life of ^{180}Tl was deduced from the β-delayed fission branch that is in agreement with the half-life determined from the α- and β-delayed γ decay branch (see further in the text, Fig. C.17 and Sec. IV B).

In order to solve this system of equations the quantities E_i and $E_i^\star$ and m_i and $m_i^\star$ have to be related. This can be done by taking into account the number of neutrons emitted in the fission ν_i, the corresponding energy carried away by the neutrons $\Delta E_{i,\nu}$, and the energy loss of the fission fragment owing to their interaction with matter during their flight from the source to the active volume of the silicon detector $\Delta E_{i,int} = \Delta E_{i,cf} + \Delta E_{i,dl}$. The latter contribution consists of the energy loss of the fragment in the implantation carbon foil $\Delta E_{i,cf}$ and in the dead layer of the detector $\Delta E_{i,dl}$ (which will increase when the fragments are detected at a certain angle). These considerations lead to the following relations

$$\begin{cases} E_i^\star &= E_i + \Delta E_{i,\nu} + \Delta E_{i,int} \\ &= E_i + \Delta E_{i,\nu} + \Delta E_{i,cf} + \Delta E_{i,dl} \\ m_i^\star &= m_i + \nu_i \end{cases} \tag{C.5}$$

In the determination of the calibration parameters, the $\Delta E_{i,dl}$ term is already taken into account in the constants a through b' if the fragments are detected under the same angle. However, our calibration constants were determined for perpendicular impingement, while the fragments in the βDF of ^{180}Tl were detected at a certain angle. Also, the $\Delta E_{i,cf}$ cannot simply be neglected, since the fission fragments from which the calibration parameters were deduced, did not need to penetrate the carbon foil.

In the literature, to estimate the energy loss caused by the emitted neutrons $\Delta E_{i,\nu}$ in the fission of trans-uranium nuclei, a procedure introduced by Balagna *et al.* [48], is used, see e.g. Fig. 8 in Ref. [49]. This procedure relies on the knowledge of the average number of neutrons emitted as a function of fragment mass, $\tilde{\nu}(M)$, which was measured for e.g. ^{257}Fm in Ref. [48] and which showed a staggering behavior in the range of $\tilde{\nu} \sim$ 1-4. As no such data exist for the very neutron-deficient nuclei in the lead region, we used a simplified estimate, as described below. However, anticipating the discussion below, we mention that based on our analysis we concluded that most probably only one neutron could be emitted in the fission of ^{180}Hg. The corresponding correction of the mass

distributions owing to the neutron emission should thus be much less than in the uranium region, where values up to $\tilde{\nu} \sim 4$ are observed.

In our case, to estimate the energy loss caused by the emitted neutrons $\Delta E_{i,\nu}$, we use the generally accepted assumption that the neutrons are emitted after the fission fragments have reached their maximum velocity $v_i^\star$. Secondly, it is assumed that the average velocity of the fission fragments is not changed by the emission of neutrons, because the neutrons will be emitted isotropically in the center of mass (the velocity distribution however will be broadened). These two assumptions are supported experimentally [1]. The average energy of the fragments after neutron emission can then be estimated by (neglecting the recoil energy [46])

$$\bar{E}_i \approx \frac{1}{2} m_i v_i^2 = \frac{1}{2} m_i {v_i^\star}^2 = \frac{m_i}{m_i^\star} E_i^\star \tag{C.6}$$

With this expression $\Delta E_{i,\nu}$ is given by

$$\Delta E_{i,\nu} = E_i^\star - E_i = \frac{\nu_i}{m_i^\star} E_i^\star \tag{C.7}$$

This gives the following set of equations that have to be solved iteratively (with $F_i = 1 - \nu_i / m_i^\star$)

$$\begin{cases} E_i^\star = (a_i/F_i + a_i' m_i^\star) x_i + b_i/F_i + b_i' m_i^\star \\ \qquad\quad + \Delta E_{i,cf}/F_i + \Delta E_{i,dl}/F_i \\ m_1^\star E_1^\star = m_2^\star E_2^\star \\ m_1^\star + m_2^\star = A_f \end{cases} \tag{C.8}$$

In a first approximation F_i will be set equal to one by setting the number of emitted neutrons ν_i to zero. In Sec. IV A we will return to this issue. The system of equations Eq. (C.8) can now be solved with respect to $m_1^\star = m_1$ (when $F_i = 1$ or $\nu_i = 0$). It follows that $m_1^\star$ must be the solution of a quadratic equation

$$A {m_1^\star}^2 + B m_1^\star + C = 0 \tag{C.9}$$

with

$$\begin{aligned} A &= a_1' x_1 + b_1' - a_2' x_2 - b_2' \\ B &= a_1 x_1 + b_1 + a_2 x_2 + b_2 + 2 A_f a_2' x_2 + 2 A_f b_2' \\ &\quad + \Delta E_{i,cf} + \Delta E_{i,dl} \\ C &= -A_f (a_2 x_2 + a_2' A_f x_2 + b_2 + A_f b_2') \end{aligned}$$

To solve this equation the energy loss in the carbon foil and the shift in energy necessary to account for the detection of fission fragments at a certain angle has to be known. These energy shifts, however, can only be estimated.

To determine the mean energy loss of the fission fragments in the carbon foil the program TRIM was used [50]. First, the distribution of the depth of implantation of the 30 keV ^{180}Tl beam was determined. This resulted in a mean implantation depth of d $\approx$ 180 Å, corresponding to the first $1/5^{th}$ part of the foil. This means that the fragments flying towards detector 1 will lose less energy than those flying towards detector 2. The distribution of the implantation depth was then used as an input to start the energy loss calculations for the fission fragments. A TRIM simulation was performed, for a range of isotopes with a different energy and mass. It was assumed that the fragments are randomly emitted in 4π. In addition, a beam spot size of 6 mm diameter with uniform density was included in the simulations. Finally, the size of the detectors (including the central hole in detector 1) was also taken into account. This resulted in a mean energy loss of 0.3(1) MeV for the fragments flying towards detector 1, and an energy loss of 1.2(3) MeV for the fragments flying to detector 2 (more details can be found in [51,52]). This energy loss was therefore taken into account by assuming that every fragment flying in direction of detector 2 loses 1.2 MeV and every fragment flying to detector 1 loses 0.3 MeV. This is only an estimation which will slightly depend on the angle of emission and mass/atomic number of the fission fragments.

To estimate the energy shift necessary to take into account the fact that the fission fragments are measured at a certain angle and do not impinge perpendicular on the detector, a dedicated measurement where the fission fragments were detected at an angle of 45° was performed during the ILL campaign. This angle is very close to the mean angle of impingement of about 43°. This measurement showed that the measured energy is smaller by about 0.3 MeV for detector 1 and about 1.0 MeV for detector 2 when the fission fragments reach the detector at an angle of 45°. However, this shift is also only an estimation, since the fission fragments reach the detectors at different angles. Therefore the systematic error on these shifts was taken as large as the shift itself.

With these energy shifts taken into account, Eq. (C.9) can be solved and gives the mass of the fragments detected in detector 1. The energy can further be deduced from Eq. (C.2). The mass of the fragments detected in detector 2 can be obtained by exchanging the labels 1 and 2 in the above equation, or simply from $m_2^\star = A_f - m_1^\star$.

As mentioned above, the used calibration procedure entails some systematic errors, which come from (i) errors on the deduced calibration constants due to

Table C.2: The different energy shifts and their systematic errors that need to be taken into account to determine the total kinetic energy are given. More details are given in the text.

Description	Shift and Systematic Error (MeV)
(i) N/Z-value detector 1	0.5(5)
(i) N/Z-value detector 2	0.5(5)
(ii) Angle detector 1	0.3(3)
(ii) Angle detector 2	1.0(10)
(iii) Carbon foil detector 1	0.3(1)
(iii) Carbon foil detector 2	1.2(3)
Total Systematic Errors	
Energy in detector 1	0.6
Energy in detector 2	1.2
TKE	1.3

the different N/Z-values, (ii) the fission fragments do not impinge the detector perpendicular but at a certain angle, while the calibration constants were deduced for perpendicular impingement and (iii) the energy loss in the carbon foil is not a constant, but varies according to the emission angle. These different energy shifts together with their systematic error are summarized in Table C.2. The total systematic error of the two detectors and of the Total Kinetic Energy (TKE) (see Sec. IV A) is also given. In the remainder of this article these total systematic errors will always be added to the statistical error of the quoted energies.

By using the procedures described in this section, we obtained the energy-calibrated and the mass spectra for fission fragments, which are discussed in the next section.

IV. EXPERIMENTAL RESULTS AND DISCUSSION

A. Energy and mass distributions resulting from the fission of ^{180}Hg

The mass spectrum for 344 coincident events is shown in Fig. C.13. The figure shows a mirror plane at $A = 180/2 = 90$, owing to the condition $m_2^\star = A_f - m_1^\star$. The result of the Gaussian fit gives $A_L = 80(1)$ amu for the light and

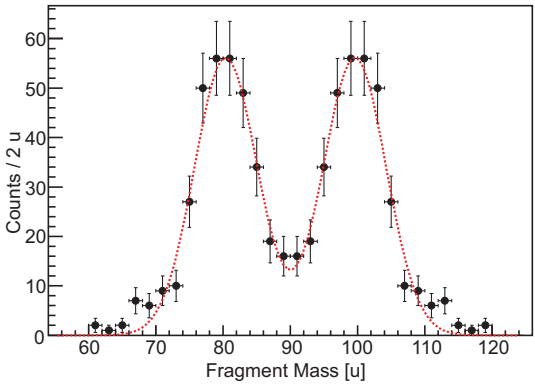

Figure C.13: (Color online) Mass distribution of the fission fragments. The red dotted line shows the Gaussian fit through the data.

$A_H = 100(1)$ amu for the heavy fragment with a full width at half maximum (FWHM) of FWHM = 10.9(5) amu for the mass distribution. From the data of the current experiment, it is not possible to deduce the Z value of the fission fragments. Therefore, the most probable Z values of the heavy and light fission fragments were deduced to be $Z_H = 44(2)$ and $Z_L = 36(2)$, respectively, by assuming that the N/Z = 1.25 ratio of the parent nucleus ^{180}Hg is approximately preserved in the fission fragments. This is a generally accepted approach in fission studies, but remains a simplification. Probably a wide range in Z-values is present among the fission fragments. Further, as the fissioning nucleus is an even-even nucleus, it is expected that the fission fragments will also be even-even nuclei, if no neutrons are emitted. These considerations lead to fission fragments in the vicinity of ^{80}Kr, which has N/Z = 1.22 and of ^{100}Ru, N/Z = 1.27, which are both accidentally stable nuclei, as the most probable fission fragments of ^{180}Hg. As is discussed below, the emission of one neutron is possible in the βDF of ^{180}Tl, which would lead to ^{79}Br, ^{80}Kr and ^{99,100}Ru as the most probable fission fragments, which are also all stable nuclei.

The fission energy distribution for 344 coincident events is shown in Fig. C.14 which, for the light fragment is centered around $E_L = 74.1(12)$ MeV (FWHM = 11.5(6) MeV) and for the heavy $E_H = 59.4(12)$ MeV (FWHM = 11.3(6) MeV), as deduced from a Gaussian fit through the data. The total kinetic energy (TKE) spectrum, determined by summing up the energies of coincident fragments is shown in Fig. C.15, which established the most probable total kinetic energy of TKE = 133.2(14) MeV with a FWHM = 15.0(9) MeV. It is interesting to note that the FWHM values obtained for the fission of ^{180}Hg are substantially smaller compared to those obtained from spontaneously fissioning nuclei in

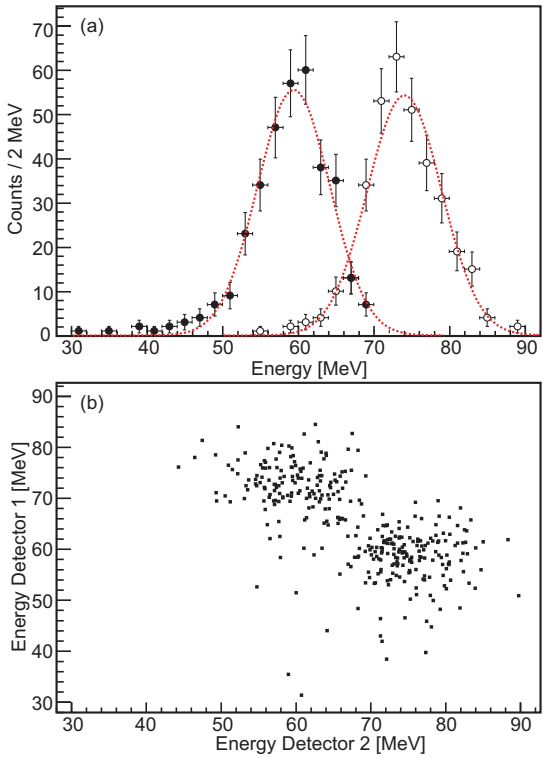

Figure C.14: (Color online) (a) Energy distribution of the fission fragments. The red dotted lines show the Gaussian fit through the data of the light and heavy fragment group. (b) Two-dimensional energy distribution of the fission fragments.

the heavy mass region (around ^{252}Cf) which are above 23 MeV [1].

The above values were deduced under the assumption of no neutrons being emitted, which was done to simplify the analysis. If neutrons are emitted, the previous results will slightly change. As neutron detectors were not employed in this experiment, no direct and precise information on the neutron emission and on the energy removed by neutrons can be extracted from our data. However, it is possible to infer the maximum number of neutrons that can be emitted in the fission of ^{180}Hg by comparing the calculated energy release $Q_{fis}(^{180}\mathrm{Hg})$ to the deduced most probable TKE(^{180}Hg), which obviously should be smaller than the Q_{fis}-value. The latter is determined as $Q_{fis}(A,Z) = \Delta M(A,Z) - \Delta M(A_1,Z_1) - \Delta M(A_2,Z_2)$, where $\mathrm{A} = \mathrm{A}_1 + \mathrm{A}_2$,

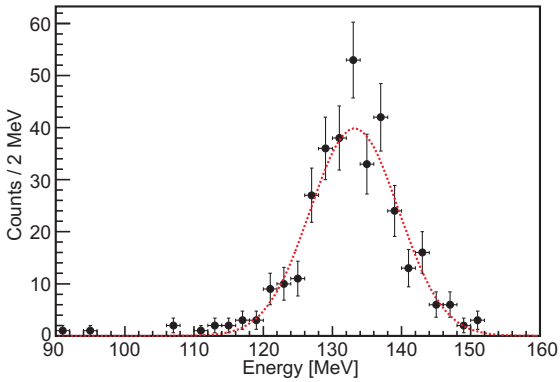

Figure C.15: (Color online) Total kinetic energy of the fission fragments. The red dotted line shows the Gaussian fit through the data.

$Z = Z_1 + Z_2$ and ΔM is the mass excess of the respective nuclei [47]. Figure C.16 shows the Q_{fis}-values for the most probable neutron-to-proton ratio $N/Z = 1.25$ of the light and heavy fragments as a function of the mass split fraction $M_{L,H}/180$. The three different symbols correspond to three different cases: a) no neutron emission, b) one neutron emission and c) two neutrons emission. In particular, assuming the fragments ^{100}Ru and ^{80}Kr (thus no neutron emission), the *maximum* fission energy release is $Q_{fis}(0n) = \Delta M(^{180}Hg) - \Delta M(^{100}Ru) - \Delta M(^{80}Kr) = 146.9$ MeV [47].

The maximum of the sum of the excitation energy of the two fission fragments can then be calculated as $E^*_{max,tot} = Q_{EC} + Q_{fis}(0n)$ - TKE $= 24.5$ MeV, by using the calculated value of $Q_{EC}(^{180}Tl) = 10.84(12)$ MeV [47]. This energy is available to be shared between the two fission fragments, γ rays and possibly emitted neutrons.

In Fig. C.17 γ rays in coincidence with the fission fragments can be seen. In the spectrum one clearly observes the Hg K X rays originating after the process of electron capture of the parent ^{180}Tl, implanted in the carbon foil. In contrast to the Hg K X rays, γ rays are emitted from excited states in the fission fragments while they fly towards the silicon detectors. Therefore these gamma transitions are Doppler shifted depending on their emission angle. This explains the non-observation of discrete γ lines, which could possibly be used to try to identify the fission fragments. The lack of statistics (only 1111 fission events were observed) and a relatively broad mass (and most probably, also charge) distribution is another reason for the non-observation of discrete gamma lines. The inset of Fig. C.17b shows the time difference between a fission fragment and

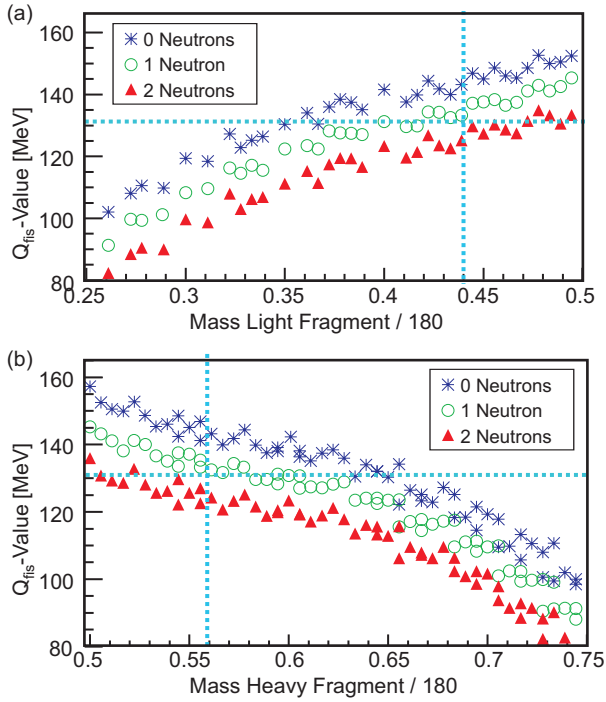

Figure C.16: (Color online) Q-values for the fission of ^{180}Hg for the ratio N/Z = 1.25(3) as a function of mass fraction, in (a) for the light fragment and (b) for the heavy fragment. The blue stars show the Q_{fis}-values for the case when no neutrons are emitted, the green dots for the emission of 1 neutron and the red triangles for the case of 2 neutron emission. The dotted blue lines give the measured most probable total kinetic energy and the most probable mass fraction for the light and heavy fragment. The masses are taken from Ref. [47].

a gamma ray, from this can be inferred that most gamma rays were detected in prompt coincidence with a fission fragment. Only 24 coincident fission-gamma events were observed in the interval of 0.5-40 μs, compared to 572 events within the coincidence window of 0.5 μs. This rules out the gamma decay from long-lived isomeric states in the fission products of ^{180}Hg.

The use of the three crystals of the Miniball (the electronic segmentation was not implemented in the current experiment) and a planar Ge detector allowed to get an estimate of the gamma multiplicity. γ rays up to a multiplicity of four were observed and the energy deposited in the Ge detectors reaches a maximum of 6.3 MeV, as can be seen in Fig. C.17b.

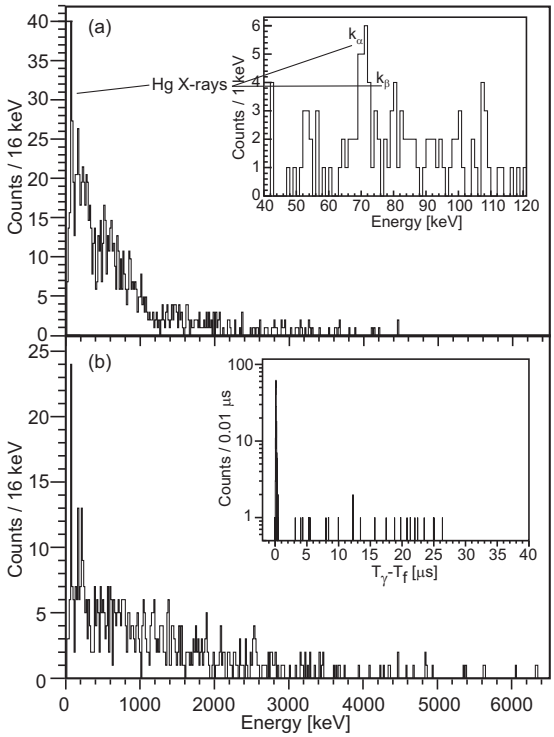

Figure C.17: (a) Gamma rays in coincidence within 0.5 μs of the detection of a fission fragment. (b) Summed gamma spectrum where the energy of gamma rays in coincidence with a fission fragment with a multiplicity larger than one are added up. No events were observed beyond 6.4 MeV. Data from both the Miniball cluster and the planar germanium detector were taken into account. The inset of (b) shows the time difference between between a fission fragment T_f and a gamma ray T_γ.

After accounting for the γ ray emission, we can conclude that there is only a small chance that two neutrons can be emitted in the βDF of ^{180}Tl. This is attributable to the relatively high neutron-separation energies S_n of nuclei in the vicinity of the most probable fission fragments ^{80}Kr and ^{100}Ru. Indeed, the sum of neutron separation energies $S_n(^{80}\mathrm{Kr})$=11.521(4) MeV and $S_n(^{100}\mathrm{Ru})$=9.67332(3) MeV [47] gives a value close to the total available $E^* \sim 24.5$ MeV. Barely enough energy is left to account for the kinetic energy of the two neutrons and the observed γ ray emission. We mention that based on the systematics in the uranium region, which should be sufficient similar

for the lead region, a typical mean kinetic energy of an emitted neutron in the center-of-mass system is expected to be about $\sim 0.74(2)$ MeV [53].

A similar analysis, performed for the case of a single neutron emission (see Fig. C.16, green open circles), suggests that the emission of one neutron is possible. In this case, the Q_{fis}(1n)-value is practically exhausted by the measured most probable TKE value, thus the total excitation energy of two fragments will be limited by the value of $Q_{EC}(^{180}\mathrm{Tl}) = 10.84(12)$ MeV. Owing to sharing of this energy between the two fragments, the emitted γ energy and kinetic energy of the neutron, the resulting individual excitation energies of each fragment will be below their respective S_n values. Therefore, it is hardly possible that a second neutron would be emitted, which also confirms the above analysis for the case of two neutron emission.

Accordingly we conclude that most probably only one neutron can be emitted in the fission of ^{180}Hg, although there is a small chance that two neutrons can be emitted. The following discussion is focused on the effect of the emission of one neutron on the mass and energy distribution. To calculate this effect, Eq. (C.8) has to be solved for $F_i \neq 1$. Here, we assume $\nu_i = 0.5$, since the total number of emitted neutrons is one, this corresponds to 0.5 neutrons emitted by each fission fragment. Eq. (C.8) can be solved through an iteration procedure by replacing a_i, b_i and $\Delta E_{i,cf}$ with a_i/F_i, b_i/F_i and $\Delta E_{i,cf}/F_i$ respectively in Eq. (C.9). The iteration process starts from the solution of Eq. (C.9) with $F_i = 1$, which gives the masses $m_i^\star$ when no neutrons are emitted. These can be used to calculate new factors F_i, which are used to solve Eq. (C.9) again, now with $F_i \neq 1$. This process is iterated until the solution obtained for $m_i^\star$ converges. This typically takes only a few iterations. By including one-neutron emission, the most probable TKE increases by about 0.8 MeV to TKE(1n) = 134.0(14) MeV (FWHM = 14.3(10) MeV), which is not that different from the value when no neutrons are emitted (TKE(0n) = 133.2(14) MeV).

A summary of all the properties of the fragments kinetic energy distribution of the βDF of ^{180}Tl can be found in Table C.3.

Now we turn to the discussion of the TKE values as a function of the mass split. As mentioned earlier and shown in Fig. C.13, apart from the dominant asymmetric mass split, a small contribution from symmetric-like events was also observed. The symmetric split of ^{180}Hg would be expected to lead to two semi-magic spherical nuclei ^{90}Zr, for which a compact scission configuration with a high total kinetic energy should result. This situation would be similar to the so-called 'high-TKE' symmetric fission mode observed in the spontaneous fission of e.g. ^{257,258}Fm, ^{258}No, ^{259,260}Md [48,54]. These nuclei demonstrate the phenomenon of bimodal fission with two distinctive groups of events with high- and low- TKE values. The events in the 'high-TKE' symmetric group

Table C.3: Fission properties of ^{180}Hg after β decay of ^{180}Tl. 0n and 1n denotes the case when respectively no and one neutron is emitted. All values are in MeV. Statistical uncertainties from the fit through the data are given in between brackets. Systematic uncertainties are shown in Table C.2.

βDF of ^{180}Tl	0n	1n
Total kinetic energy		
Most probable	133.2(14)	134.0(14)
FWHM	15.0(9)	14.3(10)
Heavy fragment energy		
Most probable	59.4(12)	59.6(12)
FWHM	11.3(6)	10.7(5)
Light fragment energy		
Most probable	74.1(12)	74.6(12)
FWHM	11.5(6)	11.3(6)

have typical TKE values in the region of 230-234 MeV, which is larger by about 30 MeV than the TKE values for the 'low-TKE' group. The higher TKE values are believed to occur because both fission fragments approach doubly-magic spherical ^{132}Sn, which leads to a compact scission configuration. The TKE as a function of mass split for this mode demonstrates a continuous increase approaching the symmetric mass split, see e.g. Fig. 4a of Ref. [48] for ^{257}Fm. In contrast, in the low-TKE mode, both fission fragments are believed to be strongly deformed, which results in an elongated scission shape with a lower TKE value. Quite often, in this mode the TKE value slightly decreases by approaching the symmetric mass split, see e.g. Fig. 4b of Ref. [48] for ^{254}Cf, which points to even more strongly-deformed shapes at scission.

A contour plot of the TKE distributions as a function of mass fraction for βDF of ^{180}Tl is shown in Fig. C.18. Because only 344 coincident pairs were measured, rather coarse data grouping of 7 MeV $\times$ 0.02 mass fraction units was used, and a smoothing procedure was utilized to obtain intermediate values. The mean TKE value for each mass interval of 0.02 mass fraction units is also shown in the plot by the full circles. Such a plot can shed more light on the specific configuration, e.g. elongation and Z_1 and Z_2, of the fragments at the scission point.

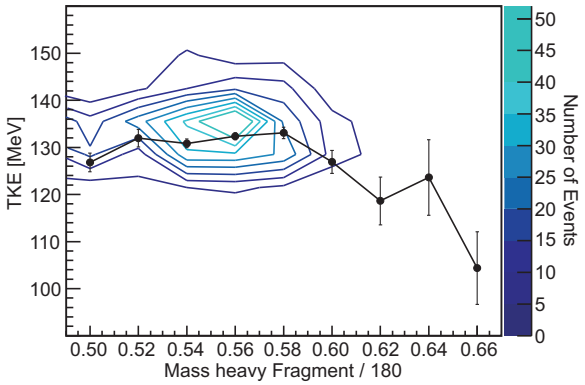

Figure C.18: (Color online) Contour diagram for the fission yield as a function of total kinetic energy and mass fraction of the heavy fragment. To draw the contours a data grouping of 7 MeV $\times$ 0.02 mass fraction units was used. The color scale gives the number of events within a contour, every contour denotes an increment of five events. The average total kinetic energy over intervals of 0.02 mass fraction units is also shown by the black dots.

An interesting and somewhat unexpected feature of this figure is that the mean TKE for the symmetric-like fission of ^{180}Hg (mass fraction of 0.5) is about the same as the mean TKE for the observed most probable asymmetric mass split (mass fraction of $100/180 = 0.56$). As shown in Fig. C.16 the Q-value for symmetric mass split has the highest value, therefore the intrinsic excitation energy TXE, being the difference of Q-value and TKE, should also become maximal at the symmetric mass split. This might result in a faster washing out of the shell effects which could be present along the symmetric fission path. This might then lead to the enhanced probability of the symmetric mass split, however, no solid conclusions can be drawn here owing to the limited number of events observed at the mass-symmetric split.

Figure C.19 compares the deduced most probable TKE values for ^{180}Hg with the known "low-TKE" data for the heavier nuclei and also with the Viola fit [55], shown by the black solid line. One can see that within the quoted experimental and systematical uncertainty the TKE(^{180}Hg) follows the systematics rather well.

B. Half-life of ^{180}Tl deduced from the βDF events

Based on the much more abundant α- and β-delayed γ decay data from the same experiment, a half-life value of $T_{1/2}(^{180}\mathrm{Tl}) = 1.09(1)$ s has been

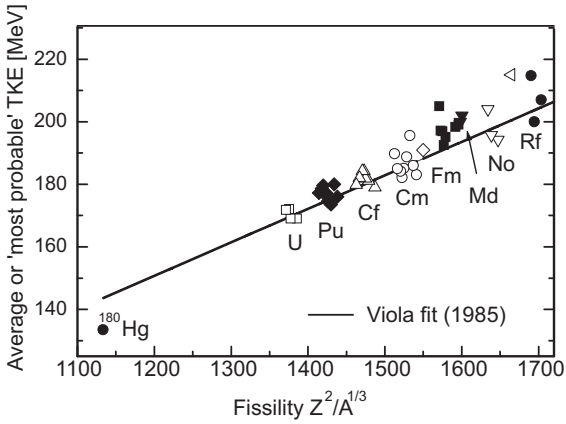

Figure C.19: A Viola plot [55], which shows the most probable TKE values for the "low-TKE" fission as a function of fissility for the known nuclei, together with the new value of ^{180}Hg (see text for details).

determined [15,26]. Here we will determine the $T_{1/2}$ value using the β-delayed fission branch. As mentioned in Sec. II, the proton pulses within the supercycle of 25.2 s were chosen in such a way that two consecutive (1.2 s apart) proton pulses were received, followed by a pure decay period of several seconds without protons, the whole sequence being repeated several times per supercycle (see also Fig. 2 of Ref. [26]). In the decay period, the implanted sample of ^{180}Tl decays without new implantation of thallium ions, which simplifies the half-life determination. Figure C.20 shows the 'decay curve' for the fission fragments resulting from the β-delayed fission of ^{180}Tl. To increase statistics, this figure was constructed by shifting in time the individual decay curves from four implantation-decay periods, corresponding to four groups of two protons within the supercycle. This decay curve was fitted by an exponential function (shown by the red dotted line) and a half-life value of $T_{1/2} = 0.94(25)$ s was deduced for the β-delayed fission of ^{180}Tl. This value is, within error bars, in agreement with the half-life determined from α and β decays [26,56]. The latter fact means that both the β decay of ^{180}Tl that feeds the fissioning state in ^{180}Hg and α decay of ^{180}Tl arise from the same state in ^{180}Tl, which is most probably the $I^\pi = (4^-,5^-)$ ground state proposed in Ref. [26] for this nucleus. The detailed α-decay [56] and β-decay [26] studies of ^{180}Tl did not provide any evidence for an isomeric state in this nucleus.

C. βDF probability of ^{180}Tl and fission barrier of ^{180}Hg

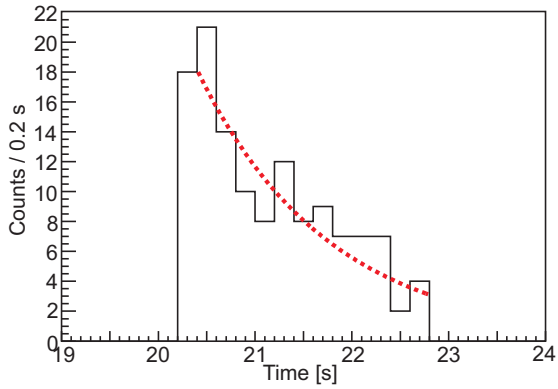

Figure C.20: (Color online) Half-life determination of ^{180}Tl through the β-delayed fission branch. The red dotted line is the exponential fit of the decay curve.

In our original Letter on the βDF of ^{180}Tl [15], the probability for β-delayed fission $\mathrm{P}_{\beta DF}(^{180}\mathrm{Tl}) = 3.6(7) \times 10^{-3}$ % was reported, based on 35 events which were selected for the analysis out of the total amount of 344 coincident fission fragments observed. The strong reduction of the number of events was attributable to the specific selection of events used to avoid the influence of the windmill movement after each supercycle of 25.2 s on the observed number of α decays of ^{180}Hg, which is necessary for the determination of $\mathrm{P}_{\beta DF}(^{180}\mathrm{Tl})$, see discussion below. This is because owing to the relatively long half-life of $T_{1/2}(^{180}\mathrm{Hg}) = 2.58(1)$ s, not all α-decays of ^{180}Hg were measured before the activity was removed from the implantation position. This loss was especially important for the implanted ions arriving at the end of the supercycle, thus such measurement periods were initially excluded from the analysis. We note that owing to the $\sim$1 s half-life of ^{180}Tl and the fact that the last implantation within the supercycle happened at least 3 s before the end of the supercycle, the influence of the windmill movement on the detection of the fission events was minimal.

In the present analysis, we were able to use the single fission events measured in the silicon detector 2. Thus increasing the total number of useful events to 533, which resulted in a more precise determination of the $\mathrm{P}_{\beta DF}(^{180}\mathrm{Tl})$ value. We also implemented a dedicated analysis procedure to account for the loss of α decays of ^{180}Hg owing to the windmill movement. This loss can be determined by fitting the activity of the α decays of ^{180}Hg with an exponential multi-

generational decay equation. Once the parameters of this fit are determined, one can calculate the fraction of α particles that are lost by the movement of the wheel inside the windmill (details can be found in [51]). This procedure reliably calculates the loss of decays as a function of the implantation time within the supercycle.

By definition, the probability of β-delayed fission of ^{180}Tl can be determined through

$$\begin{aligned} P_{\beta DF} &= \frac{N_{\beta DF}}{N_{\beta}(^{180}Tl)} \\ &= \frac{N_{\beta DF}}{N(^{180}Hg)} \\ &= \frac{N_{\beta DF}}{2 \cdot N_{\alpha}(^{180}Hg)/b_{\alpha}(^{180}Hg)} \end{aligned} \tag{C.10}$$

in which $N_{\beta DF}$ is the number of observed fission events, $N_{\beta}(^{180}Tl)$ is the total number of ^{180}Tl nuclei that decay through β decay, $N(^{180}Hg)$ and $N_{\alpha}(^{180}Hg)$ are the total number of daughter mercury nuclei, and the number of α decays of ^{180}Hg, respectively. As mentioned above, the number of α decays of ^{180}Hg was corrected for the effect of the windmill movement. The second equality relies on the fact that no direct production of ^{180}Hg is possible in our method, owing to the negligible probability of mercury isotopes, which are abundantly produced in the ISOLDE target, to be ionized and extracted from the target, see detailed discussion in Ref. [26]. Therefore, all ^{180}Hg observed in our spectra can only originate after the β decay of ^{180}Tl. The total number of ^{180}Hg nuclei can be determined from the observed (corrected) number of its α decay via the expression $N(^{180}\mathrm{Hg}) = N_{\alpha}(^{180}Hg)/b_{\alpha}(^{180}\mathrm{Hg})$ (see the third equality in Eq. (C.10)) with the use of the known branching ratio $b_{\alpha}(^{180}\mathrm{Hg}) = 48(2)\,\%$ [30]. The factor of 2 in the third equality stems from the fact that observing and measuring a fission fragment is twice as probable as observing an α particle. This is attributable to the fact that fission fragments are always emitted in pairs, flying in opposite directions. The resulting β-delayed fission probability is $P_{\beta DF}(^{180}\mathrm{Tl}) = 3.2(2) \times 10^{-3}\,\%$.

This result is consistent, within error bars, with the less precise value of $P_{\beta DF} = 3.6(7) \times 10^{-3}\,\%$ which was reported in our original Letter [15].

In the work of Lazarev *et al.* [57] a value of $P_{\beta DF}(^{180}\mathrm{Tl}) = 3 \times 10^{-(5\pm1)}\,\%$ was reported. It was deduced from the ratio of the measured fission cross section and estimated production cross section of $\sigma(^{180}\mathrm{Tl}) \sim 0.1\text{-}1\,\mathrm{mb}$ in the reaction $^{40}\mathrm{Ca} + ^{144}\mathrm{Sm} \rightarrow ^{180}\mathrm{Tl} + \mathrm{p3n}$, see also Ref. [14]. The latter rough estimate was made by the authors of Ref. [14] based on the statistical model code.

To test the correctness of this value, we performed our own statistical model calculations of the expected production cross section of ^{180}Tl in the $^{40}\mathrm{Ca} + {}^{144}\mathrm{Sm} \rightarrow {}^{180}\mathrm{Tl} + \mathrm{p3n}$ reaction. Calculations were based on the analysis of the production cross section data recently obtained in the Pb-Po region of nuclei with a large set of similar complete-fusion reactions with heavy ions, see e.g. Ref. [58] and references therein. The obtained $\sigma(^{180}\mathrm{Tl})$ was in the range of several μb, which is $\sim$100-1000 times lower than the value estimated in Ref. [14]. If one now uses our cross-section estimate instead of 0.1-1 mb, used by Lazarev *et al.* , the $P_{\beta DF}(^{180}\mathrm{Tl})$ value from Ref. [57] will increase by the corresponding factor and will become comparable, within the uncertainties, with our value from the ISOLDE experiment.

The deduced $P_{\beta DF}(^{180}\mathrm{Tl})$ value can be used to estimate the value of the fission barrier height B_f for ^{180}Hg. For this procedure, the knowledge (experimental or theoretical) of several parameters is required, the most important being the $Q_{EC}(^{180}\mathrm{Tl})$, the β-decay strength function $S_\beta(^{180}\mathrm{Tl})$, the level density and the Γ_γ width for ^{180}Hg. Though admittedly somewhat model-dependent, this approach was applied in several earlier βDF studies in the transuranium and lead regions, see e.g. Ref. [59-62].

By using this framework, and employing several sets of input parameters to check the consistency of the analysis, the fission barrier of ^{180}Hg was estimated to be in the range of 6.76-8.96 MeV, see detailed discussion in our complementary work [62]. Despite the broad range, all values are consistently lower than all theoretical fission barriers which lie in the range of 9.69-11.40 MeV. This confirms the well-known discrepancy between the experimentally-deduced and calculated fission barriers for the extremely neutron-deficient nuclei [62].

D. Recent theoretical studies of the fission of mercury isotopes

In our first paper on βDF of ^{180}Tl, the 5D fission model [63] was used to explain the observed asymmetric mass split of fission fragments. Recently, fission fragment mass yield calculations for a long chain of even-A $^{174-188}$Hg isotopes were performed [20] using the Brownian Metropolis shape-motion treatment [64]. Both types of calculations are in agreement with each other and show asymmetric mass distributions with only a small contribution from a symmetric mass split. An interesting inference of the latter work was the prediction that the mass asymmetry will be preserved at higher excitation energies, at least up to $E^* = 40$ MeV, see Fig. 6 of Ref. [20]. It would be very important to check these predictions in the future experiments by using e.g. fusion-fission reactions with heavy ions.

Furthermore, in Ref. [65], the authors calculated and analyzed five-dimensional potential-energy surfaces of twelve even $^{178-200}$Hg isotopes in the very neutron-deficient region. The most important finding in this work is that it is only for nuclei in the range $180<A<190$ that the saddle region is somewhat shielded from the symmetric fusion valley by a moderately high ridge that also has some moderate extension in the elongation direction.

Another recent theoretical study of the fission of mercury isotopes was performed in Ref. [21]. The authors used the self-consistent nuclear density functional theory employing Skyrme and Gogny energy density functionals. The potential energy surfaces in multidimensional space of collective coordinates, including elongation, triaxiality, reflection-asymmetry, and necking, were calculated for ^{180}Hg and ^{198}Hg. The asymmetric fission valleys, well separated from fusion valleys associated with nearly spherical fragments, were found in both cases. Moreover, these calculations suggest ^{100}Ru/^{80}Kr as most probably mass split, consistent with our experimental findings.

In a different approach, by using what the authors call "improved scission-point" model [23], the mass distributions were calculated for induced fission of $^{180-196}$Hg isotopes. The asymmetric mass distribution of fission fragments of ^{180}Hg was also demonstrated, with the calculated mass distribution and mean total kinetic energy of fission fragments being in good agreement with the available experimental data. The drastic change in the shape of the mass distribution from asymmetric to symmetric was predicted with increasing mass number of the fissioning mercury isotope.

Finally, the authors of Ref. [24] used the recently developed microscopic scission-point model. This model goes far beyond the liquid drop description used in the original model of Wilkins *et al.* [22]. By using this model, the asymmetric fission mass distribution for ^{180}Hg at low energy could be described on the sole basis of the fragment structure and deformed shell effects.

Thus, it appears that the conclusion on the asymmetric mass split of ^{180}Hg is a robust one also from the theoretical point of view and is well reproduced by different modern theoretical approaches.

V. CONCLUSION

In the β-delayed fission of ^{180}Tl a symmetric mass distribution centered around the semi-doubly-magic nucleus ^{90}Zr, was expected in the fission of the daughter nucleus ^{180}Hg. Instead it was observed that ^{180}Hg fissions in two fragments of unequal mass centered around mass number $A = 80$ and 100. The most probable fission fragments were determined to be ^{100}Ru and ^{80}Kr. Based on the energy balance, most probably only one neutron could be emitted.

The Total Kinetic Energy for the different mass splits was compared and has, within error bars, the same most probable value for all observed fission fragment pairs.

Additionally to the above mentioned results, in the present work a β-delayed fission probability of $P_{\beta DF}(^{180}\mathrm{Tl}) = 3.2(2) \times 10^{-3}$ % was determined.

Recently several successful experiments have been conducted at ISOLDE-CERN searching for a β-delayed fission branch in other isotopes in the neutron-deficient lead region will shed more light on low-energy fission in this part of the nuclear chart.

ACKNOWLEDGEMENTS

We thank the ISOLDE collaboration for providing excellent beams and the GSI Target Group for manufacturing the carbon foils. This work was supported by FWO-Vlaanderen (Belgium), by GOA/2010/010 (BOF KULeuven), by the IAP Belgian Science Policy (BriX network P6/23), by the European Commission within the Seventh Framework Programme through I3-ENSAR (contract no. RII3-CT-2010-262010), by a grant from the European Research Council (ERC-2011-AdG-291561-HELIOS), by the United Kingdom Science and Technology Facilities Council (STFC), by the Slovak grant agency VEGA (Contract No. 2/0105/11 1/0613/11), by the Slovak Research and Development Agency (No. APVV-0105-10) and by the Reimei Foundation of Advanced Science Research Center (ASRC) of JAEA (Tokai, Japan).

---

[1] C. Wagemans *The Nuclear Fission Process* (CRC Press, Boca Raton, FL, 1991), and references therein.

[2] H. L. Hall *et al.* , J. Radiol. Nucl. Chem. **142**, 53 (1990).

[3] R. Vandenbosch, Annu. Rev. Nucl. Part. Sci. **27**, 1 (1977).

[4] A. Bail *et al.* , Phys. Rev. C **84**, 034605 (2011), and references therein.

[5] K. -H. Schmidt *et al.* , Nucl. Phys. A **693**, 169 (2001).

[6] K. -H. Schmidt *et al.* , Nucl. Phys. A **665**, 221 (2000).

[7] V. I. Kuznetzov and N. K. Skobelev, Yad. Fiz. **4**, 279 (1966).

[8] H. L. Hall and D. C. Hoffman, Annu. Rev. Nucl. Part. Sci. **42**, 147 (1992).

[9] M. G. Itkis *et al.* , Sov. J. Nucl. Phys. **52**, 601 (1990).

[10] M. G. Itkis *et al.* , Sov. J. Nucl. Phys. **53**, 757 (1991).

[11] D. A. Shaughnessy *et al.* , Phys. Rev. C **61**, 044609 (2000).

[12] D. A. Shaughnessy *et al.* , Phys. Rev. C **65**, 024612 (2002).

[13] S. A. Kreek *et al.* , Phys. Rev. C **49**, 1859 (1994).

[14] Y. A. Lazarev *et al.* , Europhys. Lett. **4**, 893 (1987).

[15] A. N. Andreyev *et al.* , Phys. Rev. Lett. **105**, 252502 (2010).

[16] A. N. Andreyev *et al.* , Phys. Rev. C **87**, 014317 (2013).

[17] J. F. W. Lane *et al.* , Phys. Rev. C **87**, 014318 (2013).

[18] A. N. Andreyev, M. Huyse, and P. Van Duppen, Rev. Mod. Phys. **85**, 1541 (2013).

[19] P. Möller, A. J. Sierk, T. Ichikawa, A. Iwamoto, R. Bengtsson, H. Uhrenholt, and S. Aberg, Phys. Rev. C **79**, 064304 (2009).

[20] P. M¨oller, J. Randrup, and A. J. Sierk, Phys. Rev. C **85**, 024306 (2012).

[21] M. Warda, A. Staszczak, and W. Nazarewicz, Phys. Rev. C **86**, 024601 (2012).

[22] B. D. Wilkins *et al.* , Phys. Rev. C **14**, 1832 (1976).

[23] A. V. Andreev, G. G. Adamian, and N. V. Antonenko, Phys. Rev. C **86**, 044315 (2012).

[24] S. Panebianco, J. L. Sida, H. Goutte, J. F. Lemaitre, N. Dubray, and S. Hilaire, Phys. Rev. C **86**, 064601 (2012).

[25] E. Kugler, Hyperfine Interact. **129**, 23 (2000).

[26] J. Elseviers *et al.* , Phys. Rev. C **84**, 034307 (2011).

[27] V. Liberati *et al.* , preceding paper, Phys. Rev. C **88**, 044322 (2013).

[28] V. N. Fedosseev *et al.* , Rev. Sci. Instrum. **83**, 02A903 (2012).

[29] T. J. Giles *et al.* , Nucl. Instrum. Methods Phys. Res. , Sect. B **204**, 497 (2003).

[30] ENSDF-Evaluated Nuclear Structure Data File, http://www. nndc. bnl. gov-/ensdf/

[31] Ortec, http://www. ortec-online. com.

[32] Canberra, http://www. canberra. com.

[33] S. Agostinelli *et al.* , Nucl. Instrum. Methods Phys. Res. , Sect. A **506**, 250 (2003).

[34] J. Eberth *et al.* , Progr. Part. Nucl. Phys. **46**, 389 (2001).

[35] P. Van Duppen *et al.* , Nucl. Instrum. Methods Phys. Res. , Sect. A **254**, 401 (1987).

[36] X-ray Instruments Associates, http://www. xia. com.

[37] H. W. Schmitt *et al.* , Phys. Rev. **137**, B837 (1965).

[38] E. Weissenberger *et al.* , Nucl. Instrum. Methods Phys. Res. , Sect. A **248**, 506 (1986).

[39] E. P. Steinberg *et al.* , Nucl. Instrum. Methods **99**, 309 (1972).

[40] E. C. Finch *et al.* , Nucl. Instrum. Methods **113**, 29 (1973).

[41] L. Ghys *et al.* (private communication).

[42] E. C. Finch *et al.* , Nucl. Instrum. Methods **142**, 539 (1977).

[43] M. Ogihara *et al.* , Nucl. Instrum. Methods Phys. Res. , Sect. A **251**, 313 (1986).

[44] A. Menchaca-Rocha *et al.* , Nucl. Instrum. Methods Phys. Res. , Sect. B **207**, 356 (2003).

[45] Janis 3, http://www. oecd-nea. org/janis/

[46] H. W. Schmitt *et al.* , Phys. Rev. **141**, 1146 (1966).

[47] G. Audi *et al.* , Nucl. Phys. A **729**, 337 (2003).

[48] J. P. Balagna *et al.* , Phys. Rev. Lett. **26**, 145 (1971).

[49] D. C. Hoffman *et al.* , Phys. Rev. C **41**, 631 (1990).

[50] SRIM-The Stopping and Range of Ions in Matter, http://www. srim. org/

[51] J. Elseviers, MasterŠs thesis, University of Leuven, Faculteit Wetenschappen, 2009.

[52] S. Sels, MasterŠs thesis, University of Leuven, Faculteit Wetenschappen, 2013. [53] J. Terrel, Phys. Rev. **127**, 880 (1962).

[54] E. K. Hulet *et al.* , Phys. Rev. C **40**, 770 (1989).

[55] V. E. Viola, K. Kwiatkowski, and M. Walker, Phys. Rev. C **31**, 1550 (1985).

[56] A. N. Andreyev (private communication).

[57] Y. A. Lazarev *et al.* , Inst. Phys. Conf. Ser. **N132**, 739 (1992).

[58] A. N. Andreyev *et al.* , Phys. Rev. C **72**, 014612 (2005).

[59] D. Habs *et al.* , Z. Phys. A **285**, 53 (1978).

[60] A. Staudt, M. Hirsch, K. Muto, and H. V. Klapdor-Kleingrothaus, Phys. Rev. Lett. **65**, 1543 (1990).

[61] A. N. Andreyev *et al.* , Phys. Lett. B **312**, 49 (1993).

[62] M. Veselský *et al.* , Phys. Rev. C **86**, 024308 (2012).

[63] P. Möller *et al.* , Nature (London) **409**, 785 (2001).

[64] J. Randrup and P. Möller, Phys. Rev. Lett. **106**, 132503 (2011).

[65] T. Ichikawa, A. Iwamoto, P. Möller, and A. J. Sierk, Phys. Rev. C **86**, 024610 (2012).

Bibliography

[1] K. S. Krane, *Introductory Nuclear Physics*, John Wiley & Sons, 1988.

[2] R. F. Casten, *Nuclear Structure from a Simple Perspective*, Oxford University Press, 2000.

[3] J. Carlson and R. Schiavilla, *Rev. Mod. Phys.* **70**, 743 (1998).

[4] P. Navrátil et al., *Phys. Rev. Lett.* **99**, 042501 (2007).

[5] K. L. G. Heyde, *The Nuclear Shell Model*, Springer-Verlag, 1990.

[6] M. G. Mayer, *Phys. Rev.* **78**, 16 (1950).

[7] H. Grawe, Shell Model from a Practitioner's Point of View, in *The Euroschool Lectures on Physics with Exotic Beams, Vol. I*, Springer, Berlin Heidelberg, 2004.

[8] A. De Maesschalck, *The changing mean field in exotic nuclei: a shell-model point of view*, PhD thesis, Ghent University, Faculty of Science, 2006.

[9] K. L. G. Heyde, Nuclear Shell Model: From Single-Particle Motion to Collective Effects, 2012.

[10] M. Moinester et al., *Phys. Rev.* **179**, 984 (1969).

[11] O. Sorlin and M. G. Porquet, *Progr. Part. Nucl. Phys.* **61**, 602 (2008).

[12] K. Heyde and J. L. Wood, *Rev. Mod. Phys.* **83**, 1467 (2011).

[13] A. P. Zuker, *Phys. Rev. Lett.* **90**, 042502 (2003).

[14] E. Caurier et al., *Rev. Mod. Phys.* **77**, 427 (2005).

[15] T. Otsuka et al., *Phys. Rev. Lett.* **105**, 032501 (2010).

[16] T. Otsuka et al., *Phys. Rev. Lett.* **95**, 232502 (2005).

[17] T. Otsuka et al., *Phys. Rev. Lett.* **104**, 012501 (2010).

[18] K. Heyde et al., *Nucl. Phys. A* **466**, 189 (1987).

[19] B. Blank et al., *Phys. Rev. Lett.* **84**, 1116 (2000).

[20] M. Pomorski et al., *Phys. Rev. C* **83**, 061303 (2011).

[21] C. Engelmann et al., *Z. Phys. A* **352**, 351 (1995).

[22] P. T. Hosmer et al., *Phys. Rev. Lett.* **94**, 112501 (2005).

[23] E. M. Burbidge et al., *Rev. Mod. Phys.* **29**, 547 (1957).

[24] K. Sieja et al., *Phys. Rev. C* **85**, 051301 (R) (2012).

[25] ENSDF-Evaluated Nuclear Structure Data File, `http://www.nndc.bnl.gov/ensdf/`, 2013.

[26] O. Sorlin et al., *Phys. Rev. Lett.* **88**, 092501 (2002).

[27] G. Audi et al., *Nucl. Phys. A* **729**, 337 (2003).

[28] C. Mazzocchi et al., *Phys. Lett. B* **622**, 45 (2005).

[29] O. Perru et al., *Phys. Rev. Lett.* **96**, 232501 (2006).

[30] S. Rahaman et al., *Eur. Phys. J. A* **34**, 5 (2007).

[31] N. Bree et al., *Phys. Rev. C* **78**, 047301 (2008).

[32] B. Pritychenko et al., *Atomic Data and Nuclear Data Tables* **98**, 798 (2012).

[33] G. Kraus et al., *Phys. Rev. Lett.* **73**, 1773 (1994).

[34] T. Otsuka et al., *Phys. Rev. Lett.* **81**, 1588 (1998).

[35] J. Engel et al., *Phys. Lett. B* **389**, 211 (1996).

[36] R. Broda et al., *Phys. Rev. Lett.* **74**, 868 (1995).

[37] M. Bernas et al., *Phys. Lett. B* **113**, 279 (1982).

[38] C. Guénaut et al., *Phys. Rev. C* **75**, 044303 (2007).

[39] H. Grawe et al., *AIP Conf. Proc.* **561**, 287 (2001).

[40] K. Kaneko et al., *Phys. Rev. C* **74**, 024321 (2006).

[41] W. F. Mueller et al., *Phys. Rev. Lett.* **83**, 3613 (1999).

[42] E. Caurier et al., *Eur. Phys. J. A* **15**, 145 (2002).

[43] S. M. Lenzi et al., *Phys. Rev. C* **82**, 054301 (2010).

[44] K. Langanke et al., *Phys. Rev. C* **67**, 044314 (2003).

[45] F. Recchia et al., *Phys. Rev. C* **88**, 041302(R) (2013).

[46] W. F. Mueller et al., *Phys. Rev. C* **61**, 054308 (2000).

[47] C. J. Chiara et al., *Phys. Rev. C* **86**, 041304(R) (2012).

[48] M. Bernas et al., *J. Phys. (Paris) Lett.* **45**, 851 (1984).

[49] M. Girod et al., *Phys. Rev. C* **37**, 2600 (1988).

[50] R. Grzywacz et al., *Phys. Rev. Lett.* **81**, 766 (1998).

[51] F. Flavigny et al., β-decay studies of ^{68}Co, to be published.

[52] D. Pauwels et al., *Phys. Rev. C* **82**, 027304 (2010).

[53] R. Broda et al., *Phys. Rev. C* **86**, 064312 (2012).

[54] D. Pauwels et al., *Phys. Rev. C* **78**, 041307(R) (2008).

[55] A. Dijon et al., *Phys. Rev. C* **85**, 031301(R) (2012).

[56] Y. Tsunoda et al., submitted to Physical Review Letters.

[57] W. Darcey et al., *Nucl. Phys. A* **170**, 253 (1971).

[58] G. Bassani, N. M. Hintz, and C. D. Kavaloski, *Phys. Rev.* **136**, B1006 (1964).

[59] W. G. Davies et al., *Phys. Lett. B* **27**, 363 (1968).

[60] H. Nann and W. Benenson, *Phys. Rev. C* **10**, 1880 (1974).

[61] B. F. Bayman and N. M. Hintz, *Phys. Rev.* **172**, 1113 (1968).

[62] W. P. Alford et al., *Phys. Rev. C* **21**, 1203 (1980).

[63] G. Bruge and R. F. Leonard, *Phys. Rev. C* **2**, 2200 (1970).

[64] J. H. Bjerregaard et al., *Nucl. Phys. A* **103**, 33 (1967).

[65] S. Hinds et al., *Phys. Lett.* **21**, 328 (1966).

[66] S. M. Smith and A. M. Bernstein, *Nucl. Phys. A* **125**, 339 (1969).

[67] H. Hefele, U. Lynen, and R. Santo, *Nucl. Phys. A* **157**, 93 (1970).

[68] J. P. Schapira et al., *Phys. Rev. C* **5**, 1593 (1972).

[69] J. H. Bjerregaard et al., *Nucl. Phys.* **89**, 337 (1966).

[70] G. J. Igo, P. D. Barnes, and E. R. Flynn, *Ann. Phys.* **66**, 60 (1971).

[71] G. J. Igo, P. D. Barnes, and E. R. Flynn, *Phys. Rev. Lett.* **24**, 470 (1970).

[72] I. J.Thompson and F. M. Nunes, *Nuclear Reactions For Astrophysics*, Cambridge Unoversity Press, 2009.

[73] C. M. Perey and F. G. Perey, *Atomic Data and Nuclear Data Tables* **17**, 1 (1976).

[74] X. Li, C. Liang, and C. Chai, *Nucl. Phys. A* **789**, 103 (2007).

[75] A. J. Koning and J. P. Delaroche, *Nucl. Phys. A* **713**, 231 (2003).

[76] Y. Han, Y. Shi, and Q. Shen, *Phys. Rev. C* **74**, 044615 (2006).

[77] I. J. Thomspon, *Comput. Phys. Rep.* **7**, 167 (1988).

[78] J. Diriken, *Probing positive-parity states in* $^{67}_{28}Ni_{39}$ *through one-neutron transfer reactions*, PhD thesis, KU Leuven, Faculty of Science, 2013.

[79] J. Diriken et al., submitted to Phys. Rev. Lett., 2013.

[80] N. K. Glendenning, *Direct Nuclear Reactions*, World Scientific Publishing Co., 2004.

[81] B. A. Brown and W. D. M. Rae, Nushell@MSU, report, 2007.

[82] A. F. Lisetskiy et al., *Phys. Rev. C* **70**, 044314 (2004).

[83] J. M. Lohr and W. Haeberli, *Nucl. Phys. A* **232**, 381 (1974).

[84] H. An and C. Cai, *Phys. Rev. C* **73**, 054605 (2006).

[85] F. G. Perey, *Phys. Rev.* **131**, 745 (1963).

[86] F. D. Becchetti and G. W. Greenlees, *Phys. Rev.* **182**, 1190 (1969).

[87] R. L. Walter and P. P. Guss, *Rad. Effects* **95**, 73 (1986), 1985 Santa Fe Conf. Proc.

[88] B. A. Brown, private communication.

[89] J. P. Schiffer et al., *Phys. Rev. Lett.* **108**, 022501 (2012).

[90] K. Wimmer, *Discovery of the shape coexisting 0^+ state in ^{32}Mg*, PhD thesis, Technische Universität München, Fakultät für Physik, 2010.

[91] E. Kugler, *Hyperf. Int.* **129**, 23 (2000).

[92] V. N. Fedoseyev et al., *Hyperf. Int.* **127**, 409 (2000).

[93] V. N. Fedosseev et al., *Rev. Sci. Instrum.* **83**, 02A903 (2012).

[94] A. Jokinen et al., *Nucl. Instr. Meth. B* **126**, 95 (1997).

[95] V. N. Fedoseyev et al., *Nucl. Instr. Meth. B* **204**, 353 (2003).

[96] D. Habs et al., *Hyperf. Int.* **129**, 43 (2000).

[97] O. Kester et al., *Nucl. Instr. Meth. B* **204**, 20 (2003).

[98] J. Cederkäll et al., *Nucl. Phys. A* **746**, 17 (2004).

[99] F. Ames, J. Cederkäll, T. Sieber, and F. Wenander, The REX-ISOLDE Facility: Design and Commissioning Report, CERN, Geneva, 2005.

[100] D. Voulot et al., *Nucl. Instr. Meth. B* **266**, 4103 (2008).

[101] V. Bildstein et al., *Prog. Part. Nucl. Phys.* **59**, 386 (2007).

[102] V. Bildstein et al., *Eur. Phys. J. A* **48**, 85 (2012).

[103] A. N. Ostrowski et al., *Nucl. Instr. Meth. A* **480**, 448 (2002).

[104] V. Bildstein, *Exploring the island of inversion with the $d(^{30}Mg,p)^{31}Mg$ reaction*, PhD thesis, Technische Universität München, Fakultät für Physik, 2010.

[105] Micron Semiconductor Ltd., `http://www.micronsemiconductor.co.uk/`.

[106] Canberra, `http://www.canberra.com`.

[107] K. Wimmer et al., *Phys. Rev. Lett.* **105**, 252501 (2010).

[108] E. J. Sternglass, *Phys. Rev.* **108**, 1 (1957).

[109] H. Rothard, *Nucl. Instr. Meth. B* **146**, 1 (1998).

[110] N. Warr et al., *Eur. Phys. J. A* **49**, 40 (2013).

[111] X-ray Instruments Associates, `http://www.xia.com/DGF-4C.html`.

[112] Mesytec Detector Readout Systems, `http://www.mesytec.com`.

[113] R. Lutter et al., *Nucl. Sci.* **47**, 280 (2000).

[114] R. Lutter et al., *Marabou Data Acquisition*, `http://www.bl.physik.uni-muenchen.de/marabou/htmldoc/`, 2003.

[115] R. Lutter, *MED Data Structure*, `http://www.bl.physik.uni-muenchen.de/marabou/htmldoc/doc/MedStructure.pdf`, 2005.

[116] ROOT, A Data Analysis Framework, `http://root.cern.ch/drupal/`.

[117] J. F. Ziegler et al., *Nucl. Instr. Meth. B* **268**, 1818 (2010).

[118] M. Callens, Study of the ^{66}Ni(t,d)^{67}Ni transfer reaction in inverse kinematics, Master's thesis, KU Leuven, Faculty of Science, 2013.

[119] N. Kesteloot, Coulomb excitation of ^{200}Po studied at REX-ISOLDE with the Miniball γ spectrometer, Master's thesis, KU Leuven, Faculty of Science, 2010.

[120] G. Knoll, *Radiation Detection and Measurement*, John Wiley & Sons, 2000.

[121] S. Agostinelli et al., *Nucl. Instr. Meth. A* **506**, 250 (2003).

[122] O. Helene, *Nucl. Instr. Meth.* **212**, 319 (1983).

[123] J. A. Lay, L. Fortunato, and A. Vitturi, submitted to Physical Review C.

[124] H. W. Fielding et al., *Nucl. Phys. A* **269**, 125 (1976).

[125] W. P. Alford et al., *Nucl. Phys. A* **293**, 83 (1977).

[126] R. H. Day and W. C. Parkinson, *Phys. Rev. C* **10**, 941 (1974).

[127] J. L. Wood et al., *Phys. Rep.* **215**, 101 (1992).

[128] M. E. Cobern, D. J. Pisano, and P. D. Parker, *Phys. Rev. C* **14**, 491 (1976).

[129] J. Van de Walle et al., *Eur. Phys. J. A* **42**, 401 (2009).

[130] M. Lindroos et al., *Nucl. Instr. Meth. B* **266**, 4687 (2008).

[131] A. Herlert and Y. Kadi, *J. Phys.: Conf. Ser.* **312**, 052010 (2010).

[132] K. Alder and A. Winther, *Electromagnetic Excitation: Theory of Coulomb Excitation with Heavy Ions*, Noth Holland Publishing Company, 1975.

[133] L. P. Gaffney et al., Characterizing excited states in and around the semi-magic nucleus ^{68}Ni using Coulomb excitation and one-neutron transfer, CERN-INTC-2013-042 / INTC-P-398, 2013.

[134] C. Sotty et al., Characterization of the low-lying 0^+ and 2^+ states of ^{68}Ni, CERN-INTC-2013-051 / INTC-P-402, 2013.

[135] G. Vourvopoulos and J. D. Fox, *Phys. Rev.* **177**, 1558 (1969).

[136] D. Mücher et al., Study of the proton-neutron interaction around ^{68}Ni: Vibrational Structure of ^{72,74}Zn, CERN-INTC-2010-079 / INTC-P-289, 2010.

[137] A. H. Wuosmaa et al., *Nucl. Instr. Meth. A* **580**, 1290 (2007).

[138] J. C. Lighthall et al., *Nucl. Instr. Meth. A* **622**, 97 (2010).

[139] S. J. Freeman et al., A HELIcal Orbit Spectrometer (HELIOS) for HIE-ISOLDE, Letter of Intent, CERN-INTC-2010-031/INTC-I-099, 2010.

[140] B. B. Back et al., *Phys. Rev. Lett.* **104**, 132501 (2010).

[141] H. Álvarez-Pol et al., Direct and resonant reactions using an Active Target, CERN-INTC-2010-053 / INTC-I-119, 2010.

[142] R. Raabe et al., Study of ^{13}Be through isobaric analog resonances in the Maya active target, CERN-INTC-2011-018 / INTC-P-301, 2011.

FACULTY OF SCIENCE
DEPARTMENT OF PHYSICS AND ASTRONOMY
INSTITUTE FOR NUCLEAR AND RADIATION PHYSICS
Celestijnenlaan 200D box 2418
B-3001 Heverlee